Stellar Scintillation

and its Use in

Atmospheric Measurements

by

Laurence Campbell B.Sc.(Hons)

A thesis presented for the degree of

Doctor of Philosophy

in the department of

Physics and Mathematical Physics

at the

University of Adelaide

in January 1991

Table of contents

Table of contents (cont.)

Table of contents (cont.)

Table of contents (cont.)

Abstract

Starlight propagating down through the atmosphere acquires phase variations as it traverses turbulent regions containing fluctuations in refractive index. With further propagation these phase variations produce intensity fluctuations. The turbulence and the associated intensity fluctuations move with the wind, producing the familiar twinkling of the stars. This "stellar scintillation" is a subject of current research due to its application in the remote measurement of atmospheric parameters and in the study of the atmospheric propagation of laser beams.

The work reported in this thesis includes measurements of the characteristics of the stellar scintillation pattern and the development and testing of techniques to use stellar scintillation to measure atmospheric wind profiles and the atmospheric isoplanatic angle. These measurements required the development of analysis techniques for correction for photomultiplier afterpulsing and for correlation between multiple time series.

Observations of scintillation were made with two detectors whose small size and small minimum spacing allowed characteristics of the pattern to be measured at smaller scales than previously reported. Further, two recording modes (time series and frequency distribution) allowed more characteristics to be measured simultaneously. Measurements were made over a wide range of atmospheric conditions.

From these observations the general characteristics of the scintillation pattern are deduced and compared with previous work. Some results are presented which give insight into the nature of the mechanism by which the scintillation is produced.

Atmospheric wind measurements were made using a multiple-beam technique, the development and laboratory testing of which are presented. The tests showed that the position of the turbulence could be deduced with high precision. Application of the technique to stellar scintillation gave measurements of atmospheric wind speeds consistent with weather-station measurements.

A further technique was developed to measure the isoplanatic angle (the angle, looking upwards, over which the distortion produced by atmospheric turbulence is uniform) by a comparison of double and single star scintillation. Application of this technique showed that turbulence associated with the scintillation pattern was different for two paths separated by 21 μrad. Measurements under appropriate conditions confirmed that this technique can measure the isoplanatic angle associated with scintillation scales smaller than the lower limit of other methods.

Statement

This thesis contains no material which has been accepted for the award of any other degree or diploma in any University and, to the best of the author's knowledge and belief, it contains no material previously published or written by another person, except where due reference is made in the text of the thesis.

The author consents to this thesis being made available for photocopying and loan if applicable if it is accepted for the award of the degree.

Laurence Campbell

January 1991

Acknowledgements

I thank my supervisor, Dr. W. G. Elford, for his help, support and patience. The principle of the multiple-beam system developed in this thesis was suggested to me by Dr. Elford and I regret on his account that I did not publish details of it before it was independently developed elsewhere.

I thank the members of the Atmospheric Physics Group at the University of Adelaide for their support, which was given generously even though my work did not contribute to the aims of the group in the way that was originally intended. Dr. B. H. Briggs, Dr. R. A. Vincent, Dr. W. K. Hocking and Dr. I. M. Reid contributed to this project, both through their advice and through their ability, along with Dr. Elford, to provide the intellectual and technical environment necessary for this work. Credit is due to the technical staff of the group, including Mr. J. Welsby, Mr. A. Didenko and Mr. R. Hurn for general technical support. I have been aided by help from and discussion with other research students, including Mr. B. Ward, Mr. S. Young, Mr. R. Craig, Ms. S. Ball, Mr. D. Murphy, Mr. A. Phillips, Ms. J. Wang, Mr. S. Eckermann and Mr. D. Lesicar. Mr. B. Candy was especially helpful in his aid with fast pulse detection circuits.

I thank the Department of Physics and Mathematical Physics for its support of this project. I am particular indebted to Mr. J. Smith, of Electronic Services, for his advice and for keeping in service the obsolete high-voltage power supplies on which the observations depended. Mrs. J. Hobbs and Mr. A. Van Rood were very helpful in the procurement of equipment. Computing Officers, Mr. B. Inwood and Mr. M. Ferraretto, gave help that is much appreciated. I thank the staff of the workshop for their help, especially Mr. G. Eames. Mr. D. Creighton of the Mawson Institute for Antarctic Research often aided me with his advice on technical questions and his contribution towards improvement of the University's computing facilities is appreciated.

I thank the University of Adelaide for support in the form of a Postgraduate Scholarship under the University Research Grant and for the provision of computing facilities. I thank the Radio Research Board and the Australian Research Grants Scheme for financial support for this work.

Chapter 1 Introduction

1.1 Background

Starlight passing down through the atmosphere encounters turbulent regions in which the refractive index of the air varies over short distances. These refractive-index irregularities cause phase variations, distorting the initially plane wavefront of the light. With further propagation over a distance sufficient for diffraction to become significant, the phase variations produce intensity fluctuations in the starlight. As the refractive-index irregularities move with the atmospheric wind, the related diffraction patterns move or change at ground level, producing the familiar scintillation, or twinkling, of the stars.

This "stellar scintillation" provides a means of remote measurement of atmospheric phenomena. The simplest example is the deduction of wind velocity from the movement of the scintillation pattern. In recent years there has been substantial progress in such remote measurement, made possible by the development of theories which relate the characteristics of the scintillation patterns to those of the turbulence (*eg* its strength). For scintillation classified as "weak", this relationship is well understood, but is a subject of ongoing research for stronger scintillation.

A major difficulty in using stellar scintillation for remote sensing is the determination of the height of the turbulence producing it. One approach uses a theoretical relationship between the spatial spectrum of the scintillation pattern and the height. A more direct method can be applied in the case of the scintillation of a double star; similar patterns are produced at ground level in the light of each component of the double star, with a separation proportional to the height of the turbulence.

Several techniques using stellar scintillation have been developed and used to measure turbulence strength and/or wind velocity as a function of height. Generally (for weak scintillation) they give results consistent with direct measurements, but their height resolution is inferior.

Recently there has been interest in precompensating laser beams so that they emerge undistorted after passing through atmospheric turbulence. This interest is associated with plans to use ground-based lasers for optical communications with satellites

or to destroy ballistic missiles in flight. As the turbulence which produces scintillation in light coming down through the atmosphere will distort upward propagating light in a similar manner, studies of stellar scintillation are clearly relevant to the evaluation of these compensation techniques. In particular, stellar scintillation is being used in the measurement of the atmospheric isoplanatic angle. This is the small angle, looking upwards, within which there is no distortion due to turbulence.

1.2 Aims of this work

The work reported in this thesis has three aims:

a) measurement of basic parameters of the stellar scintillation pattern in order to
   1) add to knowledge of the phenomenon through improved observations and comparison with theoretical predictions, and
   2) investigate particular parameters relevant to the measurement of wind velocity, turbulence strength and the isoplanatic angle.

b) Investigation of a multiple-beam method to remotely measure wind velocity and height using stellar scintillation, incorporating
   1) the development of a multiple-correlation analysis,
   2) a laboratory test of the method, and
   3) application of the method to measure atmospheric winds using the scintillation of a double star, with the results being compared with standard weather-station measurements.

c) Development and application of a technique to measure atmospheric isoplanatism, based on a comparison of the scintillation of a double and of a single star.

1.3 Outline of this thesis

Following this introduction, a literature review is given, consisting of an outline of the historical development of stellar scintillation research (chapter 2) and a description of previous work which is directly relevant to this thesis (chapter 3). The theoretical work undertaken for this thesis is described in chapter 4. The equipment and methods of observation are described in chapter 5. Samples of the measurements are presented in chapter 6, along with the results of various tests which were applied to check the

validity of the data and some of the techniques proposed in chapter 4. The results of a laboratory test of the multiple-beam system are described in chapter 7.

Basic observations of the stellar scintillation pattern (these generally being a repetition of work done by others, but with smaller apertures in this case) are presented in chapter 8, while chapter 9 describes observations of scintillation which are believed to give new results. Measurements of atmospheric wind speed and of atmospheric anisoplanatism, derived from stellar scintillation, are presented in chapter 10.

The conclusions of this work are given in chapter 11, followed by suggestions for future work with the existing data and equipment and suggestions for new techniques.

Chapter 2 **Historical review**

The idea that the scintillation, or twinkling, of the stars is related to the intervening medium is not new. Over two thousand years ago the fact that the stars twinkle while the planets do not was observed and (incorrectly) ascribed to the greater distance of the stars (Aristotle, *circa* 330 B.C.). By the eighteenth century, the source of the twinkling was identified as being "air in perpetual tremor" in the lower atmosphere (Newton, 1730). Since then, stellar scintillation has been studied in connection with the problems it causes for astronomers, its potential for atmospheric remote sensing, and generally out of scientific curiosity. Theories which relate the characteristics of the scintillation pattern to the atmospheric turbulence which produces it are still under development, but under appropriate conditions the relationship is understood well enough to allow profiles of wind velocity and turbulence strength to be deduced from observations of scintillation. Recently, scintillation has been exploited to measure the atmospheric isoplanatic angle, a quantity which is of interest in astronomy, optical communication with satellites and laser weaponry.

2.1 Visual observations and interpretation

Most of the features of scintillation visible to the naked eye were described in the mid-nineteenth century by Arago (Mascart, 1893 and Isacker, 1953). He recorded that it consists of changes in intensity, nearly always accompanied by colour variations. It is more prominent for stars near the horizon but is sometimes seen near the zenith. It depends on atmospheric conditions, being weak in calm weather and strongest with violent winds or when the sky is alternately clear and cloudy. It is seen for planets, but the colour changes are hardly visible, especially for those with a larger apparent diameter. The frequency of the fluctuations decreases as the star approaches the horizon. The magnitude of the intensity variation decreases as the observer goes to a higher altitude.

While earlier theories ascribed scintillation to the diversion of light away from the aperture by refraction, Arago explained it as an interference effect (Rayleigh, 1893). He suggested that rays of one colour falling on one side of a lens may, in their passage through the atmosphere, have acquired a phase different to the rays on the other side.

Thus one colour may suffer destructive interference, leaving a complementary colour.

Visual observations aided by instruments had begun by the eighteenth century. Newton (1730) explained the reduction in twinkling that occurs when a star is observed through a telescope, compared to direct observation, as being due to the averaging of several independent patterns. Nicholson struck the tube of a telescope with small blows so that the image of the star followed an "acoustic curve", allowing him to see that Sirius underwent 30 colour changes per second (Mascart, 1893). By using a "slide with parallel faces turning eccentrically" to spread a projected star image into a circle, Montigny observed 70 colour changes per second (Boutet, 1949). Using a spectroscope, Montigny observed bands on the spectrum which moved and deformed, while later Wolf found these bands to be inclined to the spectrum (Mascart, 1893). Respighi found that the inclination of the bands on a horizontal spectrum increased from vertical (*ie* covering a small range of wavelengths) for stars near the horizon to horizontal for stars at elevations of 30°–40° or more. He observed that, especially for low elevations, several bands of the same inclination can follow each other in moving from one end of the spectrum to the other (Rayleigh, 1893).

Montigny, taking the older view (*ie* to Arago's) that scintillation is caused by the actual diversion of the light from the aperture by refraction, was able to explain the moving spectral bands. Due to regular atmospheric refraction, the violet ray follows a higher path through the atmosphere than the red ray and so an atmospheric irregularity moving from one path to the other produces a band moving across the spectrum (Rayleigh, 1893). Rayleigh rejected Arago's interference theory as it did not explain the spectral bands and because the light nulled by interference at the focus should appear slightly displaced in the image plane. Applying Montigny's theory to the observation by Respighi of bands of similar inclination crossing the spectrum, he argued that the source of the scintillation must be confined to a narrow layer in the atmosphere. Rayleigh was puzzled as to how the atmospheric fluctuations could be sharp enough to produce the observed scintillation patterns. Ironically this problem was to be solved many years later by a theory which starts with Arago's postulate that different paths through the atmosphere impose different phase changes.

The detrimental effect of the atmosphere on astronomical observations led to a

comprehensive review by Douglass (1897). He observed scintillation patterns on the telescope objective by putting his eye at the focus. He was thus able to compare the scintillation with the "seeing" (the actual resolution compared to the diffraction limit for the telescope), the site and the weather. He argued that scintillation is caused by temperature rather than pressure differences and that these temperature differences are produced by the settling of cold air at night, wind blowing over mountain ranges and the processes involved in cloud formation. He related the height of the atmospheric irregularities to the position of the telescope eyepiece required to see the scintillation pattern "in focus", obtaining altitudes of 3–5 km.

Thus by the end of the nineteenth century the phenomenon of stellar scintillation was well described. Ironically this information was not well known many years later, when there was a dispute in *Nature* as to whether stellar scintillation is a physiological phenomenon (Megaw, 1950).

There are two methods of direct visual observation, described in a review of scintillation by Minnaert (*circa* 1940), that indicate the size and lifetime of the scintillation patterns. If one's eyes are focussed on a nearby object so that a star is seen as two defocussed images, then these images are seen to twinkle independently, showing the pattern size to be less than a few centimetres. The persistence of the sources of scintillation can be seen by watching them move across a group of stars, such as Pleiades.

2.2 Initial quantitative observations

Quantitative records of scintillation were made by Minnaert and Houtgast (1935), who recorded a star image on a moving film and analyzed it with a microphotometer. They also measured the speed of the patterns by imaging them onto moving film, obtaining values of 6–7 ms^{-1}. They obtained estimates of the height of the sources of scintillation in daytime (0.6 and 2.5 km) by observing how much of the sun's image was simultaneously distorted by atmospheric irregularities. Photoelectric measurements, made by Whitford with a photocell, showed that the intensity of the starlight could vary by a factor of 5 in 0.05 s (Stebbins, 1944). The use of an electron-multiplier cell gave sufficient sensitivity to measure a frequency spectrum of the intensity fluctuations, showing a peak at 60 Hz (Boutet, 1949).

The introduction of the photomultiplier tube, with its superior sensitivity at low light levels, allowed measurements at higher frequencies and with smaller apertures. Frequencies up to 500 Hz were observed for stars near the zenith by Butler (1951). The lower limit of the pattern size was shown to be less than 2.5 cm (Mikesell *et al*, 1951). Mikesell *et al* found intensity records and frequency spectra to be similar for observations in different wavelength ranges, with no dependence of these on polarization. The distribution of the intensity was found to be Gaussian for stars near the zenith but more like Poisson for stars near the horizon (Butler, 1952). The rapid increase of the variance of the scintillation with decreasing aperture size was observed over a large number of different nights (Ellison and Seddon, 1952).

2.3 The origin of scintillation

By the early 1950s a clearer picture of the source of stellar scintillation had emerged from studies of radio scintillation and of turbulence. In 1933, Ratcliffe and Pawsey explained the scintillation (or "fading") of radio waves reflected from the ionosphere in terms of diffraction (Ratcliffe, 1956), with the pattern at ground level being produced by the summation of signals reflected from several parts of an irregular reflector. Taylor (1938) found that turbulent irregularities were sufficiently long lived to be regarded as unchanging objects moving with the mean flow. Kolmogorov (1941) and Obukov derived a mathematical formulation of the structure of turbulence (Tatarski, 1961), subsequently referred to as the "Kolmogorov spectrum". Megaw (1950) showed that measurements of the angular spectrum of stellar scintillation (*ie* the amount of angular fluctuation in the star's position against temporal period) were consistent with a Kolmogorov spectrum for the turbulence.

The statistical diffraction theory of radio scintillation was well established by 1950 (Booker *et al*) and was modified to explain stellar scintillation by Little (1951). Little rejected previous ideas that scintillation could be produced by refraction at single irregularities because the required temperature fluctuations, calculated as 1 K by Anderson (1935), were much higher than had been observed to occur. He also raised the more fundamental objection that the diffraction limit for a lens as small as features in the scintillation pattern precludes it from focussing over distances of kilometres. In Little's

formulation, the initially plane wavefront of the starlight becomes progressively more distorted as it propagates through a turbulent layer. It emerges from this layer with its amplitude essentially unchanged, but with phase variations across the wavefront that lead to the formation, by diffraction, of intensity variations further down in the atmosphere. (Although a statistical treatment which traces ray paths through many irregularities, as applied by Chandrasekhar (1952), can overcome the requirement for unreasonably high temperature fluctuations, the diffraction treatment is still necessary to overcome Little's second objection.)

Initial comparisons of stellar scintillation with atmospheric measurements (Gifford and Mikesell, 1953; Gifford, 1955) suggested that the scintillation was produced near the tropopause. A direct measurement of the motion of the scintillation pattern by Protheroe (1955) gave a velocity which agreed closely with that of the wind at 12 km. Mikesell (1955) conducted a systematic comparison of scintillation and balloon measurements on 100 nights and showed that the high frequency scintillation (at 150 Hz) was best correlated with the wind speed in the altitude range 8–14 km but that there was no correlation with the height of the tropopause. A similar set of observations over 207 nights showed that the level of scintillation was an excellent indicator of the wind velocity at the height of maximum vector wind shear (Protheroe, 1961).

Tatarski (1961) presented methods to calculate the statistical properties of diffraction patterns produced when electromagnetic waves pass through extended regions of turbulence. Tatarski's theory is restricted to relatively weak turbulence with a Kolmogorov spectrum. Townsend (1965) applied Tatarski's theory to predict the spatial power spectrum of stellar scintillation and found that the observations could be accounted for by assuming that the scintillation was produced by turbulence in a layer at 8 km and in the boundary layer. Measurements of the dependence of stellar scintillation on wavelength (Burke, 1970) and aperture size (Bufton and Genatt, 1971) were consistent with Tatarski's predictions.

A different approach was pursued by astronomers, who used ray optics to predict statistical characteristics of the scintillation pattern (Reiger, 1963 and Young, 1969a). They neglected diffraction on the basis that it is only significant at scales much smaller than the apertures used in astronomy. Reiger (1963) assumed that the turbulence

strength decreases exponentially with height and obtained good agreement between theoretical predictions and earlier measurements of correlation functions (measured by Protheroe), power spectra (by Mikesell, 1955) and aperture dependence (by Ellison and Seddon, 1952).

Young (1969a) extended Reiger's approach and found that the temporal power spectra for the scintillation of planets (measured by Mikesell, 1955) could be predicted by assuming the turbulence strength to decrease exponentially with height, but not by assuming it to be in a single layer. Experimental evidence against the single-layer theory came from measurements with an optical Fourier analyzer (Protheroe, 1964). In these the temporal power spectra for individual spatial wavelengths had multiple peaks, suggesting that several thin layers contributed to the scintillation pattern.

The issue of a single turbulent layer versus exponentially distributed turbulence was clarified by actual measurements of the turbulence profile by balloon-borne instruments (Bufton *et al*, 1972 and Bufton, 1973). These showed the turbulence to be in many thin transitory layers, with the strength generally decreasing with height. The strongest turbulence was observed below 5 km, above 9 km and in a region immediately above the height of a nearby mountain top.

Vernin and Roddier (1973) used observations of the temporal and spatial spectra of stellar scintillation to deduce that it is generally produced in two layers, one consistently at 10 km and the other usually below 6 km. Bufton (1973) applied Tatarski's theory to show that the turbulence above 9 km is of sufficient strength to account for the observed scintillation. Further support for the applicability of Tatarski's theory was provided by Rocca *et al* (1974), who obtained excellent agreement between the temporal cross correlation between the scintillation measured on two detectors and the prediction of this function from a wind profile measured by radiosonde.

2.4 Atmospheric sensing

2.4.1 Remote sensing of wind and turbulence strength

The main problem in using stellar scintillation for remote sensing of atmospheric parameters is the determination of the height of its source. One approach is to use the relationship between the height and the spatial spectrum of the scintillation (*ie* larger

scintillation patterns are associated with greater heights). Peskoff (1968) suggested that the observed spectrum could be inverted to give the profile of turbulence strength, but Lawrence (1970) concluded that, due to practical considerations, the resolution of this profile would be limited to only 3 or 4 different height ranges. Ochs *et al* (1976) put this idea into practice with a "scintillometer" which observed the scintillation at 7 spatial wavelengths and gave the turbulence strength for 4 height ranges. A later comparison of observations using this instrument with simultaneous observations by a VHF radar gave excellent agreement (Good *et al*, 1982).

An alternative approach to determine the height is to utilize geometry and an extended source, as Minnaert and Houtgast (1935) did with the sun. Keller (1955) proposed the use of a double star, where it is assumed that two similar patterns are produced with a separation determined by the separation of the two components of the star and the height of the turbulence. Rocca *et al* (1974) measured the spatial correlation function for a double star and deduced a turbulence profile versus height which gave reasonable values. The first comparison of the results of this method with directly measured turbulence profiles gave good agreement (Vernin *et al*, 1979), but in a second test of the method (Azouit *et al*, 1980) the optically measured turbulence strengths were always smaller than the direct measurements in the height range 9–17 km. The scintillometer in the latter case was capable of producing a profile every 10 s, allowing measurements of profiles of atmospheric turbulence as a function of time.

The difference between the optically deduced turbulence profiles and those measured by radiosonde might be explained by inadequacies in the basic assumptions, particularly with regard to the spectrum of the turbulence and the strength of the scattering. Hill and Clifford (1978) introduced a spectrum for turbulence which deviates from the Kolmogorov spectrum, with a greater contribution at the smaller scales which are important in optical scintillation. The application of photon-counting techniques allowed observations of stellar scintillation with small (less then 1-cm) apertures and narrow (5-nm) optical filters, showing the variance of the scintillation to be greater than previously thought (Jakeman *et al*, 1976). This called into question the assumption of weak scattering made in the application of Tatarski's theory, with further observations suggesting that this theory is only valid for stars near the zenith (Jakeman *et al*, 1978).

Jakeman *et al* (1978) found that the intensity distribution for strong stellar scintillation was closer to a "K distribution" than to the "log normal" distribution predicted by Tatarski (1961). To identify intensity distributions at very low light levels they introduced (to stellar scintillation studies) the technique of characterizing a distribution by measurements of the ratios between its second and higher moments. An advantage of this measurement is that it can be corrected for photon noise. They presented moment measurements for starlight which were consistent with the K distribution. Further, Parry and Walker (1980) found that the K distribution was appropriate for strong stellar scintillation. However, Ben-Yosef and Goldner (1988) have cast doubt on this moment analysis, showing theoretically and by simulation (Goldner and Ben-Yosef, 1988) that it does not give a reliable indication of the distribution for physically reasonable sample sizes.

Efforts continue to develop theories which predict the characteristics of the scintillation pattern for stronger turbulence. Whitman and Beran (1985) developed an approach which is applicable to turbulence of any strength and applied it (Beran and Whitman, 1988) to predict the variance of the light intensity as a function of elevation of a star.

Vernin and others in France have continued to use Tatarski's theory to measure wind velocity and turbulence profiles. Using an image intensifier, Vernin and Azouit (1983a) obtained "snapshots" of the scintillation pattern with resolution to better than 1 cm. The same instrument, operated in a mode that produces two-dimensional spatial and temporal cross-correlation functions, has clearly shown the double pattern produced by a double star and its movement with the wind (Vernin and Azouit, 1983b). Double-star observations with this instrument have been used in the remote investigation of atmospheric internal gravity waves (Vernin and Pelon, 1986). The instrument has also been used to obtain profiles of wind and turbulence strength from the scintillation of a single star, with the height being determined from the spatial spectrum (Caccia *et al*, 1987). The acronym "SCIDAR", for "scintillation detection and ranging", is used to describe such observations (Vernin and Pelon, 1986).

In the United States the scintillometer developed by Ochs *et al*, (1976) has been improved to measure turbulence strength in seven independent range intervals, from 2

to 20 km (Chonacky and Deuel, 1988). It is popularly known as the "Star Sensor".

2.4.2 Measurement of the isoplanatic angle

The atmospheric isoplanatic angle refers to the small angle over which the appearance of an object is not distorted by atmospheric turbulence (Loos and Hogge, 1979). During the 1970s this angle gained in practical significance with developments in astronomy, optical communications and laser weaponry. Initially it was measured directly by examination of short-exposure astronomical photographs, but recently has been determined indirectly from scintillation measurements.

Knowledge of the isoplanatic angle became important in astronomy with the advent of stellar speckle interferometry (Labeyrie, 1970). This technique can produce a diffraction-limited spatial autocorrelation function of an astronomical object if the object lies within an isoplanatic patch. Stellar speckle holography, which can produce a diffraction-limited image, requires partial isoplanatism to extend from the object of interest to a nearby reference point source (Weigelt, 1979).

In this same period, methods were being developed to get optimum power transfer along optical links to satellites. To reduce the broadening of a laser beam caused by atmospheric turbulence, it was proposed that a reference beam could be transmitted from a satellite and the distortion due to turbulence could be observed. A complementary distortion could then be applied to the transmitted beam so that it emerges undistorted after passing through the same turbulence (Shapiro, 1971). Due to the movement of the satellite, the up and down beams may be sufficiently far apart to contain different turbulent irregularities (Shapiro, 1975), so that the correction will not work if the angular displacement of the satellite during the transit time of the signals exceeds the isoplanatic angle (Loos and Hogge, 1979). The required angle can be reduced if the reference beam is transmitted from the "point-ahead position" to which the satellite moves during the transit time of the signals (Fried, 1982).

Recently it has been proposed that high-power ground-based lasers be used to destroy ballistic missiles in flight, with the beam being reflected to the target by an orbiting mirror. The need to precompensate the beam for atmospheric turbulence and the significance of the isoplanatic angle (as outlined above for communication links) has been recognized in this context (APS study, 1987).

Measurements to determine the amount of isoplanatism as a function of angular separation were initially made by examination of short-exposure photographs of double stars (*eg* Nisenson and Stachnik, 1978). This method requires a large-aperture astronomical telescope and gives an average of the isoplanatic angle over the aperture. More recently, the isoplanatic angle has been deduced indirectly from measurements of stellar scintillation on much smaller apertures.

Loos and Hogge (1979) made simultaneous measurements of the isoplanatic angle and the level of scintillation, finding these to be anticorrelated. They determined a relationship that predicts the isoplanatic angle for a given turbulence profile, showing that the weighting function with height is very similar to that for the contribution to the variance of scintillation on an aperture of a particular diameter. Thus they suggested that the isoplanatic angle can be deduced from scintillation measurements, without the turbulence profile being known. This technique has been implemented by Eaton *et al* (1985), who found agreement between the isoplanatic angle measured by this method and that predicted from a turbulence profile measured using a scintillometer. This is not a complete test as both measurements require the assumptions of a Kolmogorov spectrum and weak scattering, both of which are the subject of some dispute (see §2.4.1).

Chapter 3 Review of relevant topics

In this chapter a review is given of work by others which is directly relevant to this thesis, particularly basic measurements of scintillation and remote sensing of atmospheric parameters using scintillation. As background to this review, a brief summary is given of the structure and distribution of atmospheric turbulence and of the theoretical relationship between characteristics of the turbulence and of the scintillation pattern which it produces.

Also reviewed are some existing measurement techniques which are modified or extended in this thesis. These are the identification of intensity distributions at very low light levels and a multiple-beam method which measures fluid velocity in seeded flows.

A brief review of photomultiplier afterpulsing is also presented, as this thesis includes the development of techniques for measurement of and correction for this problem.

3.1 Kolmogorov theory of turbulence

Kolmogorov (1941) postulated that in turbulent mixing the energy passes from larger to smaller fluctuations and is dissipated as heat due to viscosity at the minimum scale size. He derived the expression

$$B_{dd}(r) = \overline{\left[u_d(M') - u_d(M)\right]^2} \sim C\overline{E}^{\frac{2}{3}} r^{\frac{2}{3}} \qquad --(3.1)$$

where $u_d(M)$ is the component of the fluid velocity at point M in the direction $\mathbf{d} = \overline{MM'}$, E is the energy dissipated per unit mass per unit time and C is a constant. $B_{dd}(r)$ is the "structure function" of the velocity components in direction d for separation r between points M and M'.

The structure function D_n of the refractive-index variations in turbulence was shown by Tatarski (1961, $p58$) to be related to the separation $r = |\overrightarrow{r_2} - \overrightarrow{r_1}|$ between 2 points in the turbulence by

$$D_n(r) = \overline{\left[n(\overrightarrow{r_1}) - n(\overrightarrow{r_2})\right]^2} = C_n^2 r^{\frac{2}{3}} \qquad --(3.2)$$

where $n(\overrightarrow{r})$ is the refractive index at position $\overrightarrow{r}$ and C_n^2 is a coefficient indicating the strength of the turbulence. Tatarski transformed this to the three-dimensional spatial

power spectrum Φ_n of fluctuations in refractive index n such that

$$\Phi_n(\kappa) = 0.033 C_n^2 \kappa^{-\frac{11}{3}} \qquad -- (3.3)$$

where κ is the spatial frequency (m^{-1}).

This spatial power spectrum is referred to as the "Kolmogorov spectrum" and C_n^2 as the "refractive index structure coefficient". The range of scale sizes where the energy dissipation is negligible and equations 3.2 and 3.3 apply is called the "inertial subrange" (Batchelor, 1953). The Kolmogorov spectrum is thought to be valid in the lower atmosphere from an inner scale l_o of several millimetres up to an outer scale L_o of several metres. Ochs and Hill (1985) found the inner scale at ground level to vary with time within the range 2–10 mm, and Coulman *et al* (1988) found the outer scale (at altitudes between 2 and 18 km) to increase with height up to a maximum of 4 m at an altitude of 10 km.

While the Kolmogorov spectrum has been used in nearly all cases where stellar scintillation work has required a model of the turbulence (*eg* Vernin and Roddier, 1973; Ochs *et al*, 1976; Winick and Marquis, 1988), it has been shown (Hill and Clifford, 1978) that this spectrum underestimates the relative strength of the turbulence at the small-scale end of the spectrum. This is particularly significant to optical scintillation, which has a strong contribution from the small-scale fluctuations. The form of the modification of the spectrum specified by Hill and Clifford depends on the inner scale l_o, which varies in size (at least at ground level, as noted in the previous paragraph). Thus discrepancies between theory and measurements of stellar scintillation may be due to an inadequate model of the spectrum of turbulence, or to an incorrect value of l_o if the spectrum suggested by Hill and Clifford is used.

3.2 The distribution of atmospheric turbulence

Figure 3-1 shows a compilation of measurements of turbulence strength (indicated by C_n^2) versus height in the atmosphere. The measurements are by Bufton *et al* (1972), Ochs and Lawrence (1972), Barletti *et al* (1976), Vernin *et al* (1979) and Brown and Good (1984a and 1984b). (Only first authors are specified in the figure.) Following Tatarski (1961, *p*79) C_n^2 is derived (for a Kolmogorov spectrum, at optical wavelengths)

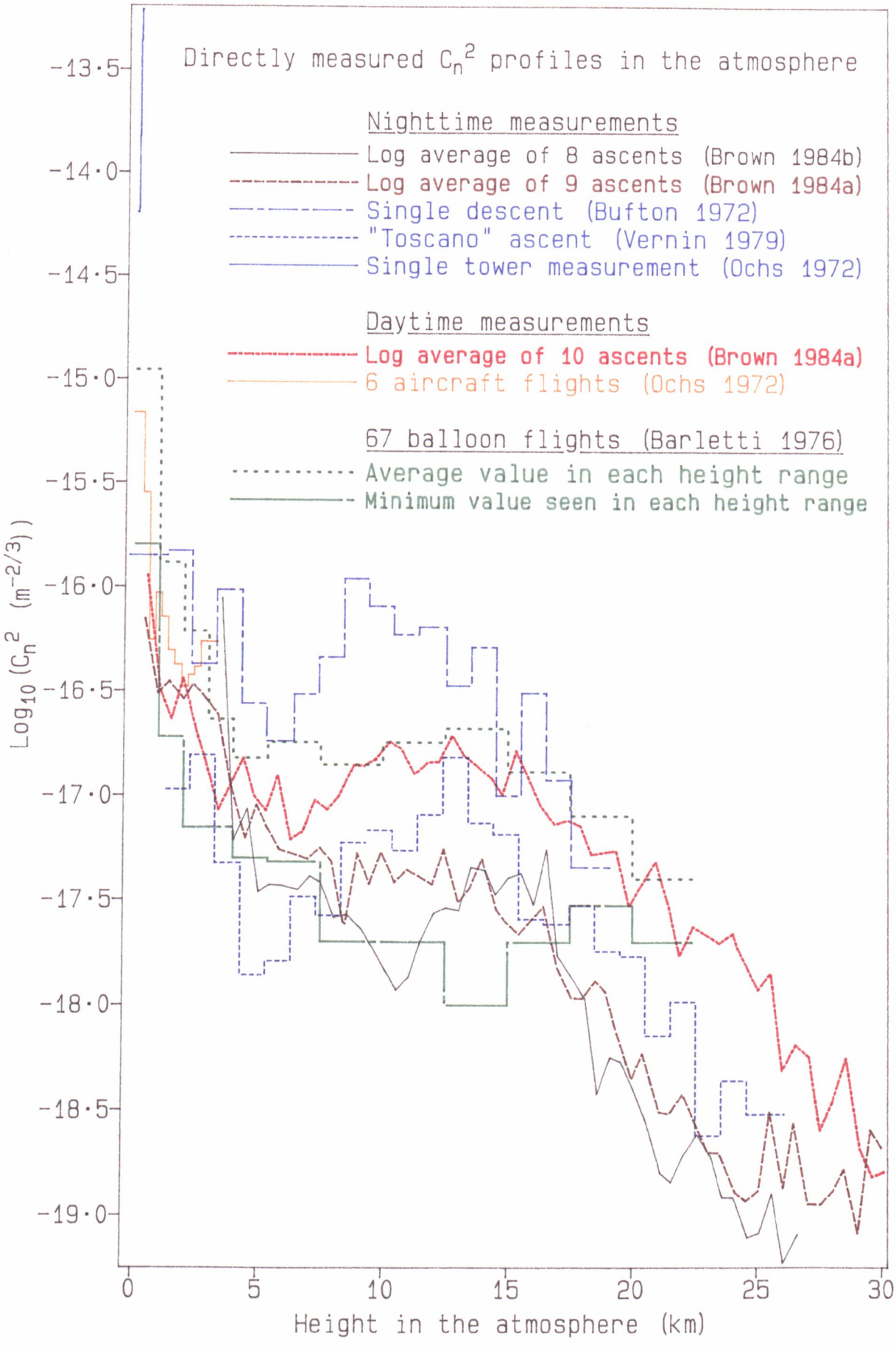

Fig. 3–1 Representative examples of in situ measurements of the optical refractive index structure coefficient as a function of height in the atmosphere. The profiles of Bufton, Vernin, and Ochs have been averaged within the height ranges indicated by the stepped lines during production of this diagram.

from the temperature structure coefficient C_T^2 using the expression

$$C_n = \frac{79 \times 10^{-6} p}{T^2} C_T \qquad --(3.4)$$

where p and T are the atmospheric pressure (mbars) and temperature (K) and C_T is derived from the temperature structure function D_T. Tatarski gave the relationship as

$$D_T(\overrightarrow{r}) = \overline{\left[T(\overrightarrow{r} + \overrightarrow{r_1}) - T(\overrightarrow{r_1})\right]^2} = C_T^2 r^{\frac{2}{3}} \qquad --(3.5)$$

where $T(\overrightarrow{r})$ is the temperature (K) at position $\overrightarrow{r}$. In practice the turbulence is assumed to be isotropic, and $D_T(r)$ is measured at only one fixed separation, using two thermometers with a high frequency response carried aloft by a balloon. Vernin *et al* (1979) used 2 sensors of 10-μm platinum wire, separated by 1 m, towed 100 m below a balloon.

From figure 3-1 it can be seen that the turbulence strength:

1) decreases rapidly with altitude up to about 5 km,
2) tends to be constant or increase slightly between 5 and 15 km and
3) decreases with increasing altitude above 15 km.

The strength is generally higher in the daytime, although the number of daytime profiles presented is not sufficient to make this a firm conclusion. (*nb* The profiles of Barletti *et al* (1976) are not divided into day and night profiles in figure 3-1.)

Barletti *et al* found from 69 flights at several sites that the turbulence above 4 km did not vary from site to site. They noted that "The top of the mountains very often produces on the lee side a layer of very strong turbulence", in agreement with earlier observations of this by Bufton *et al* (1972) and its deduction by Douglass (1897).

All profiles in figure 3-1 have been averaged over height ranges of hundreds of metres. either in the original publication or in production of the figure. The profile for the "Toscano" ascent is a smoothed version of the published profile (Vernin *et al*, 1979) which is reproduced at the top of figure 3-2. This particular profile is selected for presentation here because it has better resolution than other published profiles. It shows that atmospheric turbulence tends to be greatly enhanced in a large number of small height ranges, in agreement with previous measurements by Coulman (1973), Bufton (1973) and Barletti *et al* (1976). Bufton found that some of the regions of

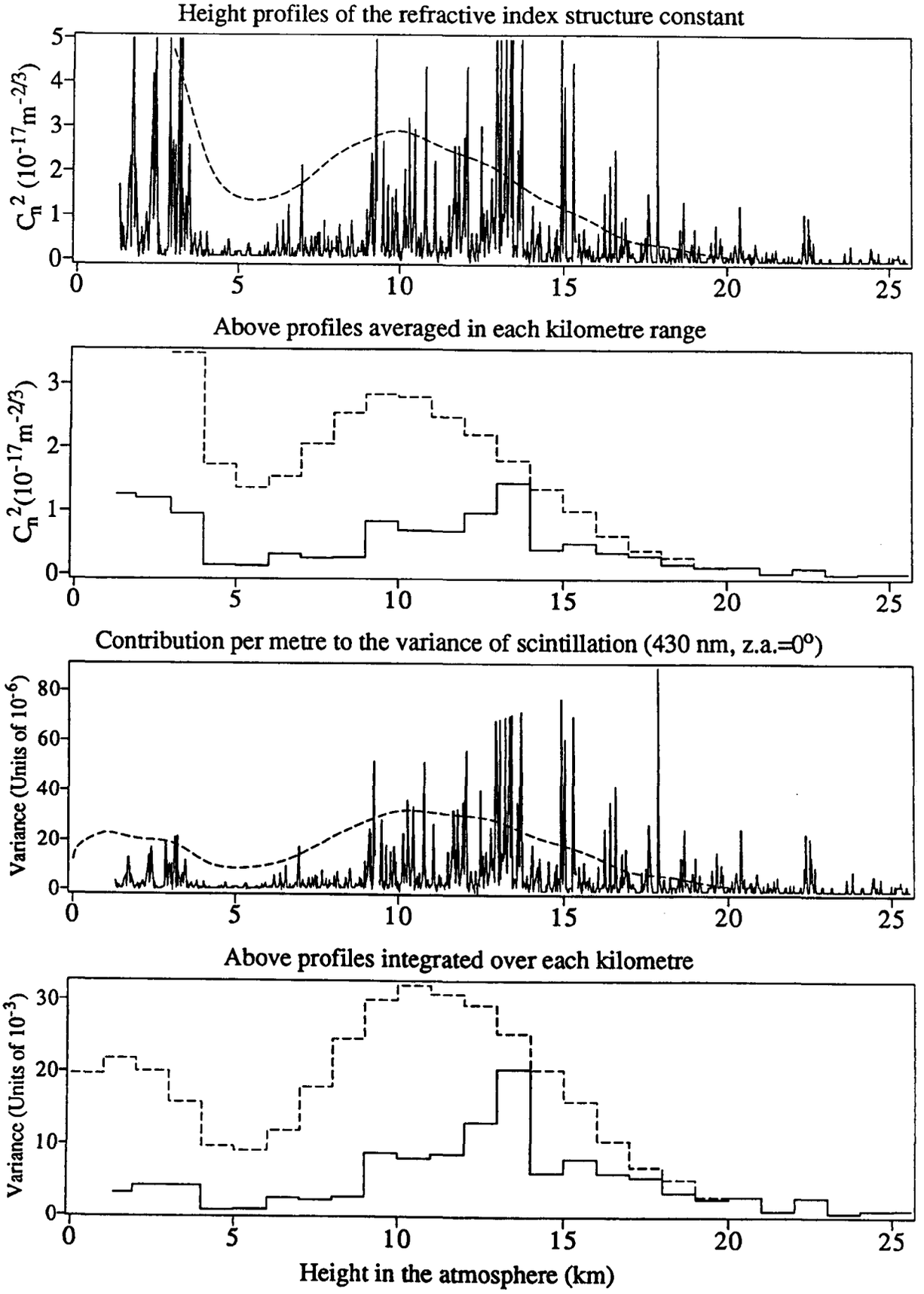

Figure 3-2 At the top a solid line shows a profile of turbulence strength (indicated by C_n^2) against height in the atmosphere, measured by Vernin *et al* (1979). The dashed line indicates a "standard" profile specified by Beran and Whitman (1988). The standard profile is not plotted for heights below 3 km as the large values would dominate the plot. The second plot shows these profiles averaged over 1 km height intervals. The lower plots show the contribution of these turbulence profiles to the variance of scintillation (per metre and per kilometre), calculated using the theory of Tatarski *ie* by application of equation 3.9.

stronger turbulence appeared on profiles taken on both ascent and descent, indicating that these regions have a significant lifetime and are layers rather than blobs.

An average turbulence profile, specified by Beran and Whitman (1988), is also plotted in figure 3-2. This is a mathematical fit to a typical nighttime profile given by R. E. Hufnagel, where values above 1 km are determined by a cubic spline approximation to Hufnagel's values at each kilometre and a height$^{-\frac{2}{3}}$ dependence is assumed below 1 km. In the second plot of figure 3-2, both profiles are averaged over 1-km intervals. It can be seen that the turbulence strengths of the Toscano flight are below average, particularly at low heights.

3.3 Theories of stellar scintillation

To calculate the effect of turbulence on light, the usual approach is to solve Maxwell's wave equation with the refractivity spectrum $\Phi_n(\kappa)$ inserted, as done by Tatarski (1961, *p*59). A general solution has not been achieved, but various approximations allow solutions in particular situations (Fante, 1980). Tatarski's approach, often referred to as the Rytov method, works well for cases where the turbulence is sufficiently weak. For paths with uniform turbulence it appears to be valid when

$$1.23k^{\frac{7}{6}}C_n^2x^{\frac{11}{6}} < 0.3 \qquad --(3.6)$$

where x is the length (m) of the path and k is the wavenumber of the light (m^{-1}) (Fante, 1975). Approximating the average profile of turbulence strength plotted in figure 3-2 by $C_n^2 = 2 \times 10^{-17}$ ($m^{-\frac{2}{3}}$) in the range 0–13 km, the left hand side in (3.6) is 0.2 for light of wavelength 450 nm. Thus the Rytov method is apparently applicable to stellar scintillation produced by an average turbulence profile.

Tatarski (1961, *p*239) derived the relationship between atmospheric turbulence and stellar scintillation as

$$\sigma^2 = \overline{\left(\ln\frac{I}{I_o}\right)^2} = 2.24k^{\frac{7}{6}}(\sec\phi)^{\frac{11}{6}}\int_0^\infty C_n^2(h)h^{\frac{5}{6}}dh \qquad --(3.7)$$

where σ^2 is the variance of the logarithm of relative intensity (*nb* the English translation of Tatarski's book uses "log" for "ln"), ϕ is the zenith angle, I is the instantaneous intensity of the scintillation pattern, I_o is the unperturbed intensity and $C_n^2(h)$ represents the turbulence strength at height h (m). As a large number of independent

turbulent regions contribute to σ^2, $\ln \frac{I}{I_o}$ is normally distributed and so I has a "log normal" distribution (Tatarski, $p209$, 1961). For this distribution, Tatarski gave

$$\sigma^2 = \overline{\left(\ln \frac{I}{I_o}\right)^2} = \ln\left(1 + \frac{\overline{(I-\bar{I})^2}}{(\bar{I})^2}\right) . \qquad --(3.8)$$

Using $\ln(1+x) \sim x$ for $0 < x \ll 1$, equations 3.7 and 3.8 can be combined to give the "scintillation index" σ_I^2 as

$$\sigma_I^2 \sim \frac{\overline{(I-\bar{I})^2}}{(\bar{I})^2} = 2.24 k^{\frac{7}{6}} (\sec\phi)^{\frac{11}{6}} \int_0^\infty C_n^2(h) h^{\frac{5}{6}} dh \qquad --(3.9)$$

as generally quoted subsequently (*eg* Roddier, 1981 and Coulman, 1985).

Equation 3.9 has been applied (with $\phi = 0$ and $k = \frac{2\pi}{\lambda}$, where $\lambda = 430$ nm) to calculate the contribution to the variance by each part of the turbulence profiles plotted in figure 3-2. The results are given in the lower two graphs in figure 3-2 and illustrate the common view that most of the scintillation has its origin at heights above 10 km.

Jakeman *et al* (1978) suggested that the log normal distribution, predicted by Tatarski, is valid only for weak scintillation of stars near the zenith. For strong scintillation and large zenith angles, they suggested that a K distribution is more appropriate. The K distribution results from the sum of a finite number of independently contributing sources, each having a defined distribution.

Recently Whitman and Beran (1985) claimed that a previously published approximate solution to the wave equation for strong turbulence is applicable to turbulence of any strength. They applied the technique to predict the elevation dependence of stellar scintillation (Beran and Whitman, 1988) and found that the $\sec\phi$ dependence of equation 3.9 falters at zenith angles greater than 50°, with a peak in the variance at ~76°. Their prediction is a complicated integral equation which simplifies to equation 3.9 for $\sigma_I^2 \ll 1$.

3.4 Measurement of the intensity distribution

For measurements at low light levels where individual photons are counted, it is necessary to measure relationships between the moments of an intensity distribution, rather than the distribution itself (Jakeman *et al*, 1978). Parry and Walker (1980) gave these relationships as

$$\frac{\langle I^m \rangle}{\langle I \rangle^m} = \frac{\langle I^2 \rangle}{\langle I \rangle^2}^{\frac{m(m-1)}{2}} \qquad --(3.10)$$

for the log normal distribution and

$$\frac{\langle I^m \rangle}{\langle I \rangle^m} = m! \frac{\Gamma(m+y)}{y^m \Gamma(y)} \qquad \text{where } y = \frac{2}{\frac{\langle I^2 \rangle}{\langle I \rangle^2} - 2} \text{ and } \frac{\langle I^2 \rangle}{\langle I \rangle^2} > 2 \qquad --(3.11)$$

for the K distribution, where $\langle\ \rangle$ specifies an ensemble average and $m = 3, 4, 5...$

Barakat (1976) warned that the probability density function for the log normal distribution is not uniquely determined by its moments. A more serious concern is the claim by Ben-Yosef and Goldner (1988) that the "moment plot" (a plot of higher versus second moments) is of no use in discriminating between different distributions for reasonable sample sizes. The maximum sample size is the number of independent fluctuations which occur during the time interval over which the atmosphere is stationary, *ie* over which the characteristics of the volume of the atmosphere under observation do not change. Ben-Yosef and Goldner suggested that this interval for the atmosphere (~1 min) is too short to allow an accurate measurement, as it will on most occasions not include very high intensities which occur infrequently. They also showed that finite data lengths result in correlated errors in the measured second and higher moments which cannot be removed by trivial point averaging. They investigated other techniques and concluded that no satisfactory technique is available to determine the intensity distribution of scintillation produced by atmospheric turbulence.

3.5 Observations of stellar scintillation

3.5.1 Observed characteristics

Electronic "photographs" of stellar scintillation published by Vernin and Azouit (1983a) are reproduced in figure 3-3a. They have been reduced to 7.6% of the original size of 51 × 38 cm. They show a trend to larger scintillation features with increasing distance from the turbulence, as predicted by Tatarski (1961, *p*140). (Tatarski showed that refractive-index homogeneities with scales of the order of $\sqrt{\lambda h}$ make the largest contribution to the scintillation pattern.)

Figures 3-3b and 3-3c show copies of photoelectric recordings of stellar scintillation on a single aperture, taken by Butler (1951) and Bufton (1971). Despite the relatively large apertures used (10 cm or greater), they show frequencies up to about 500 Hz. In spite of the technical improvement in photomultipliers since these recordings were

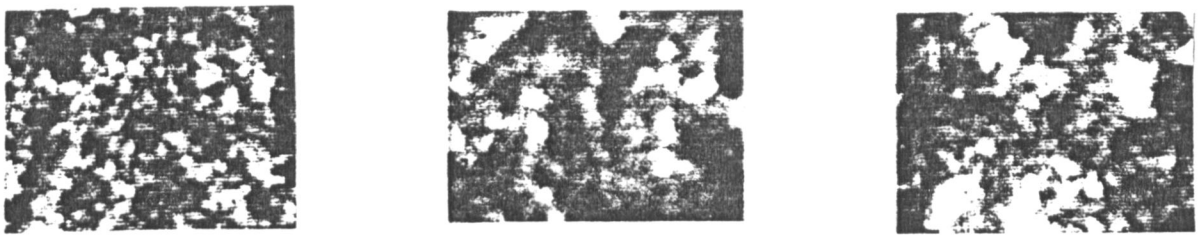

Figure 3-3a Electronic "photographs" taken by Vernin and Azouit (1983a), showing the intensity of the stellar scintillation pattern over an area of 51 cm × 38 cm. The pattern is shown for turbulence at altitudes of 5 km (on the left), 10 km (middle) and 20 km (right).

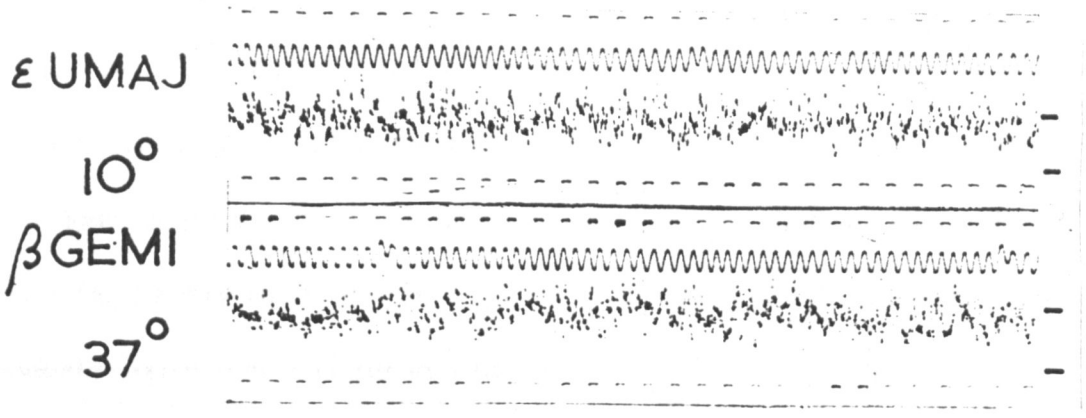

Figure 3-3b Records of the intensity of stellar scintillation made by Butler (1951) using a 10 cm aperture. The stars observed and their zenith angles are indicated on the left. A 50 Hz reference signal was also recorded.

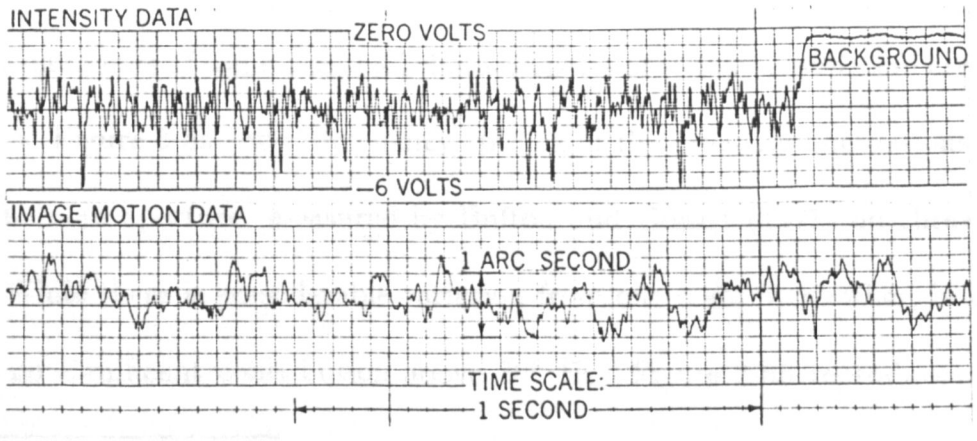

Figure 3-3c Simultaneous recordings of stellar scintillation made by Bufton (1971) using a 15.2 cm aperture, showing intensity and image position over 2 s. Note that the intensity trace is inverted.

made, such time series have not been published for smaller apertures, probably as most recent stellar scintillation measurements have been made with specialized equipment, such as correlators (*eg* Jakeman *et al*, 1976; Azouit and Vernin, 1980). Figure 3-3c also shows a time series of the apparent motion of a star measured by Bufton (1971), showing rapid fluctuations of over 5 μrad in the star's position.

If the observing aperture is larger than the smallest features in the scintillation pattern, then the recorded scintillation will be degraded by aperture averaging (*ie* spatial convolution). The upper graph in figure 3-4 shows measurements of the variance of scintillation as a function of aperture size as presented by Iyer and Bufton (1977), along with theoretical curves fitted to the data. These curves, based on the theory by Fried*, were fitted by assuming that the scintillation for a 1.2 cm aperture is the same as for a point detector. From the diagram it can be seen that the effect of aperture averaging (and hence the form of the spatial spectrum of the scintillation pattern) is in reasonable agreement with theories based on Tatarski's approach.

A more direct indication of the range of pattern sizes is given by the spatial cross-correlation function, an example of which was published by Vernin and Roddier (1975) and is reproduced in the lower graph in figure 3-4. While this was measured for a double star, it should be similar to that for a single star as it was measured perpendicular to the line joining the images of the two stars. It indicates a predominant pattern size of about 4 cm, with a small contribution from features less than 2 cm across.

Measurements of some temporal characteristics of stellar scintillation are shown in figure 3-5. Figure 3-5a shows frequency spectra of the intensity fluctuations observed with a 15.2-cm aperture, measured by Bufton and Genatt (1971) on three different nights. While there is considerable variation from one night to another, in each case there is no significant contribution above 200 Hz. Figure 3-5b reproduces measure-

* This reference was not available to the author, but another publication on the same topic by Fried (1967) starts with Tatarski's approach.

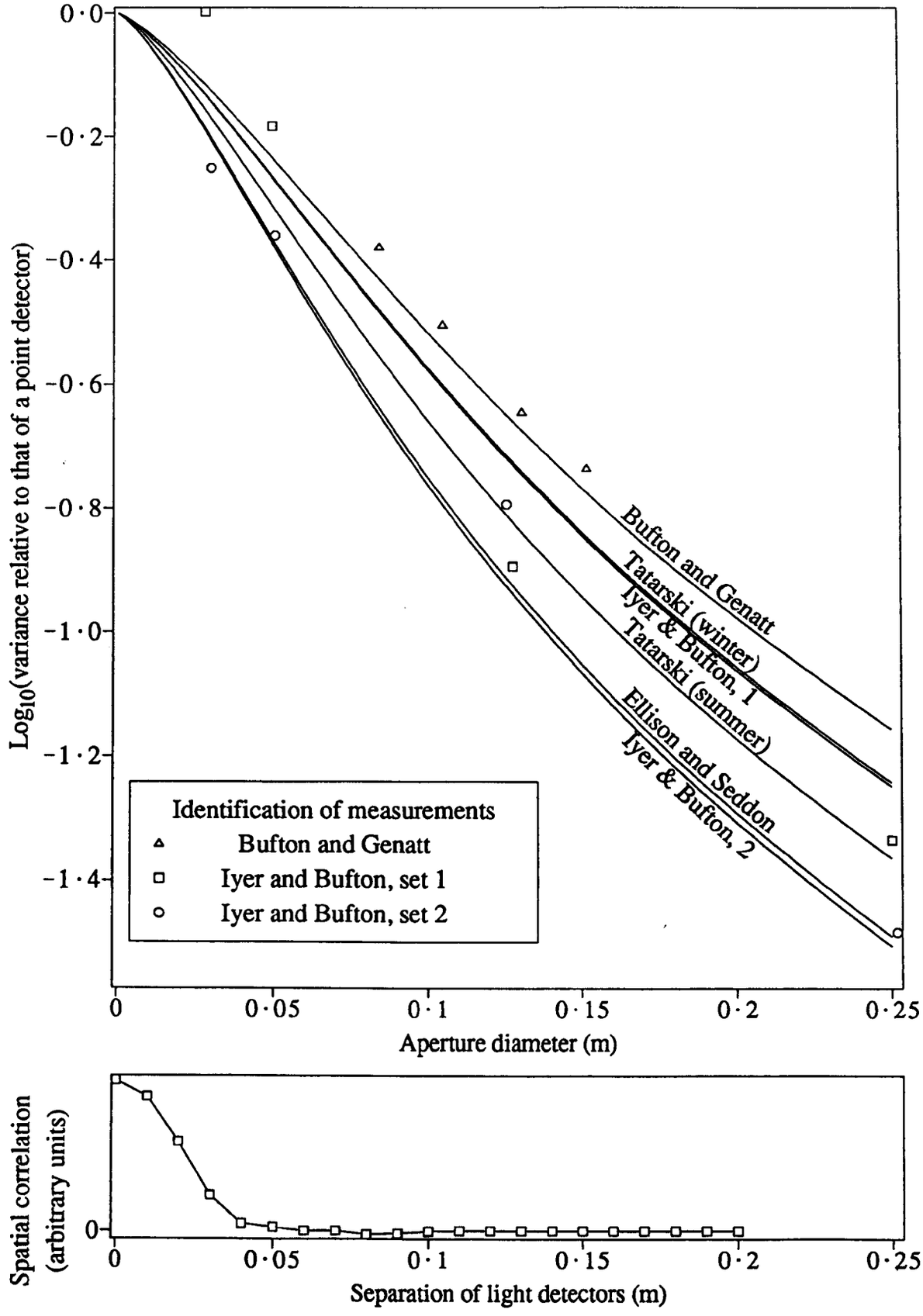

Figure 3-4 Measurements of spatial characteristics of stellar scintillation. The upper graph shows a compilation of measurements and theoretical curves of aperture averaging by Iyer and Bufton (1977). Symbols indicate measurements by Bufton and Genatt (1971) and by Iyer and Bufton (1977). Labelled curves indicate a formula which is fitted to these measurements and to others by Ellison and Seddon (1952) and Tatarski (1961). The lower graph shows a measurement of the spatial correlation function by Vernin and Roddier (1975).

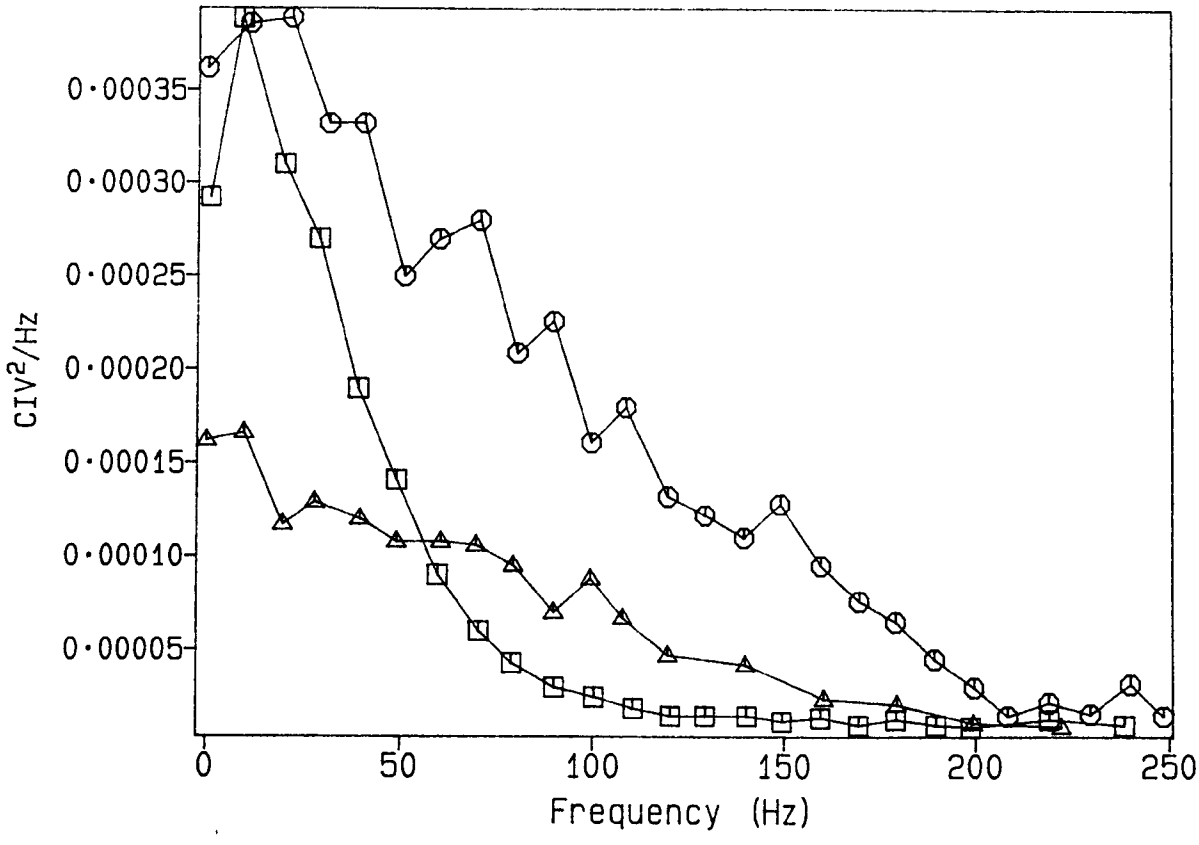

Figure 3-5a Irradiance spectra of the intensity of stellar scintillation, measured on three different nights by Bufton and Genatt (1971), using a 15.2 cm aperture.

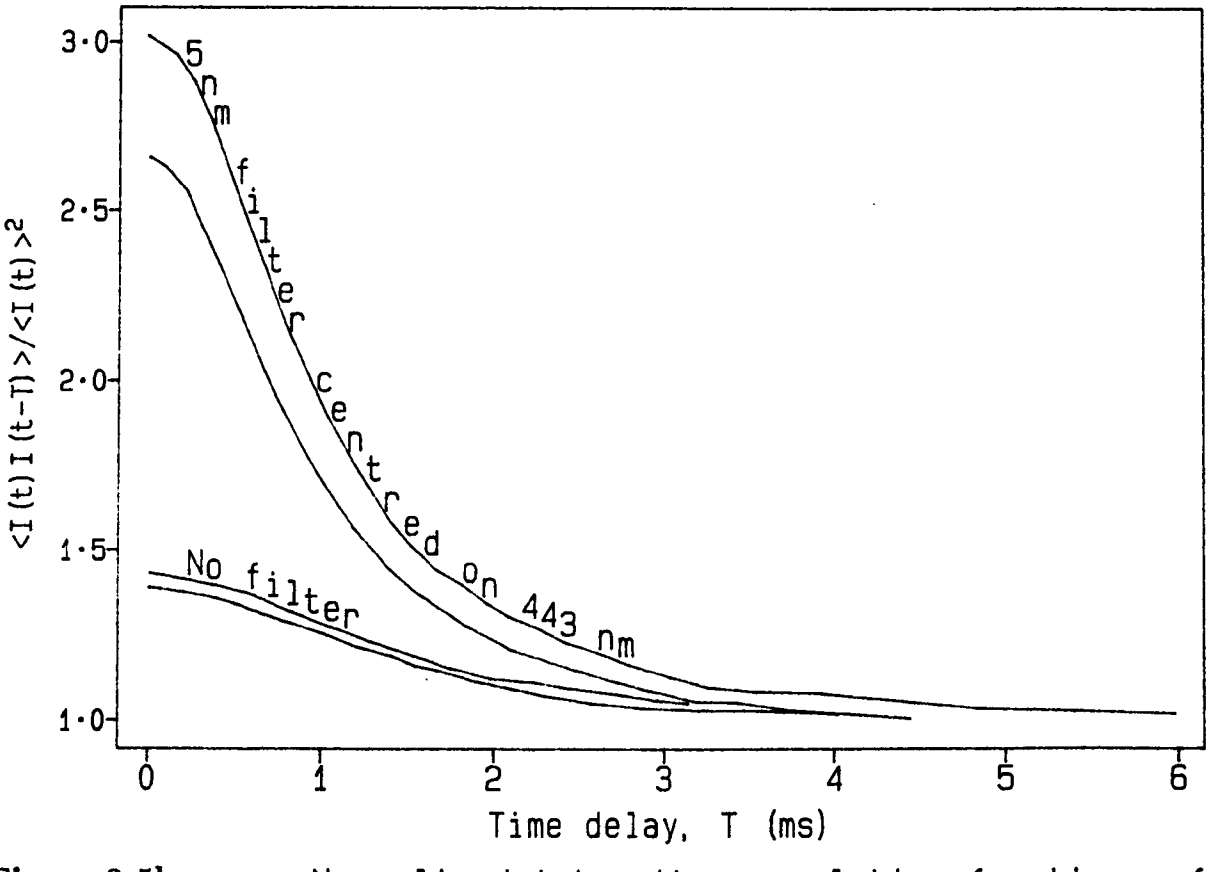

Figure 3-5b Normalized intensity correlation functions of stellar scintillation measured by Jakeman et al (1976) for an 8.4 mm aperture and two different bandwidths. The two lines for each filter indicate variation over 1.5 hours.

ments by Jakeman *et al* (1976) of the temporal autocorrelation function, taken with a sampling interval in the range 20–200 μs and a small (8.4-mm) aperture, with and without a narrow wavelength filter (5-nm width, centred on 443 nm). In contrast to the measurements with the 15.2-cm aperture, it shows that a significant proportion of the scintillation occurs at frequencies greater than 500 Hz. The much higher values of the correlation for observations with the narrow filter indicate that there is significant variation in the pattern with wavelength. These observations suggest that many other published measurements of stellar scintillation may have been affected by temporal, wavelength or aperture averaging.

3.5.2 Observations allowing comparison with theory

The elevation dependence of the intensity fluctuations of stellar scintillation was measured by Ellison and Seddon (1952), Butler (1952) and Bufton and Genatt (1971). All found the fluctuation to decrease with increasing elevation, but the measurements were not of sufficient quality to allow a definitive test between equation 3.9 and the formula recently published by Beran and Whitman (1988) and described in §3.3.

Figure 3-6 shows a compilation of measurements of the relationship between the normalized higher moments ($\frac{\langle I^m \rangle}{\langle I \rangle^m}$, $m = 3,4,5,6$) and the normalized second moment $\frac{\langle I^2 \rangle}{\langle I \rangle^2}$ of the instantaneous intensity I of stellar scintillation, taken by Parry and Walker (1980) and Dainty *et al* (1982). Parry and Walker took records of length 1–2 min with a small aperture (9 mm), narrow wavelength range (10 or 16 nm) and sampling interval of 0.1–0.5 ms. The correlation time of the fluctuations was ~1–4 ms. Dainty *et al* used similar apertures and filters but longer sampling intervals (0.5–1 ms, chosen to give $\sim 2 \times 10^4$ statistically independent fluctuations) in records of length 50–100 s. Their green light measurements were made with an 8-nm filter and their broadband measurements with a 200-nm filter. The curves indicate the predicted relationships for log normal and K distributions of the light intensity. There is good agreement

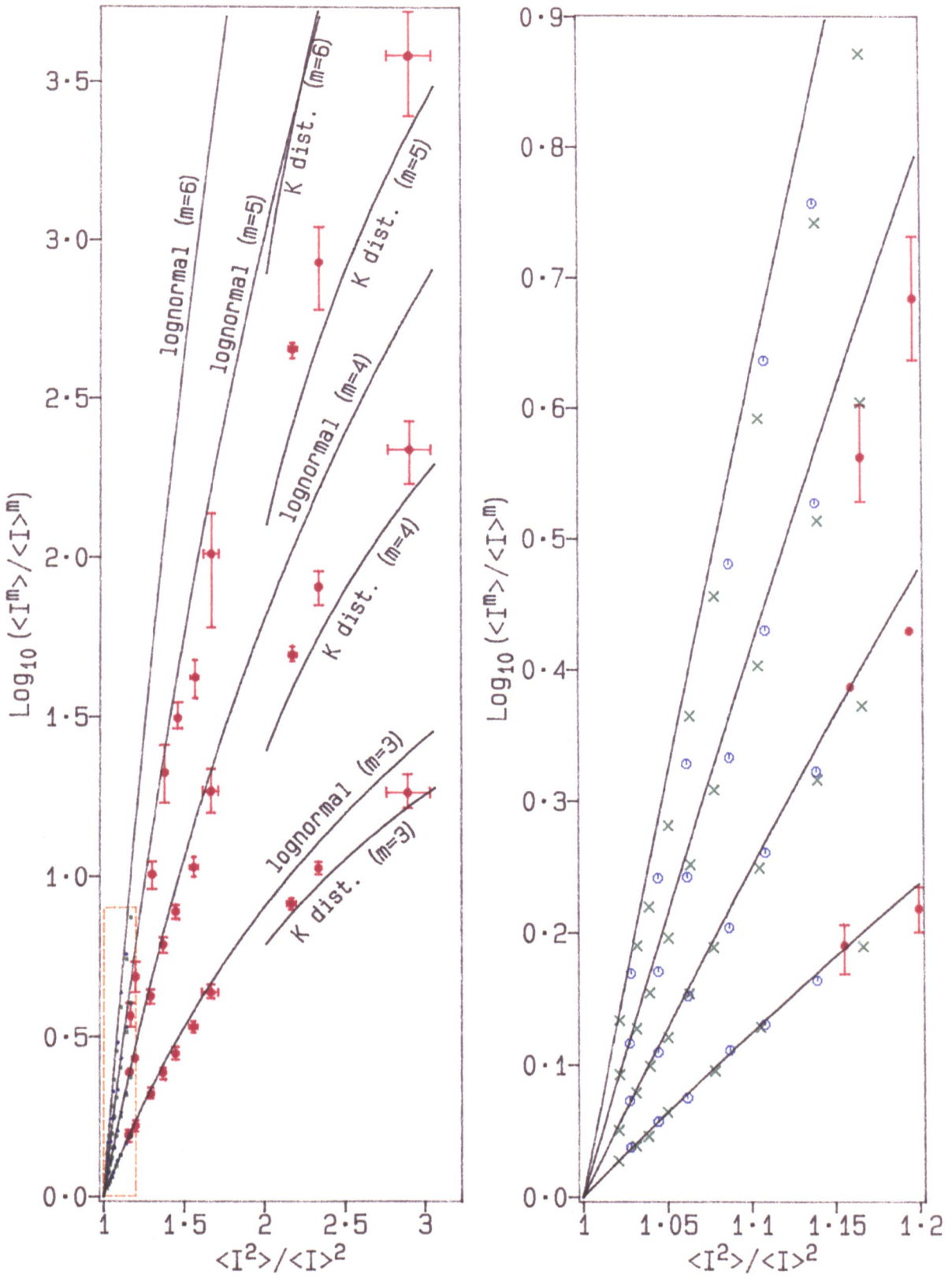

Figure 3-6 Measured values of the normalized higher moments of the intensity of stellar scintillation plotted as a function of the normalized second moment. Measurements by Parry and Walker (1980) are shown by filled red circles with error bars. Two sets of measurements by Dainty et al (1982) are indicated by green crosses for green light and blue octagons for broadband light. Labelled lines show the theoretical functions for the lognormal and K distributions. The data points within the area outlined by the dashed lines are graphed again on the right.

with the log normal distribution for low levels of scintillation, but a trend towards a K distribution at high levels.

Ben-Yosef and Goldner (1988) noted that the results of Parry and Walker are in the region of the moment plot where they predict values for observations of insufficient duration will fall, irrespective of the actual distribution. However, the theoretical moment plot published by Ben-Yosef and Goldner is based on only 5×10^3 samples, while it can be calculated from the information above that Parry and Walker had 1.5×10^4–1.2×10^5 independent samples. Thus it is not clear whether the trend towards a K distribution described above is an artefact of the sample size.

3.6 Turbulence strength from double-star scintillation

To deduce turbulence strength as a function of height Rocca *et al* (1974) applied the principle illustrated in figure 3-7. They assumed that turbulent irregularities at the crossover of the two rays produce identical signals at the two detectors. Thus, for a double star of angular separation a, turbulence at height h produces a peak in the spatial correlation function for separation S according to

$$S = ah. \qquad --(3.12)$$

(*nb* As in the original diagram by Rocca *et al*, figure 3-7 only shows the crossed rays and leaves out two non-crossing rays from each component of the star to the detector on the same side of the diagram.)

Measurements confirming the existence of the two similar patterns in double-star scintillation are presented in figure 3-8. The spatial correlation $C_\perp(S)$ along a line perpendicular to the projection of the line joining the components of the double star is shown in the top graph. The correlation $C_{||}(S)$ parallel to the double star is shown in the middle graph and measurements of the difference $C_{||}(S) - C_\perp(S)$ are shown in the bottom graph. Measurements by Rocca *et al* (1974), Vernin and Roddier (1975)

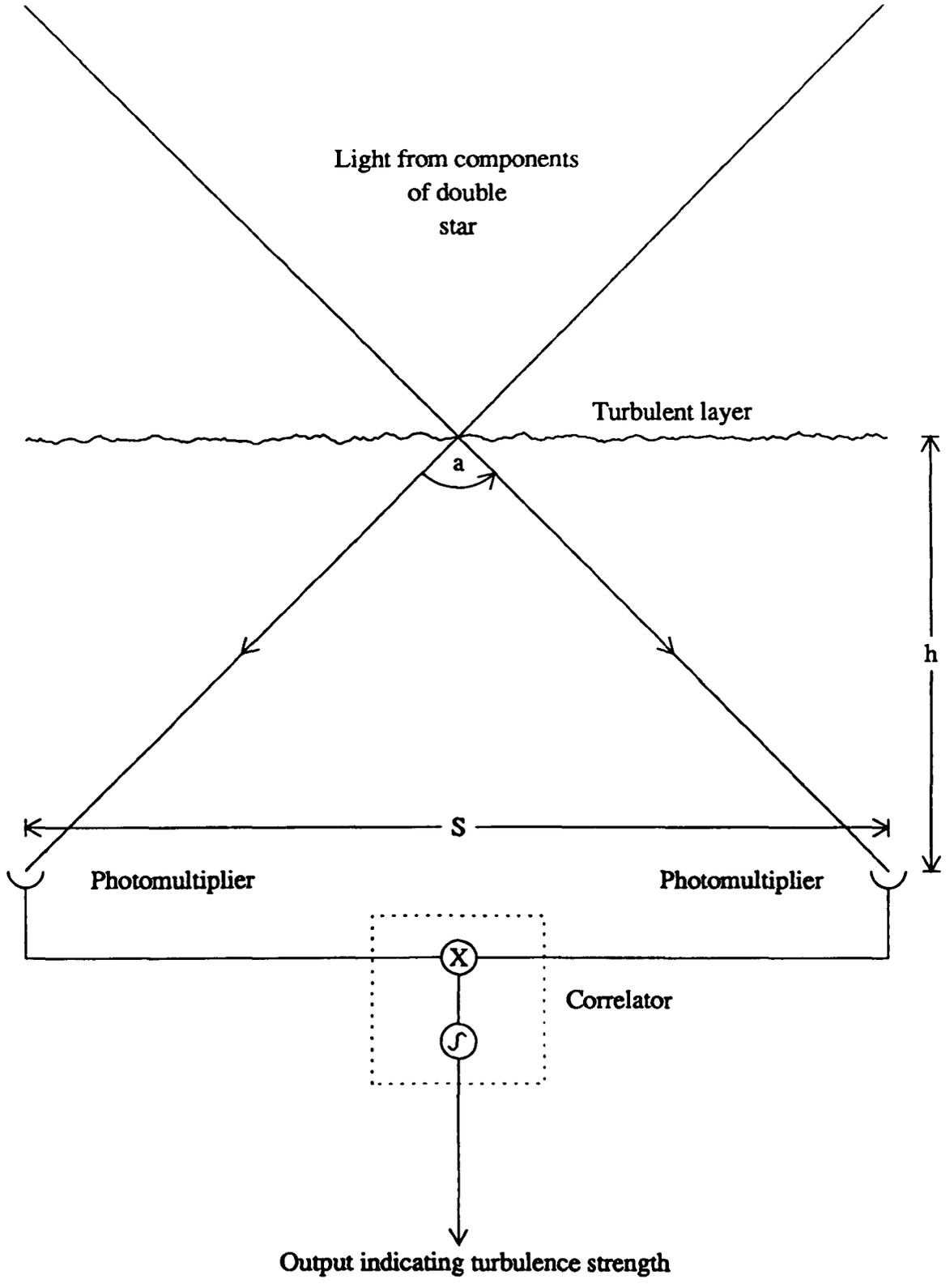

Figure 3-7 A schematic diagram showing the principle applied by Rocca *et al* (1974) to deduce the height of turbulence from stellar scintillation. For a double star of angular separation a, irregularities at height h should produce correlated signals at detectors separated by distance S, where $S = ah$. An output related to the turbulence strength is produced by a correlator which integrates the product of the two signals. (As in the original diagram by Rocca *et al*, only the crossed "beams" are drawn. Each photomultiplier will also receive light from the other component of the double star.)

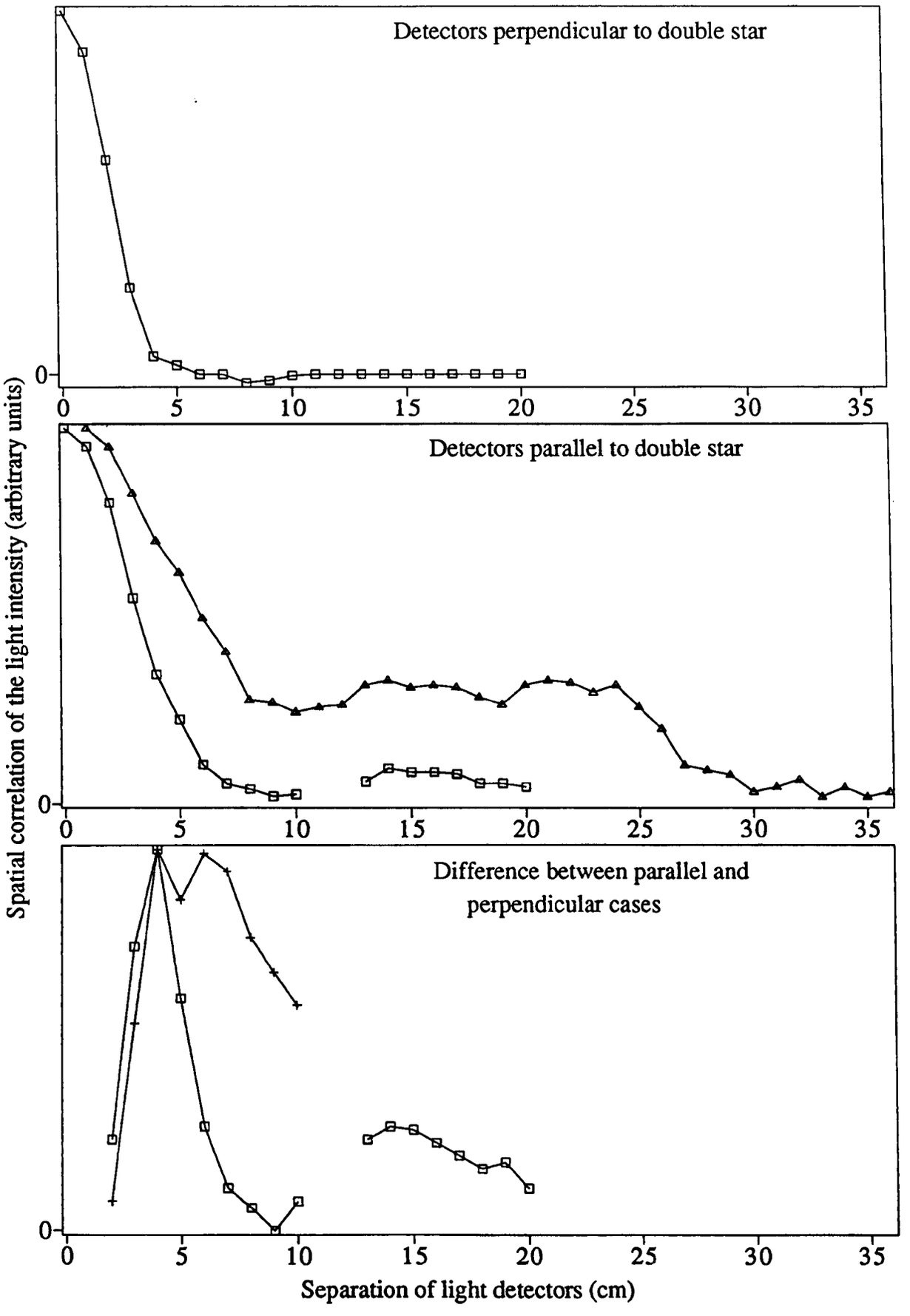

Figure 3-8 Measurements of the spatial correlation function of the light intensity of a double star, taken perpendicular and parallel to the orientation of the two components. The bottom graph shows the difference between such measurements for these two cases (*ie* $C_{||}(s) - C_{\perp}(s)$, where s is the separation). Symbols identify the source of the measurements: + Rocca *et al* (1974), □ Vernin and Roddier (1975) and △ Azouit *et al* (1980).

and Azouit *et al* (1980) are included. The peaks at finite separations (of ~5 cm and ~15 cm) in $C_{||}(S) - C_{\perp}(S)$ indicate the presence of two similar components in the scintillation pattern produced by the double star. Thus the basic assumption of the method proposed by Rocca *et al* (1974) is justified (at least in part – the displaced patterns exist, but it is not shown that they are identical).

A problem in the application of this method is that peaks in spatial correlation at different separations, produced by turbulence at different heights, can overlap. Rocca *et al* (1974) dealt with this by calculating the spatial correlation function for each of a range of possible heights and turbulence strengths and then finding a combination of these which gave the best fit to $C_{||}(S) - C_{\perp}(S)$. For the particular spatial correlation function indicated by plus signs in figure 3-8, they deduced the presence of 3 turbulent layers at 3, 6 and 10 km.

To predict the shape of the spatial correlation function for each height, Rocca *et al* took the 2D Fourier transform (*ie* the Hankel transform H_{ankel}) of the 2D spatial power spectrum $W_h(\kappa)$ of the intensity fluctuations produced at height h by a layer of thickness Δh:

$$C_h(\overrightarrow{\rho}) = H_{ankel}(W_h(\kappa)) = H_{ankel}(8\pi k^2 \Phi_n(\kappa)\Delta h \sin^2 \frac{h\kappa^2}{2k}) \qquad --(3.13)$$

where $C_h(\overrightarrow{\rho})$ is the correlation at separation $\overrightarrow{\rho}$. The expression for $W_h(\kappa)$ was obtained by extension of Tatarski's work. *nb* equation 3.13 is as quoted subsequently (*eg* Roddier and Vernin, 1977), as the original reference had a "4" in place of the "8".

If the scintillation patterns are small compared to the difference in separation $S = |\overrightarrow{\rho}|$ for different turbulent layers, then the spatial correlation can be directly transformed to a height profile of turbulence strength, using (Azouit and Vernin, 1980)

$$C(S)_{S=ah} = \frac{\langle (I(x) - \langle I(x)\rangle)(I(x+S) - \langle I(x+S)\rangle)\rangle}{\langle I(x)\rangle\langle I(x+S)\rangle} = R_{ds}C(0) \qquad --(3.14)$$

where $C(S)_{S=ah}$ is the spatial correlation at separation S corresponding to height h and R_{ds} is a ratio which relates the spatial correlation between the two components of a double star to the spatial autocorrelation, *ie*

$$R_{ds} = \frac{C(S)}{C(0)} = \frac{B_1 B_2}{(B_1 + B_2)^2} \qquad --(3.15)$$

where $\frac{B_1}{B_2}$ is the ratio of the mean intensities of the two components (Roddier and Vernin, 1977). From 3.14, $C(0) = \frac{\langle (I(x) - \langle I(x) \rangle)^2 \rangle}{\langle I(x) \rangle^2}$ and thus, for a layer of thickness Δh, $\overline{C_n^2(h)}$ can be determined by substitution in equation 3.9 *ie*

$$C(0) = 2.24 k^{\frac{7}{6}} (\sec\phi)^{\frac{11}{6}} \int_h^{h+\Delta h} C_n^2(h') h'^{\frac{5}{6}} dh'$$

$$= 2.24 k^{\frac{7}{6}} (\sec\phi)^{\frac{11}{6}} h^{\frac{5}{6}} \overline{C_n^2(h)} \Delta h \ . \qquad --(3.16)$$

(*nb* Azouit and Vernin (1980) had 0.56 rather than 2.24 as the constant in equation 3.16. This appears to come from using Tatarski's (1961, *p*169) formula for variance of ln(amplitude) in place of that for variance of irradiance.)

Tests of these methods, in which scintillation-derived turbulence profiles were compared with direct measurements by balloon-borne thermometers, have been made (Vernin *et al*, 1979; Azouit *et al*, 1980) However, it is not clear which of the two methods described above (fitting of the spatial correlation functions or use of equation 3.16) was applied to determine the turbulence profile from the optical measurements.

In the first of these tests Vernin *et al* (1979) observed the spatial correlation between the scintillation on two 3-cm apertures which could be separated by 0 to 20 cm using a beam splitter. The example showing the best agreement with *in situ* measurements is reproduced in Fig 3-9a. The *in situ* measurements are smoothed to emulate the height resolution of the optical measurements, which is set by the size of the features in the scintillation pattern. The same comparison for four other balloon flights showed good agreement when the turbulence was stable (this stability being indicated by the absence of variation in the optical measurements).

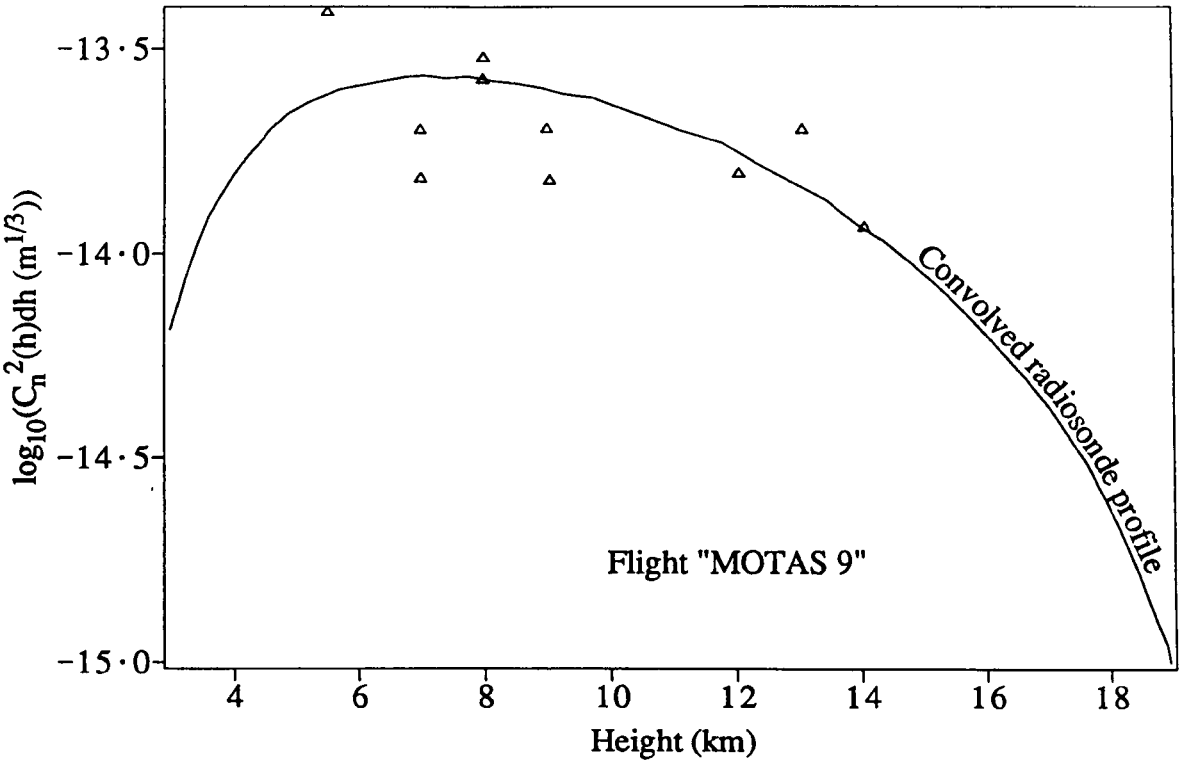

Figure 3-9a A comparison of optical and *in situ* measurements of the strength of turbulence against height, by Vernin *et al* (1979). Triangles indicate the turbulence strength deduced from the scintillation of a double star. The curve indicates a simultaneous measurement by balloon-borne instruments, convolved with the 6 km resolution of the optical system.

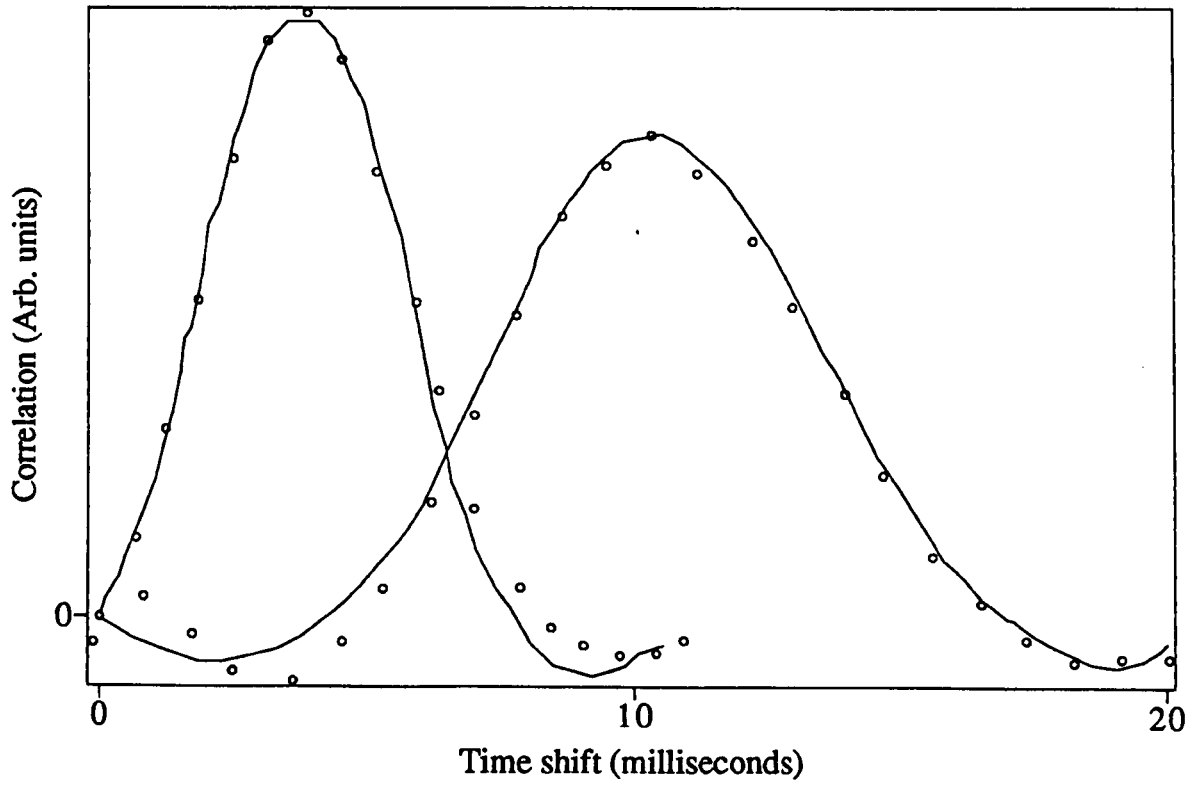

Figure 3-9b Measurements and fitted theoretical curves of the temporal cross correlation of scintillation. The cross correlation between the fluctuations on apertures separated by 6 cm is plotted as a function of the time shift applied to one of the series relative to the other. Circles indicate measured values and the curves indicate the best fitting theoretical curves. (Reproduced from fig. 4 by Rocca *et al*, 1974).

Subsequently, Azouit and Vernin introduced an improved instrument, based on a sensitive imaging detector and a fast correlator, which can measure the turbulence profile in 10 s, rather than the 20 min required by the two-detector system used for the measurements described above (Azouit and Vernin, 1980). A comparison of turbulence profiles measured by this new instrument with measurements by balloon-borne thermometers (Azouit *et al*, 1980) showed reasonable agreement, although the optically measured values were always lower than the *in situ* measurements for the height range 9–17 km. Azouit *et al* ascribed this difference to "wind shear effects on the balloon-radiosonde ensemble".

3.7 Wind measurements using stellar scintillation

The remote measurement of wind velocity using scintillation is based on the assumption that turbulent features move with the wind without changing form (often referred to as "Taylor's hypothesis", as Taylor (1938) found it to be valid in laboratory measurements). This is an approximation for the atmosphere, where small-scale turbulent features are swept around inside larger eddies. In fact, observations of fluctuations in the apparent velocity of the wind can be used to deduce turbulence intensities (*eg* Hocking, 1983).

Confirmation that features in the scintillation can be tracked from one detector to another is given in figure 3-9b. This reproduces measurements and fitted theoretical curves by Rocca *et al* (1974) of the time-shifted cross correlation between the scintillation on two apertures, spaced 6 cm apart on a line parallel to the direction of pattern motion. Taylor's hypothesis was confirmed for displacement over larger distances by Caccia *et al* (1987) in measurements of the time-shifted two-dimensional cross-correlation function, which indicated a lifetime of ~60 ms for 10-cm eddies.

Vernin and Roddier (1973) deduced the wind velocity and height for two turbulent

layers (at 5 and 9 km) from a two-parameter power spectrum (power versus temporal and spatial frequencies) of stellar scintillation. Their analysis was based on relating the spatial spectrum to the height of the turbulence, and the temporal frequency to the wind velocity. (The periodicity in time was produced by the transit of the scintillation patterns across several equally spaced strips in a spatially filtered detector.) The measured velocities agreed with radiosonde measurements.

Vernin and Azouit (1983b) used the imaging system and correlator described earlier to measure the wind at a particular height using the scintillation of a double star. The height was determined from the position of a second peak in the two-dimensional spatial correlation function at zero time delay and the velocity was then found from the displacement of this peak observed at a finite time delay.

Using a similar instrument Caccia *et al* (1987) were able to measure a wind profile from 2 to 20 km, with 1-km resolution, by observing the scintillation of a single star. They determined the height from the width of the peaks in the spatial correlation function. Good agreement with radiosonde measurements was obtained.

Recently Caccia and Vernin (1990) used the same instrument (in double-star observations) to measure the standard deviation of the horizontal wind velocity at nine heights in the atmosphere. The standard deviation was found to be 2–5% of the average value of the velocity.

3.8 Multiple-beam remote sensing

In this thesis a method is developed to measure atmospheric wind velocity by applying an existing remote-sensing technique to stellar scintillation. This technique was introduced by Sasaki and Sato (1979) for the remote measurement of velocity versus position in a fluid. The principle of the method is illustrated in figure 3-10a. Three beams of light, only two of which are parallel, pass through a fluid and fall on

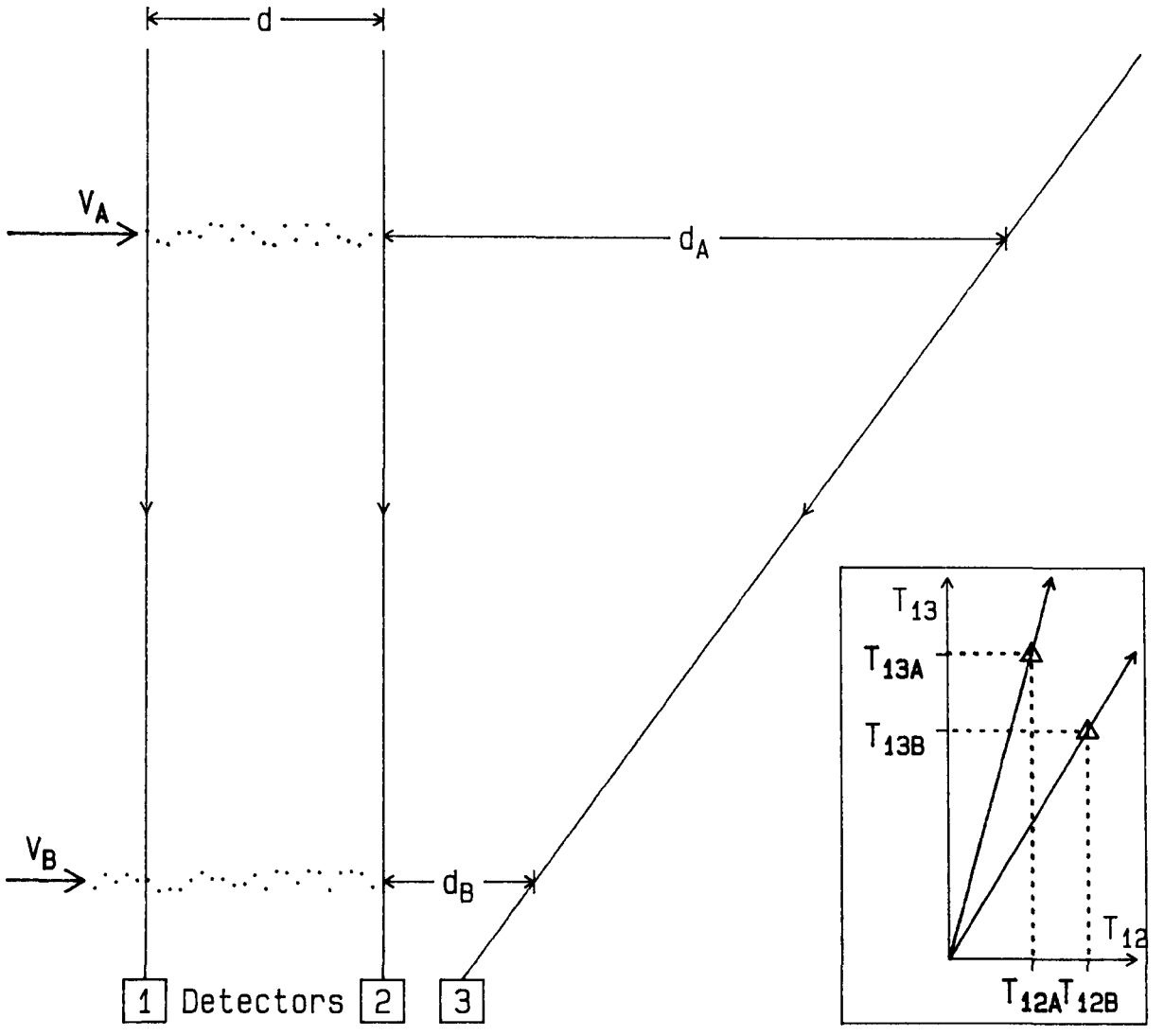

Figure 3-10a A diagram of the multiple beam method introduced by Sasaki and Sato (1979), showing scatterers moving through three light beams at two different distances from the detectors. The inset shows the triple correlation function of the signals from the three detectors, with triangles indicating the positions of the peaks in correlation due to the two velocities.

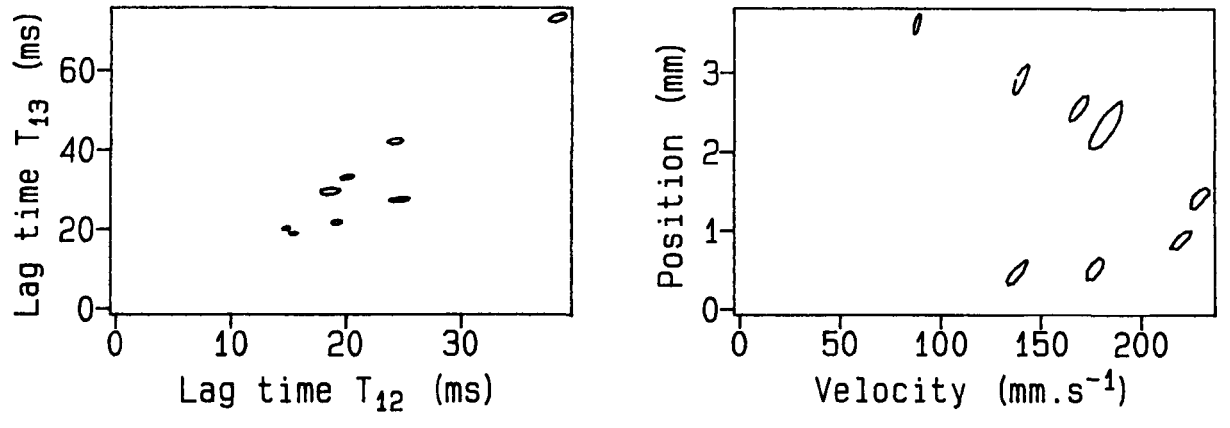

Figure 3-10b Results obtained by Sasaki and Sato (1979), using the multiple beam method to find the velocity profile across a 4 mm capillary tube. The correlogram on the left indicates where the triple correlation exceeded a set value. This is transformed to the velocity profile on the right.

detectors 1, 2 and 3. The fluid is seeded with small particles which act as tracers of the fluid velocity. Time series of the intensity recorded on the three detectors show pulses produced by the seed particles passing through the three beams. For a particular particle, the ratio between the time delays between these pulses identifies the position along the beams by

$$\frac{T_{12}}{T_{13}} = \frac{d_{12}}{d_{13}} = \text{function of distance from the detectors} \qquad -- (3.17)$$

where T_{mn} is the time delay between the pulses on detectors m and n and d_{mn} is the separation (at the position of the particle) between the beams which fall on these detectors. Thus each direction (from the origin) in the T_{12}, T_{13} plane corresponds to a position along the beams and each point along this direction corresponds to a different transverse velocity v_{trans} given by

$$v_{trans} = \frac{d_{12}}{T_{12}} \, . \qquad -- (3.18)$$

This mapping is illustrated in figure 3-10a by the two velocity vectors V_A and V_B, which map to the positions indicated by the triangles in the inset.

Sasaki and Sato calculated the triple correlation

$$C_3(T_{12}, T_{13}) = \frac{1}{T} \int_0^T I_1(t) I_2(t + T_{12}) I_3(t + T_{13}) dt \qquad -- (3.19)$$

where $I_n(t)$ is the intensity on detector n at time t. One of their measurements of this function (for the profile of transverse velocity across a 4-mm capillary tube) is reproduced in figure 3-10b, along with a transformation of this to a position-velocity profile. To measure the component of velocity along the beams, they added a fourth beam (not parallel to any of the others) and used the quadruple correlation

$$C_4(T_{12}, T_{13}, T_{14}) = \frac{1}{T} \int_0^T I_1(t) I_2(t + T_{12}) I_3(t + T_{13}) I_4(t + T_{14}) dt. \qquad -- (3.20)$$

In order to avoid false correlations (*eg* a chance correlation between pulses due to one particle at delay T_{12} and to a different particle at T_{13}), Sasaki and Sato used a low density of seed particles, so that such ambiguities would not arise.

The method described above could in principle be applied to atmospheric remote sensing, using refractive-index irregularities as tracers of the wind velocity. However, as the observer has no control over the density of such irregularities, ambiguous results would arise from chance correlations between unrelated scintillation patterns.

3.9 Measurements of atmospheric isoplanatism

The atmospheric isoplanatic angle has been measured from short-exposure photographs of double stars. More recently it has been deduced indirectly from measurements of scintillation.

The image of a double star consists of two patterns of "speckles" (one pattern for each star), where the speckles are diffraction-limited images of the individual stars, translated from their correct positions by phase variations produced by turbulence (Labeyrie, 1970). If the two components of a double star fall within the same isoplanatic patch, then the two patterns of speckles for each star will be identical. Thus Nisenson and Stachnik (1978), using short-exposure images of double stars with a range of separations of 1–23 μrad, were able to deduce the amount of isoplanatism. They found complete isoplanatism for separations less than 10 μrad, with some correlation between the speckle patterns at 23 μrad indicating partial isoplanatism. Weigelt (1979) found evidence of partial isoplanatism at separations of over 100 μrad. Summarizing these and results of other workers, Dainty (1984) suggested that the isoplanatic angle is generally in the range 5–20 μrad.

Loos and Hogge (1979) measured isoplanatism indirectly, by calculating its value from the turbulence profile determined from scintillation. They adapted a formalism

for isoplanatism developed by Fried. Their definition is most easily explained by considering the case of an adaptive laser transmitter which records the distortion on a received reference beam and uses this to apply a precorrection to a beam transmitted back in a slightly different direction, so that the turbulence along the two beams may be different. The isoplanatic angle θ_o defined by Loos and Hogge is the angle between the transmitted and reference beams at which the power on the transmitted beam is reduced to a factor of e^{-1} compared to the value expected for no turbulence. Loos and Hogge derived

$$\theta_o = 0.528\left[k^2 \int_0^\infty C_n^2(h) h^{\frac{5}{3}}\right]^{-\frac{3}{5}} . \qquad --(3.21)$$

Applying this to turbulence profiles measured with a scintillometer (following Ochs *et al*, 1976), they found $\theta_o = 7 \pm 2$ μrad.

Loos and Hogge suggested that the $h^{\frac{5}{6}}$ dependence of the scintillation variance for a point detector (equation 3.9) could be changed to match the $h^{\frac{5}{3}}$ dependence of the isoplanatic angle by selection of an appropriate aperture, which they calculated to be 11 cm in diameter. This idea was applied by Eaton *et al* (1985), who found mean values of θ_o to be 5.9 μrad and 8.7 μrad in two different measurement situations.

The isoplanatic angle is dependent on the size of the aperture for which it is measured, in addition to atmospheric properties. Based on the visual observation that planets scintillate less than stars, Schneiderman and Karo (1978) inferred that the isoplanatic angle associated with stellar scintillation patterns is less than 5 μrad.

3.10 Photocount statistics

To observe stellar scintillation without instrumental averaging requires the use of small apertures, narrow optical bandwidths and short sampling intervals. For such observations, it is not possible to directly measure the fluctuations in intensity because, at such low light levels, the detection rate is too low (*eg* less than one photon per

sampling interval). Furthermore, the detection rate of photons fluctuates statistically, according to the Poisson distribution, *ie* for an average rate of μ photons.s^{-1}, the probability $p(n;\mu\Delta t)$ of n photons in time Δt is given by

$$p(n;\mu\Delta t) = \frac{e^{-\mu\Delta t}(\mu\Delta t)^n}{n!} \; . \qquad --(3.22)$$

While it is not possible to determine the intensity distribution from photon counts, the normalized factorial moments of a photocount distribution can be converted to the normalized moments of the intensity distribution using (Jakeman *et al*, 1978)

$$\frac{\langle n(n-1)...(n-m+1)\rangle}{\langle n\rangle^m} = \frac{\langle I^m\rangle}{\langle I\rangle^m} \qquad --(3.23)$$

where n is the number of photocounts per sampling interval produced by light intensity I and $m = 2,3,4,5...$ This allows the measurement at very low light levels of the quantities which are plotted in the moment plot (*eg* figure 3-6).

To apply equation 3.23 to starlight, a correction must be made for background light and equipment noise. Pusey (1977) derived this correction for the case where the background light is of constant intensity and the equipment noise is Poisson distributed (which means that it can be treated as additional background light). For measurements of n_F counts per interval for the full intensity I_F and n_D counts per interval for the background intensity I_D, Pusey gave the second and third moments of the signal intensity I as:

$$\frac{\langle I^2\rangle}{\langle I\rangle^2} = \frac{1}{\langle n\rangle^2}\left\{\frac{\langle I_F^2\rangle}{\langle I_F\rangle^2}\langle n_F\rangle^2 - 2\langle n_F\rangle\langle n_D\rangle + \langle n_D\rangle^2\right\} \qquad --(3.24)$$

and $$\frac{\langle I^3\rangle}{\langle I\rangle^3} = \frac{1}{\langle n\rangle^3}\left\{\frac{\langle I_F^3\rangle}{\langle I_F\rangle^3}\langle n_F\rangle^3 - 3\frac{\langle I_F^2\rangle}{\langle I_F\rangle^2}\langle n_F\rangle^2\langle n_D\rangle + \right.$$

$$\left. 3\langle n_F\rangle\langle n_D\rangle^2 - \langle n_D\rangle^3\right\} \qquad --(3.25)$$

where $\langle n\rangle = \langle n_F\rangle - \langle n_D\rangle$.

The normalized covariance between light intensities on different detectors, or between samples at different times on the same detector, can be found from photocount measurements using (Jakeman and Pusey, 1980)

$$\frac{\langle I_1 I_2 \rangle}{\langle I_1 \rangle \langle I_2 \rangle} = \frac{\langle n_1 n_2 \rangle}{\langle n_1 \rangle \langle n_2 \rangle} \qquad -- (3.26)$$

where n_1 and n_2 are the numbers of counts per interval produced by light intensities I_1 and I_2.

3.11 Photomultiplier operation and afterpulsing

Equations 3.24 and 3.25 are based on the assumptions that

1) the rate of photocounts is proportional to the light intensity and has a Poisson distribution and

2) the noise counts are independent of the counts produced by the light source.

Certain characteristics of photomultipliers invalidate these assumptions, particularly if they are not operated correctly. Thus a brief description of the principle and operation of photomultipliers is given below, to indicate the approach needed to get optimum performance.

Even with correct operation, photomultiplier afterpulsing occurs, producing noise counts which are correlated with genuine photocounts. This problem has been avoided previously by "judicious choice of photomultiplier tube" (Jakeman and Pusey, 1980), but this could be an expensive option. The approach in this work is to develop methods to determine the amount of afterpulsing from the recorded data and then to make a correction for it. As background to this development, the origin of photomultiplier afterpulsing is reviewed below.

3.11.1 General description

The photomultiplier tube is the best available device for the measurement of low light intensity (Candy, 1985a). It consists of a photocathode and an electron multiplier

enclosed in a vacuum tube. Photons of light incident on the photocathode cause the ejection of single photoelectrons. These are then multiplied by acceleration to a series of dynodes, each of which is at a higher potential than the previous one. At each dynode the impact of an electron ejects several electrons, finally producing a pulse of 10^6–10^7 electrons at the anode. In "photon counting" applications an electronic amplifier is used to discharge the anode as quickly as possible and generate a pulse of very short duration. Ideally the shape of this pulse should be independent of the size of the anode pulse, which varies considerably due to statistical fluctuation in the electron-multiplication process.

The major sources of noise pulses (called "dark current") in photomultipliers are thermionic emission, ions from absorbed gases, cosmic rays and background radiation (Morton, 1968); there are also several other sources which are either minor or are the result of bad operating conditions (Candy, 1985a). Counts due to thermionic emission have a Poisson distribution, but counts due to some of the other sources do not.

3.11.2 Photomultiplier operation

The optimum operation of photomultipliers requires attention to a considerable number of factors, as reviewed by Candy (1985a). These include the distribution of voltage, capacitance, inductance and resistance along the dynode chain and the electric and magnetic environment of the tube.

Some basic factors in the operation of photomultipliers are:

1) generally the interdynode voltages are set by a resistor chain which divides the total applied voltage (~1000 V) into equal increments. The gain of the tube is adjusted by varying the applied voltage. The gain increases rapidly with increasing voltage so the applied voltage must be well regulated at the desired value.
2) The photocathode-to-first-dynode potential difference is often set with a Zener diode to maintain it at an optimum value while the applied voltage is varied. This

optimum value should be relatively large to reduce the statistical fluctuation in the amplitude of the output pulses (Candy, 1985a).

3) To reduce some sources of noise, the applied voltage should be kept as low as possible (Candy, 1985a), subject to the condition that most of the output pulses are large enough to trigger the external pulse detector. Thus it is advantageous to have an external pulse amplifier with low input noise.

4) Capacitors should be placed across the final few stages of the dynode chain so that the current pulses do not temporarily reduce the potential differences and hence the gain.

5) The cathode environment should be held at cathode potential to avoid electroluminescence due to a potential difference across the glass faceplate (Krall, 1967).

6) It is common to cool the tube during operation to reduce noise.

7) Noise and afterpulsing can be reduced by storage of the tube in a cold dark nitrogen atmosphere (Candy, 1985a) and by application of high voltage for hours before the tube is used for measurements (Young, 1969b).

3.11.3 Afterpulsing in photomultipliers

Genuine pulses from a photomultiplier may be followed by an afterpulse (Breitenberger, 1955). These can arise in a number of ways:

1) an atom or molecule of gas (either residual from manufacture, or helium, which diffuses through the glass envelope of the tube from the atmosphere over several years) is ionized by a photoelectron and the resulting positive ion is accelerated back to the photocathode. Its impact ejects several electrons, leading to a large output pulse following the initial one after 100–800 ns, the delay depending on the type of ion involved (Morton, 1967 and Coates, 1973). This mechanism generally produces most of the detected afterpulses.

2) The positive ions hit the dynodes, producing afterpulses smaller than the initial

pulse (Paske, 1974; Lo and Leskovar, 1983).

3) The de-excitation of a positive ion produces a photon which is detected at the photocathode, producing an afterpulse about 20 ns after the initiating pulse (Breitenberger, 1955).

4) Fluorescence of the later dynodes results in afterpulses after about 40 ns (Krall, 1967).

5) Luminescence of residual gas around the last few dynodes produces afterpulses after 5 μs, with luminescence around the 3rd dynode giving afterpulses after 20–40 μs (Yamashita *et al*, 1982).

6) Fluorescence in the glass envelope, caused by cosmic rays, ejects photoelectrons from the photocathode. It has a decay time of 20–50 μs (Coates, 1971).

7) "Ringing" of the pulse due to (a) oscillation (at 200–500 Mhz) of the charge in the dynode chain, (b) oscillation of the electron cloud about the anode and (c) bad design of the external pulse amplifier (Candy, 1985b) produce correlated pulses.

Excluding 7), the probability of the occurrence of an afterpulse is in the range 10^{-4}–2×10^{-2} (Coates, 1972). Measurements of this probability are made with a multichannel analyzer which is set up to record the number of pulses in specific time intervals following a light flash or initiating pulse.

An afterpulse may produce a subsequent afterpulse, with a different probability to that of the first one, as the probability is determined by the number of photoelectrons involved (Williams and Smith, 1973).

Thus there are many mechanisms which can produce afterpulses, all with different time delays and probabilities. In consequence, the methods to be developed in §4.5 to measure and correct for afterpulsing are designed to minimize dependence on unknown factors. Ways are sought so that these factors make the same contribution in both the measurements of afterpulsing and in correction for it, so that their effect cancels.

Chapter 4 New theory

This chapter describes techniques and methods of analysis which were developed in this work and are believed to be new. These include the use of stellar scintillation

1) to deduce the profile of atmospheric wind as a function of height, and
2) to measure the atmospheric isoplanatic angle.

In the first case, the wind measurement requires:

a) the development of a multiple-beam remote sensing system using a double star as a light source and turbulent irregularities as tracers of the wind velocity.
b) The development of multiple-correlation techniques to detect the presence of signals which are common to all of three or more series but hidden among other signals, which may be either uncorrelated, or correlated between some but not all of the series.
c) The determination of the extent of both atmospheric refraction and interaction of scintillation patterns which are produced by turbulence at different heights.

In the second case the measurement of the isoplanatic angle using stellar scintillation requires the development of techniques to correct photocount distributions for afterpulsing and background. These corrections are also required in order to repeat (with better resolution) some measurements made by others of the basic features of the scintillation pattern.

4.1 Wind measurement using double-star scintillation

4.1.1 Basic principle

Figure 4-1 illustrates the principle applied by Vernin and Azouit (1983b) to measure wind velocity versus height in the atmosphere, using the scintillation of a double star. It represents (with unbroken lines) light from the two components of a double star, of angular separation a, being distorted by a turbulent patch at height h and so producing two identical diffraction patterns, separated by a distance S in the receiver plane. Dashed lines show the situation after a unit time interval. Due to wind velocity V, the turbulent patch and the diffraction patterns move to new positions. In this ideal situation it is possible to measure the wind velocity at a particular height by observation of the scintillation pattern at four appropriately placed detectors.

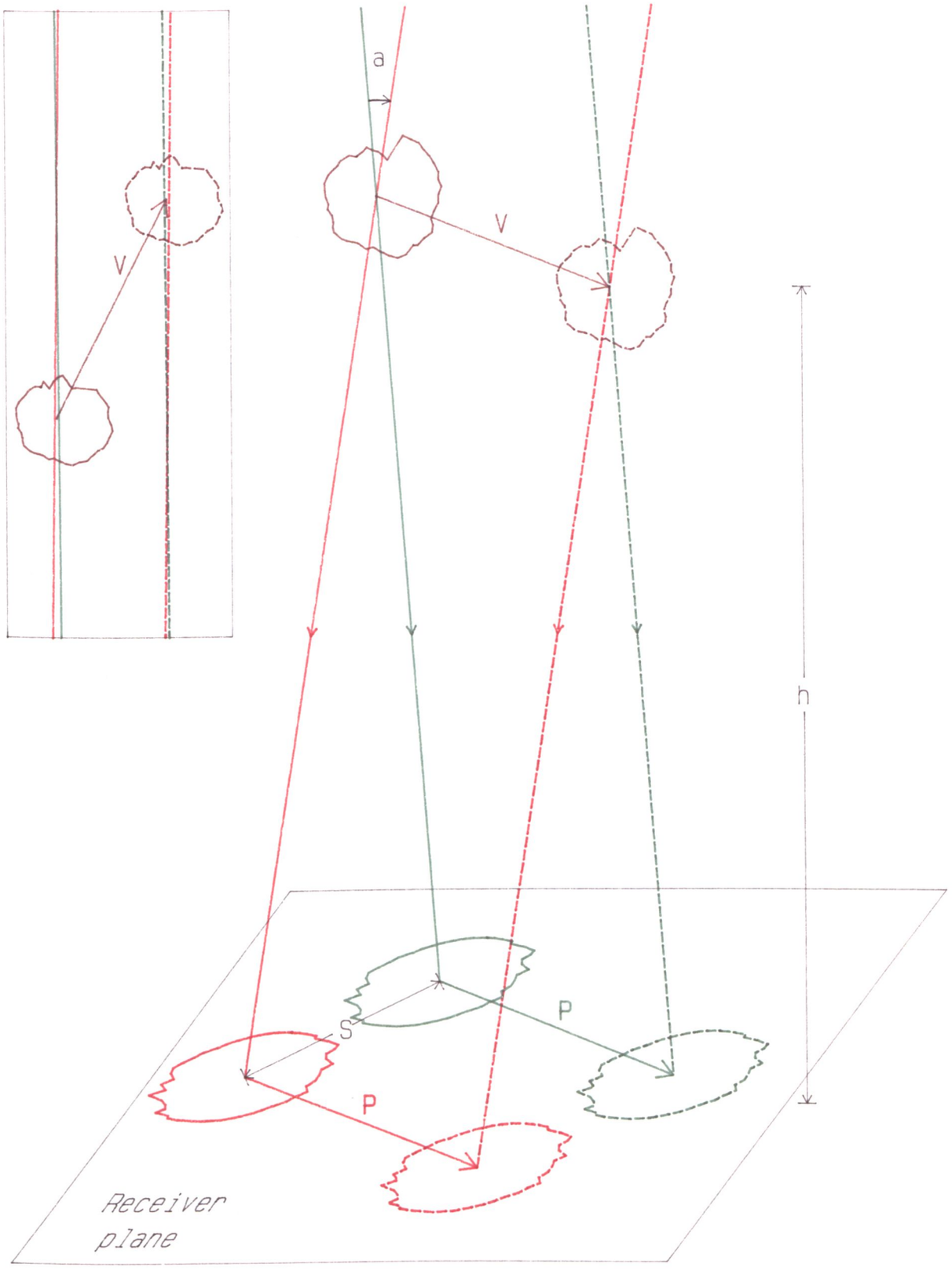

Figure 4-1 An illustration of the principle by which the wind velocity against height in the atmosphere may be deduced from the scintillation of a double star. The pattern separation "S" is related to the height "h" and the separation angle "a". The pattern velocity vector "P" is the projection of wind velocity vector "V". Due to the exaggerated size of angle "a" in the main diagram, it appears that "V" must be parallel to the receiver plane. The inset shows that this is not so when "a" is small.

The wind vector **V** does not have to be parallel to the receiver plane. The inset in the diagram shows that, with angle a drawn closer to its actual small size, the two paths are almost collinear over a large distance above and below the crossover points. Thus if the wind velocity **V** has a component along the light paths (as in the inset) rather than being parallel to the receiver plane, the change in height with time is negligible and the separation of the identical patterns will not change. In this case the pattern velocity **P** is the projection of the wind velocity on the receiver plane. The separation S of the two patterns is related to the height h of the turbulence and the elevation α of the star by

$$S = \frac{ah}{\sin\alpha} \,. \qquad --(4.1)$$

4.1.2 Atmospheric complications

The simple idea above may be complicated by atmospheric refraction, as illustrated in figure 4-2. In the context of laser beam propagation, this is referred to as beam "curvature" (Ochs and Lawrence, *circa* 1970) or beam "wander" (Fante, 1980). Its effect on a star's position is shown in figure 3-3c. The light from the two components of the double star may be refracted by turbulence above or below the intended crossover point, resulting in apparent vertical movement of this point. This would lead to an incorrect value for the height. Similarly the crossover points could move horizontally, leading to a wrong value for the deduced wind velocity. Movement of the beams out of the plane represented in the diagram would eliminate the crossover.

Further complications may arise due to the distribution of turbulence and wind velocity with height, as illustrated in figure 4-3. For a single "thin layer" of turbulence, the scintillation pattern at ground level will be as illustrated in figure 4-1. However, for a "thick layer", the turbulence is different along the two paths to the two stars, so that the two scintillation patterns are different and therefore the height cannot be deduced. If the wind velocity varies with height in the region of the crossover point, as in the "Random velocity variation" and "Wind shear" cases, then the scintillation patterns will be the same for the two stars, but these will evolve into different patterns by the time they reach the second pair of detectors. In this case the height can be measured but not the pattern velocity **P**. (*nb* The blobs in figure 4-3 do not represent individual turbulent irregularities, but rather regions of the atmosphere containing an assembly

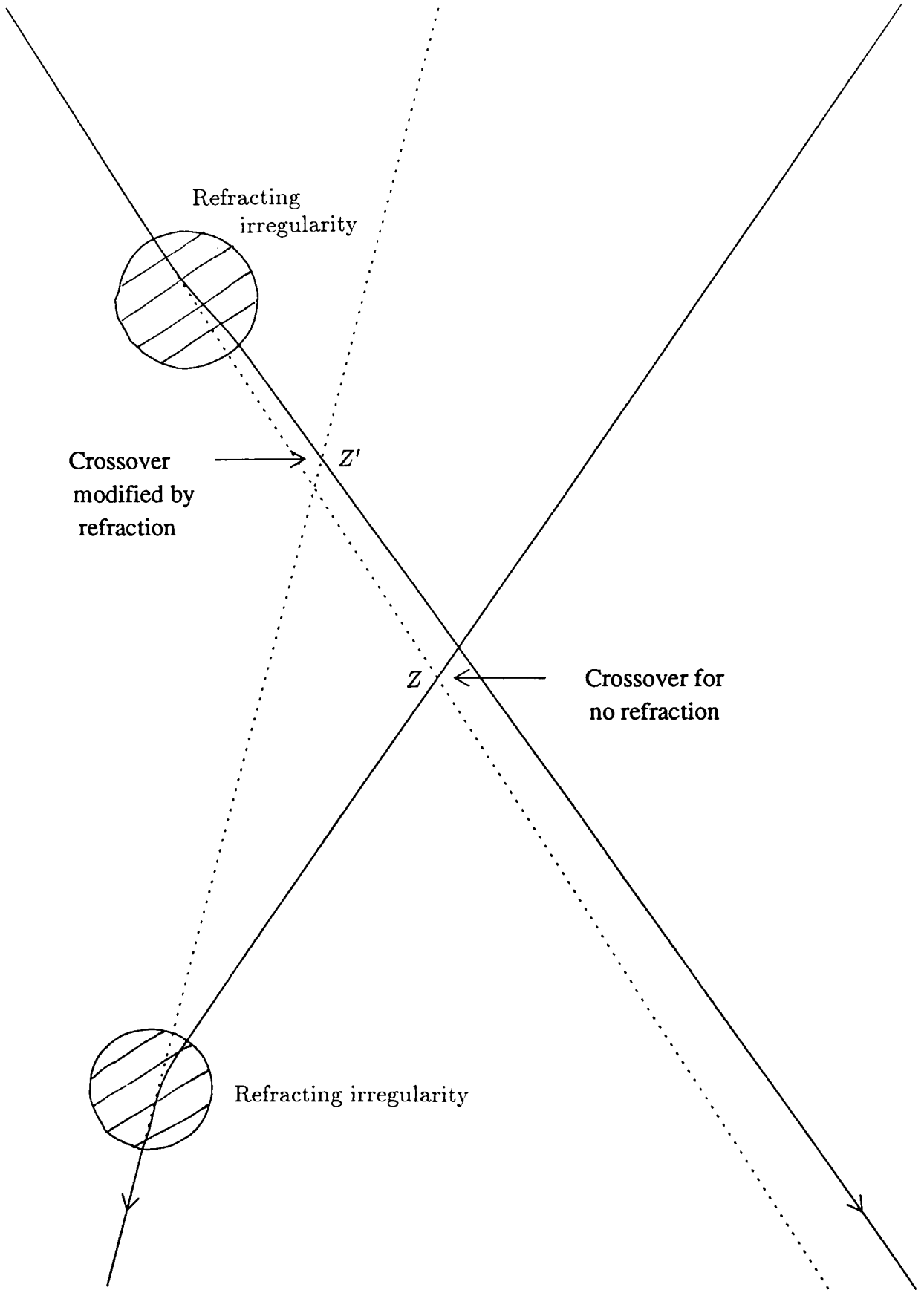

Figure 4-2 A schematic illustration of the way in which the apparent height of the crossover point Z of a multiple beam system may be changed by turbulence above or below the crossover (in this case to position Z'). The solid lines represent actual ray paths, while the dashed lines indicate the undeflected path for the upper turbulent irregularity and the apparent path for the lower one.

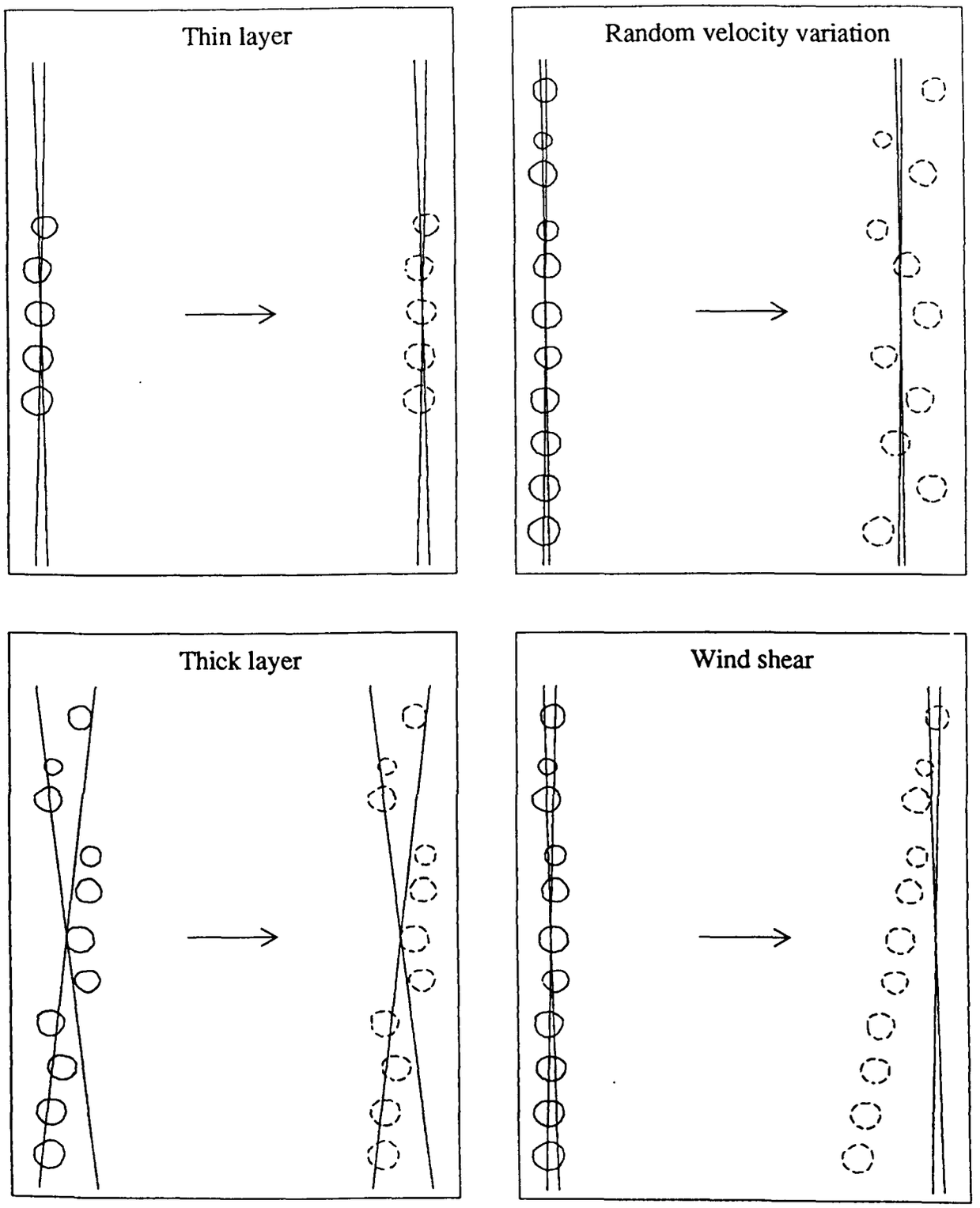

Figure 4-3 Highly schematic diagrams illustrating different distributions of atmospheric turbulence and wind velocity, relative to the four light paths of a multiple beam system. The blobs with solid boundaries represent turbulent patches at an initial time and the dashed boundaries indicate their position at a later time. For the "thin layer" case, the two detectors with crossed lines of sight will see the same scintillation simultaneously and the other two will see the same pattern at a later time. For the "thick layer" case, the signals on the crossed line of sight detectors will be unrelated but each will be repeated on a second detector at a later time. The opposite situation occurs in the "random velocity variation" and "wind shear" cases, where the crossed line of sight detectors will see similar patterns but the scintillation pattern will change substantially as it moves to the other pair of detectors.

of turbulent irregularities which does not change significantly over the time taken for the wind to transport it from one line of observation to the other.)

For the last three cases in figure 4-3, the identification of specific pairs of intensity patterns may not be possible, due to the superposition of many pairs with different separations and/or velocities. However, it may still be possible to deduce the height and wind velocity by applying correlation techniques to long data series. For example, if the scintillation pattern is the sum of contributions from several heights, the pattern would consist of overlapping pairs of identical patterns with several different separations. If the pattern is observed on two detectors with a separation appropriate to one of the heights, there will be some similarity between the time series of the intensity on the two detectors. A cross correlation of these series should give a positive value, above the noise level, if the series are sufficiently long, even if the individual fluctuations are buried among other signals.

A further complication may arise from the way in which the light fluctuations produced at different heights add together. The two extreme cases are:

1) the scintillation patterns produced at different heights are independent of each other and the intensity fluctuations add algebraically at ground level. This is commonly assumed to be the case (*eg* Rocca *et al* (1974) add together the spatial correlation functions expected for different heights in remote measurement of the turbulence profile).
2) Phase fluctuations produced at different heights add together and the scintillation pattern at ground level is the diffraction pattern that results from the total phase fluctuation. Thus features in the scintillation pattern are related to the sum of the phase variations produced at different heights. These scintillation patterns will be transitory, as relative movement of the turbulent layers at different heights will lead to rapid changes in the sum of the phase variations and the resultant diffraction pattern. Even if Taylor's "frozen in" hypothesis is valid for features within the turbulent layers, it will not be possible to track features in the scintillation pattern from one detector to another, as they will appear and disappear as different combinations of phase variations occur. Churnside *et al* (1989) refer to observations of such transitory features in the scintillation of laser beams.

In practice, one might expect the actual situation to lie somewhere between these two extremes.

Crossed-beam measurements of turbulence strength (Vernin *et al*, 1979; Azouit *et al*, 1980) have given values in reasonable agreement with *in situ* measurements. This suggests that movement of the crossover point and the interaction of phase fluctuations from well-separated heights do not occur to a significant extent. Nevertheless, it is possible that one or both of these factors explains the observation by Azouit *et al* (1980) that at some heights the optically determined turbulence values were too small. For example, if the phase fluctuations produced by turbulence near the crossover point add onto different phase fluctuations produced well away from the crossover point, where different turbulence lies on the two crossed paths, then the correlation between the scintillation patterns associated with turbulence at the crossover will be reduced, leading to underestimation of the turbulence strength.

A reduction in the correlation value is not as serious for the wind measurement system proposed above, in that it only reduces the effectiveness of the method, giving at worst no measurement rather than a false value. Movement of the crossover point would be serious in that it could give false results for both the height and wind velocity. It would be useful to be able to directly observe whether the refraction and phase interaction occur. Ways of doing so are suggested later in §4.3.

4.1.3 Multiple-beam remote sensing

Various arrangements of multiple beams are now considered, aiming towards a practical implementation of the basic idea for wind measurement outlined in §4.1.1. The aim is to measure the pattern separation and velocity, subject to the constraint that only two light detectors are available.

Figure 4-4 illustrates an arrangement of three crossed beams, suggested by Elford (1975). Three irregularities with velocities $\mathbf{V_A}$, $\mathbf{V_B}$ and $\mathbf{V_C}$ are shown passing through the three beams. The top inset illustrates the time series of intensity fluctuations that they might produce at detectors 1, 2 and 3. The lower inset depicts a correlogram of the correlation $T_{ideal}(1(t), 2(t-t_{12}), 3(t-t_{13}))$, where t_{1n} is the time delay applied to series n relative to series 1. (T_{ideal} represents an ideal triple correlation, which gives a positive value for signals common to all three series and zero for uncorrelated signals

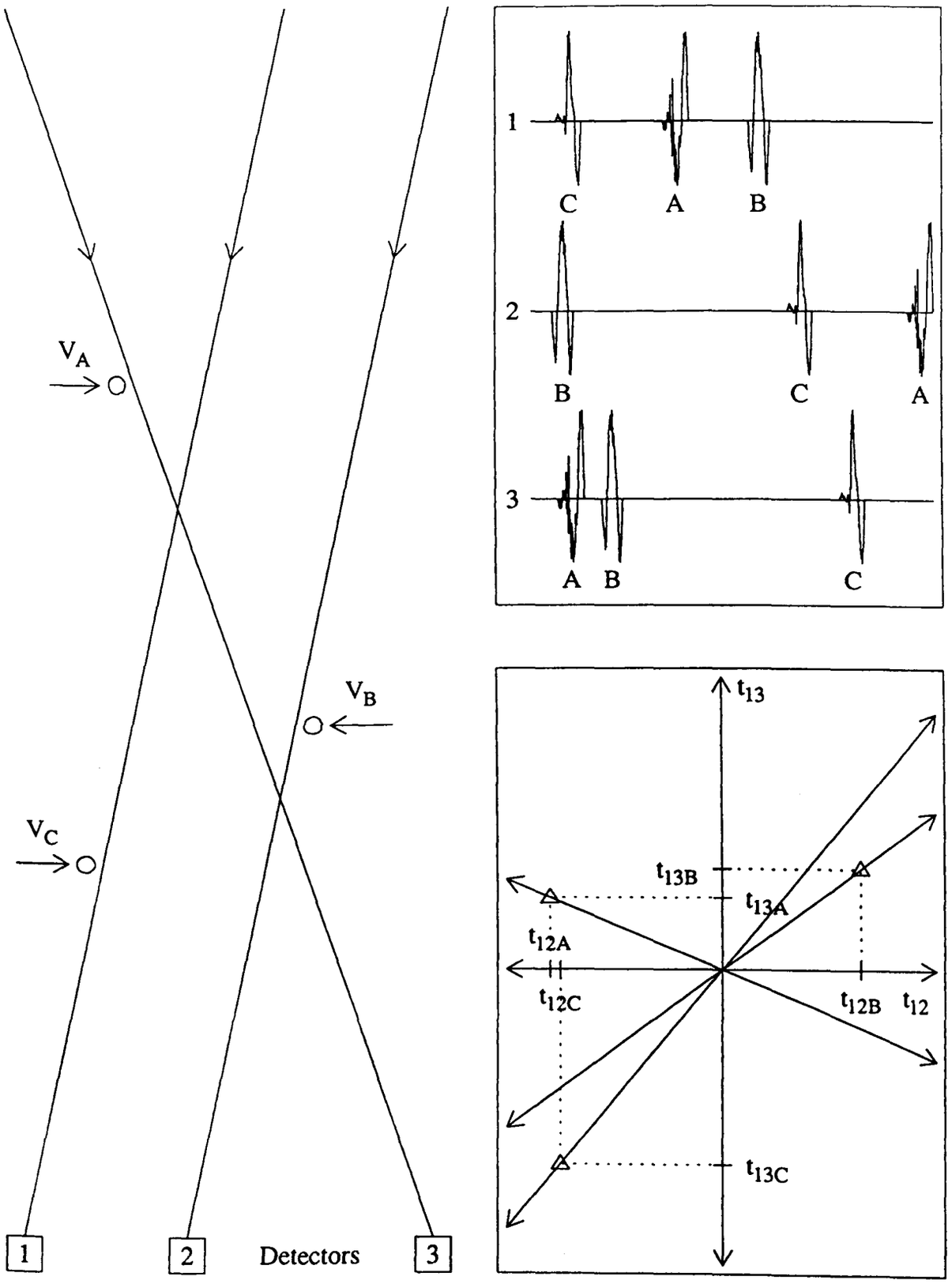

Figure 4-4 An illustration of the principle of the crossed three-beam system suggested by Elford (1975). The geometry of the system is shown on the left, with three irregularities moving with the velocity indicated by the arrows. The resulting time series on the three detectors are represented on the top right. A triple correlogram of these series is represented on the lower right. This is a plot of the triple correlation as a function of the time shifts t_{12} and t_{13}, where t_{nm} is the shift applied to series m relative to n. The triangles indicate the peaks in correlation for the three irregularities, with lines through these triangles indicating their locus for a range of transverse speeds at the same height.

or those common to only two of the series.) Each position along the beams maps to a direction in the $t_{12}t_{13}$ plane, with each possible transverse velocity mapping to a different point along this direction. These directions are indicated by lines for the three sample irregularities, with triangles indicating the positions of maximum triple correlation. The value of t_{12} at these maxima is related to the velocity $\mathbf{V}$ by

$$\mathbf{V} = -\frac{\mathbf{D_{12}}}{t_{12}} \qquad --(4.2)$$

where $\mathbf{D_{12}}$ is the displacement of detector 2 from detector 1. Thus it appears possible to measure a velocity profile by inversion of the triple correlogram of the fluctuations observed on three crossed beams.

This multiple-beam system is in principle the same as that used by Sasaki and Sato (1979), described in §3.8, except that here the non-parallel beam crosses the other two. This gives higher resolution on a portion of the path near the crossover points, as a small change in position near these points leads to a large relative change in the time delays t_{13} or t_{23}.

In this idealized example, the signals due to the three sample irregularities can be recognized, as they are drawn with different fine structure. If they had the same shape, it would not be possible to determine the velocity profile unambiguously (*eg* combining the events marked C in series 1 and 2 with that marked A in series 3 would give a false indication of an irregularity moving from left to right through the upper crossover point). Sasaki and Sato (1979) avoided this problem by setting the density of the seed particles in the fluid sufficiently low that there was no ambiguity. This option is not available when turbulence is being used as a tracer of the flow, as many irregularities will be in each beam at one time. Thus to apply multiple-beam methods for remote sensing with turbulence, methods of multiple correlation are required which can detect a signal common to all of several series, even if it is hidden among other signals which are either uncorrelated or correlated between a lesser number of the series.

Figure 4-5 repeats the presentation of figure 4-4 for a modification of this multiple-beam system which can be used when the light source is an unresolved double star. Detectors 1 and 2 both receive light from both components of the star, so that each fluctuation occurs twice in the time series of the intensity. To deduce the velocity profile

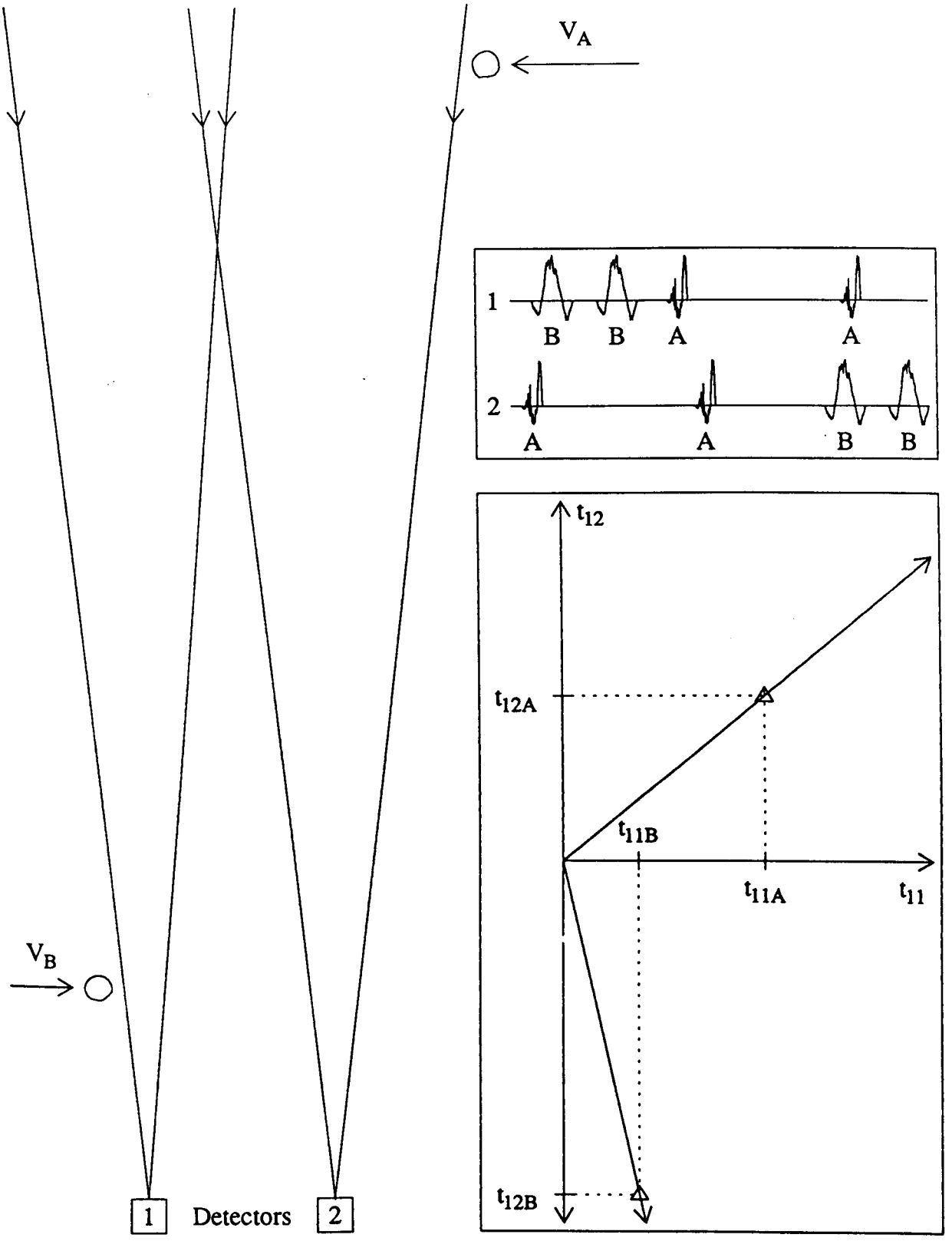

Figure 4-5 An illustration of the double source, double detector system, where the signals from the two sources are not distinguished. The geometry of the system is shown on the left, with two irregularities moving with the velocity indicated by the arrows. The resulting time series on the two detectors are represented on the top right. A quadruple correlogram of these series is represented on the lower right. This is a plot of the quadruple correlation of the series $1(t)$, $1(t-t_{11})$, $2(t-t_{12})$ and $2(t-t_{11}-t_{12})$. The triangles indicate the peaks in correlation for the two irregularities. The arrows indicate the locus of the triangles for a range of transverse speeds at the same height.

from the time series, a quadruple correlation of the form

$$Q_{ideal}(t_{11}, t_{12}) = \text{function of } (1(t), 1(t - t_{11}), 2(t - t_{12}), 2(t - t_{11} - t_{12}))$$

is required. This can be presented in two dimensions as the time shift applied in the last term is determined by time shifts applied in the other terms. A consequence of this relationship is that the combination of two uncorrelated signals, each occurring in two of the series, will occur at any value of t_{12} when t_{11} matches the repetition interval. Thus a particular requirement of Q_{ideal} is that it should be zero for the situation of two correlated pairs of signals.

4.1.4 Implementation for double-star scintillation

Possible ways in which multiple-beam remote sensing might be applied to wind measurement using double-star scintillation are illustrated in figure 4-6. On the left, an "Ideal imaging system" is shown which implements the crossed three-beam arrangement of figure 4-4. The limitations of diffraction and other problems discussed below render this system difficult, maybe impossible, to use in practice, so in this work the two methods illustrated on the right of figure 4-6 are used. These implement the arrangement of figure 4-5, where each detector receives light from both components of the double star. This leads to considerable problems in analysis, but the construction and operation of the equipment is much simpler.

To justify rejection of the "Ideal imaging system", it is necessary to consider it in detail. As illustrated in figure 4-6, a lens produces an image of the double star in the image plane, where a mask isolates the required stars. Three small detectors behind the image plane sample parts of the cones of light expanding from the point images, effectively creating two apertures in the aperture plane (indicated in the figure by larger gaps in a dashed line). Six rays (drawn in red for one star and green for the other) indicate the edges of the detected beams. Above the objective there are two parallel beams (red) and another at an angle (green), creating the three-beam system of figure 4-4 in the atmosphere.

Limitations imposed by diffraction would prevent this system working for most double stars, which have separations less than a few seconds of arc and thus require apertures at least 10 cm in diameter to separate the two images. If the detectors are

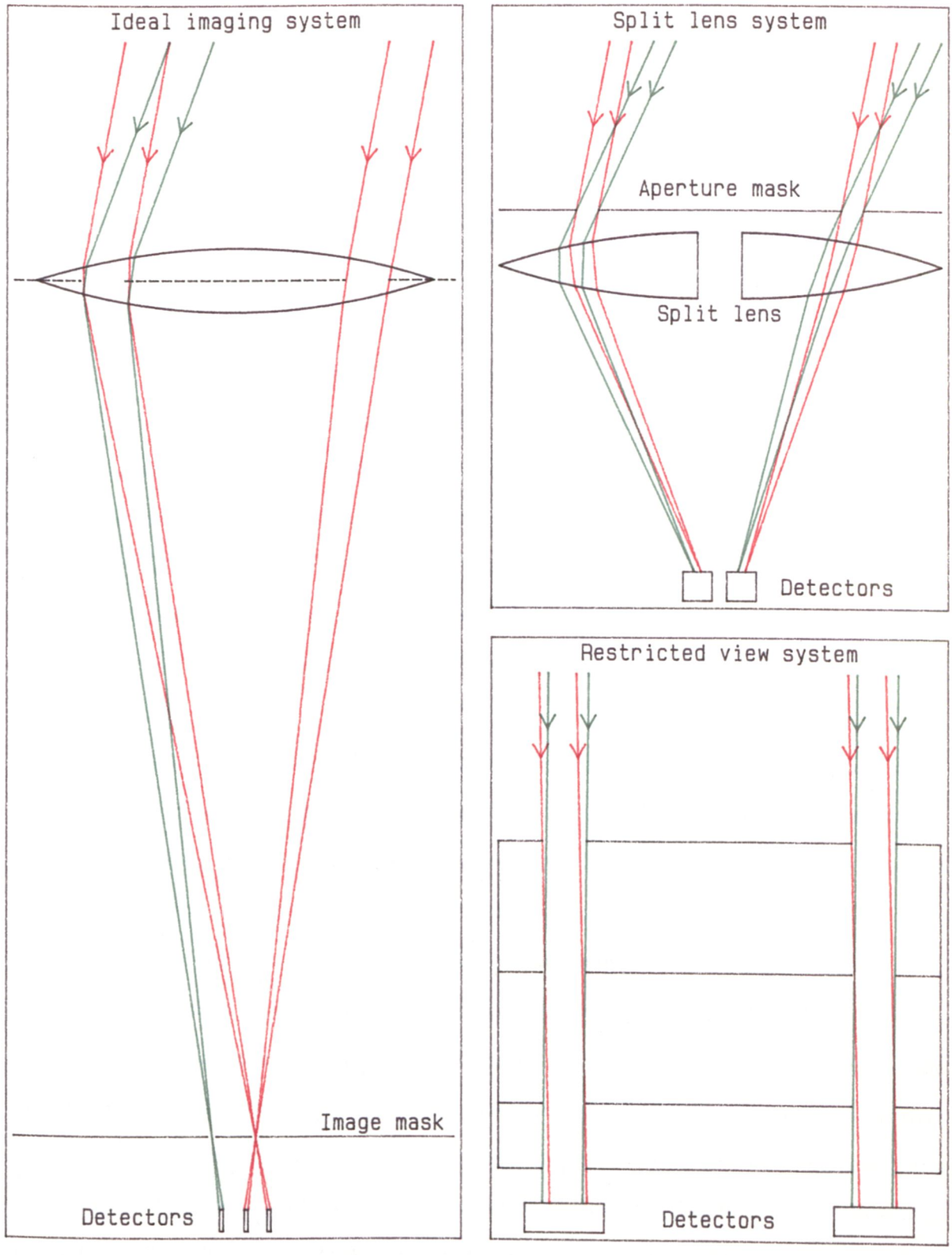

Figure 4-6 Illustrations of three devices which could be used to apply multiple beam methods to make wind measurements using the scintillation of a double star. In the ideal imaging system a large lens is used to produce a resolved image of the double star. Detectors behind the image plane then sample parts of the expanding light cones, effectively producing 2 small apertures within the objective lens (indicated by dashed lines). Simpler instruments are illustrated on the right. These do not allow the light to be separated into contributions from each star.

sufficiently close to the image plane to be able to receive the light from only one of the stars, then the Airy image of the star will act like a large aperture, rather than a point source. Each detector would thus have a line of sight to any part of the lens and the virtual apertures of figure 4-6 will be very large. Thus it does not seem possible to have an imaging system which has the small apertures required for good resolution in velocity measurement as well as the large lens required to resolve the components of a double star.

A modification of this system which should make it work would be to put optical switches over the two image-plane apertures. These could be switched so that the light of one star and then the other is transmitted alternately. Two detectors placed well behind the image plane would then effectively create the two small apertures required, with electronic switching (in phase with the optical switching) being used to separate the signals from the two stars after the light is detected.

In addition to its complexity, this "Ideal imaging system" has a number of other disadvantages:

1) phase variations due to turbulence near to the instrument would occasionally move the image sideways onto the image mask, cutting off the light at the detectors.
2) As bad seeing is often associated with strong scintillation, it may not be possible to resolve the double star on occasions when the scintillation is strong.
3) It requires imaging and tracking of the quality required for astrophotography.

The alternatives used in this work are illustrated on the right of figure 4-6. The upper diagram illustrates a "split-lens" telescope, in which a lens is split in two and the halves are moved apart. This allows two apertures which are close together to collect light from the same star, with the minimum separation between the two apertures being equal to the detector diameter. The other method (lower right) is to use collimation, so that the field of view is restricted to include only one bright star by a series of plates containing aligned apertures. The number and spacing of plates must be chosen so that there is no chance alignment of the apertures in other than the one direction desired. These non-imaging methods avoid the three disadvantages listed above for imaging systems, but as they do not resolve the double star into its components, the analysis of the signals is complicated by each fluctuation occurring twice.

An obvious alternative to the "split-lens" telescope telescope would be to have two small lenses with diameters less than the detector separation. However, the use of small circular apertures is only possible when the wind is aligned with the components of the double star, so that the signal is detected for all four beams. In the usual situation where the wind is at an angle to the double-star orientation, scintillation patterns crossing one detector would miss the other. In this case, the "split-lens" telescope can still be used, as its apertures can be slits with a length much greater than their separation.

This technique is illustrated in figure 4-7, where double slit apertures are superimposed on the double star scintillation pattern of figure 4-1. **D** is the position of slit 2 relative to slit 1, S_{11} is the projection of the separation S of the two components of the double star pattern along the direction of the pattern velocity **P**, D_{12} is the slit separation along the direction of **P**, t_{11} is the time interval between the two components of the pattern crossing the same slit and t_{21} is the time for a pattern to go from slit 1 to slit 2. Then S_P, the component of the pattern separation perpendicular to the slits, can be found using

$$\frac{S_P}{|\mathbf{D}|} = \frac{S_{11}}{D_{12}} = \frac{t_{11}}{|t_{21}|}. \qquad --(4.3)$$

$\mathbf{P_P}$, the component of the pattern velocity perpendicular to the slits, is given by

$$\mathbf{P_P} = \frac{\mathbf{D}}{t_{21}}\ . \qquad --(4.4)$$

As the orientation of the star relative to the slits is known, the pattern separation S can be deduced from S_P and substituted in equation 4.1 to give the height of the turbulence h. To deduce wind velocity **V** (assuming it is horizontal), the perpendicular pattern velocity $\mathbf{P_p}$ would need to be measured for two orientations of the slits, allowing measurement of **P** and hence **V**.

4.2 Multiple-correlation algorithms

To deduce the wind velocity profile from the time series of intensity produced by the three- and four-beam systems illustrated in figures 4-4 and 4-5, multiple-correlation functions are required which give a positive value if there is a signal common to all three or four series and zero otherwise. As the individual fluctuations in scintillation will

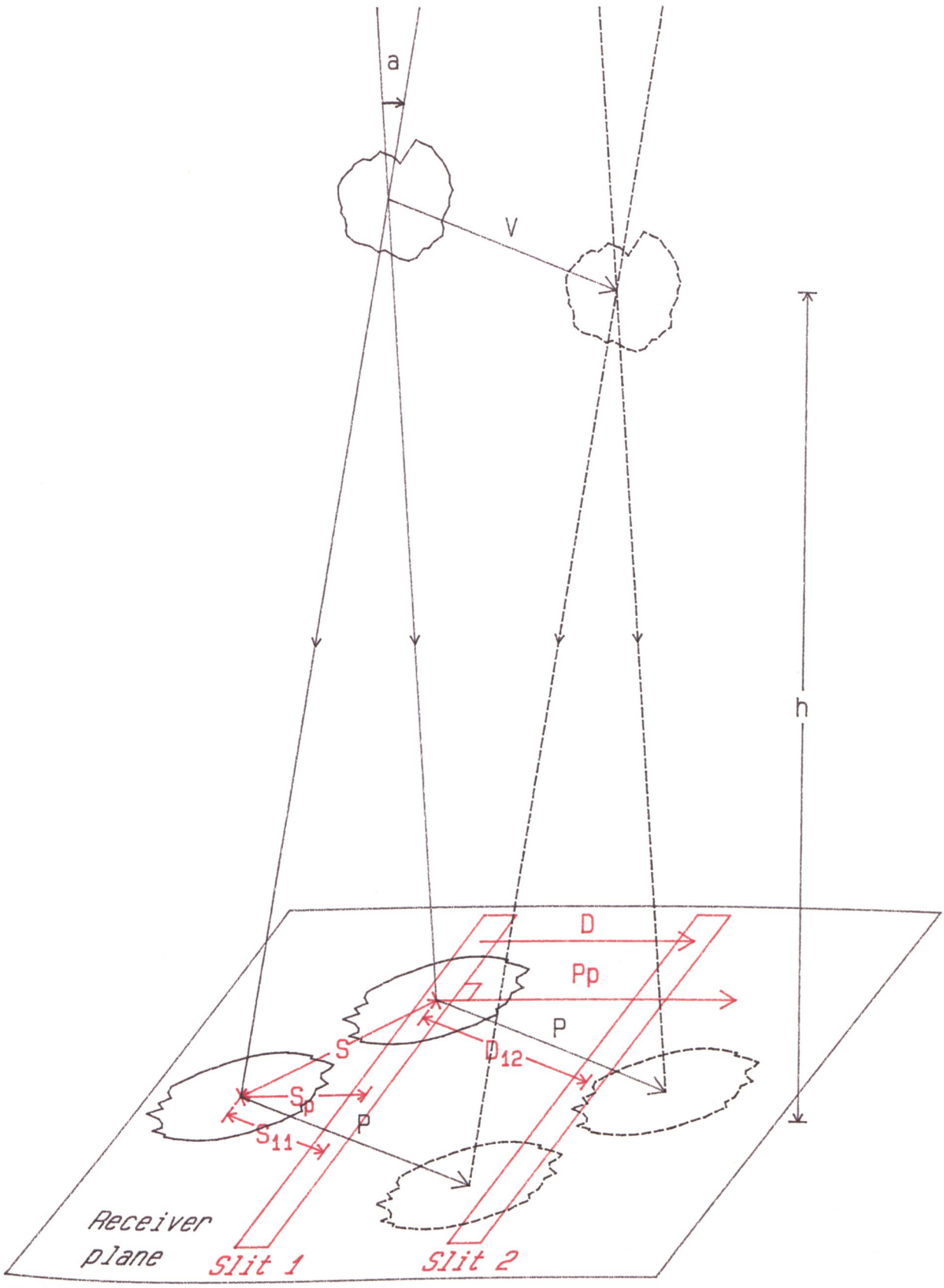

Figure 4-7 A modification of figure 4-1, showing that two slit detectors can be used to measure components of the velocity and separation of the scintillation pattern of a double star. If t_{11} is the time interval between the two patterns crossing slit 1 and t_{21} is the time for a pattern to go from slit 1 to slit 2, then the perpendicular component S_p of the separation can be found from $S_p/D=S_{11}/D_{12}=t_{11}/t_{21}$. Pp, the perpendicular component of the pattern velocity, is given by $Pp=D/t_{21}$.

generally overlap and so cannot be clearly identified, the multiple-correlation functions must have the property that the contributions from the correlated signals will accumulate over time while the contributions from all other signals cancel. In the case of the unresolved double star, the quadruple-correlation function must cope with signals where every fluctuation is repeated at a variety of different intervals (depending on the height of the turbulence and the wind velocity).

The effort to develop such functions as part of this work was not successful, hence the use of the symbols T_{ideal} and Q_{ideal} earlier. The new functions presented below are better (for scintillation analysis) than the standard functions T and Q used by Sasaki and Sato (1979) for seeded fluids, but have various deficiencies. More than one approach is presented because

a) one function may be better than another for a particular type of data, and

b) possibly one of these approaches may be used as a basis for future development of better solutions.

4.2.1 The need for new multiple-correlation methods

Standard books on statistics (*eg* Spiegel, 1972) define multiple-correlation functions such as

$$R_{1.23} = \sqrt{\frac{r_{12}^2 + r_{13}^2 - 2r_{12}r_{13}r_{23}}{1 - r_{23}^2}} \qquad --(4.5)$$

where r_{nm} is the "product-moment" or "coefficient of correlation" between series n and m. $R_{1.23}$ gives an indication of the correlation between series 1 and the best-fitting linear combination of series 2 and 3. It does not indicate the presence or absence of signals common to the three series, as is clear from the fact that when series 2 and 3 are uncorrelated, $r_{23} = 0$ and so $R_{1.23} = \sqrt{r_{12}^2 + r_{13}^2}$. T_{ideal} as defined above should give zero in this situation.

In searching for a common signal, there is a more fundamental deficiency of any multiple-correlation function which is a combination of cross-correlation coefficients. The problem is illustrated in figure 4-8a. If at different times a correlated signal is present in two of the series but not the third, then the cross correlation for each pair of series will be positive. Hence the multiple-correlation coefficient will also be positive, even though no signal is present on all three series simultaneously. Thus, to identify the presence of a signal common to three time series, it is necessary to compare each

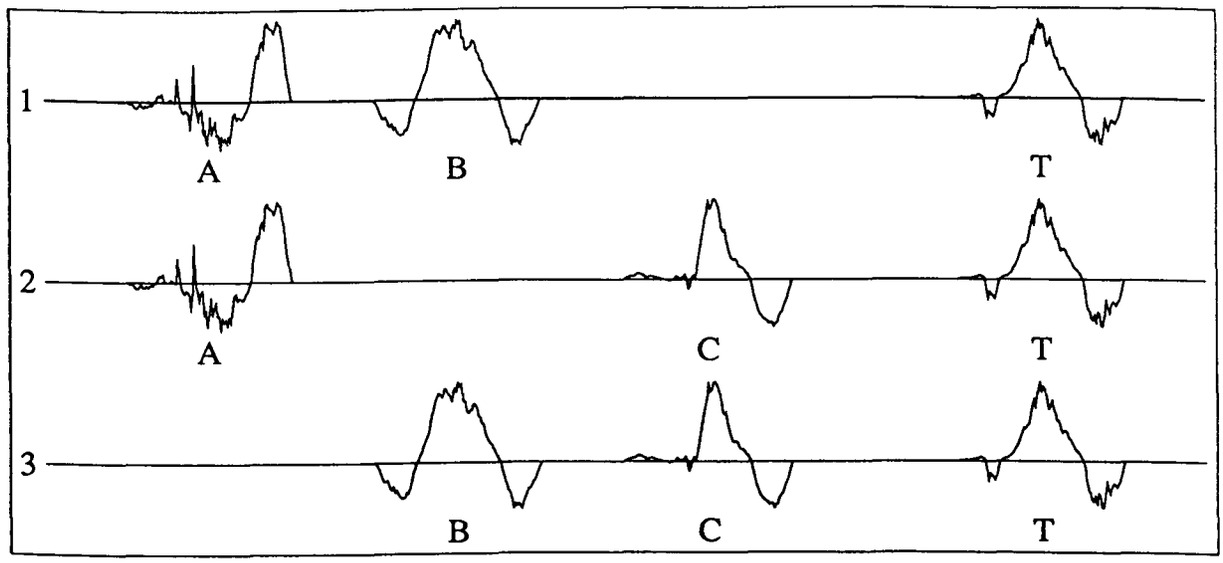

Figure 4-8a These idealized data series demonstrate the need for a triple correlation function which compares the three series at each point, rather than one which simply combines the cross correlation values for each pair of series. The signals marked A, B and C would make a contribution to the cross correlation between each pair of series and thus to any triple correlation function which is a combination of cross correlation coefficients. A triple correlation function should give a positive value only for the signal marked T.

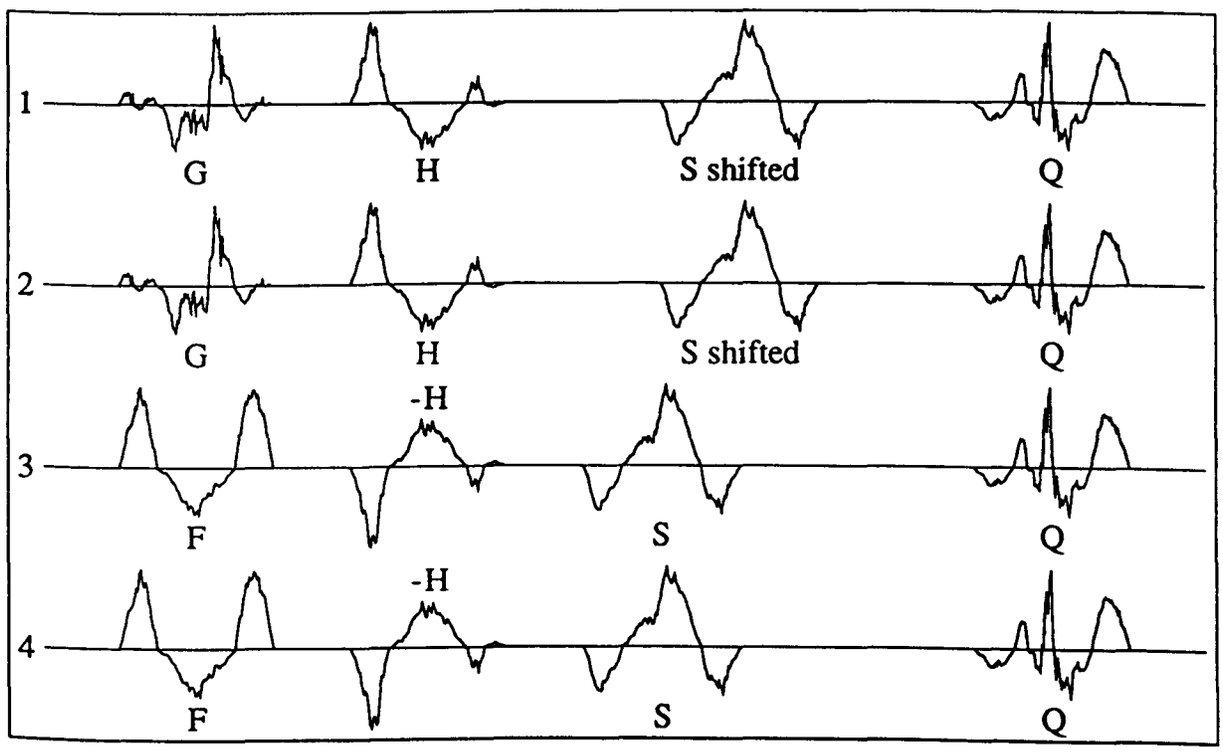

Figure 4-8b An illustration of the inadequacies of the standard quadruple correlation function $< f_1(t).f_2(t).f_3(t).f_4(t) >$. This function will be positive for two unrelated pairs of correlated signals (e.g. F and G) and for pairs of anticorrelated functions (e.g. H and $-H$). The latter can occur in practice when signals are shifted through half their period (illustrated by signal S). A quadruple correlation function is required which is positive for signal Q and zero for the other signals.

of the three series at each point. The triple correlation function

$$T(f_1, f_2, f_3) = \langle f_1 f_2 f_3 \rangle \qquad -- (4.6)$$

used by Sasaki and Sato (1979) meets this requirement, where f_1, f_2 and f_3 are three time series.

Strictly, T should be referred to as a "triple covariance", as a correlation coefficient should be normalized to vary between +1 and −1. However, it is referred to as "triple correlation" in the literature (*eg* Lohmann and Wirnitzer, 1984). Throughout this thesis the distinction between correlation and covariance will be maintained for two series, but for three or more series, "correlation" will be used in the wider sense as a measure of the similarity of the series.

T is non-zero only for signals which are asymmetrically distributed about the mean value (Lohmann and Wirnitzer, 1984); *eg* $T(\sin(t), \sin(t), \sin(t)) = \langle \sin^3(t) \rangle = 0$, even though the three series are correlated. This was not a problem in the method used by Sasaki and Sato, as seed particles produce a reduction in the light reaching the receiver, thus giving an asymmetrical distribution of intensity about its mean value. In the case of scintillation, there is no such reduction, but just a redistribution, so that enhancements in intensity must be surrounded by compensating reductions. However, the scintillation signals will still be asymmetrical, because

1) the energy is redistributed in two dimensions and so intensity fluctuations measured along a line through the pattern will not have equal positive and negative deviations, and
2) scintillation patterns can have bright regions and so cannot be symmetrical; *eg* the intensity can exceed twice the mean level, but cannot go below zero.

Thus the triple correlation T should be applicable to scintillation, but its effectiveness will be reduced by partial cancellation of the positive and negative fluctuations from the mean level.

A fundamental problem arises if the quadruple correlation

$$Q(f_1, f_2, f_3, f_4) = \langle f_1 f_2 f_3 f_4 \rangle \ , \qquad -- (4.7)$$

as used by Sasaki and Sato (1979), is applied to overlapping scintillation patterns rather than the shadows of isolated seed particles. As shown in figure 4-8b, Q will give

a false positive value where there are two pairs of correlated signals which are either uncorrelated (F and G) or anticorrelated (H and $-H$) with each other. These cases will occur when a signal which is common to all four series (*eg* S in figure 4-8b) is shifted in two series, giving the situation of signals F and G if the shift is large, or of H and $-H$ if the shift corresponds to half of the period of the fluctuation. This situation will occur frequently in the analysis of signals from an unresolved double star, due to the relationship between the time delays explained earlier in §4.1.3.

As the intensity distribution of scintillation is not symmetrical about the mean level, a triple-correlation function which can be applied to symmetrical signals is not essential. However, an attempt is made here to devise such a function because

a) a function which does not cancel out the symmetric parts of the signal may be more effective, and
b) the development of the function might provide insight into an improved quadruple-correlation function.

Three new types of multiple correlation are presented below. First, combinations of standard functions are considered, followed by two new approaches. The first, called "multiple correlation by selection", is based on the idea that if a subset of large values is selected from one series, the covariance for the corresponding elements of the other two series will be large if there is a signal common to all three. The second, called "correlation by minimum difference", is based on the principle that adding the same extra signal to all of the series does not alter the difference between any two of the signals, so that this difference approaches a minimum if there is a multiple-correlated component.

4.2.2 Combination of standard functions

A signal common to three series contributes a component of cross correlation to all three pairs of series. Thus a simple triple-correlation function is the cross-correlation function with the smallest absolute value:

$$T_C = C_{min} \text{ where } |C_{min}| = \min\{|C(f_1, f_2)|, |C(f_1, f_3)|, |C(f_2, f_3)|\} \qquad --(4.8)$$

and $C(f_n, f_m)$ is the cross correlation between series f_n and f_m. This will give a false result in the case illustrated earlier in figure 4-8a, where each pair of series contains a

correlated signal which is not present in the third.

An analogous quadruple correlation is the minimum of the six possible cross correlations:

$Q_C = C_{min}$ where $|C_{min}| = \min\{$

$$|C(f_1,f_2)|, |C(f_1,f_3)|, |C(f_1,f_4)|, |C(f_2,f_3)|, |C(f_2,f_4)|, |C(f_3,f_4)|\} \; . \qquad --(4.9)$$

For asymmetrical signals a better quadruple correlation is the smallest of the four possible triple correlations:

$Q_T = T_{min}$ where $|T_{min}| =$

$$\min\{|T(f_1,f_2,f_3)|, |T(f_1,f_2,f_4)|, |T(f_1,f_3,f_4)|, |T(f_2,f_3,f_4)|\} \qquad --(4.10)$$

as this would be zero even if there is some cross correlation for all six pairs of series. Q_T will give a false result if all four combinations of three series contain common signals which are not present in the fourth.

4.2.3 Multiple correlation by selection

The cross-correlation function gives a value of zero for uncorrelated signals because, when one value is positive, the value from the other series is equally likely to be positive or negative. To apply the same principle to a triple correlation requires another parameter which also, like the sign, produces positive and negative contributions. The formulae developed in this section achieve this by using the amplitude of one series as this extra parameter.

Consider the correlation coefficient T_3 defined by

$$T_3(f_1,f_2,f_3) = \langle f_1 f_{2|f_3|>\langle|f_3|\rangle}\rangle - \langle f_1 f_{2|f_3|<\langle|f_3|\rangle}\rangle. \qquad --(4.11)$$

This divides the contributions to the cross covariance between two of the series into two sets, depending on whether the corresponding element of the third series is large or small. If there is a component that is common to all three series, then larger values of f_3 will be associated with larger contributions to the covariance $\langle f_1 f_2\rangle$. Thus the first term on the right hand side of 4.11 will be larger than the second and T_3 will be positive. This process is illustrated on the left of figure 4-9a. The centre and right hand

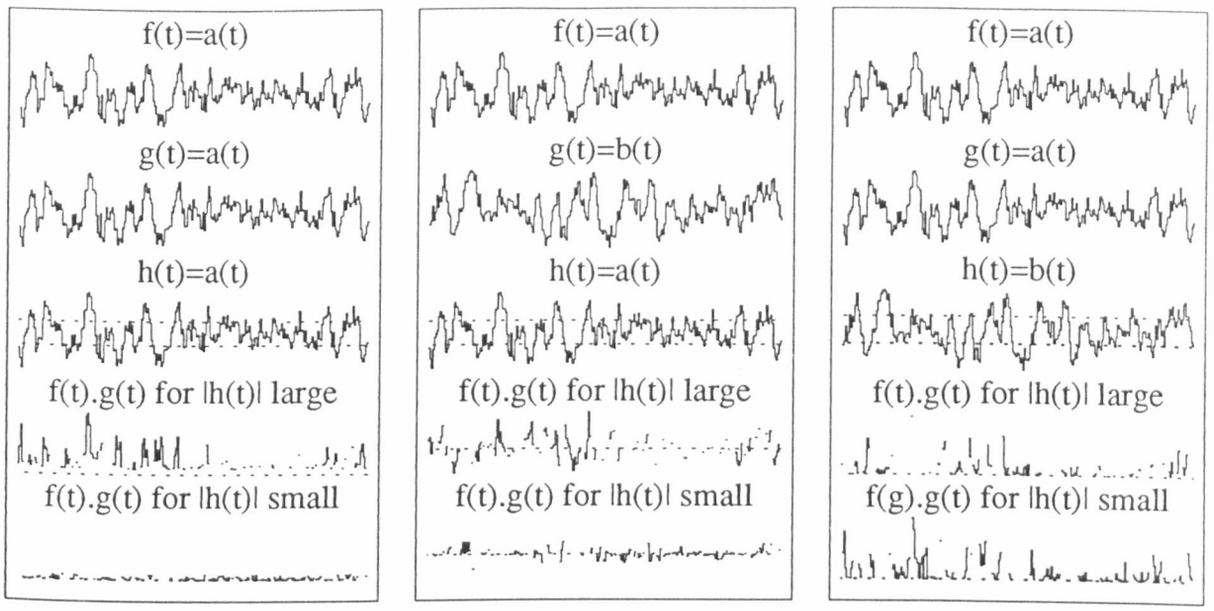

Figure 4-9a Illustration of the principle of "triple correlation by selection", applied to three correlated signals (left) and to cases where two out of three signals are correlated (centre and right). Series h is divided into large and small absolute values, at the levels indicated by the dashed lines. The corresponding values of $f(t).g(t)$ are shown for large and small values of $|h(t)|$ (with a dashed line indicating zero). These two sets of data correspond to the first and second terms in the selection function

$$T_h(f,g,h) = < f(t).g(t)_{|h(t)|large} > - < f(t).g(t)_{|h(t)|small} > .$$

T_h is positive for the triple correlated data and zero for the other two cases.

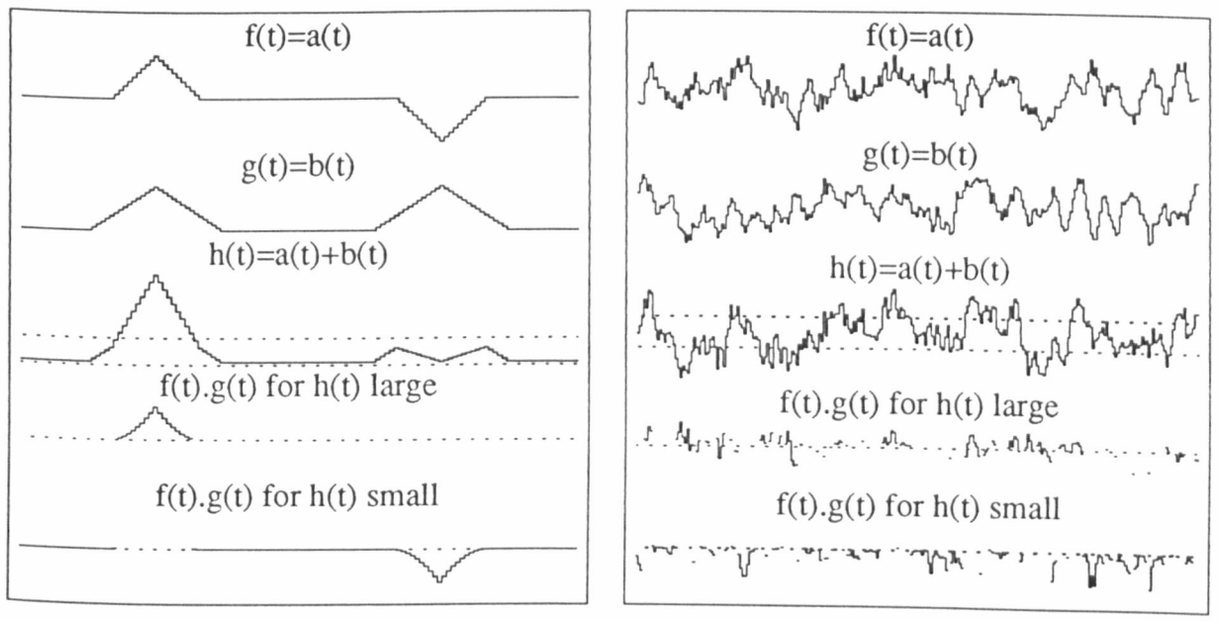

Figure 4-9b The analysis in the top figure is repeated for the situation where there are two correlated pairs of signals and each has a component in the channel being used for selection. In this case "triple correlation by selection" gives a false positive value. The reason for this is illustrated in the schematic diagram on the left. When $f(t)$ and $g(t)$ happen to be the same sign, $|h(t)|$ tends to be large and $f(t).g(t)$ will be positive. Similarly, negative values of $f(t).g(t)$ will be associated with small values of $|h(t)|$. Thus T_h will be positive, even though there is no signal that is common to all three channels. The analysis is applied to realistic time series on the right.

parts of figure 4-9a show that T_3 will be zero if only two of the series are correlated. The standard triple correlation T would give zero for all the series in figure 4-9.

There is a problem with T_3 when f_3 contains two sets of unrelated signals, each of which is correlated with one of the other two series. This problem, illustrated in figure 4-9b, occurs due to the fact that when the uncorrelated signals in f_3 happen to have the same sign (producing a positive value for $f_1 f_2$), the value of f_3 is larger on average than when they have the opposite sign and partly cancel. This gives a false positive contribution to T_3.

The ability of function T_3 to indicate the presence of a signal which is common to three series is tested in figure 4-10. The correlated signal A is obscured by noise with the same amplitude (N_1, N_2 and N_3 in the three series). The correlation T_3 is plotted as a function of the two time shifts t_{12} and t_{13}. The size of the rectangle drawn for each combination of time shifts is proportional to the correlation coefficient at that point. There is a clearly defined peak in this function at the correct position. Also plotted are the standard triple correlation T, the multiple correlation $R_{1.23}$ (equation 4.5) and the minimum cross correlation T_C (equation 4.8). As expected, T gives a random assortment of positive and negative peaks (*nb* the plots are individually normalized, so that zero correlation still produces a peak somewhere). As predicted earlier (§4.2.1), the multiple-correlation function $R_{1.23}$ gives a false positive value when only two series are correlated. T_C gives a peak in the correct place.

In figure 4-11 triple correlation by selection is applied to series which include a triple-correlated signal A and a cross-correlated component B. When the "selection" of large values is applied to the series where B is present, the resulting correlation functions (T_1 and T_2) have a false peak. This occurs at combinations of time shifts where B is lined up between f_1 and f_2 and A is still lined up between one of these series and f_3, producing the situation illustrated in figure 4-9b. This does not occur for T_3, so it is possible to define a function

$$T_M = T_i \text{ where } |T_i| \text{ is the smallest element of } \{|T_1|, |T_2|, |T_3|\} \qquad --(4.12)$$

in which the false peak is eliminated. This solution is not applicable if all three pairs of series contain a correlated component, as all three values of T_i would have a false

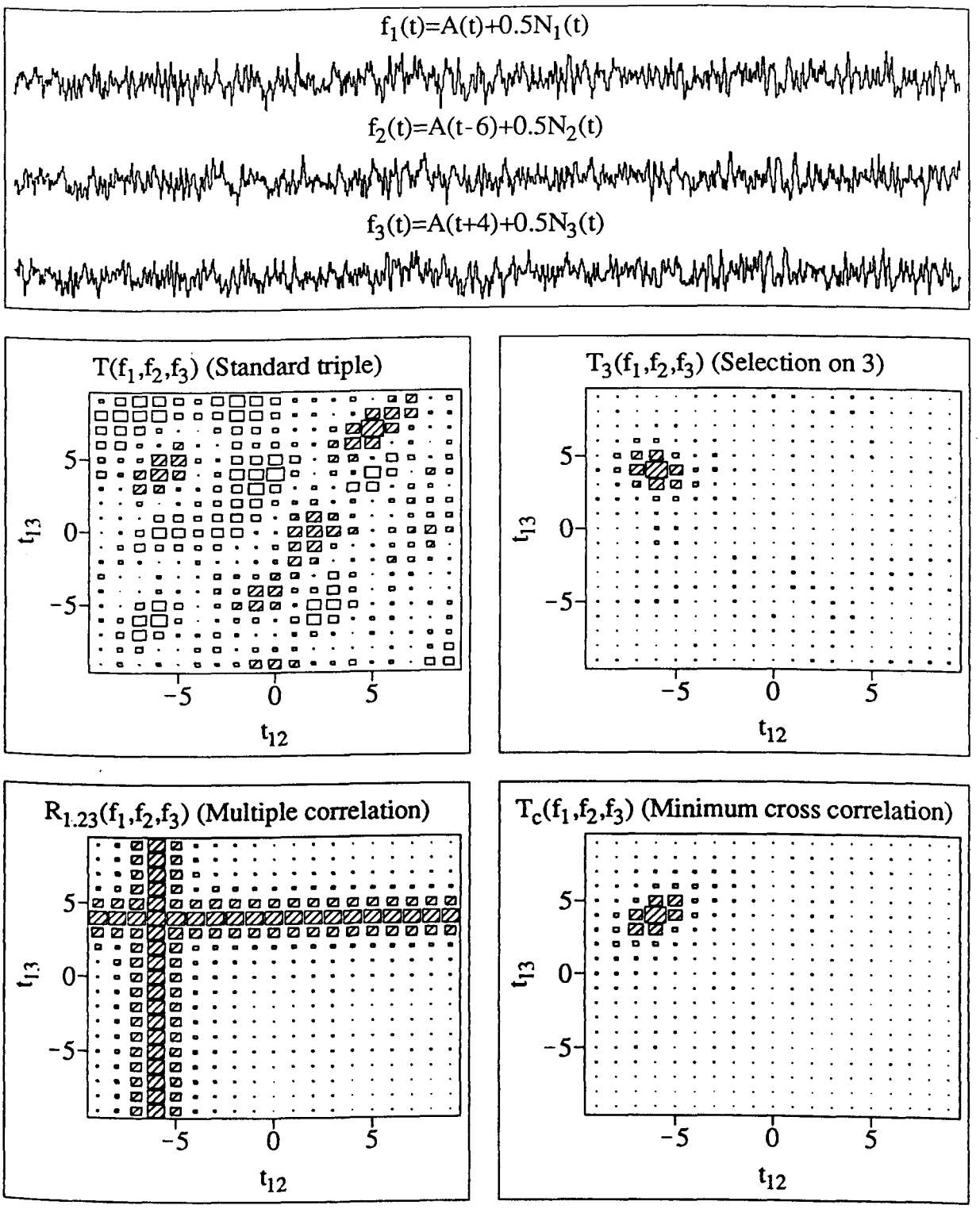

Figure 4-10 A comparison of various triple correlation functions applied to simulated data. Three time series containing a common component A (which is time shifted between the series) are plotted at the top. The signals A, N_1, N_2 and N_3 are unrelated to each other and have amplitude distributions which are symmetrical about zero. The triple correlation coefficient is represented by rectangles and plotted as a function of the time shifts t_{12} and t_{13}. The size of each rectangle is proportional to the modulus of the correlation coefficient, with the scaling normalized within each correlogram so that there is no overlap. Cross hatching indicates positive values. The desired result is a single peak at $(t_{12}, t_{13}) = (-6, 4)$. The standard triple correlation function

$$T(f_1, f_2, f_3) = \langle f_1(t) f_2(t - t_{12}) f_3(t - t_{13}) \rangle$$

fails. The multiple correlation function $R_{1.23}$ gives a positive value when only two of the series are correlated. A satisfactory result is given by the selection function T_3 and the minimum cross correlation T_C.

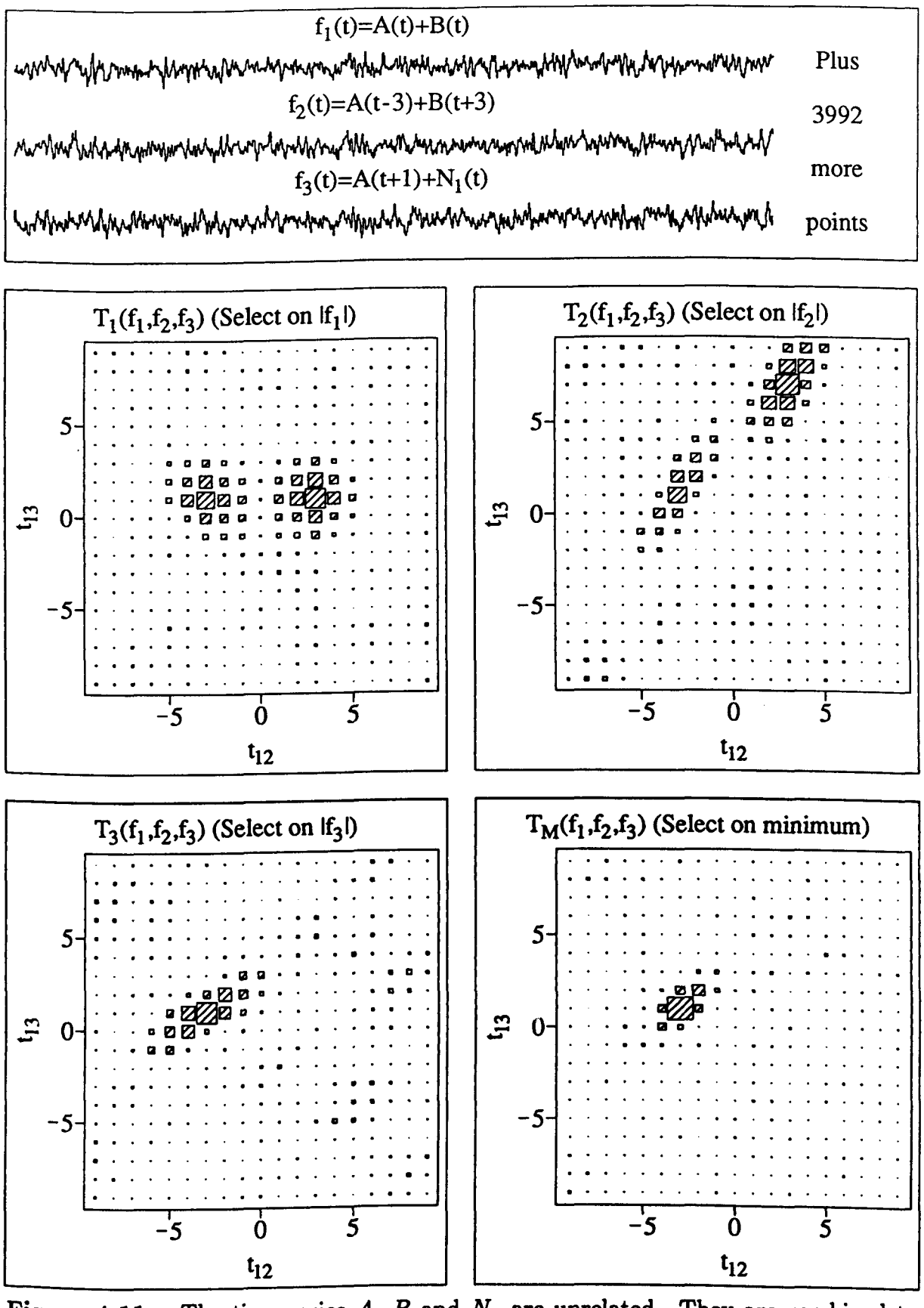

Figure 4-11 The time series A, B and N_1 are unrelated. They are combined to form the series f_1, f_2 and f_3, with A contributing to all three and B contributing only to f_1 and f_2. The triple correlogram for "selection on modulus" is shown for selection on each of the three series f_1, f_2 and f_3, where T_n designates selection on series f_n. Also shown is the correlogram for T_M, which is the element of $\{T_1, T_2, T_3\}$ that has the smallest absolute value. False peaks at $(t_{12}, t_{13}) = (3, 1)$ in T_1 and $(3, 7)$ in T_2 are produced by the presence of B in the series used for selection. No false peak occurs for selection on series f_3 and thus only the desired peak at $(-3, 1)$ occurs for T_M.

positive value.

Correlation by selection can be extended to four series in two ways. An analogous function is

$$Q_4(f_1, f_2, f_3, f_4) = T_M(f_1, f_2, f_3)_{|f_4|>\langle|f_4|\rangle} - T_M(f_1, f_2, f_3)_{|f_4|<\langle|f_4|\rangle} \qquad --(4.13)$$

ie f_4 is divided into two sets of large and small values and for each of these sets the triple correlation is calculated using equation 4.12. This triple correlation will be larger if the numbers which contribute to it are correlated with the large values of series f_4, thus giving a positive value for Q_4. The problem illustrated in figure 4-9b will also be relevant to this function and should be mitigated to some extent using

$$Q_M = Q_i \text{ where } |Q_i| \text{ is the smallest element of } \{|Q_1|, |Q_2|, |Q_3|, |Q_4|\}. \qquad --(4.14)$$

An alternative method is to divide the series into two sets with the selection based on correlation between the signs of three of the series. Where there is a component that is common to all four series, it will tend to push all values towards the same sign. This effect will be more pronounced for large values, so that where the sign on three series is the same, the value in the fourth series is likely to be larger. This principle is implemented by

$$Q_{S1}(f_1, f_2, f_3, f_4) = \langle |f_1|_{\text{same sign for } \{f_2, f_3, f_4\}} \rangle -$$

$$\langle |f_1|_{\text{different signs among } \{f_2, f_3, f_4\}} \rangle. \qquad --(4.15)$$

These quadruple-correlation functions are tested in figure 4-12. All three represent a significant improvement over the standard quadruple-correlation function Q. In particular, they do not have false peaks for two pairs of correlated series, which produce the "cross" in the correlogram for Q. More stringent tests, applied to signals containing both quadruple correlation and two uncorrelated pairs, are presented later, when the results can be compared with functions still to be introduced.

A further problem arises with these correlation functions based on selection when they are applied to series containing signals which are repeated, as will occur in the scintillation of an unresolved double star. The complication that this causes is illustrated in figure 4-13. In the top graph, two uncorrelated signals, A and B, occur in

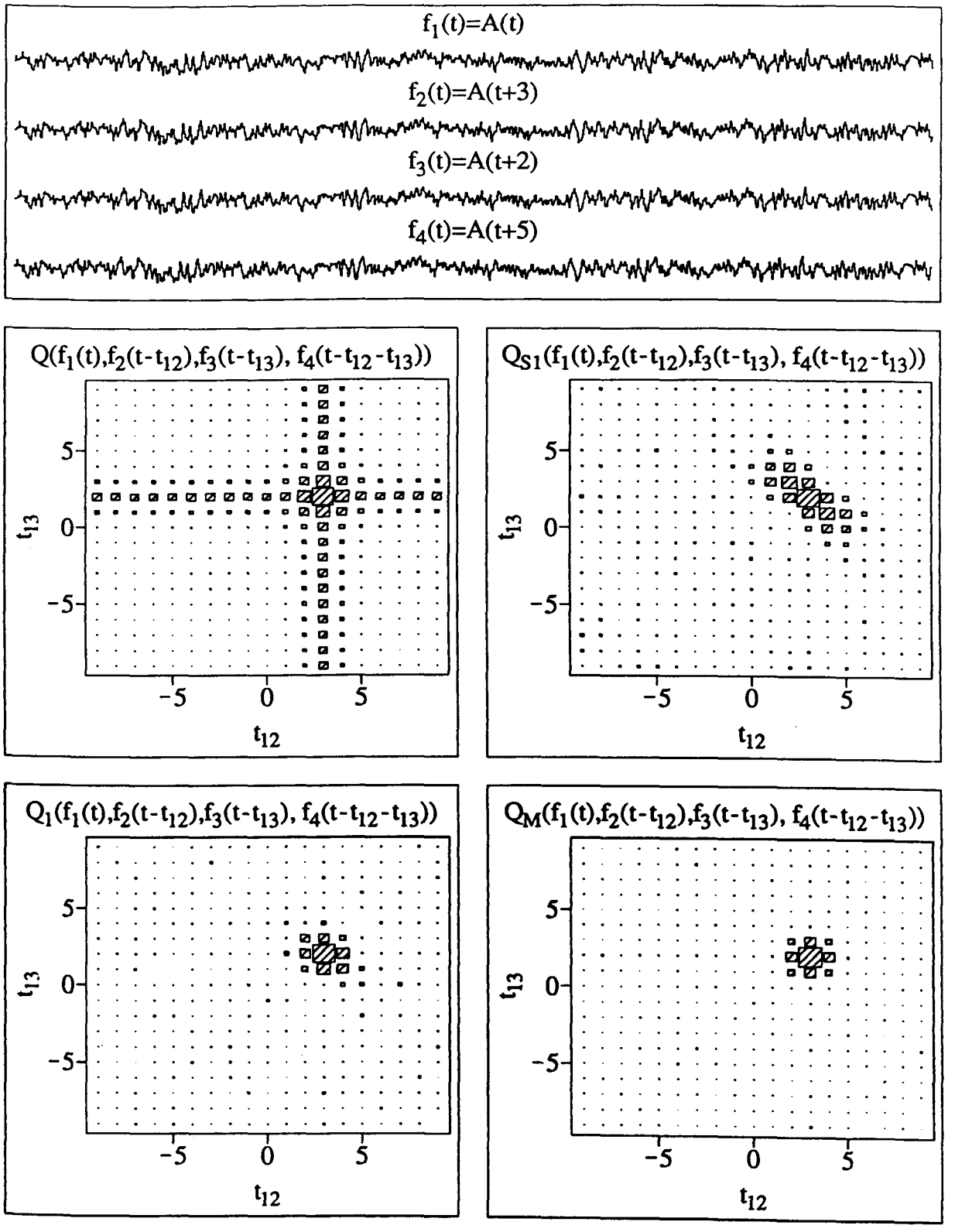

Figure 4-12 Various quadruple correlation functions are applied to the series plotted at the top. These consist of the same series shifted by different amounts. The time shift for f_4, relative to f_1, is set equal to the sum of the time shifts for f_2 and f_3. This allows the result of the quadruple correlation to be presented in two rather than three dimensions, as it can be plotted as a function of just t_{12} and t_{13} if $t_{14} = t_{12} + t_{13}$. The required result is a single peak at $(t_{12}, t_{13}) = (3, 2)$. The standard quadruple correlation function $Q(f_1, f_2, f_3, f_4)$ fails, as it gives a positive result whenever there are two correlated pairs, rather than just when all four series are correlated. Better results are obtained using the selection functions $Q_{S1}(f_1, f_2, f_3, f_4)$, $Q_1(f_1, f_2, f_3, f_4)$ or $Q_M(f_1, f_2, f_3, f_4)$, with the latter giving the best resolution.

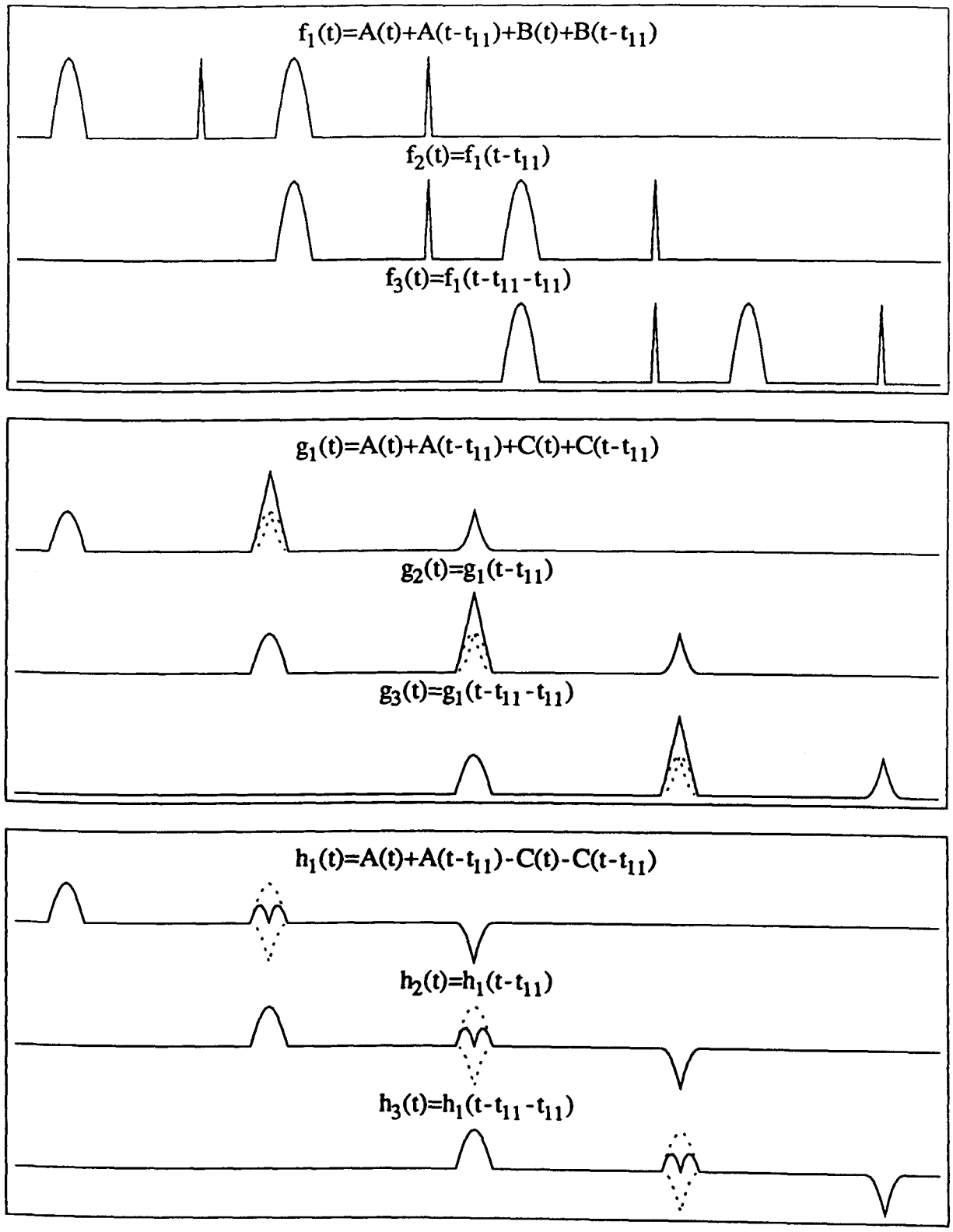

Figure 4-13 Signals which repeat once at a fixed time interval present a problem for triple correlation functions which use "selection". The three graphs above represent different parts of a series being correlated. The top one represents the normal situation, where unrelated signals do not overlap, while the lower two graphs represent the unusual situations where the unrelated signals do overlap. The dashes lines in these two cases indicate the two signals that have been added together. In the first case there is no triple correlation between f_1, f_2 and f_3. The other two cases will produce a false positive value for the selection function T_2, as the value of g_2 is large when the unrelated signals in g_1 and g_3 are the same sign and h_2 is small when h_1 and h_3 are the opposite sign.

series f_1 and each is repeated after an interval t_{11}. Series f_2 and f_3 are produced by shifting f_1 by t_{11} and $2t_{11}$. There is no correlation (at zero time delay) between these series and $T_2(f_1(t), f_2(t), f_3(t)) = 0$. In the other two graphs signal A is followed by an uncorrelated signal C which happens to be non-zero at the same time as the repeat of signal A. The amplitude of the signal in the second series is related to the sign of the other two, giving a false positive value for T_2.

This type of data is simulated in figure 4-14 and the quadruple-correlation functions Q_1, Q_{S1}, Q_M and Q_{SM} are applied to it. Q_{SM} is the minimum of the four "selection on sign" quadruple correlation functions, given by

$$Q_{SM} = Q_i \text{ where } |Q_i| = \min\{|Q_{S1}|, |Q_{S2}|, |Q_{S3}|, |Q_{S4}|\}. \qquad --(4.16)$$

The chance additions detailed in figure 4-13 produce false peaks for Q_{S1}. These are reduced but not eliminated by taking the minimum of the four possible selection functions Q_{SM}. The "selection on modulus" functions Q_1 and Q_M give better results than the "selection on sign" functions Q_{S1} and Q_{SM}. The occurrence of five peaks in the correlogram for Q_M is easily explained. Three of them lie along the line $t_{11} = 0$, which corresponds to the case of zero separation of the duplicated signals. Another peak occurs because there is no difference between positive and negative values of t_{11}; both cause the duplicated signal to be shifted onto itself.

The peak at $t_{11} = 0$ will be a problem if this analysis is applied to double star signals, where it corresponds to scintillation patterns with zero separation originating from zero height. In practice, due to the finite size of the scintillation patterns, this false peak at zero height will extend up to finite heights and may cover up a genuine peak.

In figure 4-15 the "correlation by selection" function T_1 is applied to series where the signals are asymmetric about the mean level. In this case the false peak is suppressed and the result is almost the same as for the standard triple correlation T.

In conclusion, multiple correlation by selection has advantages over standard functions in that it can detect triple correlation for signals that have distributions symmetric about the mean and can discriminate between true quadruple correlation and two correlated pairs. Unfortunately it gives a false indication of correlation when different

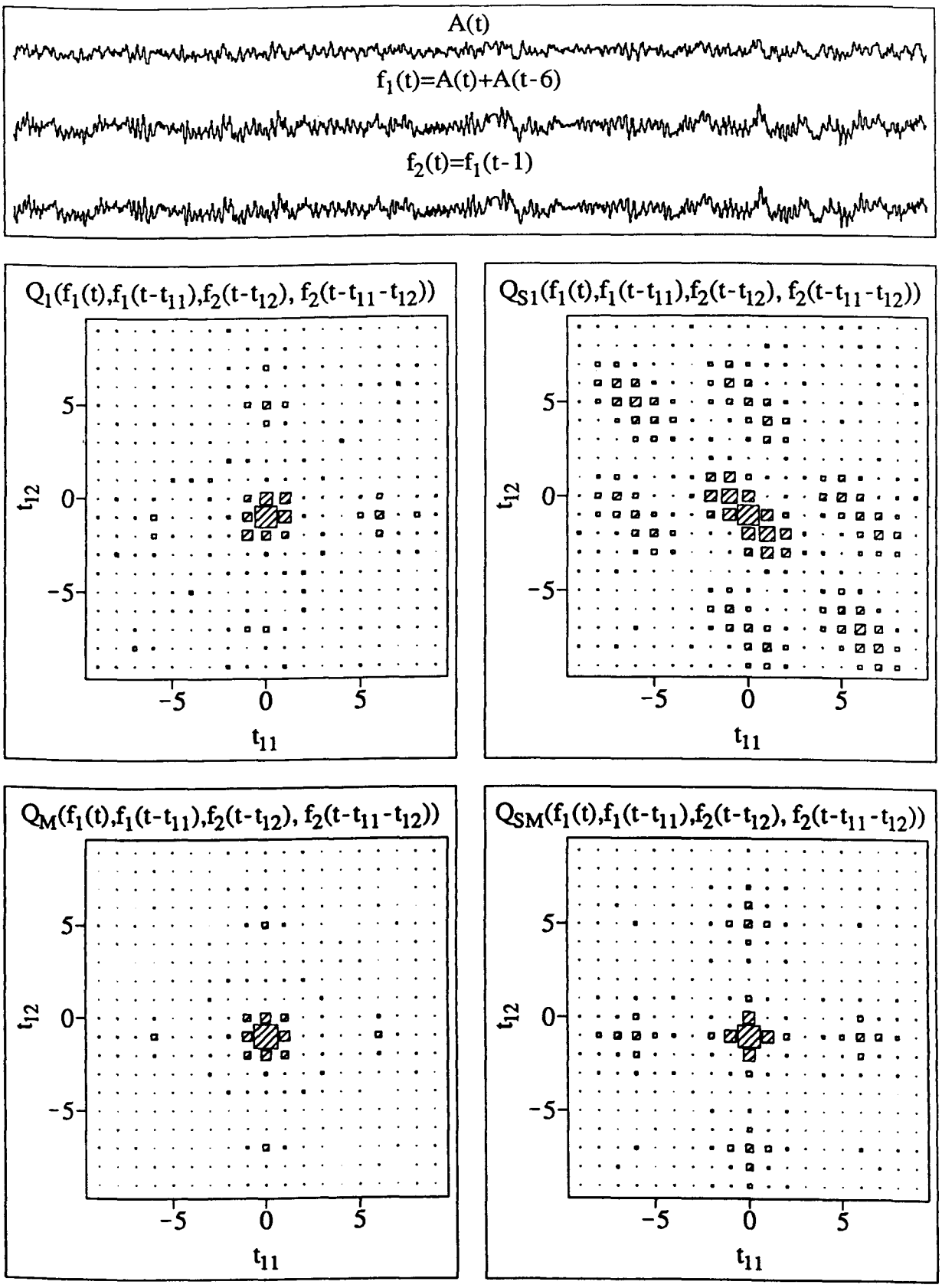

Figure 4-14 This illustrates the application of quadruple correlation to the analysis of double star signals. Series f_1 is the sum of series A and A shifted by 6 units. Series f_2 is the same as f_1 but lagging by 1 unit. A quadruple correlation of the series f_1, $f_2(t-t_{12})$, $f_1(t-t_{11})$ and $f_2(t-t_{11}-t_{12})$ should have peaks at $(t_{11},t_{12}) = (0,-1)$, $(0,5)$, $(0,-7)$, $(-6,-1)$ and $(6,-1)$. The selection functions Q_1 and Q_{S1} show peaks at these positions, but also have false peaks elsewhere. These false peaks are reduced, but not eliminated, in the functions Q_M and Q_{SM}, where Q_M is the minimum of $\{Q_1, Q_2, Q_3, Q_4\}$ and Q_{SM} is the minimum of $\{Q_{S1}, Q_{S2}, Q_{S3}, Q_{S4}\}$.

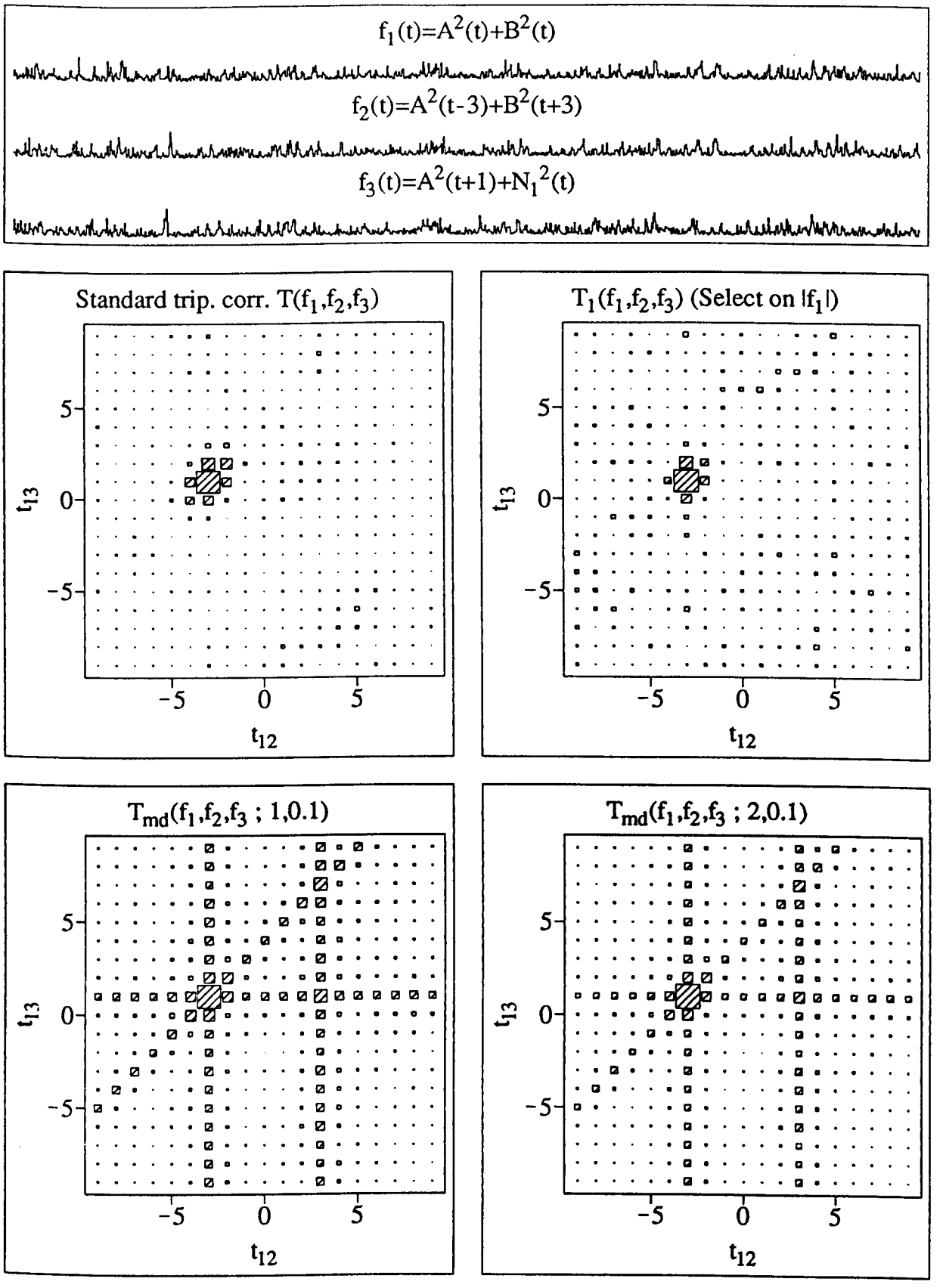

Figure 4-15 Various triple correlation functions are applied to the time series plotted at the top. These time series are asymmetrically distributed about their mean values. The standard triple correlation T gives the result on the middle left, showing a single peak at the correct postition, $(t_{12}, t_{13}) = (-3, 1)$. The selection function T_1 (middle right) gives a similar result. At the bottom "correlation by minimum difference" $T_{md}(f_1, f_2, f_3; M, 0.1)$ is applied, with $M = 1$ on the left and $M = 2$ on the right.

signals, each of which occur in some but not all of the series, contribute to the series used for selection. It can be applied to the analysis of double-star signals, but in this it produces a large peak at zero height which, due to the finite size of the patterns, may extend up to heights from which the scintillation actually originates. Due to these deficiencies, a second approach is now explored.

4.2.4 Multiple correlation by minimum difference

If two or more time series are nearly identical, the difference between even the most dissimilar of the series will be small. If an extra uncorrelated signal is added to one of the series, the difference between it and the others will increase. This suggests the idea of "correlation by minimum difference", where a small value of the difference between all pairs of series produces a large contribution to the multiple-correlation coefficient. A triple-correlation function which implements this principle is the reciprocal of the largest difference *ie*

$$\left\langle \frac{1}{\max\{f_1, f_2, f_3\} - \min\{f_1, f_2, f_3\}} \right\rangle .$$

This formula has two deficiencies: it is undefined for complete correlation (*ie* $f_1 = f_2 = f_3$) and it has a high value for smaller signals (*ie* f_1, f_2 and $f_3 \sim 0$). These two problems are overcome by adding a small non-zero value to the denominator and normalizing by the signal level, leading to a formula for the "triple correlation by minimum difference",

$$T_{md}(f_1, f_2, f_3; F) = \left\langle \frac{|f_1 + f_2 + f_3|}{\max\{f_1, f_2, f_3\} - \min\{f_1, f_2, f_3\} + F(|f_1| + |f_2| + |f_3|)} \right\rangle$$

where F is small.

For perfect correlation, $T_{md} = \frac{1}{F}$. The choice of the constant F depends on the characteristics of the series being analyzed. If it is chosen to be too small, then the contribution produced by chance coincidences could exceed that due to actual correlation.

T_{md} will be larger if two of the series are correlated than if all are uncorrelated. This is because the value of the maximum minus minimum for three independent values will be larger on average than for two independent values. Thus at first sight "correlation by minimum difference" does not seem worthy of further investigation. The reasons for continuing are:

a) it can be extended to any number of series and the deficiency above will be become less serious *eg* for 4 series, of which two are correlated, the maximum difference will be based on three independent values rather than four.

b) It will be shown later that the function is useful in the analysis of the repeated signals expected for double-star scintillation.

c) As T_{md} (for F very small) is independent of the signal level, it will have the same value at all measured points along a particular fluctuation which occurs in all the series. This differs from the standard function T, which gives a large weighting to large values. Thus it can be used for pattern matching by taking the product of M successive values:

$$T_{md}(f_1, f_2, f_3; M, F) =$$

$$\left\langle \prod_{i=1}^{M} \frac{|f_{1_i} + f_{2_i} + f_{3_i}|}{\max\{f_{1_i}, f_{2_i}, f_{3_i}\} - \min\{f_{1_i}, f_{2_i}, f_{3_i}\} + F(|f_{1_i}| + |f_{2_i}| + |f_{3_i}|)} \right\rangle . \qquad --(4.17)$$

A single fluctuation (covering M successive sampling intervals) which is well correlated between all the series would give a large contribution to $T_{md}(f_1, f_2, f_3 : M, F)$.

Extension to any number of series is straight forward:

$$Mult_{md}(f_1, ..., f_n; M, F) =$$

$$\left\langle \prod_{i=1}^{M} \frac{|\sum_{j=1}^{n} f_{j_i}|}{\max_{j=1}^{n}\{f_{j_i}\} - \min_{j=1}^{n}\{f_{j_i}\} + F\sum_{j=1}^{n}|f_{j_i}|} \right\rangle . \qquad --(4.18)$$

The "quadruple correlation by multiple difference" Q_{md} is implemented by setting $n = 4$ in this equation.

T_{md} is compared with other functions in figure 4-15, where it is applied to asymmetric data. As predicted above, it gives false peaks where only two of the series are correlated. In figure 4-16 Q_{md} is applied to symmetric series which contain both a quadruple-correlated component and two correlated pairs. Q_{md} is inferior to the standard quadruple correlation Q. The best result is given by Q_M, but it still has one false peak.

In figures 4-15 and 4-16, the choice of the constants M and F makes little difference to the result. However, the simulated data has constant statistics *ie* both signals A^2 and B^2 are present all the time. It is possible that with actual scintillation data,

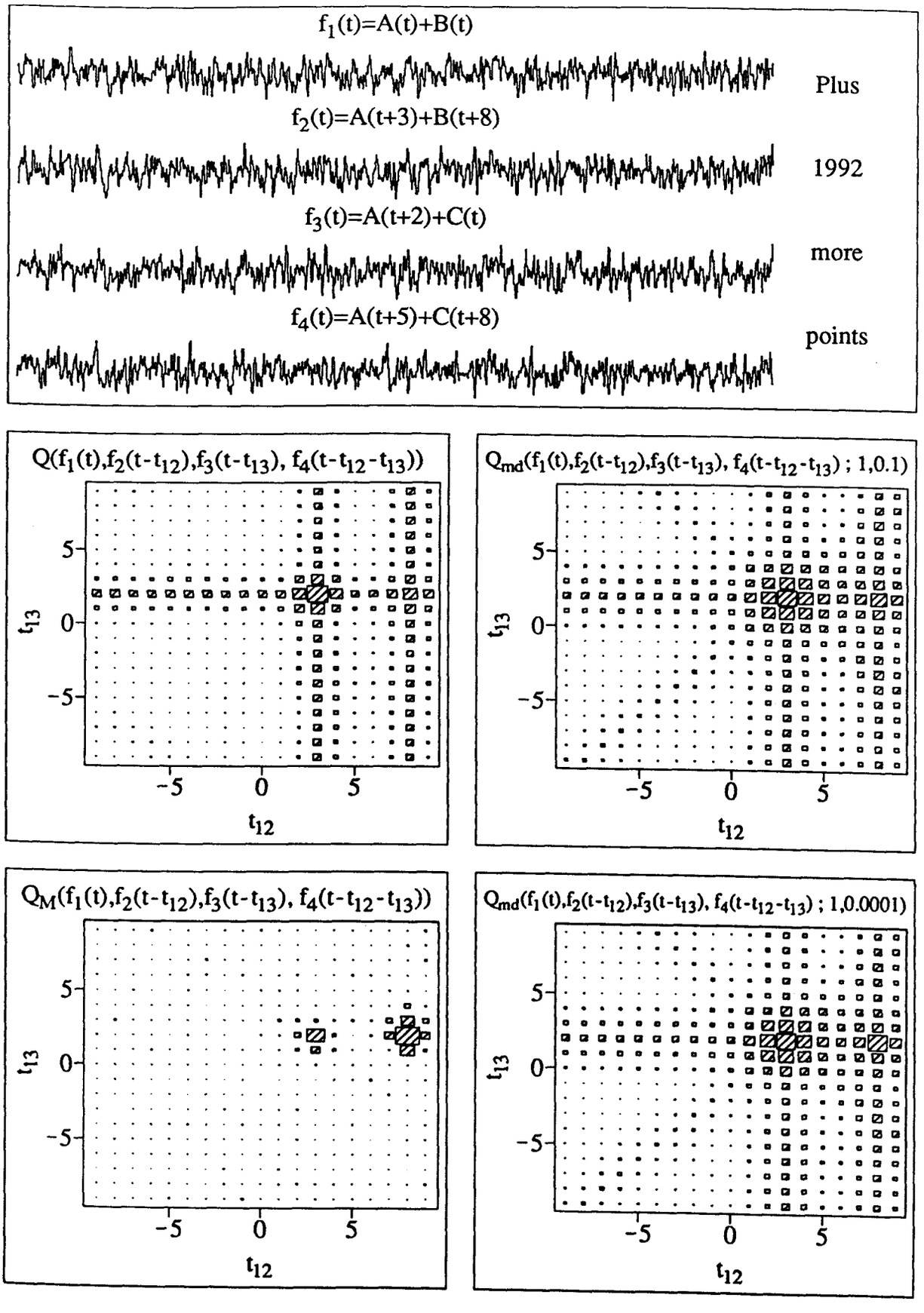

Figure 4-16 The standard quadruple correlation Q, selection function Q_M and minimum difference function Q_{md} are applied to the data at the top, in which a signal A is common to all four series and two other signals B and C are each correlated between two of the series. To allow presentation of the result in two dimensions, the time shift (relative to series 1) of A in series 4 is set to the sum of the shifts in series 2 and 3. An ideal quadruple correlation should have a peak only at $(t_{12}, t_{13}) = (3, 2)$.

different components of the signal will dominate at different times. In this situation, large values of M and small values of F may be more useful.

The application of "correlation by minimum difference" to the analysis of repeated signals is illustrated in figure 4-17. As in figure 4-14, double-star signals are simulated, but here one star has only half the intensity of the other. This asymmetry gives the opportunity to reduce the unwanted peaks which occurred at $t_{11} = 0$ in figure 4-14. If the repeated signal is doubled after being shifted to line up with the original, the two signals will be exactly the same and will make a large contribution to Q_{md}, while doubling the original after a shift the other way will increase the difference between the signals.

In figure 4-17 the function Q_M (which gave the best result in figure 4-14 for identical stars) is applied for unequal stars. The result is similar to that obtained earlier, with a slight enhancement of the desired peak at $(t_{11}, t_{12}) = (-6, -1)$. The functions Q_M, Q and Q_{md} are applied to the four series $f_1(t)$, $2f_1(t - t_{11})$, $f_2(t - t_{12})$ and $2f_2(t - t_{11} - t_{12})$, where the smaller repeated signal is doubled to match the original signal. This strategy does not work for Q_M and Q, but for Q_{md} the desired peak at $(-6, -1)$ is greatly enhanced. The value at $(6, -1)$ is slightly reduced because the larger original signal is doubled, increasing the difference between it and the smaller repeated signal. ($nb\ A^2$ is used in figure 4-17, as the result is not clear with A. Thus this analysis will only be useful if the scintillation is sufficiently asymmetrical in its amplitude distribution.)

The line of high values for Q_{md} at $t_{12} = -1$ may not be the problem that it first appears, as it can be cancelled by taking the difference between the two sides of the correlogram to produce Q_{ur}:

$$Q_{ur}(t_{11}, t_{12}) = Q_{md}(t_{11}, t_{12}) - Q_{md}(-t_{11}, t_{12}) \qquad -- (4.19)$$

where the subscripts u and r refer to "unequal" and "repeated". Naturally this will give a correlogram where $Q_{ur}(t_{11}, t_{12}) = -Q_{ur}(-t_{11}, t_{12})$. The position of the positive values of Q_{ur} depends on whether the brighter or fainter pattern arrives at the detector first. As this order will be opposite for opposite pattern velocities, the positive values of Q_{ur} should occur in two diagonally opposed quadrants of the correlogram.

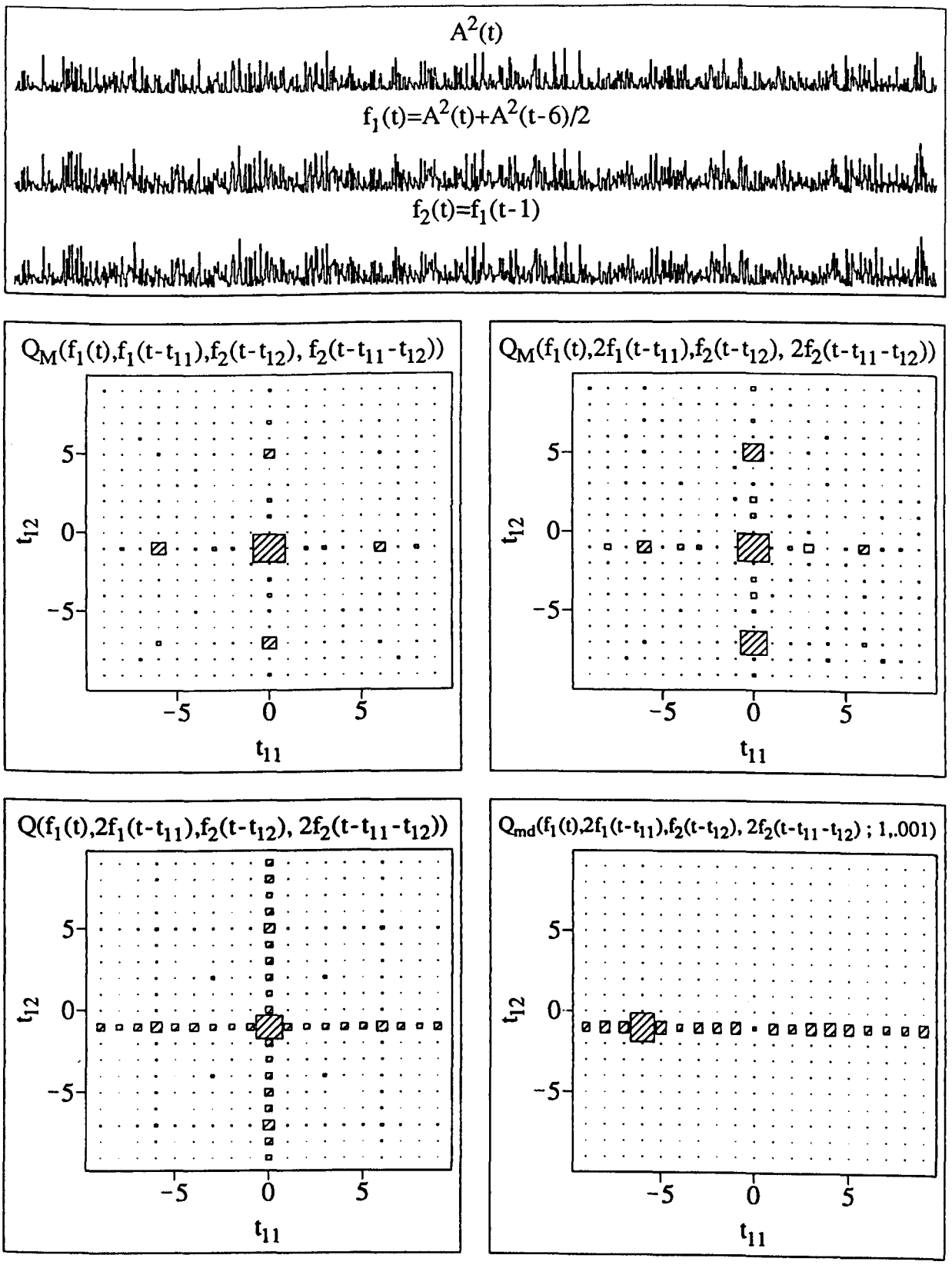

Figure 4-17 This illustrates the application of quadruple correlation to double star signals where the two stars are of different intensities, simulated by adding $0.5A^2(t-6)$ to $A^2(t)$. The ratio of the required peak at (-6,-1) to the unwanted peak at (0,0) for $Q_M(f_1(t), f_1(t-t_{11}), f_2(t-t_{12}), f_2(t-t_{11}-t_{12}))$ (middle left), is similar to its value for equal intensities in figure 4-14. In the other three correlograms, the functions Q, Q_M and Q_{md} are applied to $f_1(t), 2f_1(t-t_{11}), f_2(t-t_{12})$ and $2f(t-t_{11}-t_{12})$. By doubling the two series shifted through t_{11}, the smaller, repeated signal $0.5A^2(t-6)$ is restored to the same size as $A^2(t)$ when $t_{11} = -6$. For function Q_{md} this enhances the required peak at $(t_{11}, t_{12}) = (-6, -1)$.

This technique is tested with simulated double-star data in figure 4-18, where one star has half the intensity of the other and scintillation is produced at two different heights with different wind velocities. The vector from the fainter to the brighter scintillation patterns is in the same direction as from detector 1 to 2 (nb signal f_n is produced by detector n). Q_{md} is applied, as for figure 4-17, to the series $f_1(t)$, $2f_1(t-t_{11})$, $f_2(t-t_{12})$ and $2f_2(t-t_{11}-t_{12})$, giving the correlogram on the middle left. It transforms (using 4.19) to Q_{ur} on the right. Peaks in correlation should occur at $(t_{11},t_{12}) = (-6,-1)$ and $(3,3)$ and this in fact occurs. The same analysis applied with $M = 2$ gives the final result on the lower left, showing an improvement with the application of pattern matching produced by the larger value of M. For comparison the standard quadruple correlation Q is applied to the original series on the lower right. It can be seen that Q_{ur} is a substantial improvement, in that it does not give the large false peaks around $t_{11} = 0$ which occur with Q.

Thus "selection by minimum difference" shows considerable promise for the analysis of double star signals, if the two stars are of different intensity and the distribution of the intensity is sufficiently "spiky".

4.3 Basic measurements of stellar scintillation

Earlier, phenomena were described which could be detrimental to the remote measurement of wind and turbulence strength using multiple-beam methods. Simple techniques for observing stellar scintillation, which may be used to investigate these phenomena, are outlined below.

4.3.1 Investigation of refraction

If, as described in §4.1.2, the "beams" from star to detector are deflected by refraction, then a variable component will be added to the velocity of the scintillation patterns at ground level. A useful way to think about the effect is to consider a turbulent irregularity at a fixed position relative to the ground and a beam of starlight going through it. Refraction above the irregularity would change the apparent direction from which the beam comes. The beam would continue on in this new direction, displacing the scintillation pattern relative to its position without the deflection. Refraction below the irregularity would displace the beam and the embedded scintillation pattern. As the

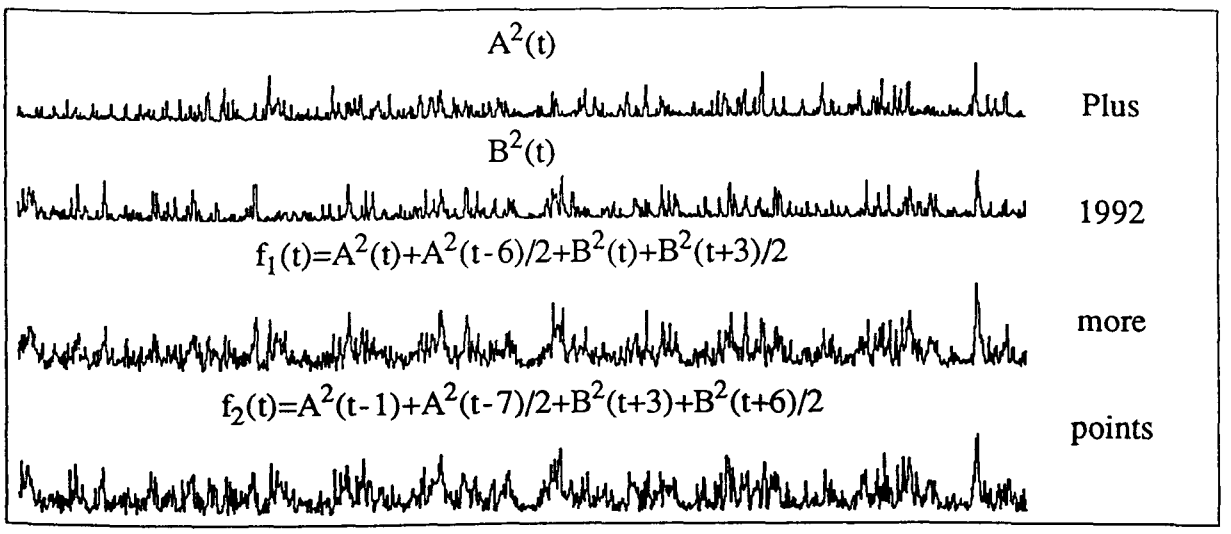

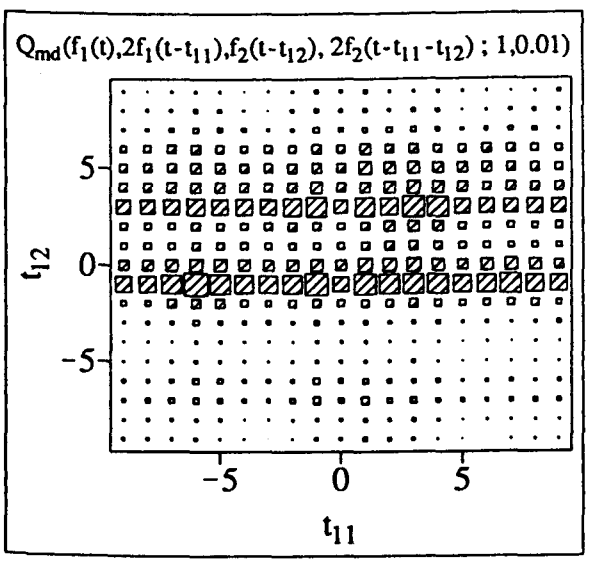

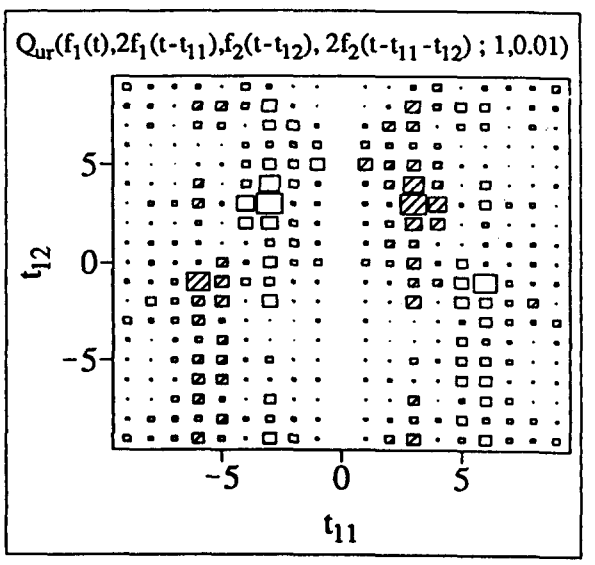

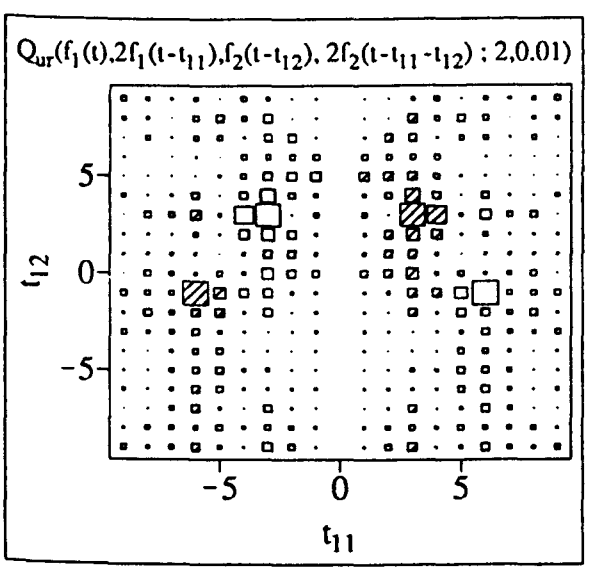

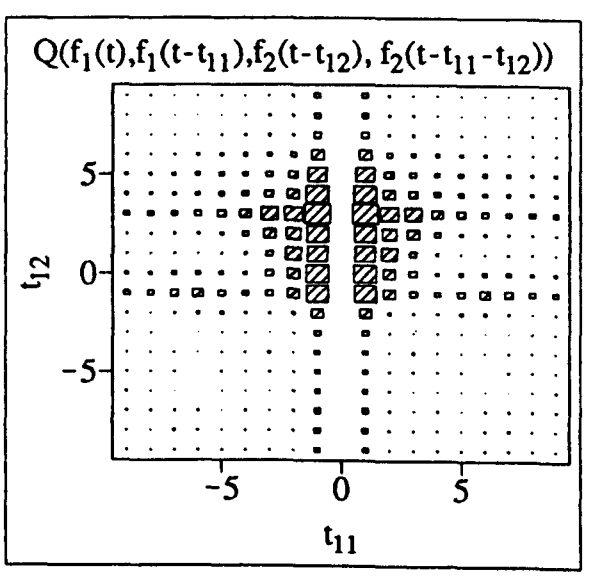

Figure 4-18 The double star data plotted at the top is simulated as for figure 4-17, except that two signals A^2 and B^2 are included, with different time delays, to simulate two turbulent layers. On the middle left, Q_{md} is applied after doubling $f_1(t - t_{11})$ and $f_2(t - t_{11} - t_{12})$. The result transforms to the correlogram for Q_{ur} on the right. The equivalent result for $M = 2$ is shown on the bottom left, where the desired peaks at $(t_{11}, t_{12}) = (-6, -1)$ and $(3, 3)$ stand out clearly. For comparison, the standard quadruple correlation Q is applied on the bottom right.

direction of deflection will vary randomly, the displacement of the scintillation pattern should add a random component to its velocity.

An observation of variability in the velocity of the scintillation pattern would not be a definitive indicator of refraction, as this variability could also arise from random motion within the turbulence producing the scintillation or from variation of the wind velocity with height. However, if the velocity of the scintillation pattern has no variability, it indicates that refraction is not significant (as well as showing that motion within the turbulence is negligible compared to the wind speed).

A method proposed here to investigate the occurrence of refraction is to record the scintillation at two detectors spaced apart on a line parallel to the pattern velocity, allowing the velocity to be determined from the time delay at which the cross correlation of the signals is a maximum. This measurement should be made over time intervals as short as possible, allowing variation of the velocity with time to be observed.

A second proposed method is to observe the separation of scintillation patterns of a double star. In the absence of refraction, the two identical patterns should travel at the same speed, separated by a constant distance. Refraction would cause this distance to vary. Given the practical difficulty in observing the faint patterns directly, the method proposed here is to measure the spatial correlation function of the double star scintillation pattern on an occasion when the pattern is produced by turbulence at only one height. This will have an autocorrelation peak with a width determined by the pattern structure and, in the absence of refraction. an identical peak at a separation specified by equation 4.1 along the line parallel to the projection of the star position angle. The occurrence of refraction will be indicated if the second peak is wider than the autocorrelation peak.

4.3.2 Investigation of phase interaction

The question as to whether the phase variations produced at different heights add together and then produce a scintillation pattern, or whether scintillation patterns from different heights add independently, may be investigated by observing scintillation which is produced under particular conditions. These are that the scintillation is produced at two different heights and the wind velocities at these two heights are substantially different. Individual fluctuations in the scintillation patterns could then

be identified as being produced at one height or another, depending on the time delay between their detection by two spaced receivers. If the scintillation pattern is produced by diffraction associated with the sum of the phase differences, then some correlation between the intensity fluctuations from the two different heights may be apparent. If there is no significant phase interaction prior to the formation of diffraction patterns, then the intensity fluctuations produced by turbulence at different heights will be uncorrelated.

The standard triple correlation T can be used to distinguish between these two situations. Let moving turbulence at one height produce signal $a(t)$ on a detector (of scintillation) and moving turbulence at another height produce an uncorrelated signal $b(t)$ on the same detector. Let these two patterns move from this detector to another in time intervals t_a and t_b. If the intensities of the different patterns add algebraically, then the total signals are $S_1(t) = a(t) + b(t)$ and $S_2(t) = A(t - t_a) + B(t - t_b)$. A and B represent non-linear functions of a and b, to allow for the evolution of the scintillation pattern. The standard triple correlation can be applied to show that signals from the two heights are uncorrelated:

$$
\begin{aligned}
&T(S_1(t), S_2(t + t_a), S_2(t + t_b)) \\
&= \langle [a(t) + b(t)]\,[A(t) + B(t - t_b + t_a)]\,[A(t - t_a + t_b) + B(t)] \rangle \\
&= \langle [a(t) + b(t)]\,[A(t) + B(t')]\,[A(t'') + B(t)] \rangle \text{ where } t' = t - t_b + t_a \text{ and } t'' = t - t_a + t_b \\
&= \langle (a(t)A(t)A(t'') + a(t)A(t)B(t) + a(t)B(t')A(t'') + a(t)B(t')B(t) \\
&\quad + b(t)A(t)A(t'') + b(t)A(t)B(t) + b(t)B(t')A(t'') + b(t)B(t')B(t) \rangle \\
&= \langle a(t)A(t) \rangle \langle A(t'') \rangle + \langle a(t)A(t) \rangle \langle B(t) \rangle + \langle a(t) \rangle \langle B(t') \rangle \langle A(t'') \rangle + \langle a(t) \rangle \langle B(t') \rangle \langle B(t) \rangle \\
&\quad + \langle b(t) \rangle \langle A(t) \rangle \langle A(t'') \rangle + \langle b(t)B(t) \rangle \langle A(t) \rangle + \langle b(t) \rangle \langle B(t') \rangle \langle A(t'') \rangle + \langle b(t)B(t) \rangle \langle B(t') \rangle \\
&= 0 \text{ as } \langle A(t'') \rangle = \langle B(t) \rangle = \langle A(t) \rangle = \langle B(t') \rangle = 0.
\end{aligned}
$$

If the phase variations produced at the two heights add together and the combined phase variation produces a scintillation pattern, it will be different to the sum of the intensity fluctuations which the two phase variations would produce on their own. For example, consider the structure of the scintillation pattern at a position where a bright point is produced at the centre of curvature of a part of a wavefront. If another identical phase fluctuation is added, increasing the curvature, then the bright point will occur at a shorter distance and the original pattern will be different.

In the case of phase interaction, the signals seen on the detectors in the situation described above are $S_1(t) = f(a(t), b(t))$ and $S_2(t) = f(A(t - t_a), B(t - t_b))$, where $f(a, b)$ represents a complicated non-linear function of a and b. The triple correlation

$$T(S_1(t), S_2(t+t_a), S_2(t+t_b)) = \langle f(a(t), b(t)) f(A(t), B(t+t_a-t_b))\, f(A(t-t_a+t_b), B(t))\rangle$$

may now be non-zero, as all three terms are related to both a and b.

To apply this test, the method proposed is to identify a situation where two scintillation patterns, moving with different velocities, are each seen on each of two spaced detectors. If the intensity fluctuations of the two patterns have added algebraically, then $T(S_1(t), S_2(t + t_{12})S_2(t + t'_{12}))$ will only be non-zero if $t_{12} = t'_{12} = t_a$ or t_b. If the scintillation patterns arise from addition of phase fluctuations, peaks in correlation may also occur at $(t_{12}, t'_{12}) = (t_a, t_b)$ or (t_b, t_a).

4.4 Measurement of isoplanatism

A recently published technique (Campbell and Elford, 1990) to measure the atmospheric isoplanatic angle was developed in this work and is now described. It is based on the concept that the scintillation of a double star, measured at a point on the ground, is the sum of two patterns produced by turbulence along two lines through the atmosphere, separated by a very small angle. By comparing the scintillation of the double star with that of a nearby single star, it is possible to determine whether the two scintillation patterns of the double star (and thus the two separate paths of turbulent irregularities) are identical, similar or different. If they are identical, then the isoplanatic angle is greater than the angular separation of the double star.

If the isoplanatic angle is much less than the angular separation of a double star, then two uncorrelated scintillation patterns will be added, reducing the normalized second moment N_d of the double star relative to N_s, its value for a single star. Let I_d and I_s represent the detected light intensity (on identical apertures) of a double star and a nearby single star. I_d is the sum of intensities I_1 and I_2 due to the two components of the double star. Assume that the average statistics of the scintillation pattern are the same for the two components of the double star and the nearby single star, *ie*

$$N_s = \frac{\langle I_s^2 \rangle}{\langle I_s \rangle^2} = \frac{\langle I_1^2 \rangle}{\langle I_1 \rangle^2} = \frac{\langle I_2^2 \rangle}{\langle I_2 \rangle^2} \ .$$

Then $N_d = \frac{\langle I_d^2 \rangle}{\langle I_d \rangle^2} = \frac{\langle (I_1 + I_2)^2 \rangle}{(\langle I_1 \rangle + \langle I_2 \rangle)^2} = \frac{\langle (I_1^2 + 2I_1 I_2 + I_2^2) \rangle}{(\langle I_1 \rangle + \langle I_2 \rangle)^2}$.

Substituting $\langle I_1 I_2 \rangle = \langle I_1 \rangle \langle I_2 \rangle$ (as these are uncorrelated), dividing through by $\langle I_1 \rangle^2$ and substituting $r = \frac{\langle I_1 \rangle}{\langle I_2 \rangle}$ gives

$$N_d = \frac{N_s(r^2+1) + 2r}{r^2 + 2r + 1} . \qquad --(4.20)$$

N_d and N_s will be equal if the isoplanatic angle exceeds the double-star separation. Thus the difference between N_d and N_s gives an indication of the similarity of the turbulent structure along paths with a particular angular separation.

This proposed method differs from previous work in that:

1) it measures the amount of isoplanatism associated with the scale of scintillation being observed, rather than an average value over a large aperture (as is required in methods which rely on imaging and is assumed in the formulation of Loos and Hogge, 1979). An advantage of this is that it can measure the isoplanatism associated with the smallest scale of the scintillation pattern. Another is that it can be used with any size or shape of aperture and so can be applied with apertures which are designed to measure other parameters.
2) It is a direct measurement and so does not require the assumptions of weak scintillation or of a Kolmogorov spectrum for the turbulence (as required in the method used by Eaton *et al*, 1985).
3) The method can be applied at much lower light levels and in the presence of higher background light, because the normalized second moments N_d and N_s can be determined in such circumstances using methods considered in the next section.

4.5 Analysis of photomultiplier pulse distributions

In order to measure the normalized moments of starlight intensity for the work in this thesis, methods are developed below to

a) calculate the moments from data contaminated by a non-Poisson background,
b) calculate the covariance between two different light intensities which are similarly contaminated,
c) measure and correct for photomultiplier afterpulsing, and
d) correct for dead time.

4.5.1 Moment calculation with a non-Poisson background

As described in §3.10, the normalized moments of faint light of fluctuating intensity I can be found from the measured values n of photocounts per interval using equation 3.23

$$\frac{\langle I^m \rangle}{\langle I \rangle^m} = \frac{\langle n(n-1)...(n-m+1) \rangle}{\langle n \rangle^m} \qquad \text{for } m = 2, 3, 4...$$

Pusey (1977) modified this equation to allow for the contribution of background light which has a Poisson distribution.

In the observations of starlight in this work, the background is not Poisson distributed, due to non-Poisson equipment noise, such as photomultiplier dark noise, and to 100-Hz fluctuation due to street lights. To allow the measurement of the moments of the starlight, equation 3.23 is modified below to allow for a non-Poisson background component. (*nb* The equipment noise is incorporated by considering it as being produced by a notional extra component of the background light.)

If the total intensity I_t is the sum of starlight of intensity I and background I_b', then

$$\frac{\langle I^2 \rangle}{\langle I \rangle^2} = \frac{\langle (I_t - I_b')^2 \rangle}{\langle I_t - I_b' \rangle^2} = \frac{\langle I_t^2 - 2 I_t I_b' + I_b'^2 \rangle}{(\langle I_t \rangle - \langle I_b' \rangle)^2} .$$

Now $\langle I_t I_b' \rangle = \langle (I + I_b') I_b' \rangle = \langle I I_b' \rangle + \langle I_b'^2 \rangle$ and $\langle I I_b' \rangle = \langle I \rangle \langle I_b' \rangle = (\langle I_t \rangle - \langle I_b' \rangle) \langle I_b' \rangle$ (as I and I_b' are uncorrelated),

$$\text{whence } \frac{\langle I^2 \rangle}{\langle I \rangle^2} = \frac{\langle I_t^2 \rangle - 2(\langle I_t \rangle - \langle I_b' \rangle)\langle I_b' \rangle - \langle I_b'^2 \rangle}{\langle I_t \rangle^2 - 2\langle I_t \rangle \langle I_b' \rangle + \langle I_b' \rangle^2} .$$

For measurements of t counts/interval produced by I_t, and b counts/interval produced by a background I_b, where I_b and I_b' have the same average statistics, equation 3.23 gives

$$\frac{\langle I_t^2 \rangle}{\langle I_t \rangle^2} = \frac{\langle t(t-1) \rangle}{\langle t \rangle^2} \qquad \text{and} \qquad \frac{\langle I_b'^2 \rangle}{\langle I_b' \rangle^2} = \frac{\langle I_b^2 \rangle}{\langle I_b \rangle^2} = \frac{\langle b(b-1) \rangle}{\langle b \rangle^2} .$$

Substituting these expressions, along with $\frac{\langle I_t \rangle}{\langle I_b' \rangle} = \frac{\langle I_t \rangle}{\langle I_b \rangle} = \frac{\langle t \rangle}{\langle b \rangle}$, gives

$$\frac{\langle I^2 \rangle}{\langle I \rangle^2} = \frac{\langle t(t-1) \rangle - 2(\langle t \rangle - \langle b \rangle)\langle b \rangle - \langle b(b-1) \rangle}{\langle t \rangle^2 - 2\langle b \rangle \langle t \rangle + \langle b \rangle^2} . \qquad --(4.21)$$

Similarly (and substituting $\langle d \rangle = \langle t \rangle - \langle b \rangle$), the higher moments of I are given by:

$$\frac{\langle I^3\rangle}{\langle I\rangle^3} = \frac{1}{\langle d\rangle^3}\Bigg\{\langle t(t-1)(t-2)\rangle - 3\frac{\langle I^2\rangle}{\langle I\rangle^2}\langle b\rangle\langle d\rangle^2 -$$

$$3\langle d\rangle\langle b(b-1)\rangle - \langle b(b-1)(b-2)\rangle\Bigg\} \qquad --(4.22)$$

$$\frac{\langle I^4\rangle}{\langle I\rangle^4} = \frac{1}{\langle d\rangle^4}\Bigg\{\langle t(t-1)(t-2)(t-3)\rangle - 4\frac{\langle I^3\rangle}{\langle I\rangle^3}\langle b\rangle\langle d\rangle^3 - 6\frac{\langle I^2\rangle}{\langle I\rangle^2}\langle b(b-1)\rangle\langle d\rangle^2 -$$

$$4\langle b(b-1)(b-2)\rangle\langle d\rangle - \langle b(b-1)(b-2)(b-3)\rangle\Bigg\} \qquad --(4.23)$$

$$\frac{\langle I^5\rangle}{\langle I\rangle^5} = \frac{1}{\langle d\rangle^5}\Bigg\{\langle t(t-1)(t-2)(t-3)(t-4)\rangle - 5\frac{\langle I^4\rangle}{\langle I\rangle^4}\langle b\rangle\langle d\rangle^4 -$$

$$10\frac{\langle I^3\rangle}{\langle I\rangle^3}\langle b(b-1)\rangle\langle d\rangle^3 - 10\frac{\langle I^2\rangle}{\langle I\rangle^2}\langle b(b-1)(b-2)\rangle\langle d\rangle^2 -$$

$$5\langle b(b-1)(b-2)(b-3)\rangle\langle d\rangle - \langle b(b-1)(b-2)(b-3)(b-4)\rangle\Bigg\}\,. \qquad --(4.24)$$

Equations 4.21 and 4.22 reduce to Pusey's formulae (equations 3.24 and 3.25), which are applicable in the case of a Poisson-distributed background, by substituting the relationships for a constant background light:

$$\frac{\langle I_b^2\rangle}{\langle I_b\rangle^2} = \frac{\langle b(b-1)\rangle}{\langle b\rangle^2} = \frac{\langle I_b^3\rangle}{\langle I_b\rangle^3} = \frac{\langle b(b-1)(b-2)\rangle}{\langle b\rangle^3} = 1\,.$$

4.5.2 Covariance calculation with a non-Poisson background

Using a similar approach to that above for the moments, the covariance between two different light sources of fluctuating intensity I_1 and I_2 can be measured in the presence of non-Poisson backgrounds (which may be correlated with each other, but not with the sources). Suppose a series of t_1 pulses/interval has been measured for the total T_1, consisting of source I_1 plus background B_1, and of b_1 pulses/interval for the background on its own. T_2, B_2, t_2 and b_2 are defined similarly for light source I_2. The normalized covariance between I_1 and I_2 is then

$$\frac{\langle I_1 I_2\rangle}{\langle I_1\rangle\langle I_2\rangle} = \frac{\langle (T_1 - B_1)(T_2 - B_2)\rangle}{\langle T_1 - B_1\rangle\langle T_2 - B_2\rangle}$$

$$= \frac{\langle T_1T_2\rangle - \langle B_1T_2\rangle - \langle B_2T_1\rangle + \langle B_1B_2\rangle}{\langle T_1\rangle\langle T_2\rangle - \langle B_1\rangle\langle T_2\rangle - \langle B_2\rangle\langle T_1\rangle + \langle B_1\rangle\langle B_2\rangle}\,.$$

Applying equation 3.26 (Jakeman and Pusey, 1980), which relates the covariance of the light fluctuations to that of the photocounts, *ie*

$$\frac{\langle T_1 T_2 \rangle}{\langle T_1 \rangle \langle T_2 \rangle} = \frac{\langle t_1 t_2 \rangle}{\langle t_1 \rangle \langle t_2 \rangle} \qquad \text{and} \qquad \frac{\langle B_1 B_2 \rangle}{\langle B_1 \rangle \langle B_2 \rangle} = \frac{\langle b_1 b_2 \rangle}{\langle b_1 \rangle \langle b_2 \rangle} ,$$

and using algebraic manipulation similar to that in the previous section, allows the derivation of

$$\frac{\langle I_1 I_2 \rangle}{\langle I_1 \rangle \langle I_2 \rangle} = \frac{\langle t_1 t_2 \rangle - \langle b_1 \rangle \langle t_2 \rangle - \langle b_2 \rangle \langle t_1 \rangle + 2\langle b_1 \rangle \langle b_2 \rangle - \langle b_1 b_2 \rangle}{\langle t_1 \rangle \langle t_2 \rangle - \langle b_1 \rangle \langle t_2 \rangle - \langle b_2 \rangle \langle t_1 \rangle + \langle b_1 \rangle \langle b_2 \rangle} . \qquad --(4.25)$$

4.5.3 Determination of afterpulse probability

It is necessary to determine the probability of afterpulsing in a photomultiplier in order to apply a correction for it in the analysis of the starlight data. Normally this probability is measured directly using a multi-channel analyzer (*eg* Williams and Smith, 1973). In the present work this measurement was not made at the time the starlight data was collected as the need for it was not foreseen. Thus it was necessary to develop techniques to determine the probability of afterpulsing from the recorded data. It turns out that this has some advantages over a direct measurement as:

a) it does not require additional equipment.

b) It provides a means to check the validity of the data-recording process.

c) The assumptions and methods used in the correction for afterpulsing are also applied in the original determination of the probabilities. This increases the scope for testing the validity of the assumptions and methods, relative to an approach in which they are only used in the correction phase. It also removes some systematic errors, as they contribute equally in determination and correction, so that their effect cancels.

The method proposed here to deduce afterpulse probabilities involves the analysis of a distribution of pulses produced by a photomultiplier illuminated by a constant light source. The pulses are due to independent events (single electrons emitted by light, thermally emitted electrons, cosmic rays and other noise sources) or to one or more afterpulses which are produced by these events. A detected pulse, irrespective of its origin, will henceforth be referred to as a count. The distribution to be analyzed is the frequency distribution of counts per interval, which has been recorded for a large number of equal time intervals.

Two approaches are developed:

1) **Direct afterpulse analysis.** The afterpulse probabilities are determined "directly" from the observed distribution, with little knowledge of the mechanisms involved. It produces sufficient information to correct count distributions (produced by fluctuating light) for the effect of afterpulsing. However, it gives the probabilities in a form which cannot be directly compared with previously published values.

2) **Afterpulse analysis.** This determines the probability of initial and subsequent afterpulses. These probabilities can be compared with previous measurements, thus allowing a check of the validity of the analysis. However, it requires several assumptions about the mechanism of afterpulsing within the photomultiplier.

Skylight was used in this work as the source of "constant" light. This raises the possibility of error due to contamination, so a method is developed to identify records of skylight in which the light is sufficiently constant.

4.5.3.1 Direct afterpulse analysis

The "direct afterpulse analysis" is based on the assumptions:

a) the light and the noise sources produce a Poisson distribution of detected events.

b) Each event may produce one or more afterpulses, which occur with a probability that is independent of the light level and of previous events.

c) All afterpulses occur in the same sample interval as the initiating event.

Correct operation of the photomultiplier is required in order to meet conditions a) and b). For example, the first is violated if the event rate is so high that there is a significant chance of two pulses occurring close enough together in time to overlap. Both conditions are violated if there is a transient reduction in gain following an event, as occurs if insufficient capacitance is present on the dynodes (as discussed in §3.11.2). To meet condition c), the sampling interval must be very much longer than the time interval between an event and any related afterpulses.

Consider a photomultiplier detecting Poisson-distributed events occurring at a rate r per unit time interval. In the absence of afterpulsing, the probabilities of 0, 1, 2, 3...

counts per interval Δt are

$$e^{-r\Delta t},\ r\Delta t e^{-r\Delta t},\ \frac{1}{2}(r\Delta t)^2 e^{-r\Delta t},\ \frac{1}{6}(r\Delta t)^3 e^{-r\Delta t}...$$

The probability $P_c(0)$ of zero counts is unchanged if afterpulsing occurs (as an afterpulse requires an initiating event) and so is given by

$$P_c(0) = e^{-r\Delta t}\ . \qquad --(4.26)$$

If P_{any} is the probability of any number of afterpulses following a particular event, then the probability $P_c(1)$ of one count per interval is reduced:

$$P_c(1) = e^{-r\Delta t} r\Delta t(1 - P_{any}) = P_c(0) r\Delta t(1 - P_{any})\ . \qquad --(4.27)$$

The probability $P_c(2)$ of two counts is reduced by afterpulses following either count (*ie* it is multiplied by $(1 - P_{any})^2$, the probability that no afterpulses follow either count), and is increased by the probability of one event being followed by a single afterpulse (*ie* $P_c(1)P_1$, where P_1 is the probability of one afterpulse only following an event). Thus

$$P_c(2) = \frac{1}{2} P_c(0)(r\Delta t)^2(1 - P_{any})^2 + P_c(0) r\Delta t P_1\ . \qquad --(4.28)$$

Similarly, the probability $P_c(3)$ of 3 counts is given by

$$P_c(3) = \frac{1}{6} P_c(0)(r\Delta t)^3(1 - P_{any})^3 +$$

$$2 \times \frac{1}{2} P_c(0)(r\Delta t)^2(1 - P_{any}) P_1 + P_c(0) r\Delta t P_2 \qquad --(4.29)$$

where P_2 is the probability of two and only two afterpulses following an event.

Manipulation of these equations allows the event rate r and the probabilities of particular numbers of afterpulses to be deduced from the observed probabilities of 0, 1, 2 and 3 counts:

$$r = -\frac{1}{\Delta t} \ln P_c(0) \qquad --(4.30)$$

$$P_{any} = 1 - \frac{P_c(1)}{P_c(0) r\Delta t} \qquad --(4.31)$$

$$P_1 = \left[\frac{P_c(2)}{P_c(0)} - \frac{1}{2}(r\Delta t)^2(1 - P_{any})^2\right] \frac{1}{r\Delta t} \qquad --(4.32)$$

$$P_2 = \left[\frac{P_c(3)}{P_c(0)} - \frac{1}{6}(r\Delta t)^3(1 - P_{any})^3 - (r\Delta t)^2(1 - P_{any}) P_1\right] \frac{1}{r\Delta t}\ . \qquad --(4.33)$$

Violations of assumption c), that all afterpulses occur in the same sample interval as the events that cause them, can be divided into two categories:

1) the event occurs in one sample interval and an associated afterpulse occurs in a later sample interval.
2) The time interval between an event and an associated afterpulse is less than the dead time interval of the pulse counter. In this case, either the event occurs in the sample interval and the afterpulse is lost in the dead time, or the event occurs in dead time and the afterpulse is then seen in the next sample interval. Reference to §3.11.3 indicates that most afterpulses would be in this category if the counter has a dead time interval of $\sim$1 μs between sample intervals.

While both these violations will produce errors in the calculated probabilities P_1, P_2 and P_{any}, the error for the second category will cancel when these probabilities are used to correct a distribution for the effect of afterpulsing, if that distribution is measured for the same sample interval Δt. This is explained for the two possible cases:

d) the event occurs in the sample interval and the afterpulse is lost in the following dead time interval. The probabilities P_1, P_2 and P_{any} are reduced (as some afterpulses are lost), but this will occur both in the count distributions used to determine the probabilities and in the distributions being corrected.
e) The event occurs in a dead time interval and the afterpulse occurs in the following sample interval. One can regard this as a situation where the sample interval is effectively extended to include part of the dead time. As this extension occurs both in the distribution used to determine afterpulsing and the one to be corrected, the calculated probabilities are modified by the same amount in both cases.

Note that the effective increase in Δt does not have to be known to evaluate P_{any}, P_1, and P_2, as occurrences of $r\Delta t$ in equations 4.31 to 4.33 can be replaced by the measured quantity $-\ln P_c(0)$ (using 4.30).

4.5.3.2 Afterpulse analysis

The approach in the "afterpulse analysis" is to define a model for the different modes of afterpulsing and derive the expected count distribution for this model. Here, the afterpulses are divided into "initial afterpulses" which follow an event (*eg* due to electrons ejected from the photocathode by the impact of a positive ion produced by

ionization of residual gas by a photoelectron), "subsequent" afterpulses which follow a first afterpulse (*eg* due to production of a second positive ion by the electrons ejected by the impact of the first positive ion) and "second subsequent afterpulses" triggered by the subsequent afterpulse. Any further afterpulses, triggered by the second subsequent afterpulses, are neglected, due to their very small probability.

More than one initial or subsequent afterpulse may be produced by the same initiating event, *eg* if a photoelectron has produced a positive ion by collision with a residual gas molecule, it can still produce further initial afterpulses by this or other mechanisms. Similarly, one of the electrons ejected by a positive ion can collide with more than one gas molecule at different times and so produce more than one subsequent afterpulse.

Assuming that the initial afterpulses are independent of each other and distinguishable, the probability of one or more initial afterpulses p' is given by

$$p' = p + p^2 + p^3 ... = \frac{p}{1-p} \qquad --(4.34)$$

where p is the probability of a single initial afterpulse. If an initial afterpulse produces a single subsequent afterpulse with probability P_s, then the probability of it producing one or more subsequent afterpulses P_s' is

$$P_s' = P_s + {P_s}^2 + {P_s}^3 ... = \frac{P_s}{1-P_s} . \qquad --(4.35)$$

Similarly, the probability P_{ss}' of a subsequent afterpulse producing one or more second subsequent afterpulses is related to the probability P_{ss} of it producing a single second subsequent afterpulse by

$${P_{ss}}' = P_{ss} + {P_{ss}}^2 + {P_{ss}}^3 ... = \frac{P_{ss}}{1-P_{ss}} . \qquad --(4.36)$$

In terms of these probabilities equations 4.27 to 4.29 can be rewritten as

$$P_c(1) = P_c(0) r\Delta t (1-p') \qquad --(4.37)$$

$$P_c(2) = \frac{1}{2} P_c(0) (r\Delta t)^2 (1-p')^2 + P_c(0) r\Delta t p (1-{P_s}') \qquad --(4.38)$$

$$P_c(3) = \frac{1}{6} P_c(0) (r\Delta t)^3 (1-p')^3 + 2 \times \frac{1}{2} P_c(0) (r\Delta t)^2 p (1-{P_s}')(1-p') +$$

$$P_c(0) r\Delta t p^2 (1-{P_s}')^2 + P_c(0) r\Delta t p P_s (1-{P_{ss}}') . \qquad --(4.39)$$

Combining 4.34 and 4.37 gives the single initial afterpulse probability p in terms of measurable quantities:

$$p = \frac{p'}{1+p'} \text{ where } p' = 1 - \frac{P_c(1)}{P_c(0) r \Delta t} \,. \qquad --(4.40)$$

Similarly the single first and second subsequent afterpulse probabilities are:

$$P_s = \frac{P_s'}{1+P_s'} \text{ where } P_s' = 1 - \frac{P_c(2)}{P_c(0) r \Delta t p} + \frac{1}{2p} r \Delta t (1-p')^2 \qquad --(4.41)$$

and $$P_{ss} = \frac{P_{ss}'}{1+P_{ss}'} \text{ where } P_{ss}' = 1 - \frac{P_c(3)}{P_c(0) r \Delta t p P_s} +$$

$$\frac{(r\Delta t)^2 (1-p')^3}{6pP_s} + \frac{r\Delta t (1-P_s')(1-p')}{P_s} + \frac{p(1-P_s')^2}{P_s}. \qquad --(4.42)$$

4.5.3.3 Testing for constant light

The methods outlined above to determine photomultiplier-afterpulse probabilities require a light source of constant intensity. In this work the "constant" light source is skylight, contaminated by a small component of artificial light fluctuating at 100 Hz. The possibility exists that the skylight fluctuated occasionally (over the 2.8 s in which the count distribution was collected) due to unnoticed smoke, cirrus cloud, birds, insects, etc. Therefore a method is required to determine that the light is sufficiently constant over the recording interval.

If the same light source is observed with two detectors, it is possible to determine whether the intensity is constant over the total observation interval if the joint probability distribution P_j is recorded, where $P_j(n_1, n_2)$ is the probability of n_1 pulses on one detector and n_2 pulses on the other. If the intensity of the light source is constant, then the pulses will be uncorrelated between the two detectors and

$$P_j(j,k) = P_{c1}(j) P_{c2}(k) \qquad --(4.43)$$

where $P_{ci}(n)$ is the measured probability of n pulses for detector i. If the light source fluctuates, then the occurrence of n pulses on both detectors will be correlated and equation 4.43 will not be obeyed.

In §6.3, where the probability of afterpulsing is deduced from records of skylight, the analysis is applied only to records for which condition 4.43 is satisfied to within a small discrepancy.

4.5.4 Correction for afterpulsing

A method is developed in this section to remove the effect of afterpulsing from a photomultiplier count distribution. This correction is required so that the methods developed in §4.5.1 can be applied to evaluate the normalized moments of stellar scintillation. The method of correction is designed to use the afterpulse probabilities determined by the *direct afterpulse analysis* (rather than those of the *afterpulse analysis*) because it is based on fewer assumptions and (as discussed in §4.5.3.1) the effect of events or afterpulses occurring in the dead time of the pulse counter is incorporated in the afterpulse probabilities.

The aim is to predict the actual distribution of events $E(i)$ from the observed distribution $O(i)$ of counts, where $E(i) = m$ specifies m occurrences of i events per interval, for $i = 0, 1, ..., i_x$ and i_x is the maximum number of events that can occur. $O(i)$ is defined similarly. The approach is to correct, in turn, the observed number of occurrences for one count per interval, then two counts per interval and so on.

$E(0) = O(0)$ as no afterpulses can occur if there are no events. (Any afterpulses which occur in a sample interval due to an event in the previous dead time interval are equivalent to events in an extension of the sample interval, as described in §4.5.3.1, case "e".) As one count in an interval can only occur if one event, unaffected by afterpulsing, is present,

$$O(1) = E(1)P_a(1,0)$$

where $P_a(n,m)$ is the probability that m afterpulses occur in an interval with n events. Thus the number of occurrences of one event can be derived from the observed distribution of counts using

$$E(1) = \frac{O(1)}{P_a(1,0)} \qquad --(4.44)$$

The number of occurrences of two events $E(2)$ can then be determined by first subtracting the predicted number of single events followed by a single afterpulse $E(1)P_a(1,1)$ from the observed number of occurrences of two counts $O(2)$, and then correcting this for the reduction due to afterpulsing, *ie*

$$E(2) = \frac{O(2) - E(1)P_a(1,1)}{P_a(2,0).} \qquad --(4.45)$$

This procedure can be generalized to

$$E(i) = \frac{O(i) - \sum_{j=1}^{i-1} E(j)P_a(j, i-j)}{P_a(i,0).} \qquad --(4.46)$$

To reduce the accumulation of rounding errors, the values of E are not converted to integers until the calculation is complete.

Due to statistical variation, application of equation 4.46 can fail at large values of i, where an unphysical negative value for E may occur and subsequent application of 4.46 produces increasingly large positive and negative values. The following procedure is used to avoid this problem: for each value of i in the application of 4.46, the current result for E (ie $E(k)$ for $k = 1, 2, ..., i$) is transformed to a prediction O' of the observed distribution by restoring the effect of afterpulsing, using

$$O'(i) = E(i) - \sum_{j=i+1}^{i_x} E(i)P_a(i, j-i) + \sum_{j=1}^{i-1} E(j)P_a(j, i-j)\ . \qquad --(4.47)$$

As O' is calculated with some values of E missing, it is expected that

$$\sum_{j=1}^{i_x} O'(j) < \sum_{j=1}^{i_x} O(j) \qquad \text{for } i < i_x\ . \qquad --(4.48)$$

If this condition is violated, the value of $E(i)$ is reduced so that the condition holds.

The probability $P_a(n, m)$ of m afterpulses following n events (required in equations 4.46 and 4.47) can be calculated from the afterpulse probabilities P_1, P_2 and P_{any} determined by methods in §4.5.3.1. If only single afterpulses occur, then the probability of m afterpulses following n events is given by

$$P_a(n, m) = C_m^n {P_1}^m (1 - P_1)^{n-m} \qquad \text{where } C_m^n = \frac{n!}{(n-m)!m!}\ .$$

Extending this to single, double and triple afterpulses,

$$P_a(n, m) = \sum_{\{m_1, m_2, m_3 : m_1 + 2m_2 + 3m_3 = m\}} \Big\{ C_{m_1}^n {P_1}^{m_1} \times$$

$$C_{m_2}^{n-m_1} {P_2}^{m_2} C_{m_3}^{n-m_1-m_2} {P_3}^{m_3} (1 - P_1 - P_2 - P_3)^{n-m_1-m_2-m_3} \Big\} \qquad --(4.49)$$

where m_1, m_2 and m_3 are the numbers of single, double and triple afterpulses contributing to the total m (ie $m = m_1 + 2m_2 + 3m_3$). As occurrences of more than three afterpulses for one event are neglected, $P_3 = P_{any} - P_1 - P_2$.

For large values of n (such as 255, the maximum in this work), equation 4.49 would take too long to compute. In practice many combinations can be ignored: if the probability for a particular combination of m_1, m_2 and m_3 is very small, all combinations of two of these numbers with a higher value of the third can be neglected, as the probability would be even smaller. Further efficiency is obtained by producing a table of values of $P_a(n,m)$ and consulting it during the evaluation of equations 4.46 and 4.47. The use of a table avoids the problem of finding values of m_1, m_2 and m_3 which satisfy the condition $m_1 + 2m_2 + 3m_3 = m$. All combinations are considered and the contribution of those which meet the condition is added to the appropriate element of the table.

4.5.5 Correction for dead time

After the detection of an event, a photomultiplier-amplifier combination has a "dead time" in which subsequent events are not detected. The probability of losing a subsequent event in dead time increases with count rate, altering the moments of a count distribution. Thus a method is required to restore "lost" events to an observed distribution. A previous approach to this problem (Mandel, 1980) requires measurements of the frequency distribution of events in several sampling intervals ranging from Δt to $\Delta t + i_x \Delta t_d$, where Δt_d is the dead time. As such measurements are not available here, a different approach is now developed.

If, for an average rate r and a dead time Δt_d, n counts occur in an interval Δt, the total dead time is $n\Delta t_d$ and so the probability p_l of l lost counts in the interval is

$$p_l(n,l) = \frac{e^{-rn\Delta t_d}(rn\Delta t_d)^l}{l!} . \qquad --(4.50)$$

If the observed light is fluctuating, the instantaneous value of r is not known, but an approximate value r_a can be determined from the number of counts in each interval, *ie*

$$r_a = \frac{n}{\Delta t - n\Delta t_d} . \qquad --(4.51)$$

An approximation to the original distribution of events E can therefore be deduced from an observed distribution O, using

$$E(k) = O(k)p_l(k,0) + \sum_{i=1}^{k-1} O(k-i)p_l(k-i,i) . \qquad --(4.52)$$

Chapter 5 Equipment and methods

This chapter describes equipment and methods used for a laboratory investigation of multiple-beam remote sensing and for observations of stellar scintillation. A detailed description of the equipment is given if it is required for interpretation of the observations, or if it is considered to be helpful to others making similar observations. In cases where the equipment (*eg* that for data logging) has been made obsolete by technical developments, only a cursory description is given.

5.1 A laboratory multiple-beam experiment

This was actually a "corridor" experiment, in which a crossed-laser-beam system was set up over a 40-m path along the 4th-floor corridor of the Oliphant Building at the University of Adelaide. It was conducted at weekends, with both warning signs and physical barriers to prevent anyone looking at the laser sources and damaging their eyesight.

A top view of this system is represented in figure 5-1. Two laser beams were set up so that they intersected about halfway along the 40-m path. Four detectors, two in each beam, were used to observe the scintillation produced in the laser beams by one or two turbulent streams moving perpendicular to the beams in the crossover region. As indicated by the lines drawn from the lasers to the detectors, the system is effectively a four-beam system, allowing a test of the three-beam system suggested earlier in §4.1.3 and its extension to four beams.

5.1.1 Equipment

As the equipment had to be set up each time it was used, the tiles on the corridor floor were numbered and measured. This allowed positions on the 40-m path to be recorded quickly during observations, as a tile number and an offset distance.

Two Helium-Neon lasers (with continuous outputs of 3 and 5 mW at 632.8 nm) were used. Turbulent streams were produced by household hair driers, run with the heating elements on. Cardboard tubes containing obstacles were added to constrict the airflow. This presumably increased the turbulence, as it had the effect of increasing the strength of the scintillation. The turbulent streams were about 3 cm wide.

The detectors were 10-mm x 4-mm photovoltaic cells, each placed behind a 14-mm

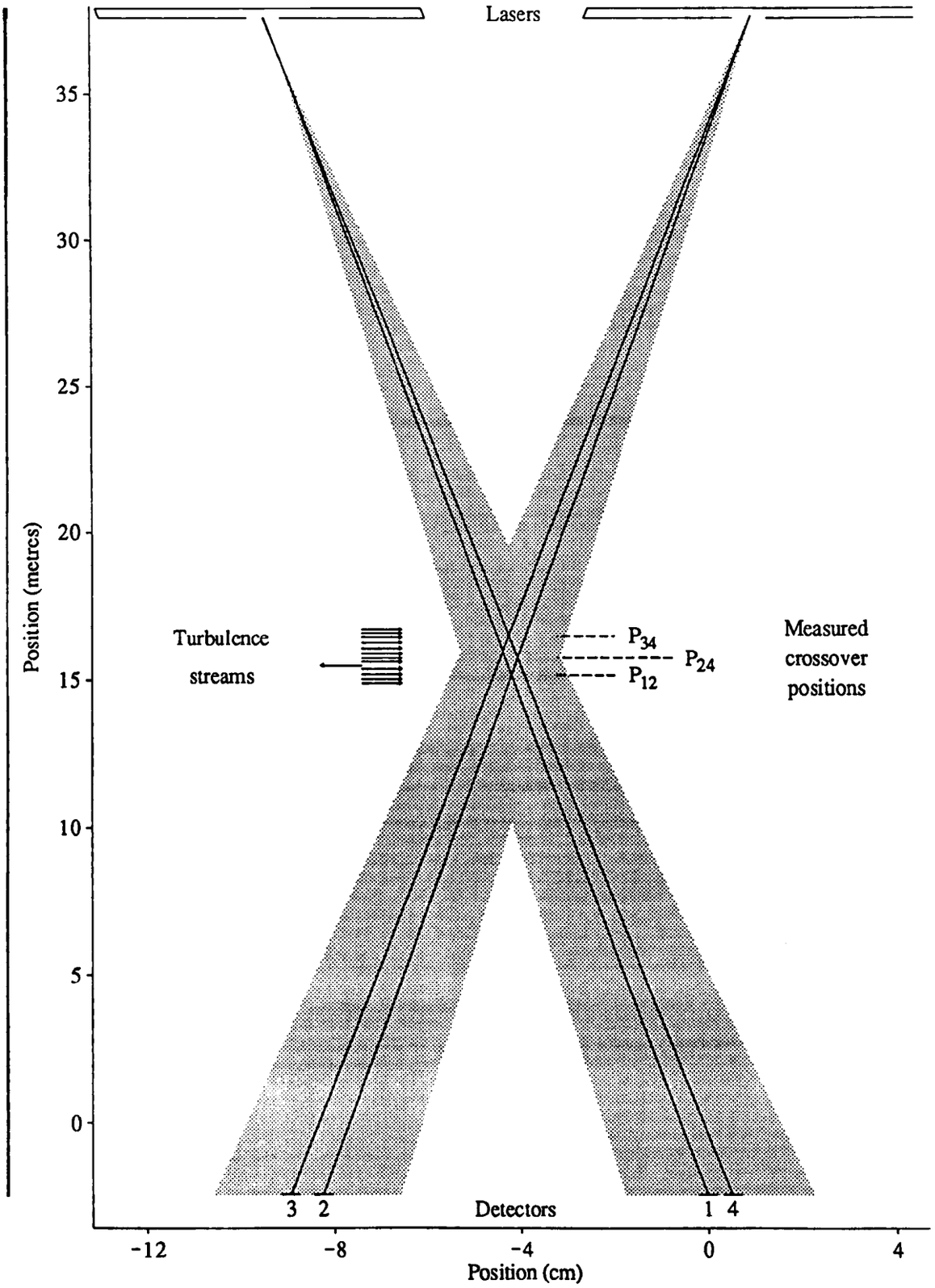

Figure 5-1 A schematic of the geometry of the crossed laser beam experiment (run 1). The shaded region indicates two laser beams which cross over and then illuminate four detectors. An aperture mask (not shown) reduces the width of the detectors, effectively creating the four narrow beams indicated by the lines. The beam geometry is determined from the transverse positions of the detectors and the distance from the detector plane of the crossover positions P_{12}, P_{24} and P_{34}. Note that the transverse dimension is highly enlarged compared to distance along the beam. To emphasize this, the lasers and beams are redrawn with the correct aspect ratio on the far left.

x 0.5-mm clear rectangle in a negative produced with standard printed-circuit-board facilities. Figure 5-2a shows the arrangement of these detectors and the direction which is defined as positive for the measurements. Slit detectors were used, rather than point detectors, as the turbulent irregularities were presumed to follow irregular paths rather than straight lines.

The fluctuating component of the light intensity was converted to a voltage fluctuation using the circuit in figure 5-2b. The photovoltaic cell produces a current proportional to the light intensity, if the load resistance is sufficiently low (Witherell and Faulhaber, 1970). A simple RC filter removes the DC component. A 741 operational amplifier, operated as a current-to-voltage converter, produces a voltage proportional to the fluctuating component of the current. This voltage is then further amplified by the circuit in figure 5-2c, to produce a signal that varies over the full ± 5 V range of a 5357 A/D (analogue-to-digital) converter.

The input of the converter was switched sequentially between the four channels by a CMOS CD4051 analogue multiplexer. The A/D converter requires 50 μs to settle to the correct value, thus the four channels were sampled over a 200-μs interval. The converter produces a digital value between 0 and 63. These digital values were written to 7-track computer tape using a Kennedy 1600 Incremental recorder. This operation was controlled by a data logger which stored 4096 data values into a memory at the 20 kHz sampling rate and then controlled the transfer of this information to the Kennedy recorder at its 300-Hz limit. This circuit no longer exists, as it was upgraded into a more sophisticated "Analogue Digitizer", used later in stellar scintillation observations.

5.1.2 Methods of observation

The results of two measurement runs, referred to as "crossed-laser run 1" and "crossed-laser run 2", are analyzed in this thesis. In the first run the two turbulent streams were moving in opposite directions, while they were moving in the same direction for run 2.

The lasers were aimed so that the two detectors within each beam were evenly illuminated. Three crossover positions (marked P_{12}, P_{24} and P_{34} in figure 5-1) were measured by moving a straight edge within the crossover region until corresponding parts of the fringe pattern coincided with the two appropriate detectors. The positions

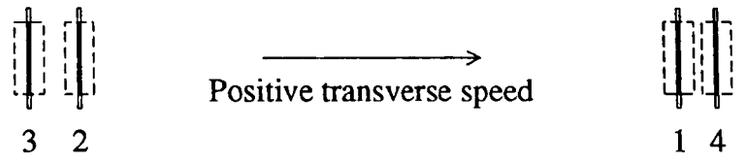

Figure 5-2a The layout of the detectors for the crossed laser observations. Narrow apertures (solid outline) in front of 10 mm × 4 mm photovoltaic cells (dashed outline) produce 10 mm × 0.5 mm detectors (solid fill). These are labelled with the channel numbers 1-4. The arrow shows the direction defined as positive for the transverse speed of scintillation patterns moving across the detectors.

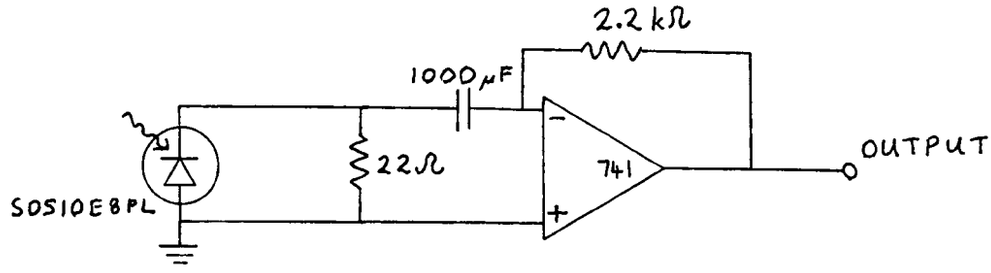

Figure 5-2b A circuit diagram of the "detector-amplifier" circuit. The photodiode produces a current proportional to the light level. The high frequency component of this current is passed to the negative input of the operational amplifier. The amplifier produces an output voltage proportional to this current.

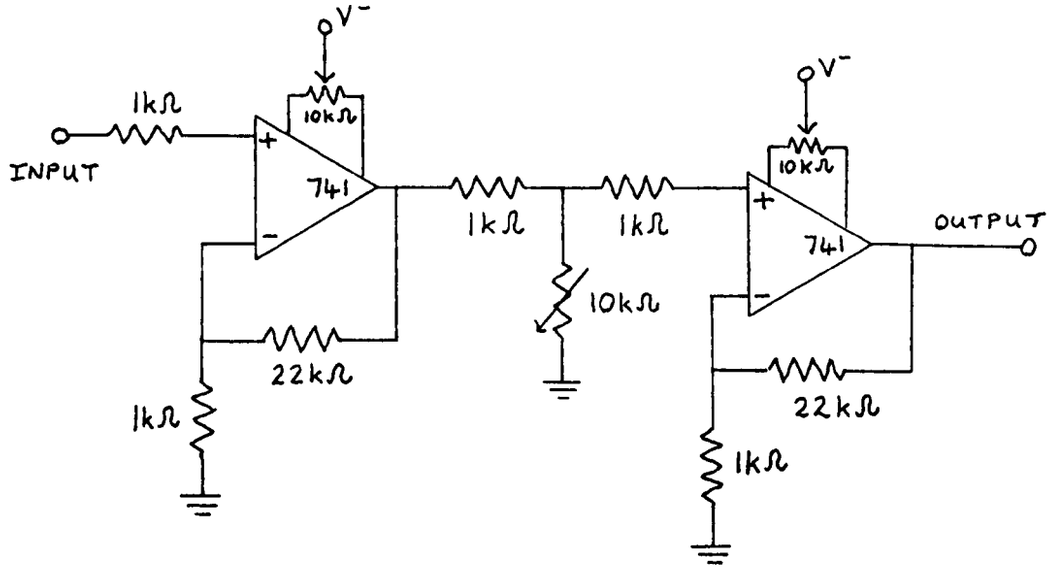

Figure 5-2c A circuit diagram of the voltage amplifier used to amplify the output of the "detector-amplifier" above. It has a maximum gain of ~ 440.

of the detectors were measured directly. The positions of the light sources were calculated from the crossover and detector positions, based on the assumption that the beam emanates from a point source.

Throughout each run, one turbulent stream was kept at a fixed position and the other was moved to a number of different positions (shown by arrows in the crossover region in figure 5-1 for run 1). Measurements were taken of the scintillation produced by each turbulent stream on its own and by each combination of two streams present simultaneously.

About twenty 0.2-s data records were taken for each situation. Between each such set of twenty records, a calibration record was made by illuminating the detectors with a fluorescent light and recording the 100-Hz signal. (The mains supply has a frequency of 50 Hz, so that two current maxima per cycle produce a 100-Hz fluctuation in AC lighting.) This calibration record provided a recognizable boundary between data for different situations, ensuring that the electronically recorded data could be reliably matched to a handwritten record of the experimental situation.

The results of these observations are presented and discussed in chapter 7.

5.2 Observation of stellar scintillation

5.2.1 Stellar sources and observing site

Observations were made of the stars Sirius, Canopus, α Crucis, β Crucis, α Centauri and β Centauri. The positions of these in the Southern sky at Adelaide's latitude are shown in figure 5-3. Most of these are double stars, with parameters as listed below.

Table 5-1a Parameters of double stars.

Star	Year	Position angle	Separation	Source
α Crucis	1972	114.09°	4.260″	Van Albada-Van Dien (1983)
α Crucis	1974	114.01°	4.216″	Van Albada-Van Dien (1983)
α Crucis	1985	113°	4″	H. M. Naut. Almanac Off., 1984
α Centauri	1985	211°	21″	H. M. Naut. Almanac Off., 1984
β Centauri			1.2″	Illingworth (1979)
Sirius	1985	40°	6″	Huffer *et al* (1967)

Sirius and β Centauri are not useful as sources for the remote-sensing methods described in chapter 4 because one star is much fainter than the other, as is shown by

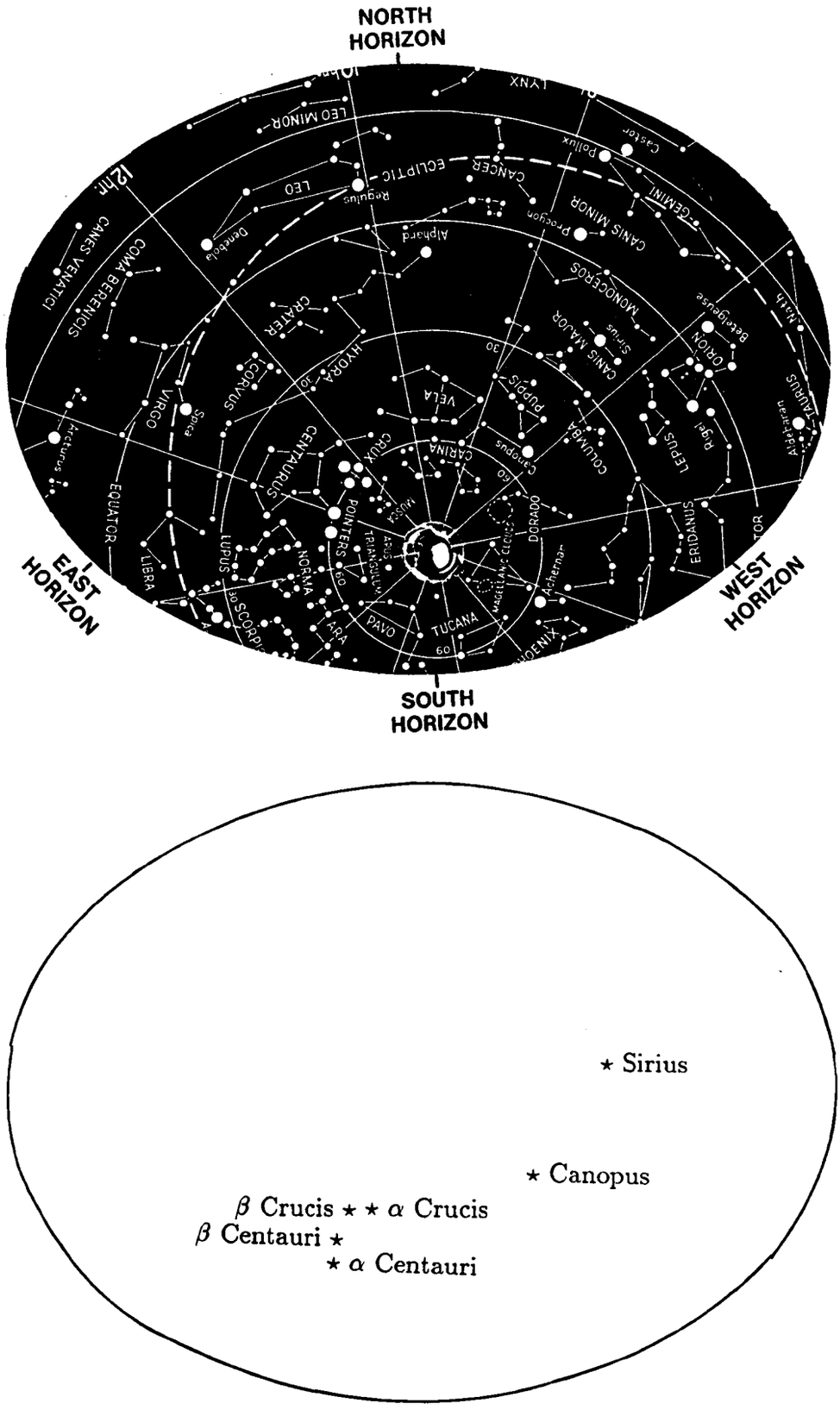

Figure 5-3 At the top is a view of the Southern sky for latitude 35° South, which includes all the stars used in this work. The lower diagram identifies these particular stars.

the magnitudes in table 5-1b below (*eg* the primary of β Centauri is 22 times brighter than the secondary star).

Table 5-1b Parameters of individual stars.

Star	Year	Right ascension	Declination	Magnitude	Spectral type	Source
α Crucis[1]	1975	$12^h25.2'$	$-63°00'$	1.6	B1 iv	Illingworth, 1979
α Crucis[2]	1975			2.1	B3	Illingworth, 1979
β Crucis	1975	$12^h46.2'$	$-59°33'$	1.29	B0.5 iv	Illingworth, 1979
α Centauri[1]	1975	$14^h38.0'$	$-60°44'$	0.0	G2 v	Illingworth, 1979
α Centauri[2]	1975			1.38	K5 v	Illingworth, 1979
β Centauri[1]	1975	$14^h02.1'$	$-60°15'$	0.63	B1 iii	Illingworth, 1979
β Centauri[2]	1950	$14^h00.3'$	$-60°08'$	4.	?	Huffer *et al*, 1967
Sirius[1]	1975	$6^h44.0'$	$-16°41'$	-1.46	A1 v	Illingworth, 1979
Sirius[2]	1975			8.67	wdA5	Illingworth, 1979
Canopus	1975	$6^h23.6'$	$-52°41'$	-0.72	F0 ib	Illingworth, 1979

From the above tables, it can be seen that α Crucis is the best double star for this work, as its two components are similar in both brightness and spectral type. The wider separation of α Centauri makes it potentially useful for observing scintillation produced at lower altitudes, where the patterns for α Crucis may overlap, but its brightness ratio of 3.6 makes it difficult to detect the fainter pattern. Sirius and Canopus are useful for observing the characteristics of the scintillation pattern for a single star, particularly Sirius, which is bright and passes close to the zenith. β Crucis and β Centauri are useful as single stars which are relatively close to α Crucis and α Centauri, allowing a comparison of the single and double star scintillation patterns. The listed values of the right ascension and declination allow the elevation and azimuth of the stars to be predicted for any time (H. M. Nautical Almanac Office, 1961).

Observations were made from the "Moonwatch platform" of the Physics Building at the University of Adelaide. Although subject to scattered street lighting and scattering by urban pollutants, this site had the advantage that observations could be set up on occasions when other commitments would have precluded travel to a remote site, as well as saving the time and money involved in such travel. In practice, scattered full moonlight was more detrimental to the observations than the scattered street lighting.

Figure 5-4 shows the location of the observing site relative to several relevant features, such as the Central Business District of Adelaide, the local launch site of

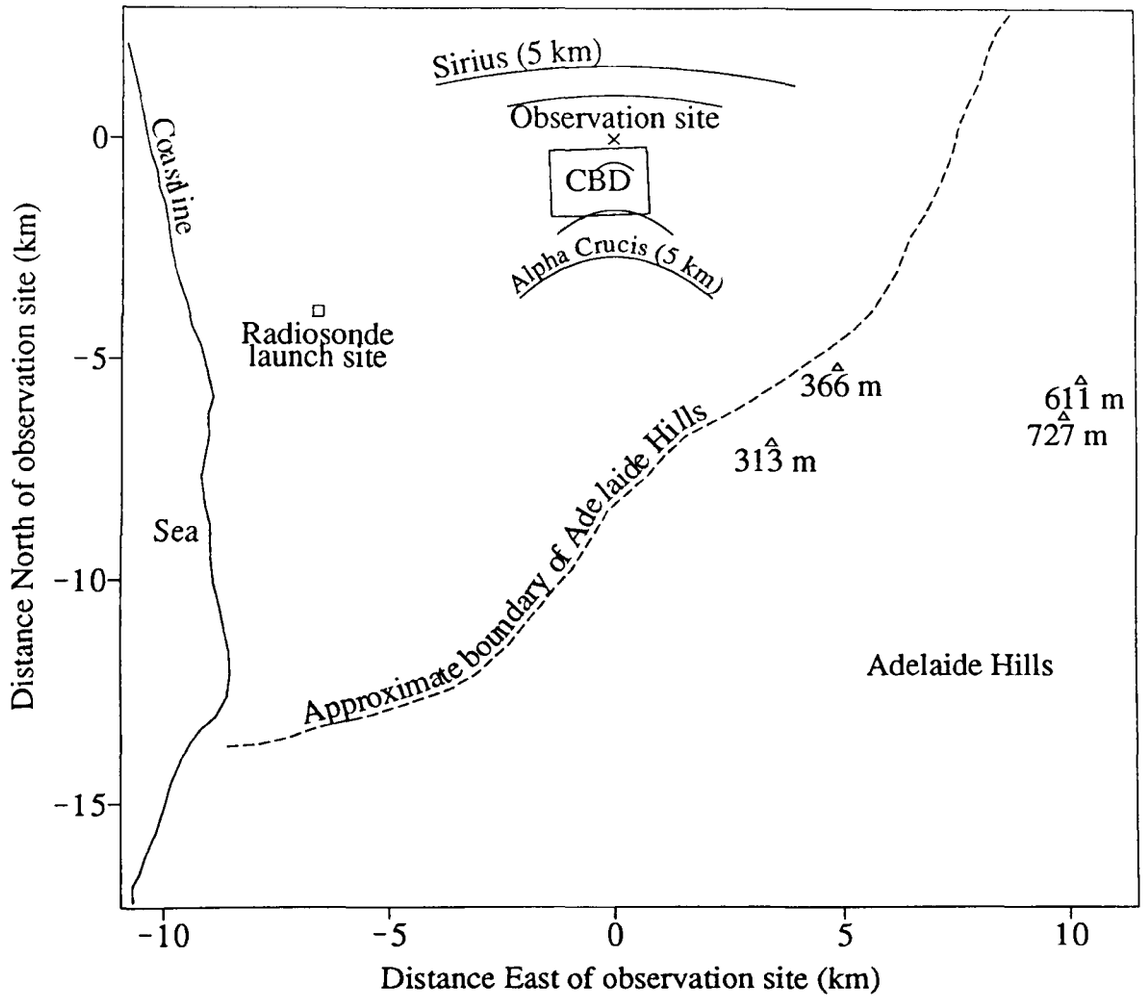

Figure 5-4 A map showing the location of some relevant features relative to the observation site (×) at the University of Adelaide. Just to the south is the Central Business District (CBD) of Adelaide. The launch site for radiosondes (□) is at Adelaide airport, about 8 kilometres to the west south west. The observation site is surrounded by relatively flat land, with the Adelaide Hills rising steeply at the boundary indicated by the dashed line. The hills tend to be elongated along the SW-NE direction, parallel to the boundary. Four high points are indicated (△), along with their height in metres. The two curved lines north of the observation site indicate the intersection of the line of sight to Sirius with horizontal planes at altitudes of 3 and 5 km. This intersection is also shown for Alpha Crucis for 1, 3 and 5 km. Only a portion of each curve is plotted, indicating the intersection when the star is at an elevation of more than 50°.

meteorological balloons and the hills to the southeast. The intersection of the line of sight to Sirius with horizontal planes at altitudes of 3 and 5 km is shown for elevation angles greater than 50°. This intersection is also shown for altitudes of 1, 3 and 5 km for α Crucis, indicating that any scintillation for this star produced by turbulence below 3 km originates above the Central Business District.

The prevailing ground-level wind in Adelaide is from the southwest, off the sea. Winds from any other direction occur with lower probability. Wind from the east-to-south quadrant tends to be associated with cloud. In summer, however, it is common to have a southeasterly wind at night and clear conditions. This creates the opportunity to look for scintillation produced by orographic turbulence, when the observing site is downwind of the hills. In winter, clear weather is uncommon but when it occurs it is often associated with calm conditions at ground level, allowing the contribution from higher altitudes to dominate the scintillation pattern.

5.2.2 Light collectors

Two light collectors, a "split-lens" telescope and a "multiple collimator", were built for this work, implementing the principles described in §4.1.4. The split-lens system produces two telescopes side by side, with apertures which can separated by a distance much smaller than the lens diameter. The focussing ability of the lens pieces is used to restrict light collection to that from one bright star (or double star). The "multiple collimator" has a series of closely spaced parallel light paths, allowing the intensity of the scintillation pattern to be sampled at many different separations. The light collected is restricted to that of one bright star by the small field of view through any of the light paths.

The *"split-lens" telescope.* This instrument, shown in cross section in figure 5-5, has a plastic 25-cm Fresnel lens divided into two pieces (using a hacksaw), with these two halves shifted apart by 1.8 cm to produce two separated focal points. Two metal tubes are positioned so that two optical cables can be inserted with their faces at these focal points. A stiff cardboard sheet containing the desired apertures is inserted just in front of the lens. This is labelled "aperture plane mask" and shows the cross section of two parallel 3-mm slits, separated by 2.4 cm, which implements the double slit detector drawn earlier in figure 4-7. Using the mounting shown in the figure, the

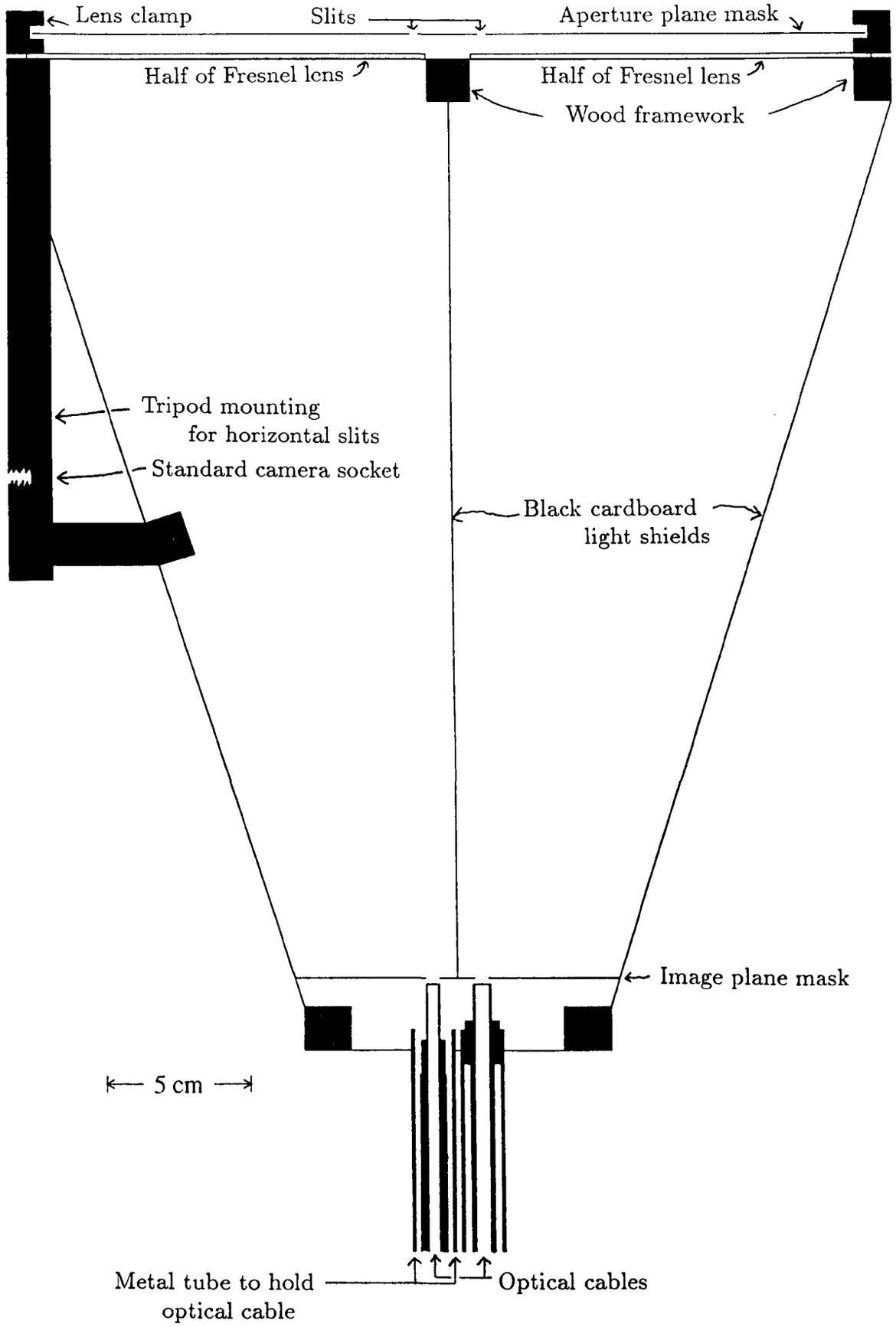

Figure 5-5 A horizontal cross section of the split lens telescope, when used with a mask containing two vertical slits. Light enters through the two slits in the aperture plane mask and is focussed by the two halves of the Fresnel lens to images within the aperture stops in the image plane. The light is then collected by two optical cables which transfer it to photomultipliers. The tripod mounting on the left allows the telescope to be used with horizontal slits. A similar mounting underneath is used when, as illustrated here, the slits are vertical.

slits are horizontal. Another mounting on an adjacent side of the telescope allows them to be vertical. A shell of black cardboard between the struts of the wooden framework keeps out unwanted light.

The instrument is mounted on a standard 35-mm camera tripod. This works well for low elevations, but at high elevations the telescope's weight and bulk makes it difficult to point it in the desired direction. The use of a mount that does not track the star has three disadvantages:

a) the instrument has to be realigned on the star at regular intervals (every 3 min in this work).

b) The aperture in the image plane must be sufficiently large that the image is not lost over the interval of observation. The unwanted signal due to skylight is proportional to the square of the aperture diameter.

c) As the star moves across the detector, the measured intensity will be modified by spatial variations in the efficiency of the detector.

The advantages are that the equipment is cheap and portable.

The size of the fluctuations caused by c) is not known. It is presumed to be mitigated by the poor optical quality of the Fresnel lens, as this increases the size of the image of the star relative to an astronomical quality lens. Such fluctuations are also expected due to spatial variations in the sensitivity of the light detector at the other end of the optical cable. During observations, these fluctuations were found to be insignificant:

i) on some nights the observed scintillation was very low compared to others. As the fluctuations described above should occur on any night, it is thus very small compared to the stellar scintillation on a normal night.

ii) A test to be reported in §6.8 shows no evidence for this fluctuation.

Front and rear photographs of the "split-lens" telescope are copied in figure 5-6. The front view shows the two halves of the Fresnel lens, made visible by multiple reflected images. The aperture plane mask containing two 50-mm × 3-mm slits, separated by 24 mm, is shown partly inserted.

The rear view shows two small circles in the centre, these being aperture stops in the image plane. These are coincident with the ends of the optical cables (when these

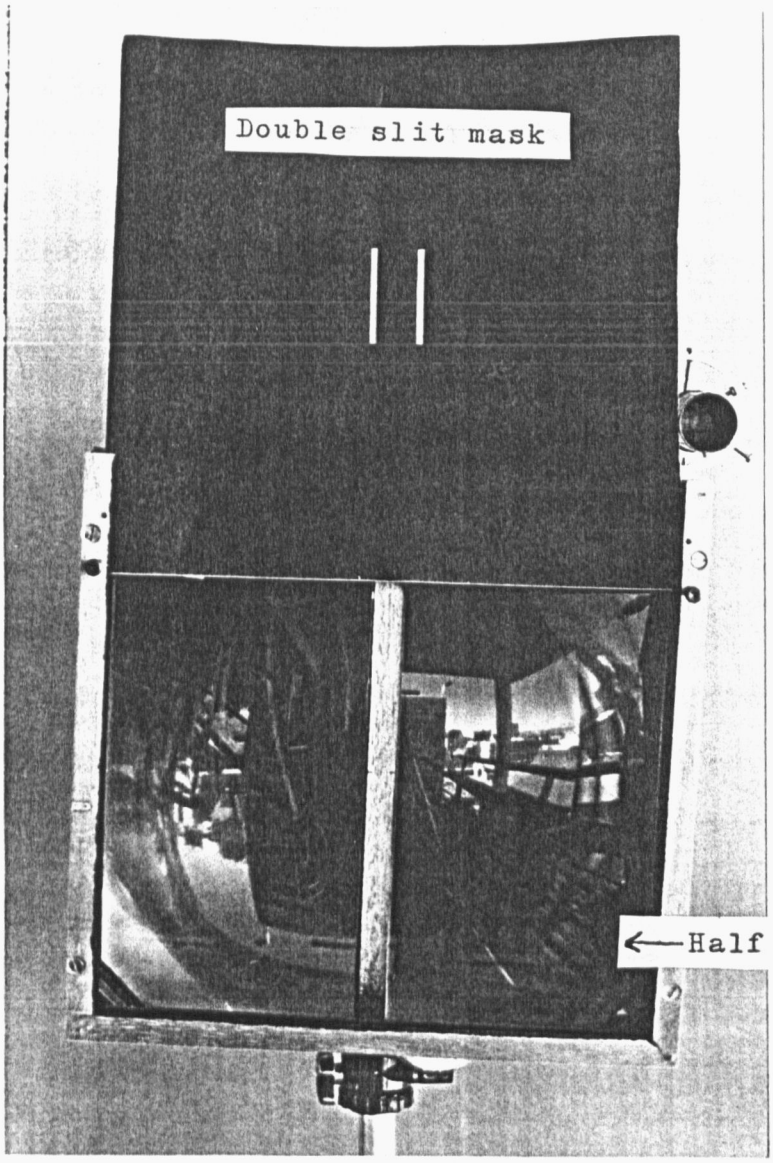

Figure 5-6
Front and rear views of the split lens telescope. On the left, the front view shows the Fresnel lens split into two parts. The double slit mask is partially inserted. A rear view below shows the two focal plane aperture stops. In the background of this picture the location of the starlight observations (the "Moonwatch platform") and the Adelaide Hills are identified.

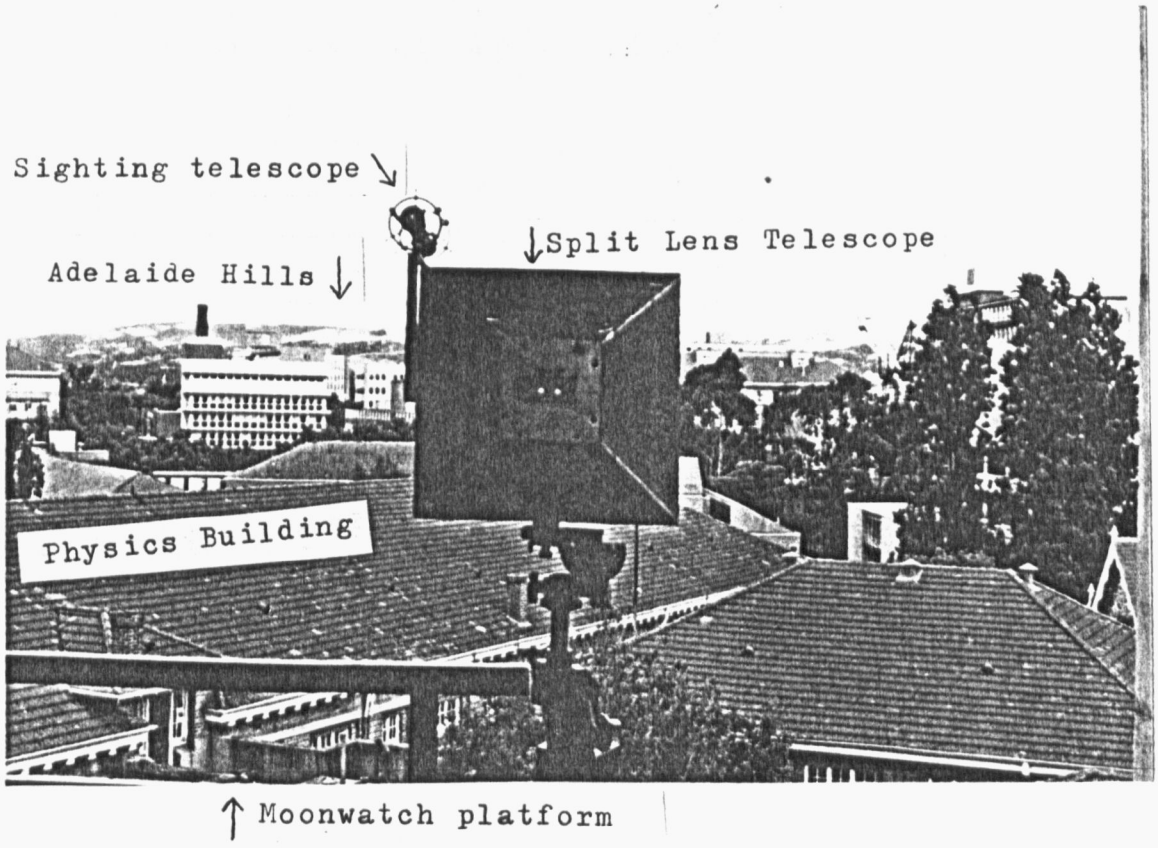

are inserted) and are required to align the two halves of the lens so that the image of the star is on both cables at the same time. This alignment is made in the circumstances shown in the picture, with the instrument pointed towards distant scenery. The images can be seen by focussing one's eyes on the image-plane apertures. One lens section is then moved until the images are the same in both apertures. The sighting telescope on the top left of the instrument is a standard astronomical sighting scope. This picture also shows the observing site (on the "Moonwatch platform") and part of the Adelaide Hills in the background.

The *"multiple collimator"*, shown in cross section in figure 5-7, has nine aluminium baffles, each of which has twenty 4.8-mm holes at 1-cm intervals along a line. These baffles are positioned so that there is only one line of sight through the instrument, perpendicular to the baffles. To cut down reflection of light from other directions the edges of the holes are bevelled and the interior is coated with matt black paint. Two optical cables, inserted at the back of the box, detect light arriving only within an angle of $\sim 2°$. The separation of these cables can be varied from 1.1 to 19.1 cm in steps of 1.0 cm by moving the cable on the left. Note that the right-hand cable is slightly wider and only fits in the right-hand aperture, so the cables cannot be mixed up during connection. This wider cable is designated channel 1 and the other channel 2.

The "multiple collimator" is also mounted on a non-tracking camera tripod. As the star moves away from the centre of the field of view, the area of the optical cable illuminated by the star decreases, effectively reducing the size of the aperture. For channel 1, where the holes and the optical cable are both 4.8 mm in diameter, this reduction occurs unless the "multiple collimator" is exactly aligned on the star. The diameter of the optical cable for channel 2 is only 4 mm, so it can still be fully illuminated when the star is slightly away from the centre of the field of view. The instrument was realigned on the star every 3 min so that the reduction was not significant on either channel. An advantage of this instrument, compared to an imaging system, is that the starlight is uniformly spread over the face of the optical cable, so that the effect of spatial variation in the efficiency of the optical cable or the light detector will be much smaller than for the "split-lens" telescope (as described in case "c" above).

An attachment to reduce the size of the apertures of the "multiple collimator"

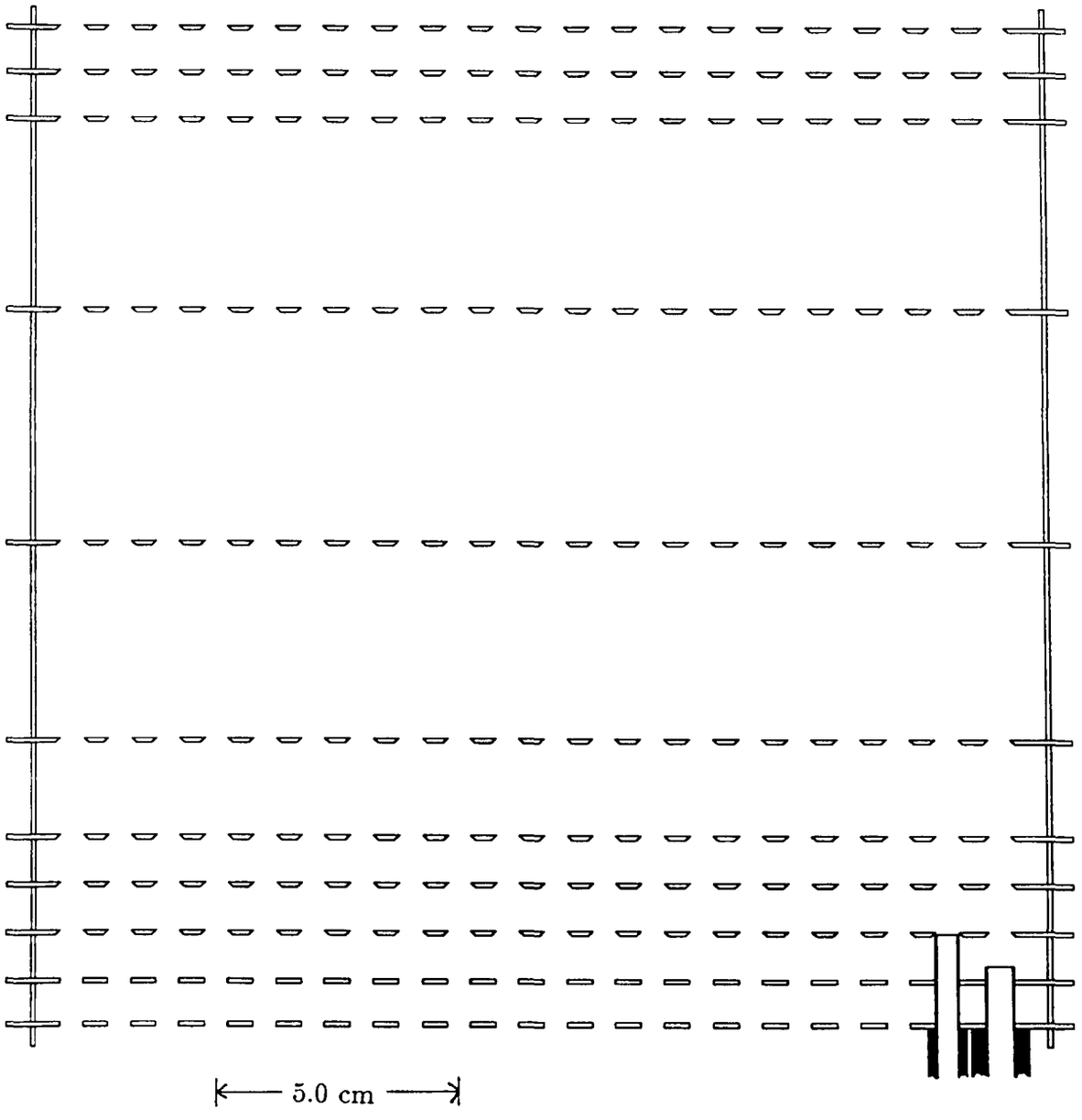

Figure 5-7 A cross section of the "multiple collimator". Nine aluminium baffles restrict the field of view of the optical cables (bottom right) to a small angle around the vertical direction in the diagram. The optical cables are positioned by insertion into the two baffles at the bottom. The cables are shown at the minimum spacing of 1.1 cm. This spacing is varied (to 2.1 cm, 3.1cm,...,19.1 cm) by moving the optical cable on the left to the other available positions.

consists of a stiff cardboard strip, containing twenty 2-mm (inside diameter) washers, which can be put on the front of the instrument. For these 2-mm apertures, the star can move further from the centre of the field of view (relative to the situation with the 4.8-mm holes) without any of the light that passes through the front aperture being lost.

Photographs of the "multiple collimator" are reproduced in figure 5-8, showing front and rear views of it, mounted on a tripod. The platform of the tripod can be rotated through 90°, allowing the two detectors to be moved within a quadrant in the plane perpendicular to the line of sight. A mounted protractor allows the tilt angle to be measured.

The sighting scope is a commercial rifle sight, which is roughly aligned with the lines of apertures by adjustment of a crude mounting. A fine adjustment is then performed using adjusting screws on the rifle sight that move its image. To make this adjustment at night, the "multiple collimator" is pointed towards a distant light (~50 m away) which is bright enough to produce a visible shadow. With the "multiple collimator" positioned so that the light passes through, the rifle sight is adjusted to put the image of the light source in the centre.

During observations it is desirable to transfer the movable optical cable quickly from one aperture to the next. It is necessary to keep the end of the cable shaded from surrounding lights during this transfer, to avoid high illumination of the photomultiplier. These operations are facilitated by a cardboard strip which is mounted on the back of the "multiple collimator" and has two long flaps which can be raised up above and below the line of apertures. These flaps provide a guide in which the cable can be slid along the surface between the apertures. This surface is covered with smooth black cardboard to reduce wear of the optical cable surface. After more than 50000 such transfers the end of the optical cable shows some wear.

The optical cables (used with both the "multiple collimator" and the "split-lens" telescope), are 4-ft long flexible light guides, each consisting of a bundle of glass fibres. The bundle of fibres is sheathed in PVC, except at the ends, where metal is used. The bundle diameter is 4.8 mm ($\frac{3}{16}$ inch) for the wider cable and 4 mm for the narrower one. The packing of the fibres is partly coherent, in that an image transferred along

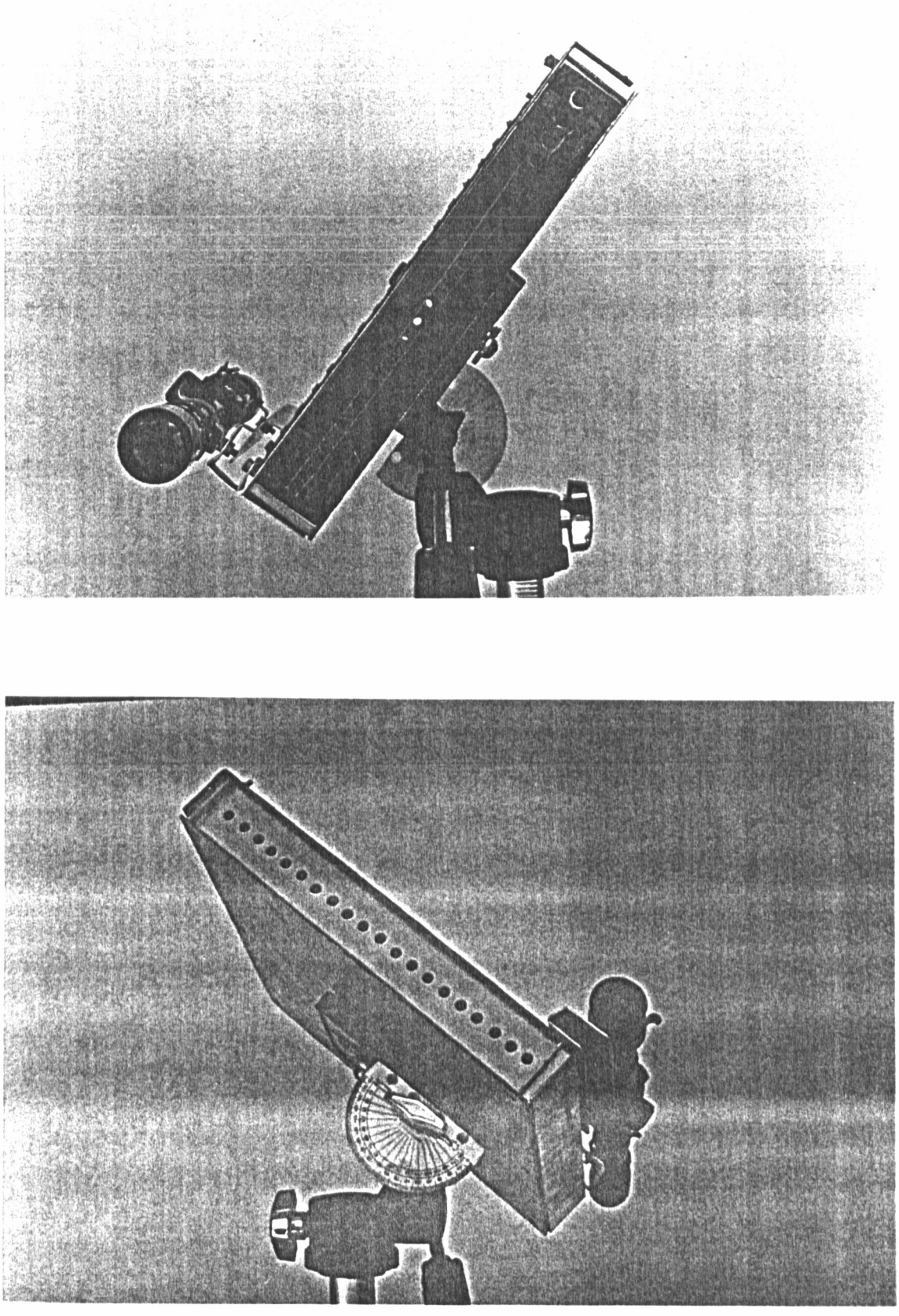

Figure 5-8 Two views of the "multiple collimator" used for observations of starlight. The upper picture shows the rear of the instrument, where the optical cables are inserted. Light can be seen through three of the passages, illustrating the small field of view. The lower picture shows the front of the instrument and also the mounted protractor which facilitates the setting of the angle between the line through the front apertures and the vertical.

the cable is split into sections but parts of it are still recognizable. The wider cable was manufactured by Electro Fiberoptics. The origin of the other is not certain, due to changes in product lines by the distributors.

5.2.3 Light detection

The starlight is detected by EMI photomultiplier tubes, type 9789B. This type is designed for astronomical applications and has a high gain, with typically 4 $\times 10^7$ electrons produced at the anode for a single photoelectron ejected from the photocathode. It has a small (10-mm diameter) photocathode to keep dark noise low, at less than 50 events s^{-1}.

Figure 5-9 shows the way in which the optical cable is mounted to deliver light to the photomultiplier tube. It enters the photomultiplier housing through a hole which is relatively wide to admit the widest part of the cable. This hole also allows the entry of electromagnetic noise, which is substantially reduced, but not completely eliminated, by the small metal box added on the outside of the photomultiplier housing around the cable entry aperture. This box has a split lid so that it can be closed up after the cable is in place, allowing the entry hole for the optical cable to have the minimum size, determined by the thinnest part of the cable. The cable is held in position by a perspex and an aluminium plate, which have holes just large enough to admit the end of the cable.

The end of the optical cable is about 1 mm away from the photomultiplier glass envelope and several millimetres from the photocathode, where the light is detected. The transferred light does not spread out significantly over this distance, so that all light exiting the cable falls on the photocathode. Some spreading is desirable, as it reduces the effect of spatial variations in the sensitivity of the photocathode.

The photocathode is at a high negative voltage (-1200 V). The metal sheath at the end of the optical cable is set to this voltage in order to avoid distorting the electric field inside the photomultiplier. The original design did this by setting the aluminium plate to the photocathode potential, with insulation from the box (at Earth potential) being provided by the perspex plate on which it is mounted. There was some doubt as to whether the aluminium would provide a reliable contact to the cable, so a phosphor bronze strip was added between the two plates. This strip is mounted so that it presses

Emerging optical cable

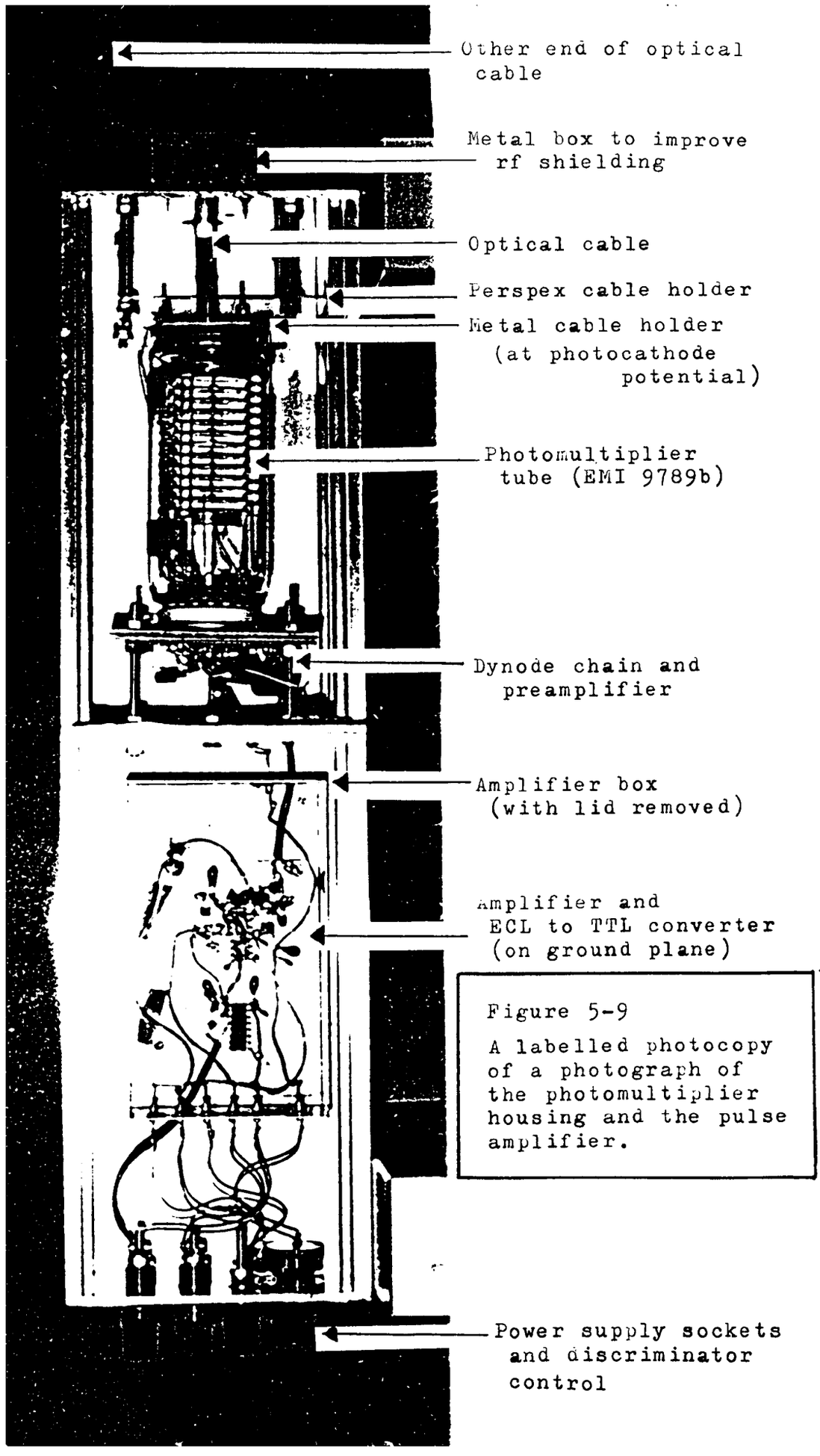

Figure 5-9

A labelled photocopy of a photograph of the photomultiplier housing and the pulse amplifier.

against the metal part of the optical cable.

A socket is used so that the photomultiplier can be plugged in to it after the base circuitry has been added and the socket has been mounted. This proved to be a problem during observations, as one of the tubes moved slightly in its socket over time, resulting in a misalignment between the channel-1 optical cable and the photocathode and hence in some loss of signal.

A preamplifier is mounted close to the anode of the photomultiplier. The output of this goes to another amplifier in a brass box in the other chamber. Together these amplifiers produce a 30-ns TTL (Transistor-Transistor Logic) pulse in response to a current pulse on the anode of the photomultiplier, provided the anode pulse reaches a certain minimum level set by a "discriminator". This minimum level is controlled by a potentiometer, with the control knob mounted outside the box.

5.2.4 Optical system performance

The expected response of the system described above to starlight is shown as a function of wavelength λ in the bottom plot in figure 5-10. This response is deduced from the stellar, solar and equipment spectra which are also plotted in the figure.

At the top, the light flux $F_{st}(\lambda)$ outside the Earth's atmosphere is shown for stars of zero magnitude with spectral types st = A0 and B0. These spectra were calculated by linear interpolation between values quoted by Allen (1973). The second graph shows the solar spectrum $F_s(\lambda)$ outside the Earth's atmosphere and the solar spectrum $F_g(\lambda)$ at ground level (Air Force Cambridge Research Laboratories, 1965). The spectral response of the equipment used in this work is shown in the third plot. The "quantum efficiency" $Q_e(\lambda)$ of a typical 9789B photomultiplier has a peak in the blue region, where 20% of the incident photons produce a current pulse. The manufacturer measures the efficiency of each tube at 420 nm and this calibration Q_{ch} is indicated in the figure by crosses, labelled with the channel number ch = 1 or 2. The transmission efficiency $T_o(\lambda)$ (from the manufacturer's data sheet) of the optical cable is about 50%, but falls off at the blue end of the spectrum. The transmission efficiency $T_{34}(\lambda)$ of one layer of the blue filter (Kodak Wratten gelatin filter no. 34) is 70% in the blue region and negligible for the range 490–620 nm (Kodak, 1965).

Combining all the above factors gives the predicted rate $R_{dp}(\lambda, ch, A_d, \alpha)$ of de-

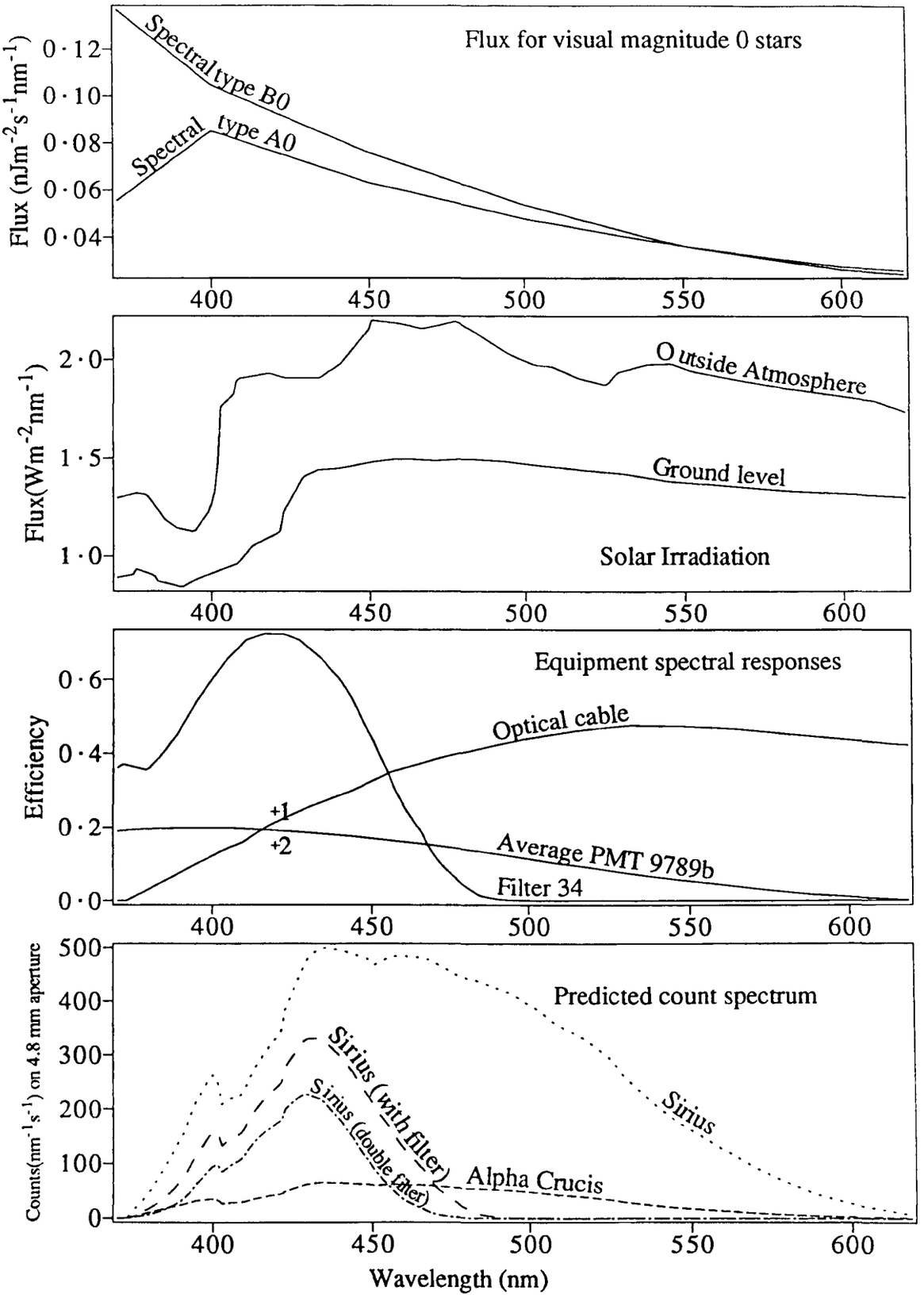

Figure 5-10 The expected photocount rate versus wavelength for starlight (bottom), derived from the stellar, solar and equipment response spectra plotted above. (The plotted photomultiplier efficiency is the nominal one. The manufacturer's calibration for individual tubes at 420 nm is indicated by crosses, numbered with the channel number.) The photocount rate is predicted for Alpha Crucis and Sirius, at their maximum elevation in Adelaide, observed through a circular 4.8 mm aperture on channel 1. The effect of 1 and 2 layers of Kodak Wratten filter no. 34 is shown.

tected photons.nm^{-1}s^{-1}

$$R_{dp} = A_d F_{st}(\lambda) 10^{-0.4M} \frac{F_g(\lambda)}{F_s(\lambda)}^{\sec(\alpha)} \frac{Q_e(\lambda)Q_{ch}}{Q_e(420nm)} T_o(\lambda) T_{34}^{nfil}(\lambda) 10^{-9} \frac{\lambda}{hc} \qquad --(5.1)$$

where A_d is the detector area (m^2), α is the elevation angle of the star, M is the visual magnitude of the star, $nfil$ is the number of layers of the blue filter, h is Planck's constant and c is the speed of light. This formula is used to predict the expected photon detection rates for Sirius and α Crucis on a 4.8-mm circular aperture, plotted at the bottom of figure 5-10. (*nb* The available A0 spectrum is substituted for the A1 spectrum of Sirius and the B0 spectrum for the superposition of B1 and B3 spectra of α Crucis. This approximation is valid as the trailing digit divides the A or B type spectrum into 10 ranges and there is not a great difference between the A0 and B0 spectra over the range of wavelengths detected.) For both stars there is a significant system response from 400 to 550 nm.

The effect of 1 and 2 layers of the blue filter is shown for Sirius. One layer of the filter reduces the response to the range 400–460 nm. The second layer does not change this range significantly, but reduces the total transmission. This may be exploited to ensure that effects attributed to wavelength dependence are not in fact an artefact of lower light levels.

5.2.5 Electronic circuitry

An overview of the entire starlight recording system is given in figure 5-11. The optical system described above is represented at the top of the diagram, along with a high-voltage power supply for the photomultipliers and low-voltage supplies for the amplifiers. Equipment essential to recording the output from the pulse amplifiers is represented on the right. The pulses are counted by pulse counters, the contents of which can be read and reset by the SYM-1 microcomputer. A digital multiplexer allows the computer to read different combinations of lines from the counters in a single operation. The computer stores the total counts for many successive intervals and then transfers the information, through an interface circuit, to a digital tape recorder which writes it to standard computer tape. The other equipment, represented by the section of figure 5-11 within the dashed line boundary, is not necessary to record the data, but allows the author to check that most of the essential equipment is operating correctly

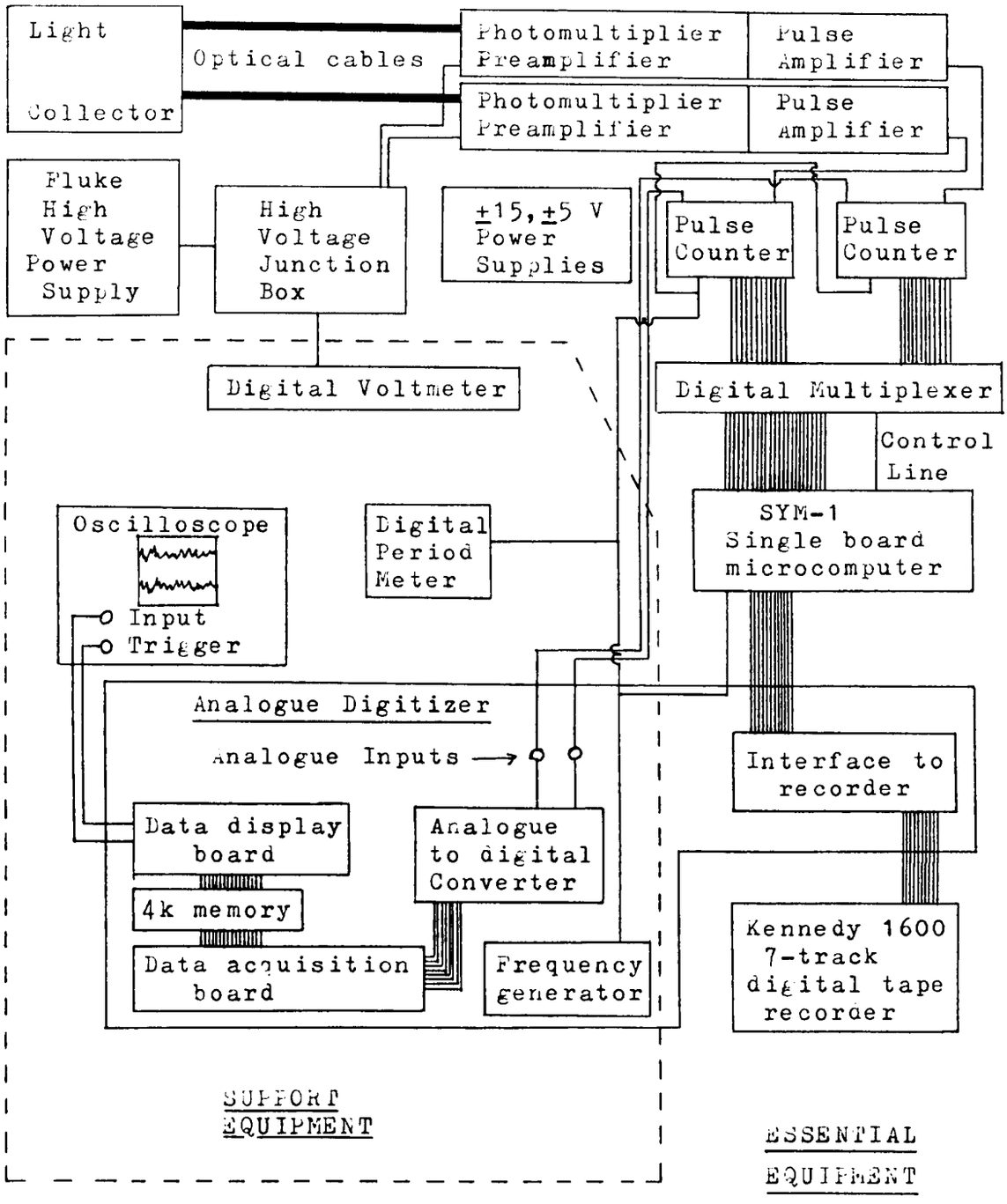

Figure 5-11 A block diagram of the equipment for recording stellar scintillation. The dashed line divides it into "Essential equipment" and "Support equipment", the latter being used to check for correct operation. Starlight collected by the light collector (top left) is transferred to photomultipliers by optical cables. A junction box allows both photomultipliers to use the same high voltage supply. Current pulses produced by the photomultipliers are converted to TTL pulses by the preamplifiers and pulse amplifiers. These are counted by the pulse counters in sample intervals set by the frequency generator. The accumulated counts are read by the computer, with a digital multiplexer allowing it to read different combinations of 8 lines in a single operation. The computer collects a block of data and then transfers it to computer tape. The analogue digitizer records the analogue output of the pulse counters into a 4k memory which is constantly converted to an oscilloscope display. The digital voltmeter and period meter monitor the high voltage and the sampling frequency.

and to have an instant view of the data being recorded. Parts of this system are now described in detail.

The photomultipliers are both operated from a single Fluke 412B high-voltage power supply, set at -1200 V. This voltage is a compromise between the need to set it as low as possible to reduce "microdischarges" (Candy, 1985a) but high enough to make the anode pulses sufficiently large to be detected. A junction box provides two high-voltage connectors, so that the two photomultipliers can be used with one supply. This junction box also contains a voltage divider which produces an output which is 0.1% of the high voltage. This fraction is monitored on a digital voltmeter.

The high voltage is distributed between the electrodes of the photomultiplier by a circuit called a "dynode chain", for which the circuit diagram is given in figure 5-12a. A zener diode maintains the potential difference between the photocathode and first dynode at 200 V. The remainder of the high voltage is equally divided between the dynodes by resistors. Capacitors are put across the final stages of the chain to reduce fluctuations in the interstage voltages as the current pulses propagate through.

The small pulses (typically 4×10^7 electrons) produced at the anode are converted to 30-ns TTL pulses by the combination of a preamplifier and a pulse amplifier. These are simple versions of circuits designed by Candy (1985b). Figure 5-12b is the circuit diagram of the fast, low-noise preamplifier which is mounted close to the anode. The signal is further amplified by the transistor in the pulse amplifier (figure 5-12c). To discriminate between overlapping pulses the signal is differentiated by an ECL (Emitter-Coupled Logic) 10116 differential amplifier and further amplified by a second 10116. The resultant ECL pulses ($\sim$1 V in height) are then converted to TTL pulses by a 10125 ECL to TTL converter. To avoid feedback and self oscillation, the leads on all components are cut as short as possible and the components are mounted close to a ground plane.

The TTL pulses are transferred to the pulse counters along short (10-cm) coaxial connectors. Figure 5-13 gives a circuit diagram for the pulse counter. Its purpose is to count the number of pulses that occur within an interval delineated by positive edges of the signal *SFQ*. At the end of the interval, the number of pulses is transferred to a memory, the counter is reset to zero and counting recommences. The number in the

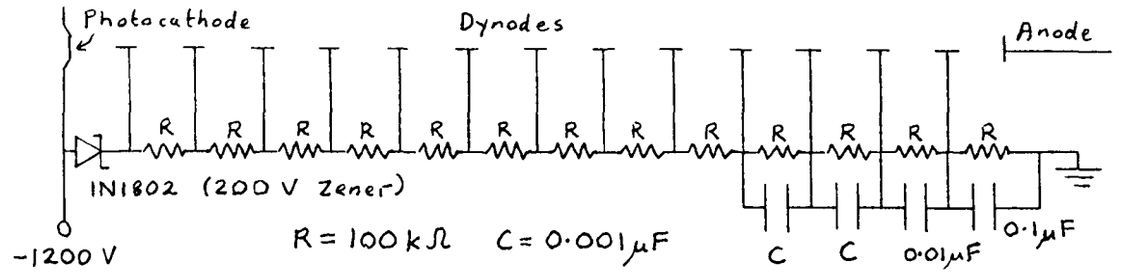

Figure 5-12a A circuit diagram of the "dynode chain". This is the circuit which is built on the base of the photomultiplier tube to set and maintain the voltages between its stages. A zener diode maintains the first dynode at 200 V above the potential of the photocathode. The remainder of the high voltage is divided equally between the other stages by resistors. Capacitors reduce the voltage fluctuations on the stages near the anode, where the current pulses become relatively big.

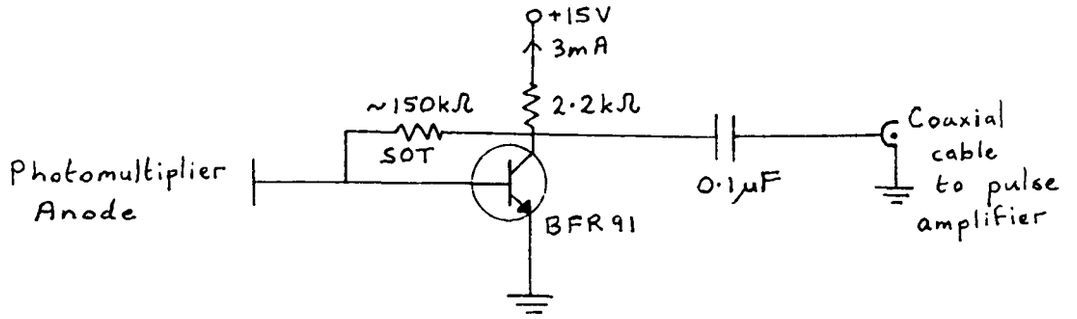

Figure 5-12b A circuit diagram of the preamplifier. This is built close to the anode of the photomultiplier. "SOT" means "select on test" and indicates that the resistor must be chosen to set the current through the 2.2 kΩ resistor to 3 mA.

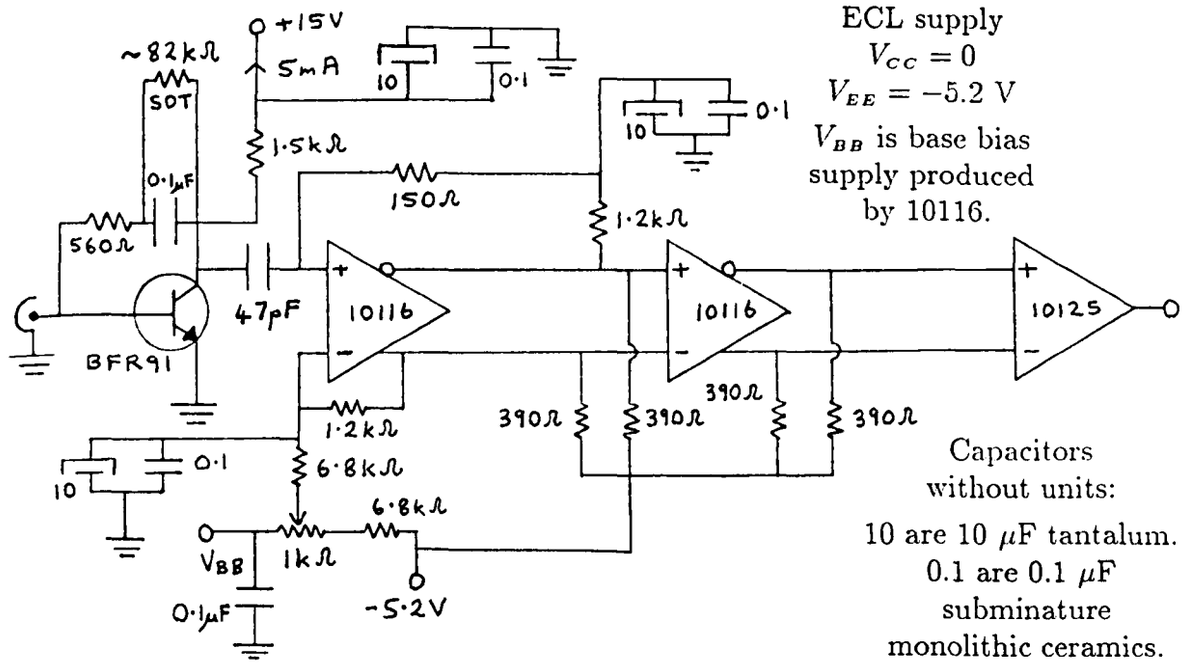

Figure 5-12c A circuit diagram of the pulse amplifier, which converts the small pulses from the preamplifier to TTL pulses. The input pulses are amplified by the transistor stage. The ECL 10116 differential amplifiers produce ECL pulses in response to the sharp leading edge of the input pulses. These are then converted to TTL pulses by the 10125.

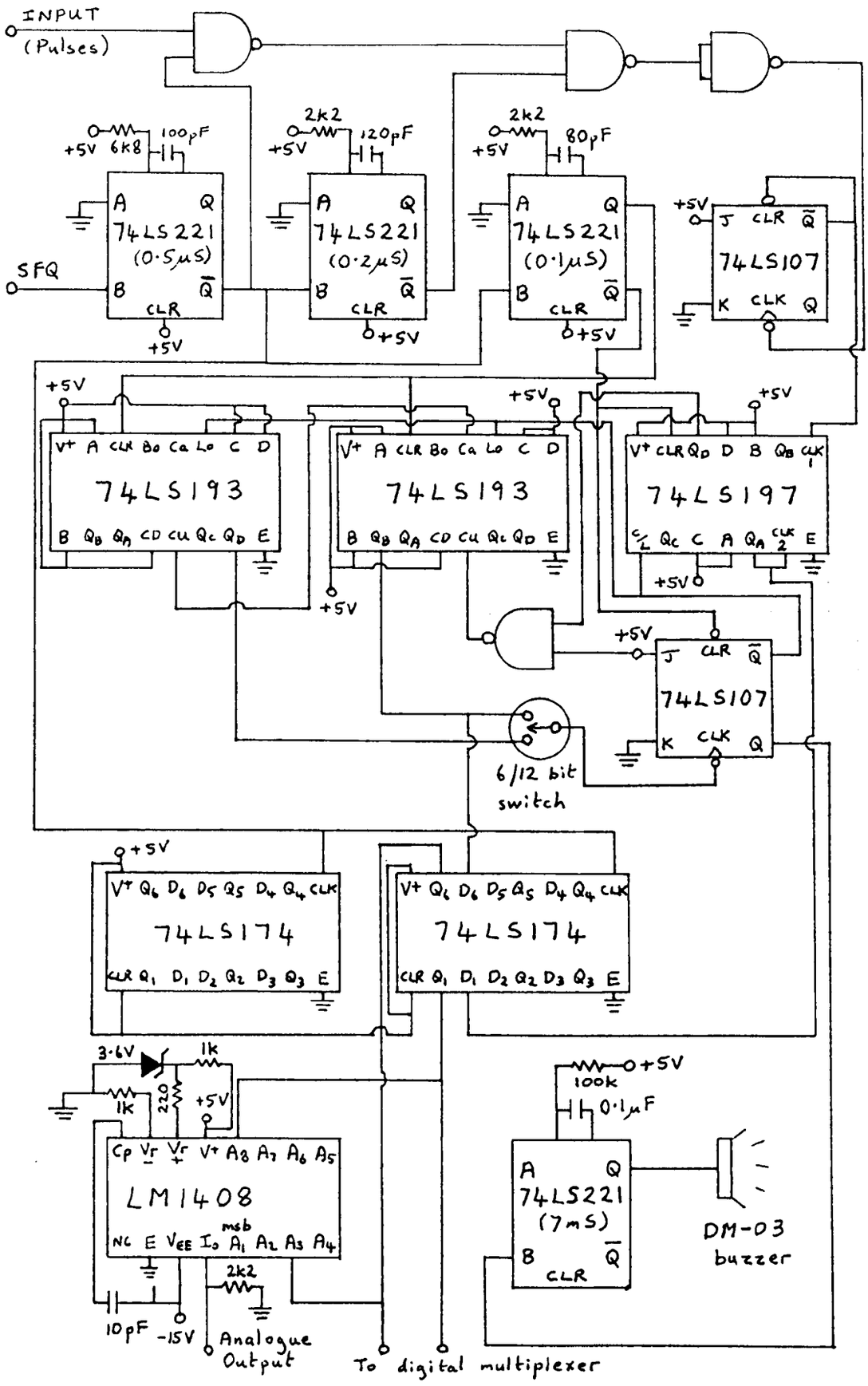

Figure 5-13 A circuit diagram to illustrate the operation of the pulse counter. TTL input pulses are counted on a 12-bit counter for successive intervals defined by positive transitions of the sampling frequency *SFQ*. The contents of the counter are transferred to latches, whose contents are available as both digital and analogue outputs. For clarity, the data lines are drawn only for bits 0 and 5 of the 12-bit number.

memory is made available as both a digital and an analogue output. If the number of pulses reaches a limit of 63 or 4095 (depending on the setting of the 6/12 bit switch), the counter is held at this value for the rest of the sampling interval and an alarm sounds. This circuit is explained in detail below as it is critical for the measurement of photocount distributions that it should operate correctly. Furthermore the circuit may be of interest to anyone building a modern photon-counting system, as an inexpensive alternative to a commercial photon counter.

The pulses are counted by a 12-bit counter consisting of two 74LS193 4-bit counters and a 74LS197, set up as a 4-bit counter. The '197 is used for the lowest bits as it has a higher frequency response than the '193. The total is transferred to a 12-bit memory formed by two 74LS174 latches. This transfer and the resetting of the counter is controlled by three 74LS221 monostables which implement the sequence:

1) the first monostable, clocked by SFQ, inhibits further input through the first NAND gate for 0.5 μs, allowing any counts already detected by the '197 to propagate through to the highest bit of the 12-bit counter.
2) The contents of the 12-bit counter are transferred to the 12-bit latch and the other two monostables are triggered.
3) The counter is cleared by the signal from the 0.1 μs monostable while the 0.2 μs monostable inhibits input through the second NAND gate for this clearing interval and another 0.1 μs thereafter to give the counter time to recover from the clearing operation.

Thus the pulse counter has a dead time of 0.7 μs at the start of each sampling interval.

The 74LS197 and 74LS193 counters can be set to a desired output by loading the values on their inputs A, B, C and D. This feature is used here to set the counter back to its highest value (of 63 or 4095) if it overflows. The highest relevant bit (selected by the 6/12 bit switch) clocks a J-K flip flop (a 74LS107) which then activates the "load" function of the counter, setting all the outputs high.

If an input pulse arrives on the boundary of the counter dead time, it can be truncated by the inhibiting signal at the NAND gates, producing an undersize pulse as a result. Such small pulses can cause the '197 counter to increment by 2, as they fail to switch the lowest bit on the counter, but the transitory change in the voltage

of the lowest bit is amplified and thus capable of switching the second bit. Counting two pulses where only one occurs will cause serious errors in the analysis of photocount distributions. The probability of this double count is made negligible in this circuit by using a 74LS107 J-K flip flop as a pulse shaper, which converts most of the undersize pulses to full TTL pulses. Its inverting output $\overline{Q}$, which goes low in response to a positive transition on its CLK input, is fed back to its clear input CLR, so that its output cancels itself. The width (~30 ns) of the resultant output pulse is determined by the propagation time of the flip flop and is sufficiently large to reliably trigger the '197.

The contents of the latches in the pulse counter are connected to input/output ports on the SYM-1 microcomputer, so that the numbers on the pulse counters are available at particular memory locations in the computer. The digital multiplexer uses a 74LS257 integrated circuit to swap one of the computer's input/output ports to either the low 8 bits of the pulse counter on channel 1 or to a combination of the low 4 bits from each of the two channels. This allows the low 4 bits for both channels to be read in a single computer operation, thus increasing the maximum sampling frequency. The multiplexer includes circuitry to detect overflow into bits 5 or 9.

The primitive DTL (Diode-Transistor Logic) of the Kennedy recorder means that an interface circuit is required for the computer to control it. As this recorder is obsolete, there is no point in giving details. The Analogue Digitizer is a flexible data logger with eight analogue input channels, controlled by the SYM-1 microcomputer. It was used here only to give the author a picture of the signals during observations. The analogue output of the pulse counters was digitized and stored by the Analogue Digitizer, which displays the contents of its memory on an oscilloscope. This hybrid arrangement (incorporating redundant conversion to an analogue signal and then back to digital) arose through historical progression: the Analogue Digitizer had already been built when the computer was acquired and provided the simplest route to producing a display of the data.

The SYM-1 microcomputer was used to control the other equipment and to provide a number of other functions, including a 100-hr clock, updated at 0.1-s intervals, detection of overflow in the digital multiplexer, and accumulation of time series and

frequency distributions of the values on the pulse counters. It is mentally and physically tedious to use, requiring programs to be written in hexadecimal machine code and to be stored in 2716 memories which require 20 min of exposure to ultraviolet light for erasure.

5.2.6 Methods of observation

Most of the observations of starlight were made using the "multiple collimator", taking "scans" in which the separation of the two active apertures was varied between 1.1 and 7.1 cm in steps of 1.0 cm and the angle between the line joining the apertures and the vertical was varied from 0° to 90° in steps of 10°. The general procedure at each angle was to make measurements at each of seven separations and then point the instrument at the closest "blank" area of sky (*ie* an area with no bright stars) at the same elevation to take a skylight record.

For each combination of apertures the most common sequence was for the computer to acquire a frequency distribution and a time series of the numbers in the pulse counters. During the time taken to write the time series to computer tape (10 s), the optical cable would be moved (by hand) to the next aperture. Each block of 16 records commenced at 3-min intervals, giving the author about 1 min to realign the instrument on the star and change the orientation angle. A "scan" over 90° would thus take 30 min. Variations from this procedure included measurements at separations of up to 19.1 cm, for which the orientation angle was incremented in smaller steps (3° or 5°). On some occasions the frequency distribution was not taken, allowing a time series to be recorded for 10 different separations during the 3-min cycle.

For the frequency distribution the digital multiplexer fed the lowest four bits from each pulse counter to one 8-bit digital input port of the computer. A frequency distribution of the number on this port for 65535 42-μs intervals was recorded. For the time series the lowest eight bits from each pulse counter were fed to different 8-bit input ports of the computer and the number of pulses in each of 1792 consecutive 542-μs intervals was recorded for each channel. The sampling interval of 42 μs is set by the minimum time in which the microcomputer can execute the necessary instructions. The longer sampling interval for the time series is set at 542 μs so that it is easy to change between it and the 42 μs for the frequency distributions.

The "split-lens" telescope was used with the same data-recording program as used for the "multiple collimator". In this case no changes in the apparatus were necessary during acquisition of the 7 or 10 starlight records.

On some occasions, 255 records were acquired consecutively without the 1-min breaks and without background records, to allow the statistics of scintillation to be uniformly sampled over about 40 min.

Chapter 6 **Verification**

This chapter presents examples of the observations and the results of tests which were applied to investigate the performance of the equipment and the accuracy of the data recording and processing. Some of the techniques developed by the author and presented in chapter 4 are also tested.

Examples of data records for both the multiple-beam and the starlight observations are presented. Qualitative examination of these indicates that the data are substantially correct. An overview of one month's starlight observations is presented to indicate the reliability of the procedures that the author followed in operating the equipment. A comparison of observed count rates for two different sampling intervals provides a quantitative check on the validity of the recording and processing of the starlight observations.

The methods presented in chapter 4 for the measurement of photomultiplier-afterpulse probability are applied to observations of skylight. The deduced afterpulse values are then used to correct both skylight and starlight data for the effect of afterpulsing. The success of this correction validates the methods used and provides a rigorous quantitative test of the validity of the recorded data. A test of the method of correction for background light is also made.

The entire starlight system is tested by a comparison of the observed photocount rates with predictions and by the analysis of records of artificial light fluctuating at a known rate. A comparison is made of scintillation observed simultaneously by a non-imaging and an imaging light collector. Finally the "correlation by minimum difference" function developed in chapter 4 is tested using records of artificial light. This allows the effect of photon noise on this function to be assessed.

6.1 Multiple-beam data

A photograph of the scintillation patterns produced in the multiple-beam experiment (described in §5.1) is reproduced in figure 6-1. A hair drier introduced turbulent fluctuations in the crossover region of two crossed laser beams, producing the scintillation patterns shown. In the picture the patterns are similar but not identical. This is probably because one laser was 70% brighter than the other, so that different parts

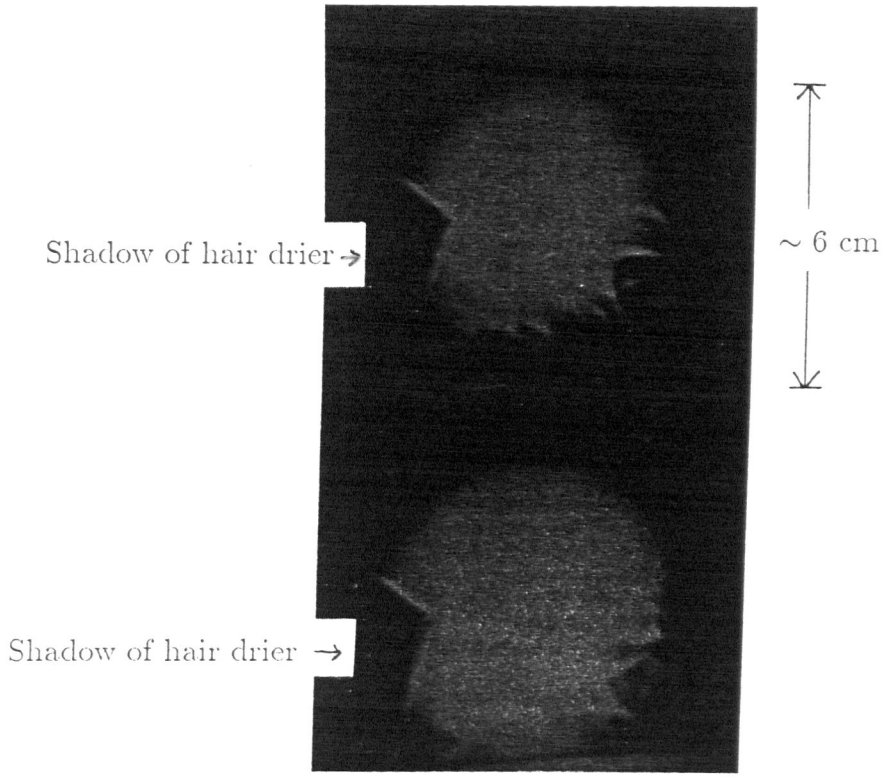

Figure 6-1 Reproductions of a photographic slide of scintillation patterns in the crossed laser beams. A rough photocopy (left) provides some reference labelling. A better reproduction is given on the facing page. In this the red colour of the laser light has been changed to green as it gives better contrast.

The photograph is of a screen with the two laser beams falling on it. The beams traversed a 40-m path and were crossed to illuminate a common volume about halfway along the path. A hair drier in the crossover region produced the shadow in each beam on the left. The turbulent stream produced by the hair drier caused scintillation in both beams. This can be seen only at the edge of the beam, presumably because the image of the beam is overexposed in the centre. Some similarity between the scintillation patterns on the right hand edge is apparent. The difference between the patterns may be due to the different intensity of the two lasers (3 and 5 mW), which causes the best contrast to occur for different parts of the pattern.

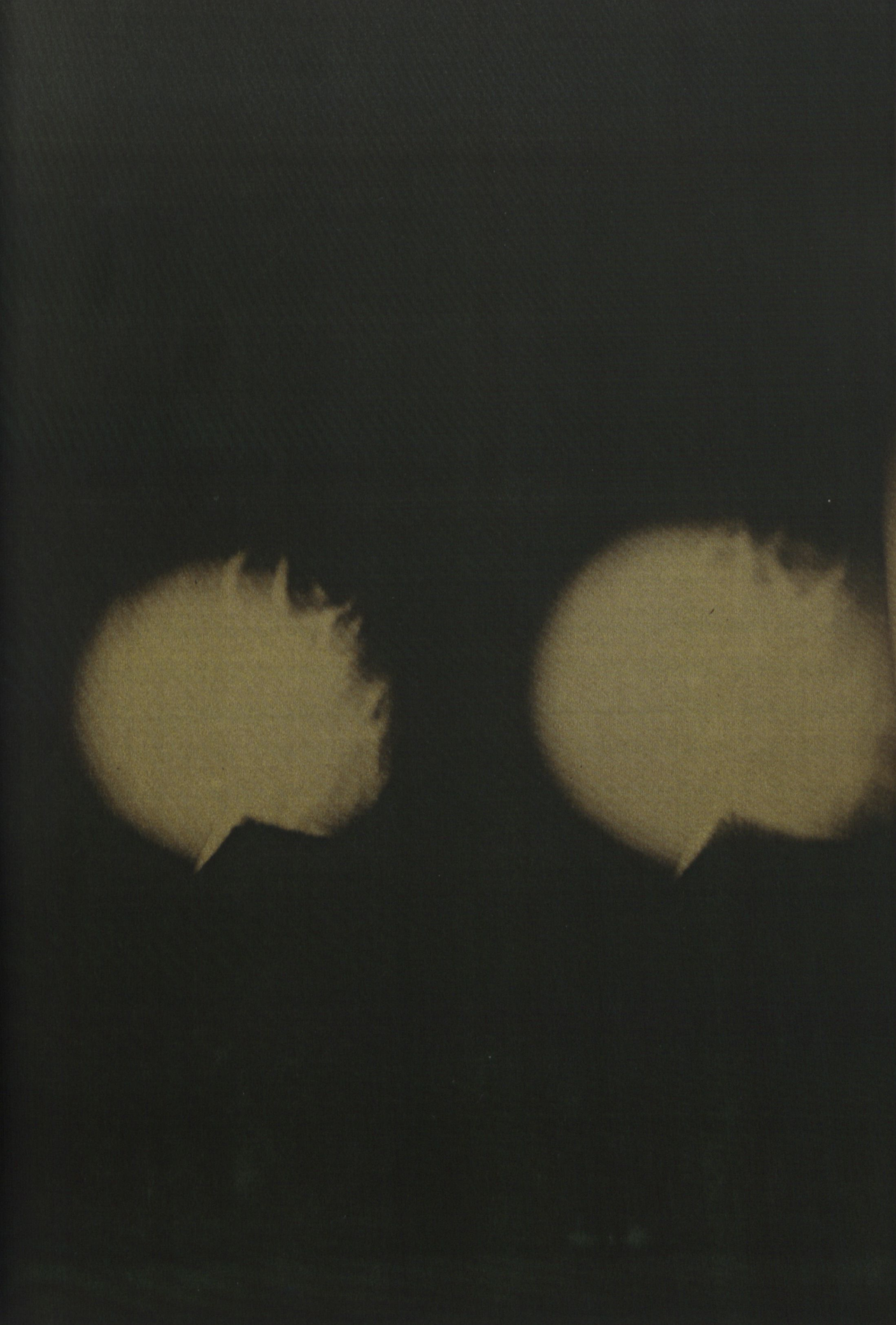

of the two patterns show maximum contrast in the picture. Patterns with sizes in the range 0.1–1 cm can be seen. (*nb* In figure 6-1, the crossed beams are in a vertical plane. In all the measurements to be discussed, the two beams are in the same horizontal plane.)

Figure 6-2 shows three 0.2-s records of data produced by the multiple-beam system. Record 1-1 was taken with fluorescent lights illuminating the detectors, producing a 100-Hz fluctuation. In record 2-5, detectors 1 and 4 were shielded from the lights, with detector 2 partly shielded. There is no trace of the 100-Hz signal on channel 4, but a slight trace of it on channel 1. As the channels are sampled in the order 1,2,3,4,1..., this suggests that the A/D (see §5.1.1, *para* 5) is settling to the correct value during the sampling interval (otherwise a residual fraction of the signal on channel 3 would show on channel 4), and that the small 100-Hz signal on channel 1 must be due either to incomplete shielding of the detector from the light source, or due to leakage in the analogue multiplexer. Whatever the cause, the amount involved is insignificant in this application.

Record 1-6 (the 3rd graph) is typical of the approximately 1000 data records (in runs 1 and 2) of the scintillation produced by the turbulent streams. It was recorded with a hair drier blowing turbulent air in the positive direction (defined in figure 5-2a) at the crossover of the parts of the beams falling on detectors 2 and 4. This position, labelled P_{24} in figure 5-1, is close to the crossover for detectors 1 and 3. From figure 5-1 it can be predicted that the scintillation patterns should arrive at the detectors in the order 3, then 1 and then 2 and 4 together. Looking at the record it can seen that the scintillation

1) is almost identical on channels 2 and 4,
2) is similar on channels 1 and 3, with the signal on channel 3 leading in time, and
3) shows lesser similarity between other combinations of channels, but with individual features appearing in the order predicted above.

The lesser degree of similarity between channels 1 and 4 and between 2 and 3 indicates that the scintillation pattern changes substantially as the turbulence moves 1 cm.

Part of record 1-1 is plotted at the bottom of figure 6-2. Individual data points are labelled with the number of the channel (1–4) on which they were recorded, illustrating

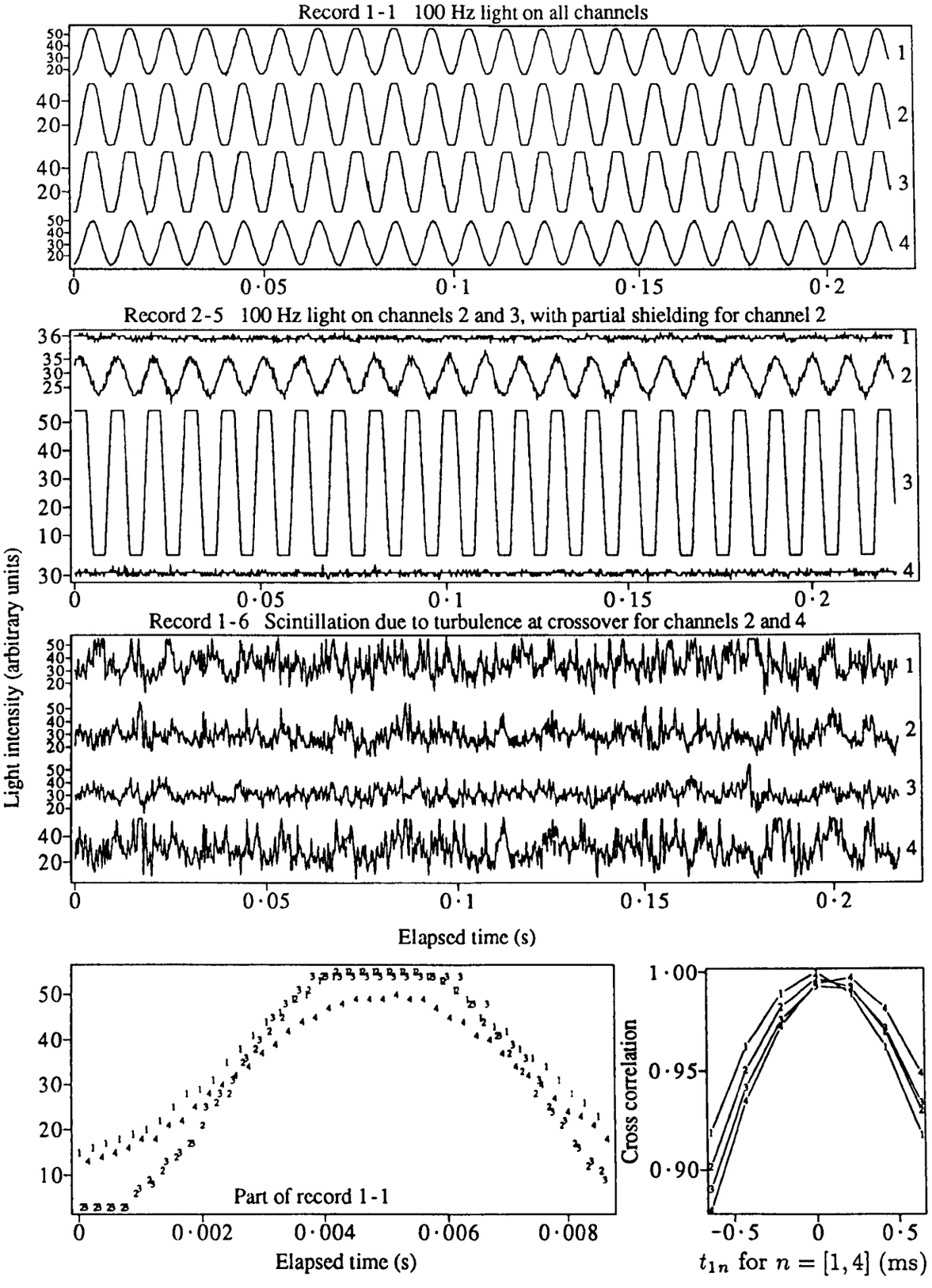

Figure 6-2 Three sample records of the crossed laser beam measurements, for 100 Hz fluorescent lights, on all four channels and on two channels only, and for scintillation produced by a single stream of turbulence in the crossover region. A small part of the first record is replotted at the bottom to illustrate the recording sequence. The correlation versus time shift $C_{1n}(t_{1n})$ for this record is plotted on the right for n = 1,2,3 and 4 (without allowance for the time shift introduced by the sampling delay between channels). The four channels are identified in each plot by the digits 1 to 4, either at the end of the time series, or centred on each data point.

the sequential sampling of the 4 channels by a single A/D converter. It is not possible to check in this plot whether the measurements have been reproduced in the correct order, as the waveforms are different between channels due to truncation of the signals. This check can be made, however, using the plot of cross correlation at the bottom right. The time shifted cross correlation between the intensity I_1 on channel 1 and I_n on channel n

$$C_{1n}(t_{1n}) = \frac{\langle I_1(t)I_n(t-t_{1n})\rangle - \langle I_1(t)\rangle\langle I_n(t)\rangle}{\sqrt{(\langle I_1^2(t)\rangle - \langle I_1(t)\rangle^2)(\langle I_n^2(t)\rangle - \langle I_n(t)\rangle^2)}} \qquad --(6.1)$$

is plotted as a function of time shift t_{1n}, for channels $n = 1$ to 4, using the false assumption that each sequence of four samples on channels 1–4 were recorded simultaneously. It shows, as expected, that

i) the correlation at almost any particular time shift increases or decreases in the order of channels 1 to 4, and

ii) the maximum correlation between channels 1 and 4 occurs for a positive time shift of channel 4 (of one interval), as expected if the sample on channel 4 is taken just before the next sample on channel 1.

From the tests above, it can be concluded that:

a) the scintillation patterns produced by the same turbulence were very similar in the two beams.

b) Two detectors observing equivalent parts of these scintillation patterns produced similar electrical signals.

c) The digital recording and processing of these signals involves no major errors.

6.2 Starlight data

Records of starlight are examined in this section to make a preliminary assessment of the accuracy of the equipment and methods described in §5.2.

6.2.1 Sample data records

Six consecutive records of observations, using the "multiple collimator" described in §5.2.2, are shown in figure 6-3. These records alternate between frequency distributions (of the number of counts on channels 1 and 2 in each of 65535 intervals of 42 μs) and time series (of the number of counts in each of 1792 consecutive intervals of 542

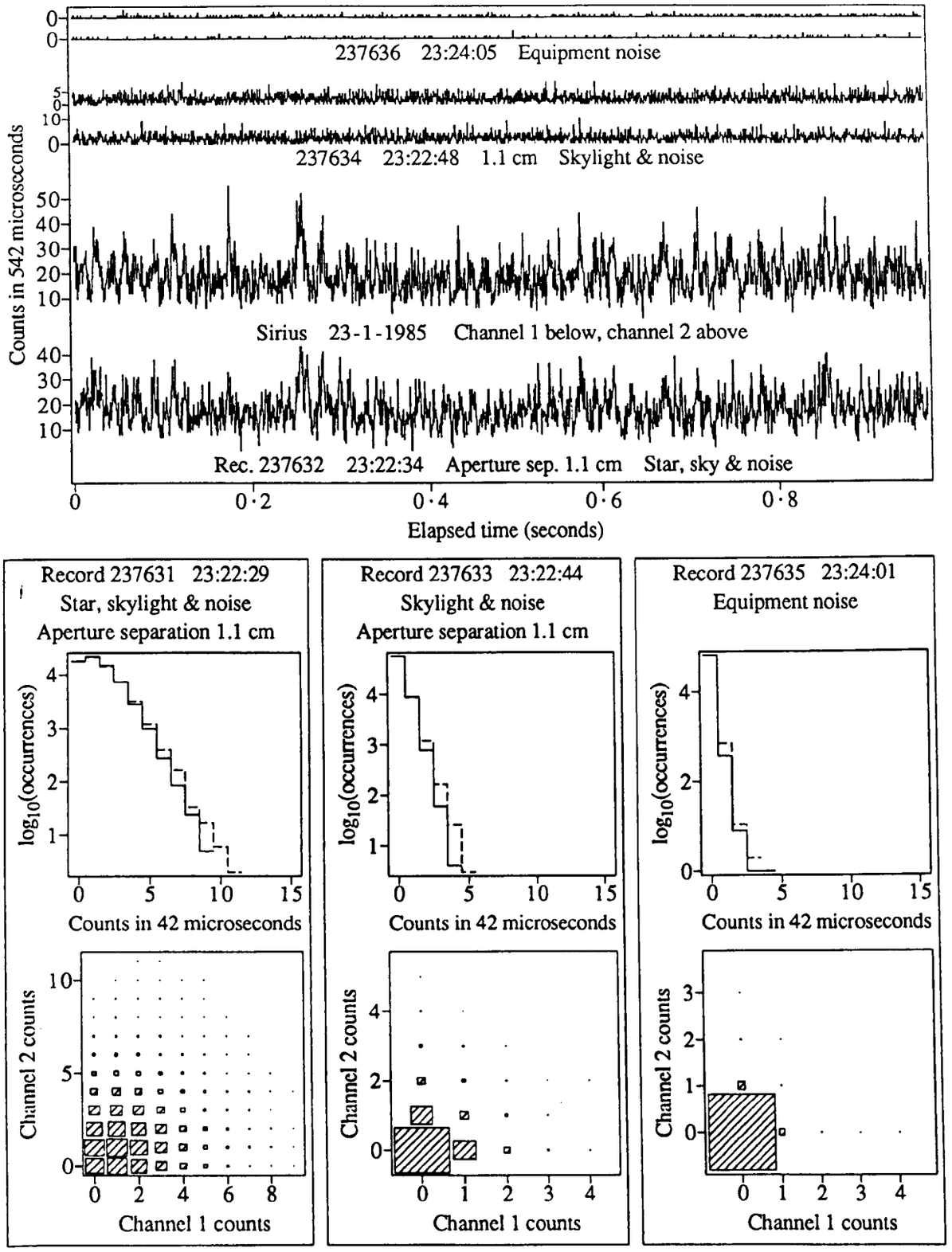

Figure 6-3 A sample of the stellar scintillation data, showing six successive records which allow a comparison of starlight, skylight and equipment noise. The mode of data collection alternated between a photocount distribution (for 65535 intervals of 42μs - lower graphs) and a time series (for 1792 intervals of 542μs - top). The photocount distribution was recorded as the number of occurrences of each of 256 different combinations of the counts on channels 1 and 2, with a possible range of 0-15 on each channel. This is plotted at the bottom, with the area of each rectangle being proportional to the number of occurrences (the area being normalized within each plot). The frequency distribution for each channel is derived and plotted above, with a solid line for channel 1 and a dashed line for channel 2.

μs, on channels 1 and 2). The three successive pairs (of a frequency distribution and a time series, taken within a 5-s interval) were recorded for starlight plus skylight and dark noise, skylight plus dark noise, and dark noise only. The maximum possible count in each sampling interval is 255 for time series and 15 for frequency distributions.

The three records of time series are plotted on the same scale at the top of figure 6-3. It can be seen that there are fluctuations in the starlight which are apparent on both channels. No such correlation is apparent between the photon noise of the skylight record or the "dark" pulses and other equipment noise. The equipment noise is small compared to the skylight, which in turn is small compared to the starlight (for Sirius – this is not the case for α and β Crucis).

The frequency distributions are represented graphically in figure 6-3 in two ways. The logarithm_{10} of the number of occurrences is plotted against counts per interval, with a solid line showing values for channel 1 and a dashed line for channel 2. The joint frequency distribution (*ie* the number of occurrences of particular combinations of counts on channels 1 and 2) is plotted at the bottom of figure 6-3, with the area of the rectangles being proportional to the number of occurrences of each combination.

The starlight record in figure 6-3 is for weak scintillation. Examples of strong scintillation are given in figure 6-4, which shows a "block" of 8 records of time series, including 7 records of starlight and one of skylight (measured by turning the "multiple collimator" so that the star was just outside the field of view). Most of the data taken in this work consisted of such blocks of 8 time series, with a frequency distribution for the same aperture measured just before each time series.

In the block shown in figure 6-4, the aperture separation was increased from 1.1 to 7.1 cm in steps of 1.0 cm for successive records. It is possible to see by eye that there is significant correlation between the intensity fluctuations on the two apertures separated by 1.1 cm (plotted at the bottom), with less correlation at greater separations and apparently none at more than 4.1 cm. The fluctuations on channel 1 can be seen to lead those on channel 2, with the time shift becoming larger as the separation increases. Thus it appears that the recorded signals are at least a reasonable representation of the light intensity. Quantitative tests will be applied later.

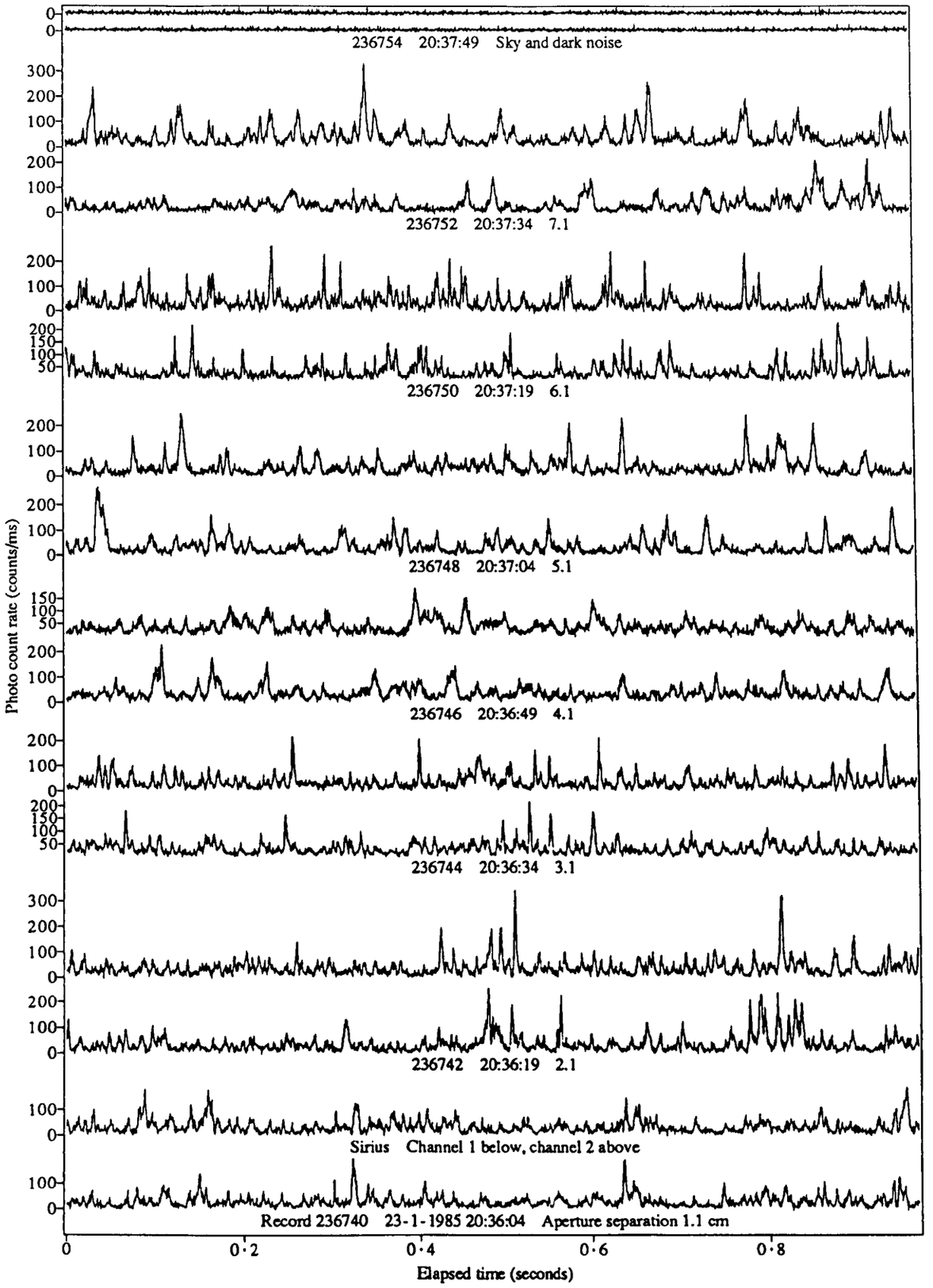

Figure 6-4 A plot of the time series in a standard "block" of data, consisting of seven records of the scintillation of Sirius and a background record of the sky and equipment noise. Each starlight record shows the photocount rate on two 4.8mm circular apertures at a different separation. Correlated signals can clearly be seen for separations of 1.1, 2.1 and 3.1 cm, with the time shift by which channel 2 lags channel 1 increasing with the separation. The scintillation itself is unusual. It was chosen because its combination of relatively low frequency and large variance allows identification of individual patterns and their motion.

6.2.2 Sample observation schedule

Figure 6-5 shows a compilation of the light levels recorded in January 1985, using time series of starlight on channel 1 of the "multiple collimator". In this particular month observations were usually taken of Sirius, which was near the zenith in the evening, then of α Crucis, which reached its maximum elevation near dawn. Sometimes Sirius was observed again at low elevation, just prior to first light. A break near midnight was usually for the author's supper. Otherwise long breaks were generally caused by cloud, while short breaks were for calibration readings of dark noise and for dealing with problems.

When recording of data stopped before first light, the halt was due either to the arrival of cloud, the filling of the recording tape or a lack of observable scintillation. No observations were attempted on some nights due to an incorrect forecast of cloud or to other commitments of the author. Thus the incidence of clear weather for January 1985 was even greater than is indicated in the figure. In contrast, in some winter months the number of clear nights was as low as four.

In the figure the average count rate in each record is plotted as a function of time. The values for the 7 or 10 successive records in each block are joined by lines, giving a short trace on the graph. A dot at a lower count rate is for the associated skylight record.

6.2.3 Operator reliability

As described in §5.2.6, the running of the equipment required fast manual work on the author's part to align the "multiple collimator" on the star and select apertures (by moving an optical cable) and the tilt angle. Occasionally the change was not made in time, and bad records were also caused by thin cloud, smoke, fireworks *etc.* These events were recorded in a handwritten log. Thus there was substantial scope for problems to occur and possibly be incorrectly documented.

Figure 6-5 shows that the final data set has not been badly corrupted by such problems. Records which are known to be bad have been excluded. The author's reliability is indicated by:

1) generally the level of the starlight does not change markedly from the maximum value, indicating that the "multiple collimator" was correctly aligned.

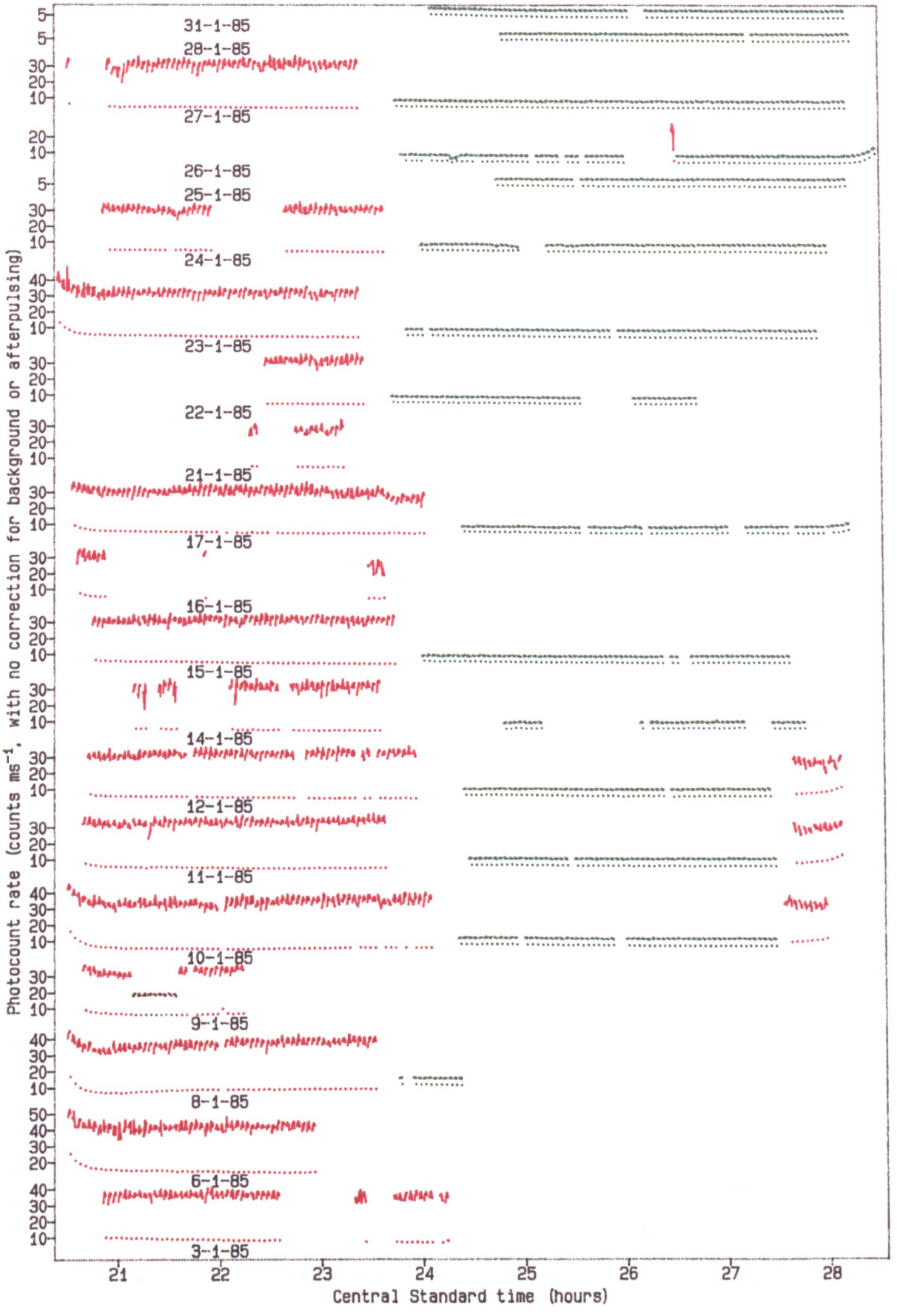

Figure 6-5 The photocount rate of starlight (on channel 1) on a 4.8 mm circular aperture for Sirius (red), Alpha Crucis (green) and Canopus (brown). Solid lines join values for several records of starlight plus background, followed by a dot indicating the background level.

2) Most of the traces show a rise to a maximum and then a fall for each data block, indicating that the star's movement took it through the centre of the field of view during each 2-min observation interval.

3) There is a tendency for the first record in a block to be at a lower intensity than the final one, indicating that the author tended to overestimate the rate at which the star would move through the field of view when pointing the "multiple collimator".

Most discrepancies can be explained by events recorded in the log sheets:

a) thin cloud caused a reduction in light level (on 14-1 and 24-1).

b) The optical cable for channel 1 came loose for a few minutes (on 26-1 and 27-1), reducing the recorded light level significantly.

c) A small reduction in light level prior to a break in recording which was prompted by the presence of cirrus cloud (on 17-1 and 24-1). It is possible that the approach of this cloud was preceeded by thinner cloud which the author could not see.

Thus the only unexplained features in a month's observations are low light levels during one block on each of 11-1 and 26-1.

6.2.4 Count rate test

In the usual recording sequence described above, a frequency distribution with a sampling interval of 41.3 μs (this being a sampling interval of 42 μs reduced by the 0.7-μs dead time of the counter described in §5.2.5) and a time series with a sampling interval of 541.3 μs were recorded for the same source (*ie* starlight, skylight or dark noise) within a 5-s interval. The count rates should be almost the same for the two records, so a comparison between them constitutes a test of the accuracy of the system from the stage where the pulses are counted by the pulse counter, through all subsequent stages including data recording and processing. (*eg* an intermittant fault in the connector for bit 0 between the counter and the microcomputer would introduce a larger relative error for the frequency distribution, which has fewer counts per interval.)

The result of this comparison is shown in figure 6-6. For both channels, the ratio of the count rates for the different sampling intervals is plotted as a function of the average of the two rates. A large number of individual pairs are compared, grouped together in a way which will be used several times in this thesis. The horizontal axis is divided into subranges which contain approximately the same number of the individual

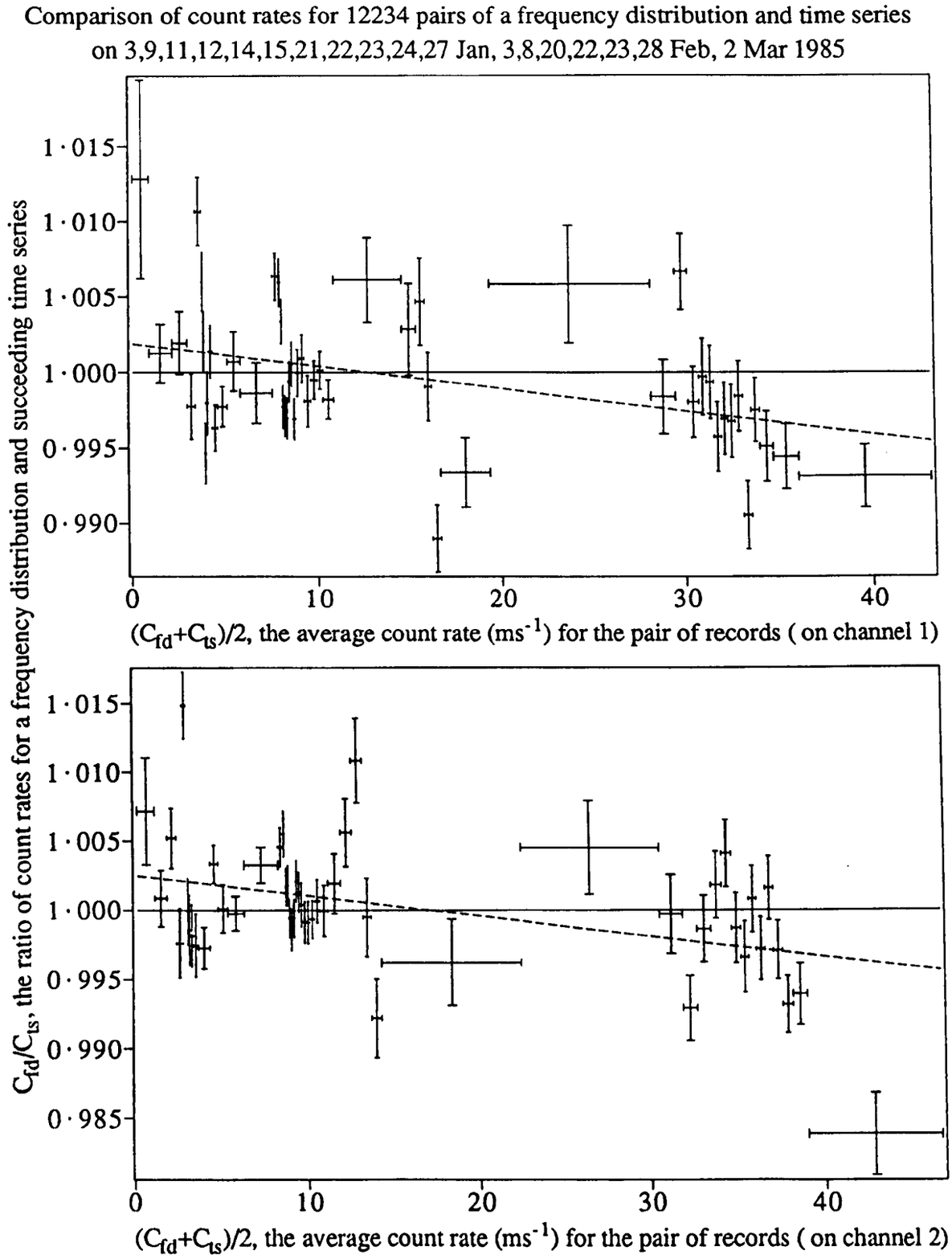

Figure 6-6 The count rate is compared for many pairs consisting of a frequency distribution and a time series. These rates should be equal as the two records were recorded within the same 5-second interval. The ratio C_{fd}/C_{ts}, where C_{fd} is the count rate for a frequency distribution and C_{ts} is the count rate for the related time series, is plotted on the vertical axis as a function of the average rate $(C_{fd} + C_{ts})/2$. The range of average rates is divided into 50 subranges containing approximately the same number of pairs. For all pairs within each subrange, the mean $\pm$ the standard error of the ratio C_{fd}/C_{ts} is indicated by error bars. A dashed line indicates a fit by regression to the values for all the pairs and a horizontal line indicates the expected value of 1.

points. Bars are used to indicate the extent of this subrange and the standard error of the corresponding values on the vertical axis.

The expected value of 1 is shown by a solid line in figure 6-6, with a dashed line indicating a fit by regression to the data for individual record pairs. There is good agreement at low count rates, but a tendency for the rate for frequency distributions to be less than for time series at high count rates.

This discrepancy is consistent with the observation from figure 6-5 that, for Sirius, the count rate tends to rise rather than fall through a block of records (point 3 in §6.2.3). In this case the count rate is higher for the time series than for the preceeding frequency distribution and the ratio in figure 6-6 therefore is less than 1 at high count rates. The effect does not occur at low count rates because these are produced by

a) stars which move less quickly (than Sirius) through the field of view, and

b) skylight, which should not vary significantly over 5 s.

As the discrepancy between the average count rates for frequency distributions and time series is generally less than 0.5%, it is concluded that there are no major errors in the system between the counting of pulses by the pulse counters and the reconstitution of data records on the mainframe computer.

6.3 Determination of afterpulse probability

The two methods for measurement of afterpulse probability developed in §4.5.3 are applied here to dark noise and skylight records. The purpose is to find the afterpulse probabilities so that these can be used to correct records of starlight for the effect of afterpulsing. The *afterpulse analysis*, which determines the probabilities of initial and subsequent afterpulse probabilities, is applied first to dark noise and then to skylight records. These probabilities can be compared with previous observations and expectations and so provide a test of the analysis. The *direct afterpulse analysis* (which is based on a smaller number of the same assumptions and cancels some systematic errors) is then applied to skylight records, in order to determine the probabilities required to implement the correction technique proposed in §4.5.4.

6.3.1 Afterpulse analysis

If the *afterpulse analysis* is correct, it should yield afterpulse probabilities consis-

tent with previous knowledge summarized in §3.11. In particular,

1) the initial afterpulse probability should be in the range 10^{-4}–2×10^{-2} (Coates, 1972),

2) the afterpulse probability should be the same for thermionic emission and photoelectric emission from the photocathode, as both eject a single electron, and

3) the subsequent afterpulse probability should be about four times that of the initial afterpulse (Williams and Smith, 1973).

Equations 4.40 to 4.42, applied to records of the dark noise for the two photomultipliers, give the results plotted in figure 6-7. The probabilities p of an initial afterpulse, P_s of a subsequent afterpulse and P_{ss} of a second subsequent afterpulse are calculated for each of 148 frequency distribution records of dark noise on channels 1 and 2. Frequency distributions, rather than time series, are used because the probabilities of 0, 1 and 2 counts are much higher (see figure 6-3) and they have a much larger number of sampling intervals. The calculated probabilities are plotted as a function of the event rate r (calculated from the observed probability $P_c(0)$ of 0 events per interval, using equation 4.30).

Dots indicate the probabilities calculated for individual records. Some of the calculated probabilities are very large or are negative. Plotting these outlying values would reduce the resolution in the region where most of the values occur, so a smaller range has been chosen for the vertical axis and values outside this range have been plotted on the nearest boundary (top or bottom).

Both the large scatter and the occurrence of unphysical results (*ie* probabilities less than zero), suggest that it is not valid to take an average of these values. Therefore a second approach is followed, in which the probabilities of particular numbers of counts are predicted for each of a range of values of the afterpulse probabilities. The predicted values can be summed over many records, as they are equally likely to be too large or too small due to statistical fluctuations. The event rate r_i for record number i is determined, as above, from $P_{c_i}(0)$, where this is the observed probability of zero counts for record i. r_i will have a small relative error due to statistical fluctuation, as the number of intervals with zero counts is large ($\sim 5 \times 10^4$). The probability of the initial

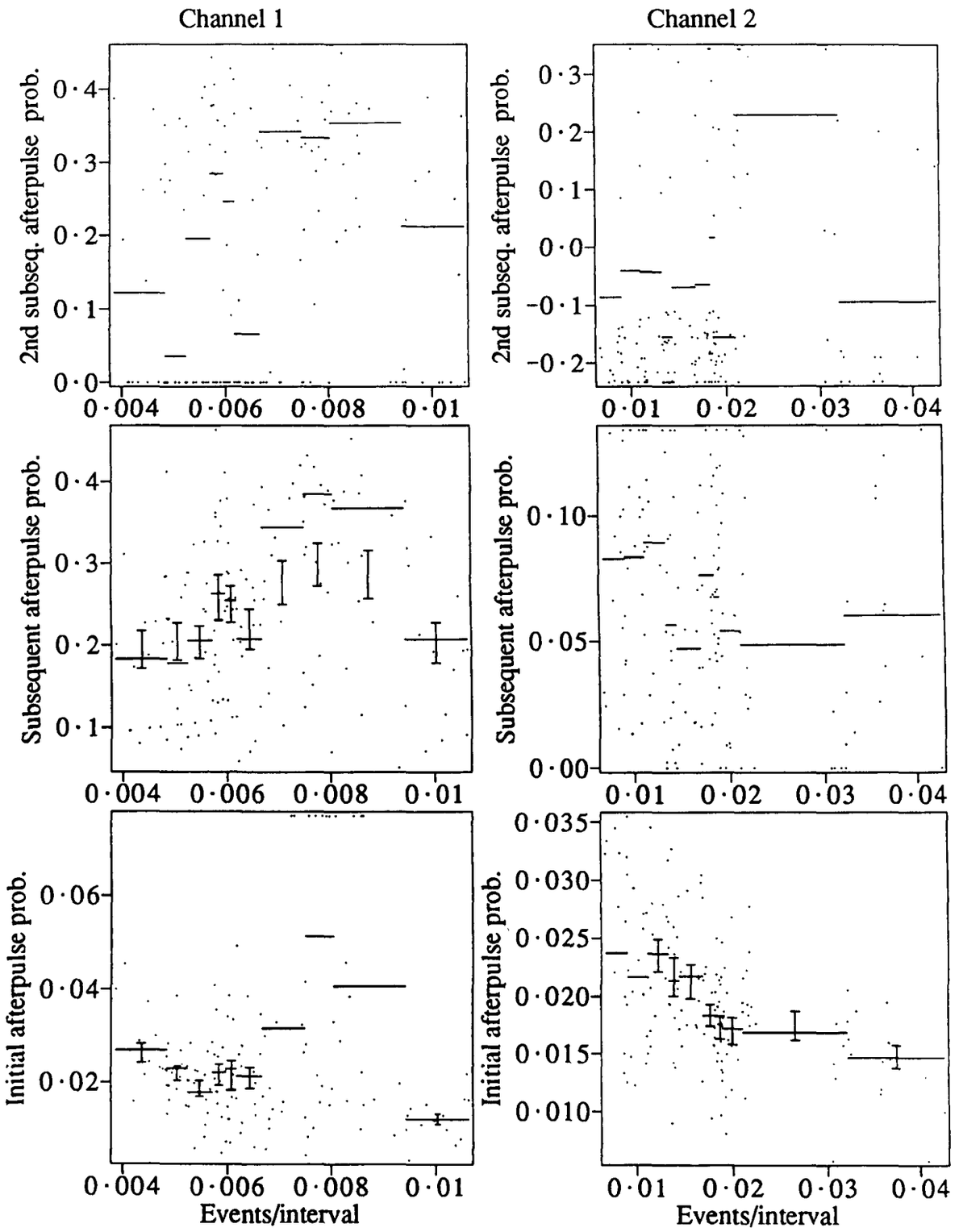

Figure 6-7 The afterpulse analysis is applied to dark noise records. Dots show the afterpulse probability deduced from individual records versus the event rate. Outlying values of the probability have been plotted at the top or bottom of the graph. The horizontal lines indicate a fit of the probability to all the records with an event rate within the subrange indicated by the extent of the line. (These subranges are chosen so that each contains about the same number of records.) For subranges in which there are no outlying values, the mean ± the standard error of the probabilities for individual records is shown by the error bars.

afterpulse p' is then found by numerical solution of equation 4.37, applied to n records:

$$\sum_{i=1}^{n} P_{c_i}(1) = \sum_{i=1}^{n} P_{c_i}(0) r_i \Delta t (1 - p') \; . \qquad -- \; (6.2)$$

The subsequent afterpulse probability P_s' is then found by numerical solution of equation 4.38, applied to n records:

$$\sum_{i=1}^{n} P_{c_i}(2) = \sum_{i=1}^{n} \left\{ \frac{1}{2} P_{c_i}(0)(r_i \Delta t)^2 (1 - p')^2 + P_{c_i}(0) r_i \Delta t p (1 - P_s') \right\} , \qquad -- \; (6.3)$$

where p is the value determined using 6.2 and 4.34. Finally the second subsequent afterpulse probability P_{ss}' is found by solving

$$\sum_{i=1}^{n} P_{c_i}(3) = \sum_{i=1}^{n} \left\{ \frac{1}{6} P_{c_i}(0)(r_i \Delta t)^3 (1 - p')^3 + 2 \times \frac{1}{2} P_{c_i}(0)(r_i \Delta t)^2 p (1 - P_s')(1 - p') + \right.$$

$$\left. P_{c_i}(0) r_i \Delta t p^2 (1 - P_s')^2 + P_{c_i}(0) r_i \Delta t p P_s (1 - P_{ss}') \right\} . \qquad -- \; (6.4)$$

In figure 6-7, the range of event rates r is divided into 10 subranges, each containing an approximately equal number of records. For each of these subranges the afterpulse probabilities p', P_s' and P_{ss}' are deduced using equations 6.2 to 6.4 and converted to the single afterpulse probabilities p, P_s and P_{ss} using equations 4.34 to 4.36. These probabilities are shown in figure 6-7 by horizontal line segments, where the extent of the segment indicates the subrange of event rates to which the summation is applied.

Within each subrange, the mean of the values deduced for individual records (represented by dots) is calculated. The error bars indicate this mean $\pm$ the standard error. This calculation is only applied in subranges where there is no replotting of any outlying values. There is agreement between the averages of individual records and the probabilities found by fitting to many records, except in three cases. This suggests that averaging of probabilities determined from individual records gives correct results only in cases where the scatter of values is not too high. Conclusions will therefore only be drawn from the results of the summation technique, represented by horizontal lines.

The following features can be seen in figure 6-7:

a) the probability of an afterpulse following a dark-noise event is about 1.5% for both tubes at high event rates, but is higher at particular event rates ($\sim$0.008 events/interval) on channel 1.

b) There is a general tendency for the initial afterpulse probability to decline with increasing event rate.

c) The probability of a subsequent afterpulse is > 20% on channel 1, with a maximum at the same event rate as the maximum for the initial afterpulse probability. On channel 2 it declines from 9% at low event rates to 5% at high event rates.

d) The probability of a second subsequent afterpulse P_{ss} is clearly wrong for channel 2, where most of the values are negative. For channel 1 there is an enormous variation in the values, but the average result (~20%) is similar to the value for the first subsequent afterpulse.

Based on information presented in §3.11, points a) to d) above can be interpreted in a way consistent with expectations:

1) the probability of an initial afterpulse following thermionic emission is less than 1.5% (the value observed at the highest event rates), which is at the high end of the range suggested by Coates (1972). This is not unreasonable, given that the tubes were several years old and so diffusion of helium into the tubes would cause significant positive-ion afterpulsing (Coates, 1973).

2) Cosmic ray events which have a high afterpulse probability, such as fluorescence in the glass of the photomultiplier tube lasting 20–50 μs (Coates, 1971), will be less significant when the temperature and hence thermionic emission are higher. This accounts for the decrease in afterpulse probability with increasing event rate.

3) The higher afterpulse probabilities for some event rates (~0.008 events per interval) on channel 1 are probably related to the electromagnetic interference mentioned in §5.2.3. This occasionally caused a large number of spurious counts in a short time. For this situation, where a number of pulses follow each other, the probability of afterpulses must be large and almost equal *ie* $p \sim P_s \sim P_{ss}$. This is seen in the figure, where $P_s \sim P_{ss} \sim 0.3$. (The lower value of p is explained by the averaging of this probability with the lower values for other events.)

4) On channel 2, for which the results are not affected by the electromagnetic noise problem, the subsequent afterpulse probability is about 4 times that of the initial afterpulse probability, as measured by Williams and Smith (1973).

This ***afterpulse analysis*** is repeated in figure 6-8 for 815 skylight records, but

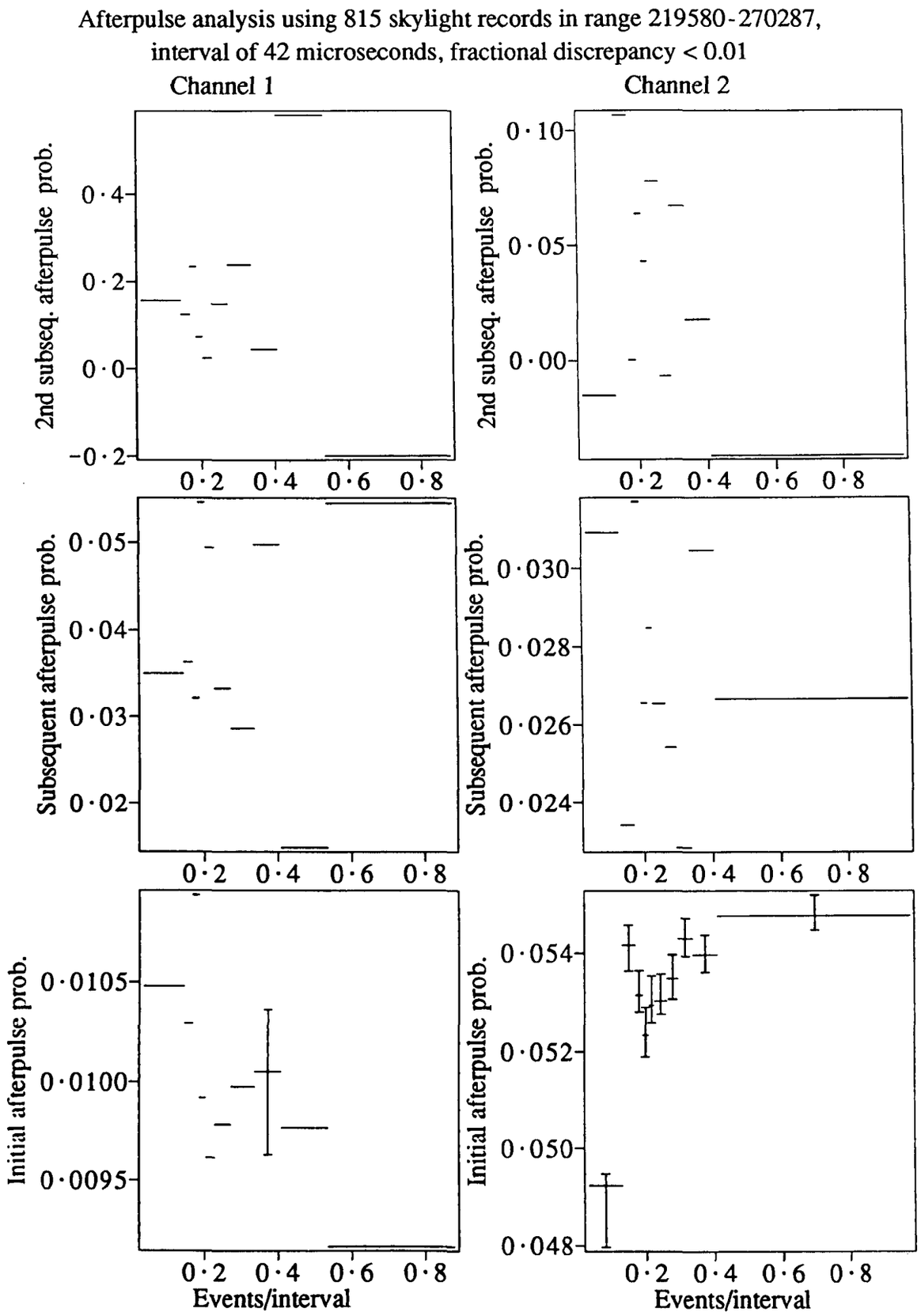

Figure 6-8 The afterpulse analysis is applied to skylight records. The horizontal lines indicate a fit of the probability to all the records with an event rate within the subrange indicated by the extent of the line. (These subranges are chosen so that each contains about the same number of records.) The error bars indicate the mean ± the standard error of the probabilities calculated for all individual records within subranges in which there are no outlying values.

the dots for individual records are not plotted. As this analysis requires the light to be constant over the record, skylight fluctuation and contamination by 100-Hz street lighting will introduce error. This error is presumably reduced by selecting records for which the correlation between the two channels is a minimum, as explained in §4.5.3.3. Here, the criterion used is that the fractional discrepancy between the probability of a particular combination of counts on both channels and the value predicted from the probabilities of these counts on individual channels is less than 0.01 *ie*

$$\frac{|P_j(i,k) - P_{c1}(i)P_{c2}(k)|}{P_j(i,k)} < 0.01 \text{ for } i = 0,1 \text{ and } k = 0,1 \qquad --(6.5)$$

where $P_j(i,k)$ is the observed joint probability of i counts on channel 1 and k on channel 2 in the same sample interval and $P_{cm}(n)$ is the observed probability of n counts on channel m.

From figure 6-8 it can be seen that

a) at all event rates the initial afterpulse probability p is about 1% on channel 1, while on channel 2 it varies from 4.9% to 5.4% as the event rate increases.

b) The afterpulse probabilities are independent of the event rate, except for the lowest event rates on channel 2).

c) The value of the subsequent afterpulse probability P_s varies randomly with event rate, with values from 3% to 5% for channel 1 and 2% to 3% for channel 2.

d) There is too much variation in the observed value of the second subsequent afterpulse probability P_{ss} to make any conclusion.

The results for channel 1 are in agreement with the three predictions made at the beginning of this section:

1) the afterpulse probability of 1% is in the range of 10^{-4}–2×10^{-2}.

2) This value of 1% for photoemission is consistent with the value of < 1.5% for thermal emission deduced from the dark noise records, as the latter has a much smaller count rate and so other sources with a higher afterpulse probability make a greater relative contribution.

3) The ratio of the subsequent to initial afterpulse probability of 3–5 is consistent with measurements by Williams and Smith (1973).

The results for channel 2 disagree with all three predictions, although for dark

noise this channel had given agreement with predictions 1) and 3). This suggests that there is a fundamental difference between the mechanism of afterpulsing on channel 2 for thermionic emission and photoemission. This is supported by the fact that the initial afterpulse probability in figure 6-8 is smaller for the lowest event rate, where the light level is low enough for the thermionic emission to be significant.

A plausible explanation for the results for channel 2 is that the discriminator in the pulse amplifier (see §5.2.3) was set to detect pulses which were very small, so that there was a greater probability of detecting:

1) afterpulses caused by positive ions hitting the dynodes (Candy, 1985a). This is consistent with the lower subsequent afterpulse probability for channel 2 (2–3%), relative to channel 1 (3–5%). As the afterpulses originating at the dynodes contain fewer electrons and traverse a smaller path relative to those produced at the photocathode, there is a smaller probability that they will produce a subsequent afterpulse.
2) Pulses due to thermal emission from the dynodes. These would have a small probability of producing an afterpulse (for the same reasons given above for dynode afterpulses), thus reducing the overall probability of an afterpulse from the 5% for emission at the photocathode to the 2% observed in the analysis of dark noise.

This explanation cannot be checked as the *afterpulse analysis* was developed after the demise of the recording system.

In summary, the *afterpulse analysis* gives results for channel 1 which are consistent with predictions. This suggests that the approach and underlying assumptions of the *afterpulse analysis* are correct. However, the results for channel 2 can be explained only by postulating that the threshold of the pulse discriminator was set too low and that the assumed effects of this account for the observed results. Thus there is an unresolved problem in either the *afterpulse analysis* or the characteristics of the photomultiplier on channel 2.

6.3.2 Direct afterpulse analysis

The *direct afterpulse analysis* is applied here to records of skylight to determine afterpulse probabilities which can then be used to remove the effect of afterpulsing from records of starlight.

The *direct afterpulse analysis* is applied to skylight records with the result presented in figure 6-9. The probabilities of one (P_1), two (P_2) and more than two ($P_{any} - P_1 - P_2$) afterpulses following an event are plotted as functions of event rate. Equations 4.31 to 4.33 are used to calculate the probabilities for individual records. As in the previous two diagrams, error bars indicate the mean $\pm$ the standard error of these values, in subranges of the event rate in which there are no outlying values. The extent of the horizontal line segments indicates these subranges, while their position on the vertical axis indicates the probability for the subrange determined by numerical solution of equations 4.27 to 4.29, modified for summation over n records:

$$\sum_{i=1}^{n} P_c(1) = \sum_{i=1}^{n} P_{c_i}(0) r_i \Delta t (1 - P_{any}) \qquad -- (6.6)$$

$$\sum_{i=1}^{n} P_c(2) = \sum_{i=1}^{n} \left\{ \frac{1}{2} P_{c_i}(0)(r_i \Delta t)^2 (1 - P_{any})^2 + P_{c_i}(0) r_i \Delta t P_1 \right\} \qquad -- (6.7)$$

and $$\sum_{i=1}^{n} P_c(3) = \sum_{i=1}^{n} \left\{ \frac{1}{6} P_{c_i}(0)(r_i \Delta t)^3 (1 - P_{any})^3 + \right.$$

$$\left. 2 \times \frac{1}{2} P_{c_i}(0)(r_i \Delta t)^2 (1 - P_{any}) P_1 + P_{c_i}(0) r_i \Delta t P_2 \right\} \qquad -- (6.8)$$

where the event rate r_i for record i is determined from $P_c(0)$.

The values of P_1, P_2 and $P_3 (\sim P_{any} - P_1 - P_2)$ to be used later in correcting for afterpulsing were determined by taking the average of the solutions of equations 6.6 to 6.8 for nine of the ten subranges of event rates. The value for the subrange with the smallest event rates was not used because it is biassed by the inclusion of records where the light level was very low and the probabilities for afterpulses following dark-noise events are significant. The average values thus determined were P_1=0.00935, P_2=0.00043 and P_3=0.00008 for channel 1 and P_1=0.05210, P_2=0.00409 and P_3=0.00040 for channel 2.

6.4 Correction for afterpulsing

Having determined the afterpulse probabilities, the afterpulse correction techniques developed in §4.5.4 can now be tested. Tests are applied to check that, after correction for afterpulsing,

1) the count distribution for a constant light source is Poisson, and

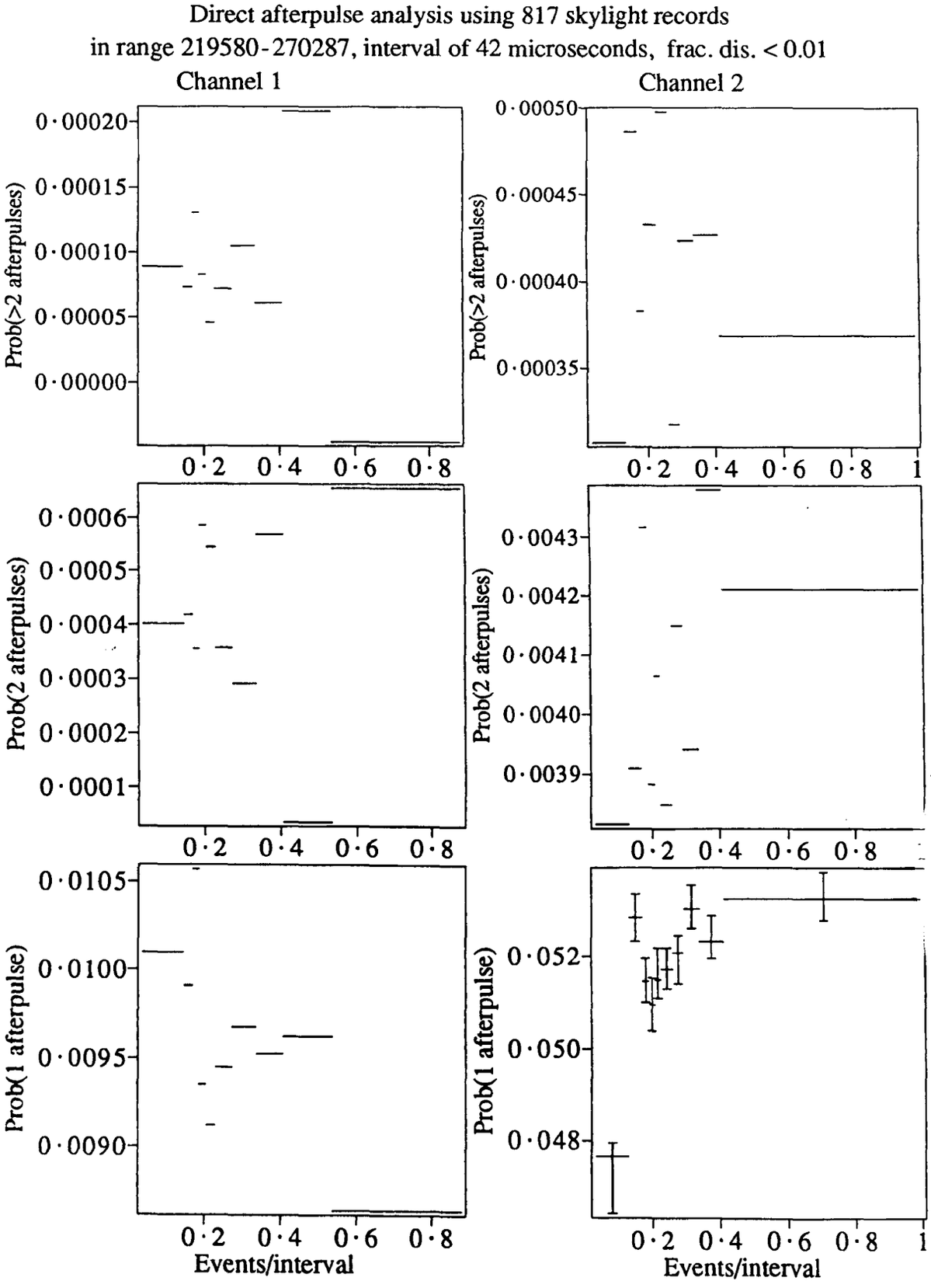

Figure 6-9 The direct afterpulse analysis is applied to skylight records, to deduce the probability of one, two and more than two afterpulses. The horizontal lines indicate a fit of the probability to all the records with an event rate within the subrange indicated by the extent of the line. (These subranges are chosen so that each contains about the same number of records.) The error bars indicate the mean ± the standard error of the probabilities for all individual records within subranges in which there are no outlying values.

2) the moments for a fluctuating light source are consistent between different channels and at different sampling rates.

To identify a Poisson distribution of counts for the first test, equation 3.23 is applied to verify that the normalized second moment is equal to 1. For a constant light intensity I_c,

$$\frac{\langle b(b-1)\rangle}{\langle b\rangle^2} = \frac{\langle I_c^2\rangle}{\langle I_c\rangle^2} = \frac{\frac{NI_c^2}{N}}{\left(\frac{NI_c}{N}\right)^2} = 1 \qquad --(6.9)$$

where b is the number of photocounts in each of N sampling intervals. If afterpulsing is present, the term $b(b-1)$ will be proportionally larger for larger values of b, giving a value greater than 1 in equation 6.9.

The result of this test is presented in figure 6-10, where the normalized second moment $\frac{\langle I_c^2\rangle}{\langle I_c\rangle^2}$ is calculated for records of skylight on one night, before and after correction for afterpulsing. This particular night was selected because the Moon was close to full, thus reducing the relative contribution of the 100-Hz fluctuation of the street lights to the skylight.

Comparisons are plotted between the 2 channels and between 2 different sampling rates on the same channel, where each pair of compared records come from the usual recording sequence of a frequency distribution followed by a time series. These moment comparisons are plotted in the upper part of figure 6-10 for the recorded data and in the lower part for the same data, corrected using equation 4.46 with the values of P_1, P_2 and P_3 determined in the previous section.

In each comparison of figure 6-10, each dot indicates the second-moment values for a pair of records. As expected, nearly all of the values for the uncorrected data are greater than 1. The dashed line shows a fit by regression to these points. The solid square indicates the average of the values along each axis, while the hollow square indicates the same average after application of a correction (using equation 4.52) for a dead time of 30 ns (which is set by the width of the pulse produced by the pulse shaper described in §5.2.5). The solid triangle indicates the expected value of 1 for no afterpulsing or dead time.

The comparison for the corrected data shows a significant improvement relative to the original distributions, with the average values of the normalized second moment

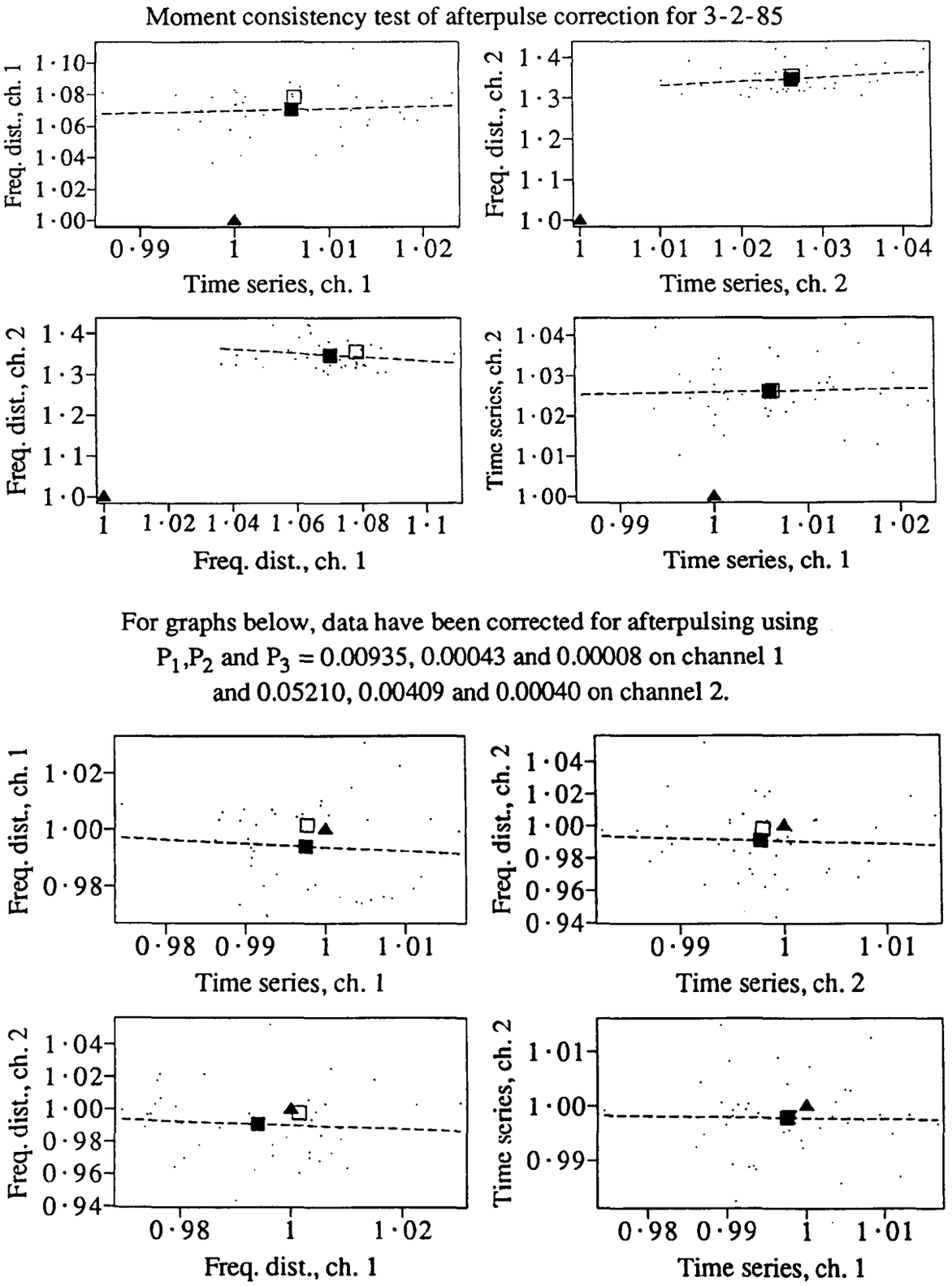

Figure 6-10 The afterpulse correction is tested by comparison of the moments of pairs of skylight records. Values of the normalized second factorial moment $\frac{\langle n(n-1)\rangle}{\langle n\rangle^2}$ (n being counts/interval) are compared for different record types (frequency distribution and time series) and for different channels (1 and 2). The four comparisons are made for the original records in the upper graphs and after correction for afterpulsing in the lower graphs. Dots indicate the comparison for individual records, dashed lines indicate fits by regression to these, solid squares indicate the comparison for the average of the values along each axis and solid triangles indicate the expected value of 1. Hollow squares indicate the average values after a subsidiary correction for dead time.

being much closer to 1 in all cases. The correction for dead time is small compared to that for afterpulsing, but in all cases it moves the measurement closer to the expected value.

In the comparison of the moments for different channels in figure 6-10, the regression line fitted to the values for individual records is close to horizontal. This indicates that the skylight varies little over the time covered by each record, otherwise there would be correlation between the moments on the two channels and the regression line would have a slope near 1.

In figure 6-11 the moment consistency test of figure 6-10 is applied to starlight data for a night when the scintillation had high variance and low frequency. (High frequency scintillation would be detrimental in this test as the time series observations would suffer temporal averaging, reducing the calculated moments relative to those for the frequency distributions.) The presentation is similar to figure 6-10, but the solid triangle is no longer relevant and the result expected here (equal moments for both records) is indicated by a solid line. For the uncorrected data there are large differences between the moments on the two channels for the frequency distributions and between the moments on the same channel for different sampling intervals. There is relatively good agreement between the two channels for time series, indicating that the effect of afterpulsing on values of the second moment is small for a longer sampling interval.

The lower part of figure 6-11 shows that the correction for afterpulsing works very well. The regression line fitted to the data and the average values are close to the expected relationship indicated by the solid line in all cases.

The overall success of this afterpulse correction suggests that the theory developed in chapter 4 for the calculation of and correction for afterpulsing is correct. It also suggests that the equipment, data recording and analysis were all working as expected.

6.5 Correction for background

In the usual recording sequence, several records of starlight (which include an unwanted background of skylight and equipment noise) were taken, followed by a background record. Equation 4.21 can be applied to a starlight and a background record

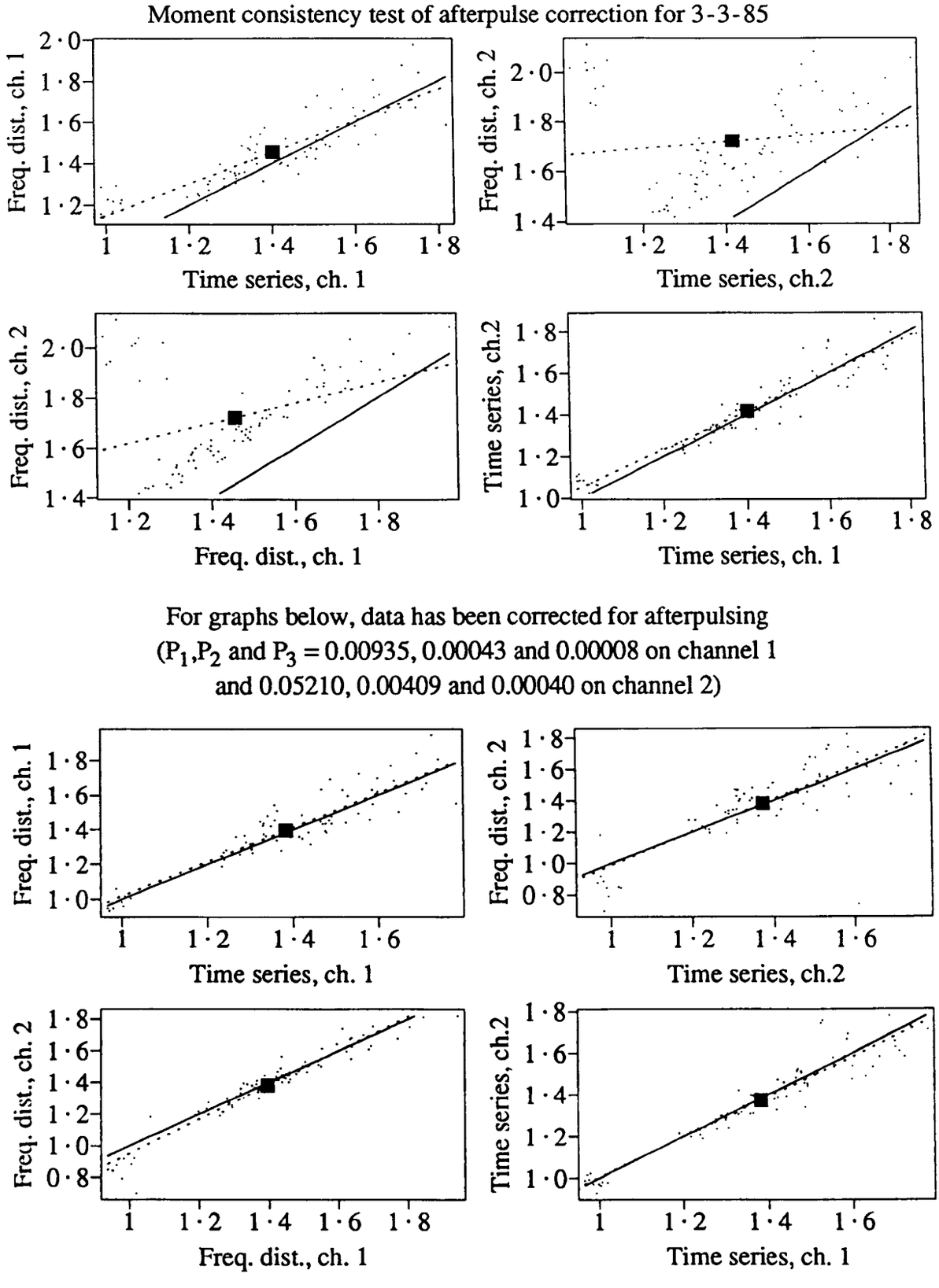

Figure 6-11 The afterpulse correction is tested by comparison of the moments of pairs of records. Most of the pairs are of starlight, but some are of skylight. Values of the normalized second factorial moment ($< n(n-1) > / < n >^2$, where n is the number of counts per interval) are compared for two sampling intervals (542 μs for time series and 42 μs for frequency distributions) and for two photomultipliers (channels 1 and 2). The four comparisons are performed before and after the data is corrected for afterpulsing. In each graph the dots indicate the comparison for individual records, the solid square indicates the comparison for the average of the values along each axis, the dashed line is a fit by regression to the data and the solid line indicates equal values.

to deduce the normalized second moment for the starlight alone. A way to test this correction for background is to compare the moments on the two channels in a situation where the starlight is the same on the two channels but the skylight is different. In such a case the moments should be different for the light plus background, but the same after correction for background. This situation arises in the "multiple collimator", used with 2-mm apertures added at the front. In this case, all of the starlight passing through the apertures should fall on the optical cables (as they are larger than the apertures) and so the amount of starlight detected should be the same on both channels. As each point on the optical cable receives the same contribution from skylight, the total skylight will be smaller on channel 2 as the diameter of the cable is smaller.

The result of this test is shown in figure 6-12, where the normalized second moment is compared between two 2-mm apertures, separated by 1.1 cm, for the total signal I_t (starlight plus background) at the top and for just starlight I (after application of equation 4.21 to correct for background) at the bottom. The test is restricted to the smallest available aperture separation of 1.1 cm to reduce the difference in the scintillation on the two detectors to a minimum. The analysis is applied to frequency distributions on the left and to time series on the right. Each dot compares the normalized second moment between the two channels for one record. A line indicates the expected equal values and the bars indicate the mean $\pm$ the standard error of the observed value on channel 2 for subranges of the channel 1 values.

The average values of the second normalized moment on the two channels are substantially the same whether or not the correction is applied, except at high levels of variance, where there is insufficient data to expect agreement. For both frequency distributions and time series, the fit by regression is closer to the equal value line for the corrected data. Thus the correction for background appears to work satisfactorily, but the initial discrepancy (before correction) is not large enough to provide a conclusive test.

6.6 Optical system performance

The predicted and measured photocount rates for various stars, aperture sizes and filters are compared in figure 6-13. The predicted rate is calculated using equation 5.1

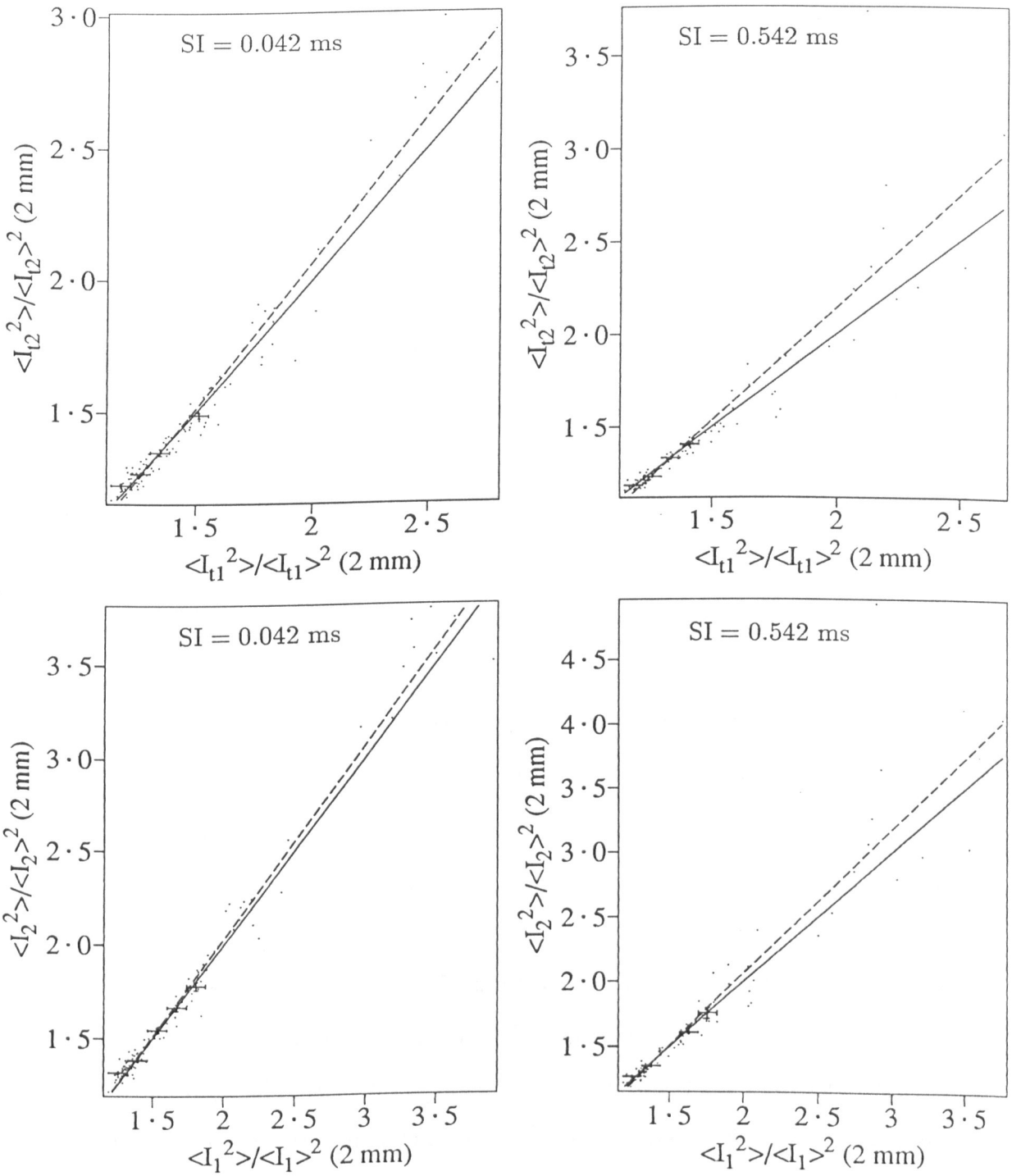

Figure 6-12 A test of the method of correction for background. The normalized second moments on channels 1 and 2 are compared for records of the scintillation of Sirius, observed with two 2 mm apertures, separated by 1.1 cm. In the upper graphs the comparison is made for the total light intensity (I_{tn}, where n is the channel number), while in the lower graphs the correction for background has been applied to yield the values for starlight only (I_1 and I_2). The comparison is made for frequency distributions on the left and time series on the right (identified by the sampling interval SI). In all cases the correction for afterpulsing has been applied. In each plot, dots indicate the comparison for individual records, a line indicates equal values, a dashed line indicates a fit by regression to the data and error bars indicate the mean $\pm$ the standard error of the normalized second moments for channel 2 and the range of channel 1 values for which this mean is calculated.

and is represented in the figure by a curve drawn against star elevation. The observed rates (which have been corrected to remove the effects of afterpulsing and background) are shown as individual values with bars. The range of elevations for which data is available is divided into 10 subranges and the mean ± the standard deviation of the count rates for all records within each subrange is shown. The standard deviation is used to give an indication of the variation in observed values. Such variation is expected because:

a) the optical cable in channel 1 was cleaned and its alignment on the photomultiplier reset on Feb. 6th, halfway through the observation interval. The large standard deviations in some plots for channel 1 (particularly for α Crucis with a 4.8-mm aperture) show the effect of this change.

b) Atmospheric transmission varies.

From figure 6-13, it can be seen:

1) there is good agreement between observations and the prediction for Sirius with a 4-mm aperture on channel 2.

2) For unfiltered channel-1 values with a 4.8-mm aperture, the observed rates are only 40% to 70% of the predictions. This is not unreasonable, due to

   a) the problems mentioned above and

   b) loss of light when the "multiple collimator" is not exactly aligned on the star (see §5.2.2).

3) For 2-mm apertures, the ratio of observed to predicted rates is about 20% higher on channel 2 than on channel 1. This may be due to errors in the manufacturer's efficiency measurements (which are not specified), aging of the photomultiplier tubes and different discriminator settings on the two channels. (The lower discriminator setting postulated above to explain the high channel-2 afterpulse probability would increase the signal level.)

4) For channel 2 with 2-mm apertures, the observed/predicted ratio is about 30% higher than for 4-mm apertures. A plausible explanation is that, with the smaller aperture on the front of the "multiple collimator", the star can be further away from the centre of the field of view before any light is lost (see §5.2.2).

5) The observed rates for β Crucis, relative to predictions, are higher than for α

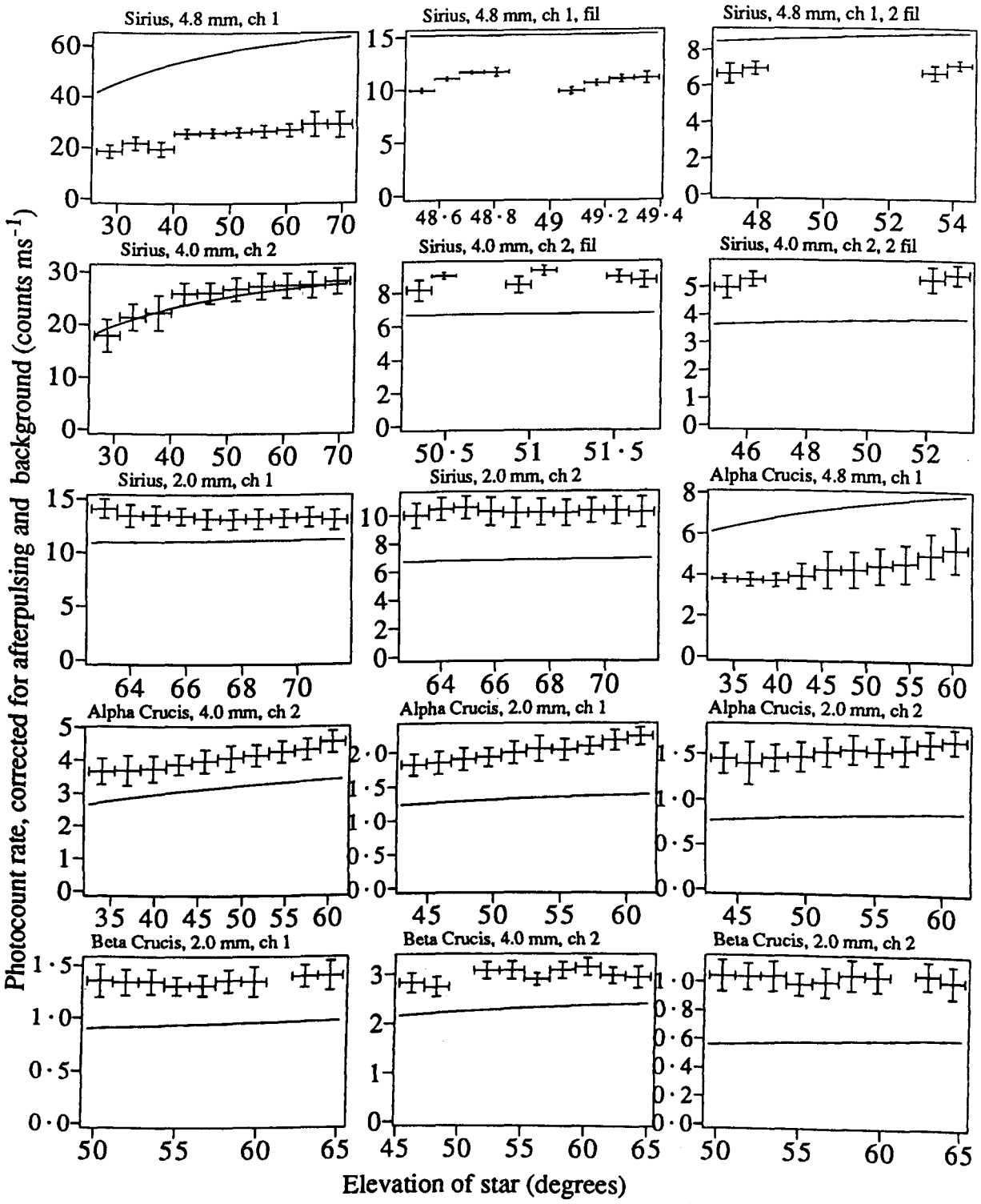

Figure 6-13 A comparison of observed and predicted photocount rates as a function of star elevation for various stars, apertures, filters and channels. In each plot the continuous curve shows the predicted photocount rate as a function of elevation angle, over the range of elevation angles for which observations are available. This range is divided into ten equal subranges. The mean of the observed photocount rates for all records within each subrange is plotted as an individual value, with bars indicating the standard error in the mean and the limits of the subrange. The comparison is made for the stars Sirius, α Crucis and β Crucis, for various combinations of aperture size, filter and channel number. (*nb* "fil" and "2 fil" indicate 1 and 2 layers of the blue filter.)

Crucis, which are in turn higher than for Sirius. A plausible explanation is that the spectra for individual stars may be different to the average for their spectral class, which was used in the calculation.

6) Generally, for channel 2, the observed elevation dependence follows the predicted curve.

7) The ratio of observed to predicted rates is the same for 1 and 2 layers of the blue filter, so there is no indication of any gross error in the calculated spectral response of the system.

Thus most of the discrepancies in figure 6-13 can be explained, except that the observed photocount rates on channel 2 exceed predictions by up to 50%. The main conclusion relevant to the work in this thesis is that there is no gross loss of signal in the system, other than that described above for channel 1.

6.7 Observation of street lights

Although contamination by street lights is generally a problem in this work, it does have the advantage of providing a signal for calibration purposes. In figure 6-14, frequency spectra are plotted for records which are contaminated with varying amounts of artificial light, operating on a 50-Hz mains supply. These frequency spectra are calculated using the FFT (Fast Fourier Transform) Fortran subroutine by Singleton (1969).

In the middle graph of figure 6-14, spectra are plotted for 8 time series taken with the "split-lens" telescope when it was not shielded from a nearby security light. (*nb* The light was not imaged onto the detector. The telescope was pointing at the sky and the detected artificial light was scattered by the Fresnel lens.) There is a peak at 100 Hz and harmonics at 200 Hz and 300 Hz, as expected, verifying that there is no significant error in the system timebase.

The other plots in figure 6-14 indicate the level of contamination by artificial light for representative skylight records measured with the "multiple collimator" and the "split-lens" telescope. The upper plot shows that for the "multiple collimator" the amplitude of the 100-Hz signal is only about 4% of the mean light level (which is indicated by the peak on the left at 0 Hz). The artificial light component for the "split-

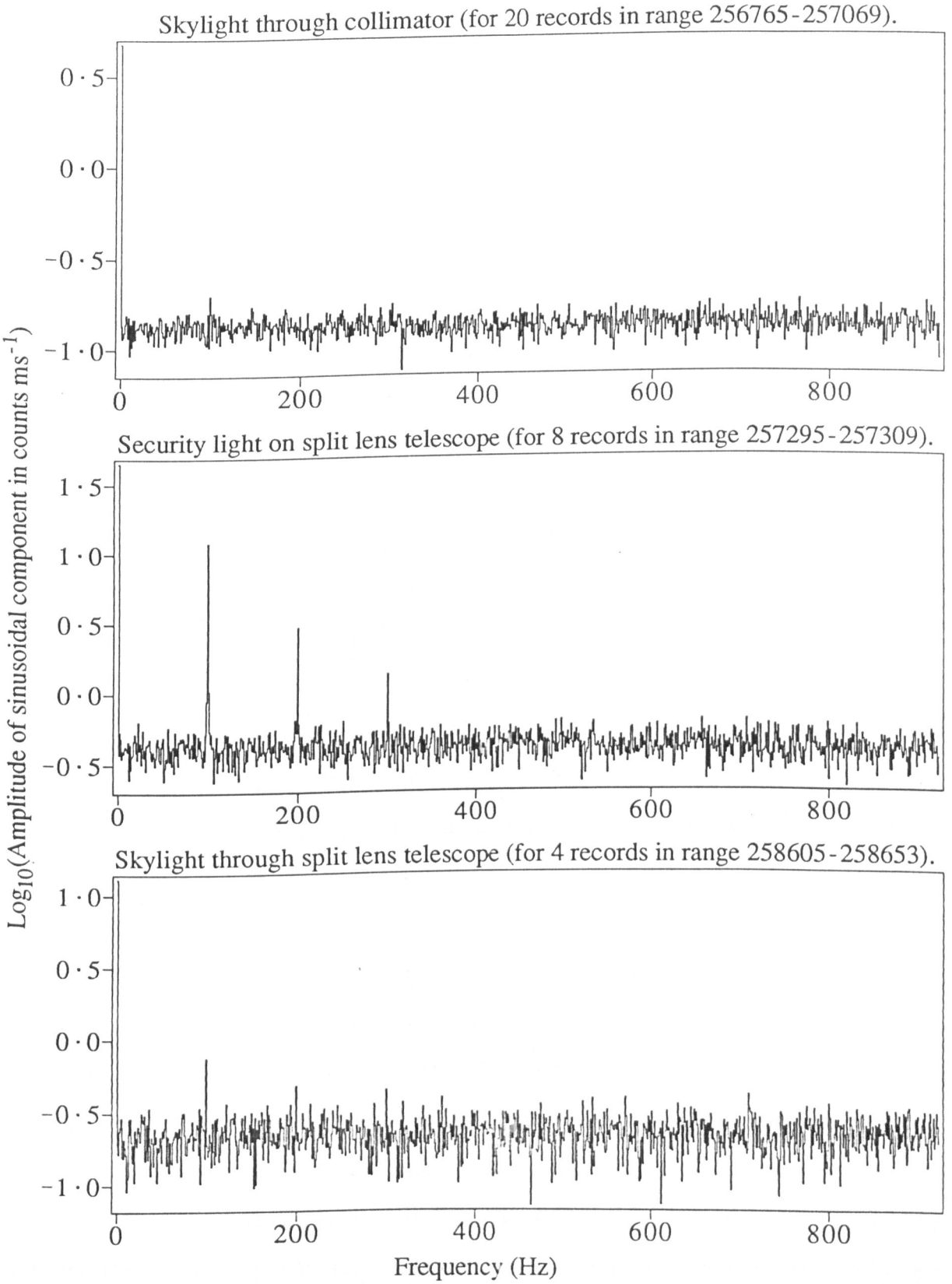

Figure 6-14 Logarithmic amplitude spectra for records contaminated with different fractions of artificial light, running on 50 Hz mains supply. The fraction can be judged by the ratio of the 100 Hz component to the value at 0 Hz in each spectrum. The spectrum for typical skylight records taken with the collimator is shown at the top. The middle spectrum is produced when light from a nearby security light is scattered by the Fresnel lens in the split lens telescope. The typical skylight spectrum for this instrument (with the lens shielded from the security light, but not from other fainter lights) is plotted at the bottom.

lens" telescope (lower plot) is slightly higher, presumably because, although it was shielded from the brightest nearby light, it was not shielded from some other, fainter lights. These measurements were made when there was no moonlight, so the ratio of the 100-Hz component to the skylight is presumably close to the maximum.

6.8 Comparison of different instruments

Some data was taken with the "multiple collimator" and the "split-lens" telescope at the same time to determine whether there were any differences in the statistics of the signals on the two channels. Such differences could be due to:

a) a different transmitted spectrum, due to absorption by the Fresnel lens in the "split-lens" telescope.

b) An effect of focussing in the telescope, *eg* phase variations in the wavefront could shift the image of the star rapidly in the focal plane, so that spatial variations in the optical cable or photomultiplier would produce intensity fluctuations.

c) Similar fluctuations caused by the movement of the focussed image due to the Earth's rotation, as discussed in §5.2.2.

Figure 6-15 indicates that such differences between the two telescopes are not detectable in the available data. It compares, at two sampling rates, the normalized second moment $\frac{\langle I^2 \rangle}{\langle I \rangle^2}$ of the light intensity I observed on 4.8-mm apertures with the "multiple collimator" and the "split-lens" telescope for two stars, Canopus and Sirius. Unfortunately a correction for background cannot be made, as suitable skylight records were not taken. As the field of view of the two instruments is different, the signals consist of the same starlight signal with a different skylight component added, so that without correction for background the moment values will differ between channels. As Sirius is much brighter than Canopus, the effect of the background is much less significant for Sirius. It can be seen in figure 6-15 that there is much better agreement between the two instruments for Sirius than for Canopus. It is concluded that there is no major difference between scintillation detected by the two different instruments.

6.9 Tests of correlation functions

In §4.2.4 a "correlation by minimum difference" function was developed for application to the remote sensing of wind velocity using the scintillation of a double star.

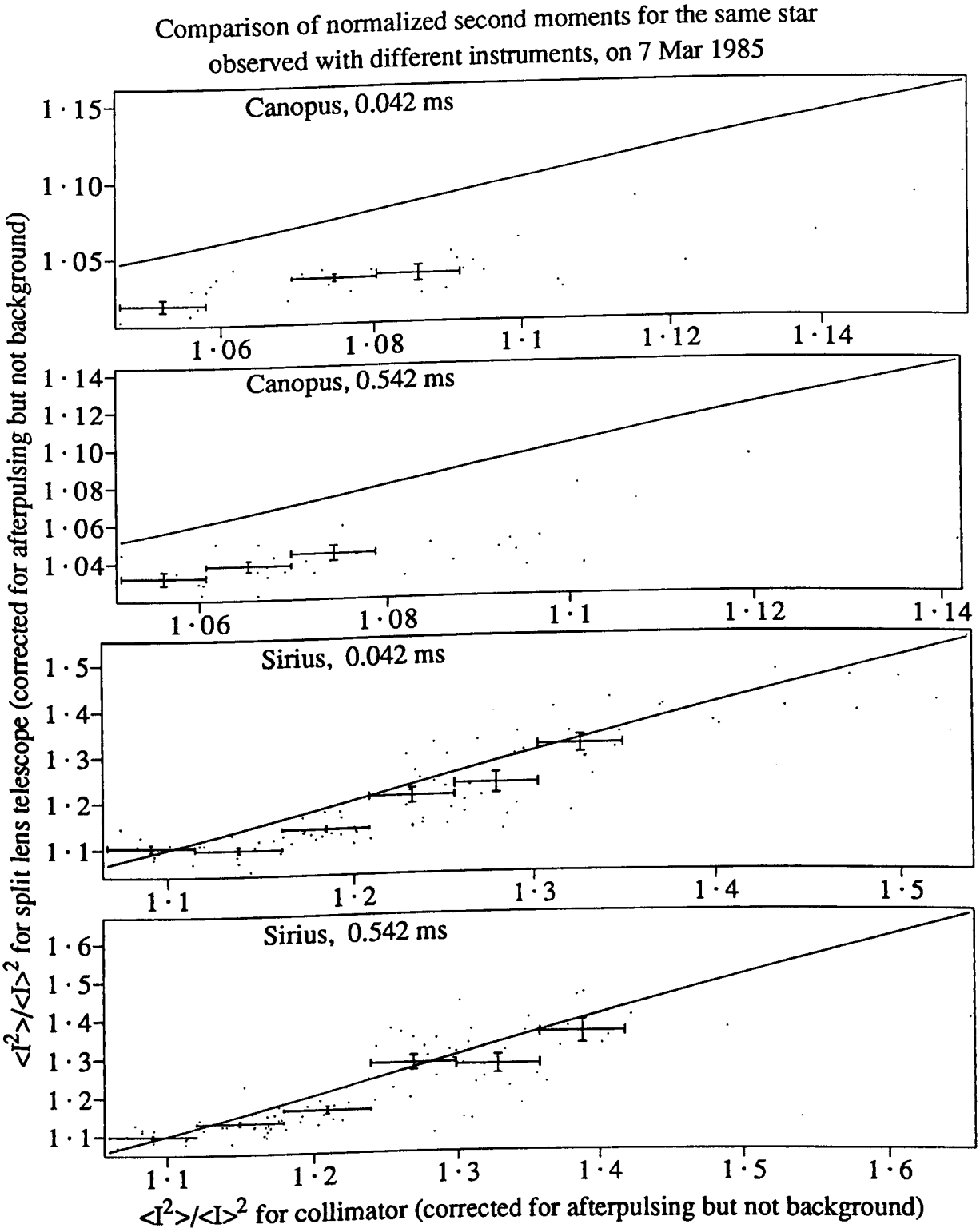

Figure 6-15 A comparison of the variance of starlight observed with an imaging and a non-imaging detector. The normalized second moment $\langle I^2 \rangle / \langle I \rangle^2$, corrected for afterpulsing but not background, is compared for simultaneous observations with the "multiple collimator" and the "split lens" telescope (both with a 4.8 mm aperture). The comparison for each record is indicated by a dot, with bars indicating the mean and standard error of the values for the "split lens" telescope within selected ranges for the "multiple collimator". The line indicates equal values. The comparison is made for two stars (Sirius and Canopus) and two sampling intervals (42 μs and 542 μs).

It was shown to give good results for simulated data. Before applying the method to scintillation, where the situation is complicated by both photon noise and unknown atmospheric factors, it is sensible to test it on a signal of known characteristics, where the photon noise is the only new factor. The records of 100-Hz light (used earlier in §6.7) provide suitable data for this test. This also provides an opportunity to test equation 3.23 (given by Jakeman *et al*, 1978), to ensure that it is being applied correctly by this author.

In figure 6-16 various correlation functions are applied to a record of time series containing 100-Hz signals. The time series are plotted at the top and various temporal auto- and cross-correlation functions of this record are plotted below. (*nb* The large spike on channel 1 near the beginning of the record is an extreme case of the electromagnetic noise referred to in §5.2.3.)

The normalized second moment $\frac{\langle I^2 \rangle}{\langle I \rangle^2}$ is calculated using equation 3.23 and its generalization $\frac{\langle I_1(t) I_n(t-t_{1n}) \rangle}{\langle I_1 \rangle \langle I_n \rangle}$ (for channels $n = 1, 2$ and time shift t_{1n} of channel n relative to channel 1, excluding $t_{11} = 0$) is calculated using equation 3.26. The plot of these functions in figure 6-16 (second graph) shows results as expected, with peaks in the auto- and cross correlation where the time shift is a multiple of 0.01 s and with the same shape for both functions. Note in particular that there is no discontinuity in $\frac{\langle I_1(t) I_1(t-t_{11}) \rangle}{\langle I_1 \rangle^2}$ at $t_{11} = 0$, which confirms that equation 3.23 correctly removes the effect of photon noise.

The impact of this correction for photon noise can be appreciated by reference to the second correlation plot in figure 6-16, where the covariance is calculated for the time series of count values (where the subscript *nor* indicates that the time series have been normalized to zero mean and unit standard deviation). There is a large spike in the autocovariance at zero time delay, because at all other time delays there is significant decorrelation due to photon noise.

The new function, "correlation by minimum difference" (equation 4.18), is applied to produce the third correlation plot in figure 6-16, using $C_{md}(1_{nor}(t) n_{nor}(t - t_{1n}))$. This function gives a large value at zero time delay in the autocorrelation, so much so that the logarithm is plotted in the figure. There is close agreement, as required, between the auto- and cross-correlation functions at other time delays.

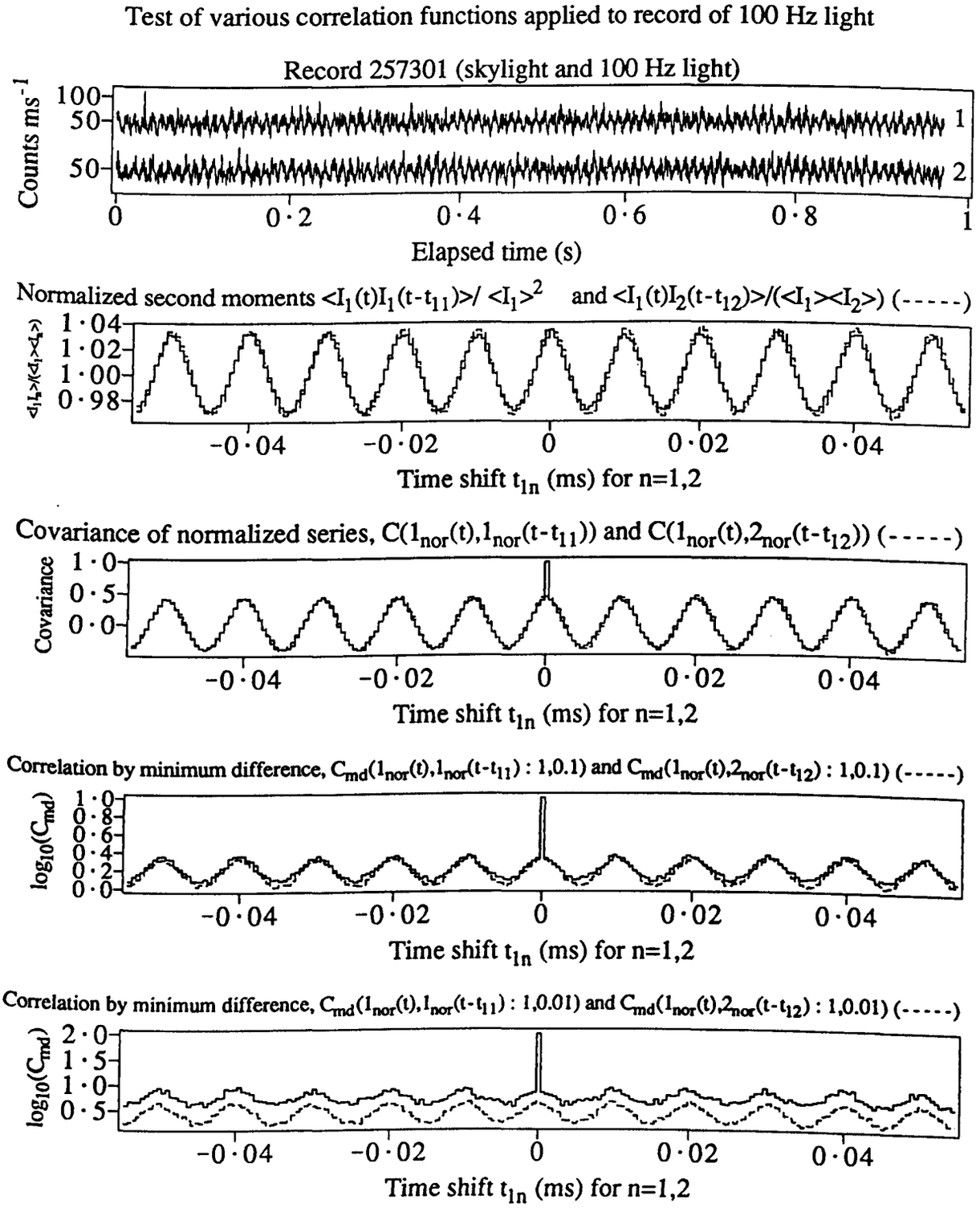

Figure 6-16 A test of various correlation functions applied to a record of artificial light fluctuating at 100 Hz. This record is plotted at the top. Below, the auto correlation for channel 1 (solid lines) and the cross correlation between channels 1 and 2 (dashed lines) are plotted against time shift for each of the four functions:

- $\frac{\langle I_1(t) I_n(t-t_{1n})\rangle}{\langle I_1(t)\rangle\langle I_n(t-t_{1n})\rangle}$, the normalized second moment, where $n = 1$ or 2, $I_n(t)$ is the light intensity on channel n at time t and t_{1n} is the time shift applied to channel n relative to channel 1.
- $Cov(1_{nor}(t) n_{nor}(t - t_{1n}))$, the covariance of series 1 and n, where these are normalized to zero mean and unity standard deviation.
- $C_{md}(1_{nor}(t) n_{nor}(t - t_{1n}); 1, 0.1)$, the correlation by minimum difference.
- $C_{md}(1_{nor}(t) n_{nor}(t - t_{1n}); 1, 0.01)$.

In the plot at the bottom of figure 6-16 the value of this test becomes apparent. With a higher degree of pattern matching (using $F = 0.01$ to give a high weighting to very close values) the autocorrelation function becomes less clearly defined and the value of the cross correlation is greatly reduced relative to the autocorrelation. These erroneous results are due to the combination of the small F value and the fact that the data series have only integer values. Thus, irrespective of the phase of the 100-Hz signal in the series being compared, there is a small probability that the count value will be the same on both channels and will give a large but meaningless contribution to the value of C_{md}.

In figure 6-17 the effect of changing the other pattern matching parameter M is investigated. This is done by using "correlation by minimum difference" to deduce the ratio between the two channels of the amplitude of the 100-Hz signal. For reference, the amplitude spectra are given and these show that the 100-Hz signal on channel 2 is 11% larger than on channel 1. At the bottom, an attempt is made to deduce this ratio by calculating $C_{md}(1_{ms}, R \times 2_{ms}; M, 0.1)$ as a function of R for $M = 1$ and 5, where the subscript "ms" indicates that the mean value has been subtracted. The value of R found using the amplitude spectra is indicated by a dashed line. It can be seen that correlation by minimum difference gives a maximum at the correct value of R, but only gives good resolution on this maximum for the larger value of M.

The conclusion is that "correlation by minimum difference" can be applied to signals which include photon noise, but only where the correlated fluctuations persist over at least several consecutive measurement intervals.

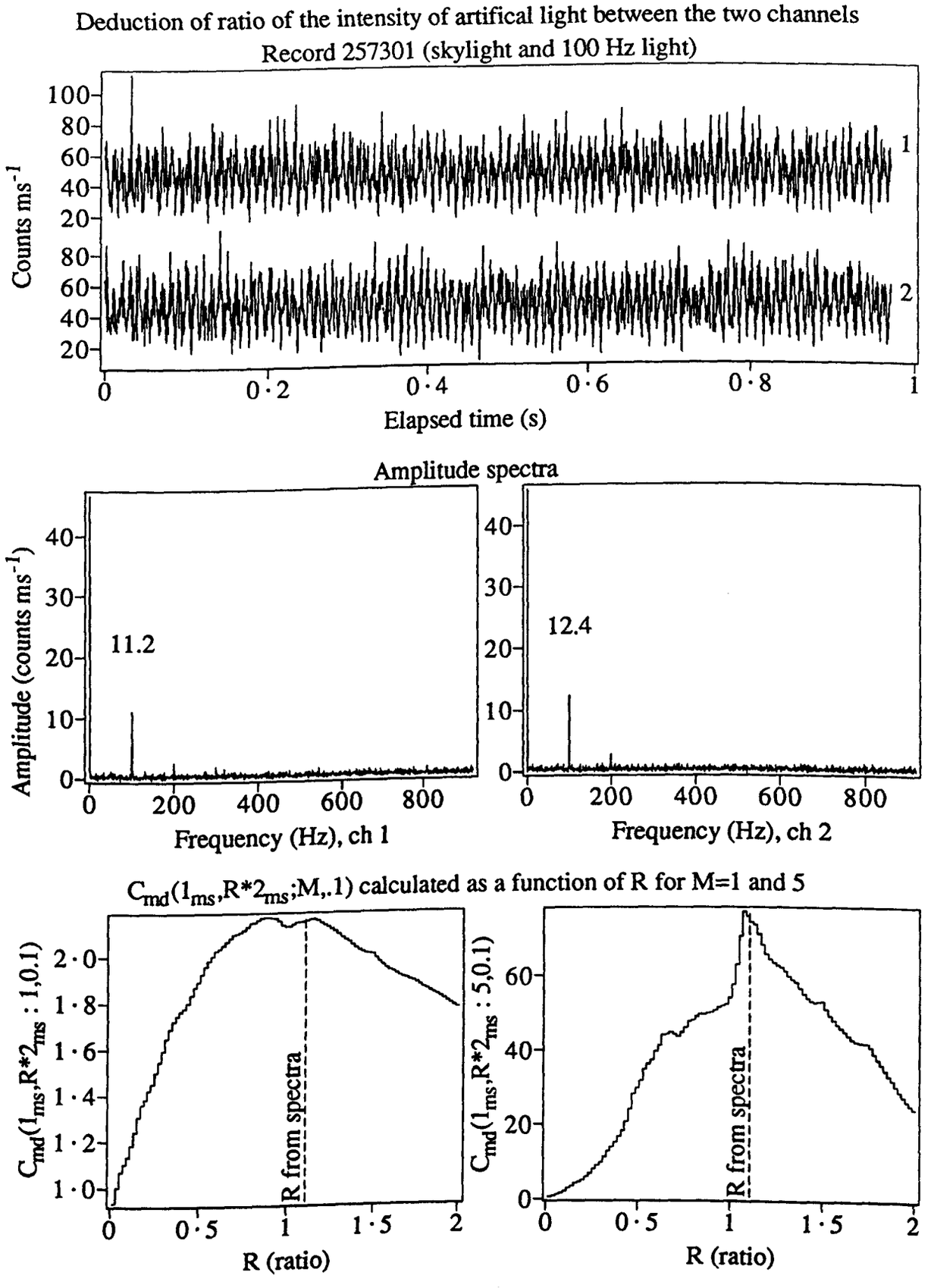

Figure 6-17 A test of the application of C_{md} (correlation by minimum difference) to data which includes photon noise. A recording of skylight plus 100-Hz artificial light is plotted at the top. A frequency spectrum for each of the two channels is plotted in the middle. The peaks at 100 Hz are annotated with their amplitude. At the bottom $C_{md}(1_{ms}, R * 2_{ms}; M, 0.1)$ is plotted against R, for $M = 1$ and 5. The subscript ms indicates that the mean value has been subtracted from the time series.

Chapter 7 Multiple-beam test

This chapter presents results of a laboratory test of the multiple-beam techniques introduced in §4.1.3 and of some of the associated multiple-correlation methods developed in §4.2. The observations were made using the crossed-laser arrangement, equipment and methods described in §5.1, producing the scintillation patterns and intensity records illustrated in §6.1.

In the arrangement used, hot hair driers produce turbulence in a small section of a 40-m path. This is not a good simulation of stellar scintillation as the refractive-index variations are greater than occur in the atmosphere and the distance over which the scintillation can develop (about 18 m) is much shorter than the several kilometres for stellar scintillation. However, this test has value in that it does simulate two factors that are critical in the application of multiple-beam remote sensing to stellar scintillation but were not relevant in the previous application using a seeded flow (Sasaki and Sato, 1979), *viz*:

a) the refractive-index variations do not absorb or scatter the light, but redistribute it to produce a scintillation pattern. This creates problems in the application of the standard triple correlation, as explained in §4.2.1.

b) More than one irregularity can contribute simultaneously to the scintillation pattern, leading to false correlations (as illustrated in figure 4-8).

Some of the measurements were of scintillation produced by two turbulent streams with different velocities acting simultaneously. These are used to test the method proposed in §4.3.2 to investigate whether there is interaction between the scintillation patterns produced at different positions.

7.1 Temporal covariance

The multiple-beam method of remote sensing determines position and velocity from the combination of time delays between similar patterns arriving at different detectors (§4.1.3). Before applying this method, it is sensible to investigate the simpler case of the movement of the scintillation pattern from one detector to another.

As shown earlier in figure 6-2, the scintillation pattern produced in the crossed-laser experiment changed significantly in moving only a few millimetres. This makes it

difficult to determine whether particular features are related, so it is necessary to apply a correlation analysis. In order to investigate the addition of scintillation patterns, the correlation function should not be normalized. An appropriate function to meet these requirements is the cross covariance as a function of time shift between the signals on the two detectors.

A 0.2-s crossed-laser record of the scintillation produced by a single turbulent stream is plotted in figure 7-1. The position and direction of this particular stream is indicated by the leftward pointing arrow in figure 5-1. The scintillation patterns produced by this stream should cross the detectors in the order 4, 2, 1 then 3. It is easy to see correlated features between channels 1 and 2 in the time series, with channel 2 leading. In the middle left of figure 7-1 the time-shifted cross-covariance function

$$Cov(I_1(t), I_n(t - t_{1n})) = \langle (I_1(t) - \langle I_1 \rangle)(I_n(t - t_{1n}) - \langle I_n \rangle) \rangle \qquad --(7.1)$$

is applied to pairs of series in the record plotted at the top, where $I_n(t)$ represents the light intensity on channel n at time t. As expected there is a peak in covariance at some positive values of t_{12} for the covariance between channels 1 and 2. There is no clear peak in the covariance of channel 1 with channels 3 and 4.

On the lower left of figure 7-1, the same covariance analysis is applied to the scintillation produced by a single stream in a different position (close to P_{24} in figure 5-1, blowing in the positive direction). In this case there are clear peaks in cross covariance between channel 1 and each of the other three channels. The finite width of these peaks is partly explained by the finite size of the patterns, as seen in figure 6-1. However, this factor on its own would produce symmetrical peaks. The asymmetry of the peaks, with the sharp drop in covariance near zero time delay, suggests that the scintillation patterns have a range of speeds.

There is a tendency for the correlation to be negative at zero time delay. Two possible explanations are that:

a) the predominant scintillation pattern size is such that the separation between a bright region and the surrounding dark region is equal to the separation of the detectors, and

b) refractive bending of the light beams causes anticorrelated fluctuations. (As the

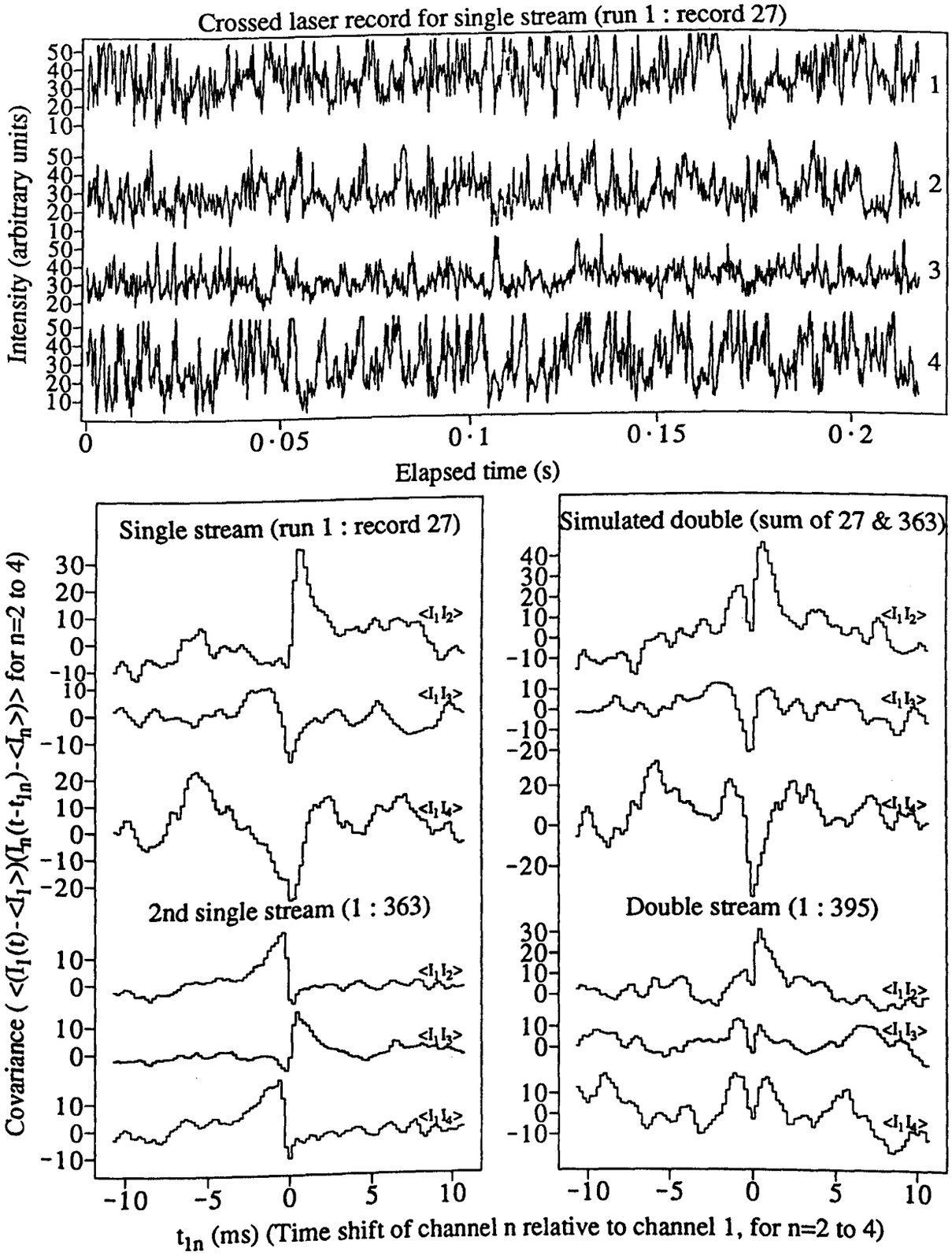

Figure 7-1 An analysis of the temporal cross covariance of the scintillation produced by two turbulent streams on spaced detectors. A record of the scintillation produced by a single turbulent stream is plotted at the top, showing time series of the intensity on the four detectors (labelled 1-4 on the right). The cross covariance as a function of time shift between channel 1 and the other three channels for this record is plotted at the middle left. Beneath this, the covariance is plotted for a second single stream in a different position, showing a different distribution of peaks. On the middle right the covariance is shown for a simulated double stream, produced by adding the time series for the two single streams. On the lower right, the analysis is applied for a record of scintillation produced by the two streams acting simultaneously.

intensity falls off towards the edge of the laser beam, two detectors in the same beam would produce anticorrelated signals as the beam moves to and fro.)

Reference to figure 5-1 shows that refractive bending should produce correlated fluctuations on detectors 1 and 3 and anticorrelated fluctuations between detectors 1 and 2 and between 1 and 4. In figure 7-1 the anticorrelation occurs on all pairs, so it seems that a) rather than b) is the cause.

On the right hand side of figure 7-1 the effect of combining the scintillation of the two streams is investigated. On the middle right, the addition of the scintillation patterns is simulated by adding the time series for the individual records and then calculating the covariance for the sum. In the covariance between channels 1 and 2 of the summed series, both of the peaks for the individual series are present, with their original heights. On the lower right the covariance is calculated for a record in which both of the turbulent streams were present simultaneously. The peak which occurred for the first individual stream (record 27) is clearly visible but all other features are below the noise level.

To improve the signal-to-noise ratio, the above covariance analysis is repeated in figure 7-2, using 20 records for each situation. The average of the 20 covariance values is plotted, with error bars indicating the standard error. It can be seen that:

a) all covariance peaks present for the individual streams are visible for the combination, both for the simulated and actual double-stream cases.

b) Generally the covariance functions for the actual and simulated double streams are similar.

c) For channels 1 and 2, the smaller of the two covariance peaks is reduced relative to the other in the actual double-stream case.

d) The large negative covariance at zero time delay is reduced in the case of the actual double stream.

Thus it appears that the summation of the two scintillation patterns for the two turbulent streams is similar to direct addition of the individual intensity fluctuations, but that there are also other types of interaction, indicated by the reduction in both the smaller peaks and the covariance at zero delay. One possible interaction is investigated in the next section.

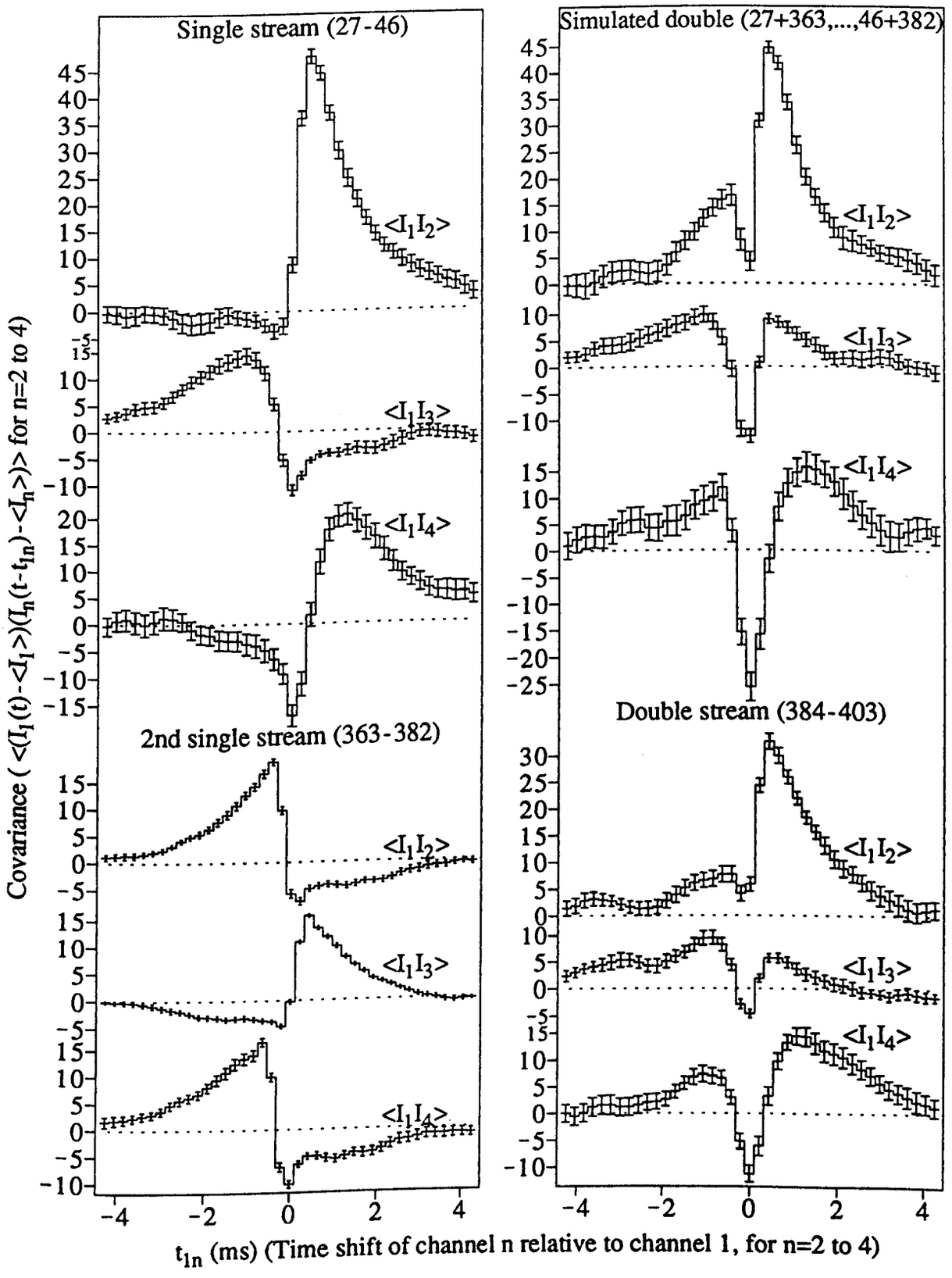

Figure 7-2 The analysis of the previous figure is repeated, but twenty records are used in each case, rather than one. The cross covariance between the scintillation on detector 1 and each of detectors 2, 3 and 4 is plotted as a function of time shift. The scintillation was produced by a single turbulent stream (top left), a second single stream in a different position (bottom left) and both streams acting at once (bottom right). Successive pairs of the single stream records were added together to simulate double stream data, for which the covariance is plotted at the top right. For each covariance function, a stepped line shows the average of the twenty covariance values at each time shift and the error bars indicate the standard error.

7.2 Investigation of phase interaction

The technique suggested in §4.3.2 is applied to search for the interaction of phase variations produced by the two turbulent streams, with the results presented in figure 7-3. The analysis is applied to two channels from twenty records, one of which is plotted at the top of the figure. The standard triple correlation is calculated for two different time shifts of channel 4 relative to channel 2:

$T(I_2(t), I_4(t-t_{24}), I_4(t-t'_{24})) =$

$$\langle (I_2(t) - \langle I_2 \rangle)(I_4(t-t_{24}) - \langle I_4 \rangle)(I_4(t-t'_{24}) - \langle I_4 \rangle) \rangle \qquad --(7.2)$$

where t_{24} and t'_{24} are time shifts applied to channel 4. As in the previous section, the analysis is applied for two single streams and to simulated and actual records where both streams are present.

The value of $T(I_2(t), I_4(t-t_{24}), I_4(t-t'_{24}))$ is represented using the rectangle representation introduced in chapter 4, *ie* the size of rectangles is proportional to $|T|$ and hatching indicates positive values. Only half of each correlogram is plotted as the function is symmetrical about the diagonal. The scaling of the rectangles is common to the four plots.

For the single streams, non-zero values of T occur only on the diagonal, where $t_{24} = t'_{24}$. For the simulated double-stream data, both of the peaks occur in the same place on the diagonal as for the single streams. For the actual double stream, the result is substantially different to that for the simulated data, with the peak for the 2nd stream shifted towards $t_{24} = 0$. Possibly this is caused by refractive bending of parts of the laser beams so that, as explained in §4.1.2, the effective positions of the crossover points change with time. While this bending should both increase and decrease the beam separation at different times, the rapid change of the scintillation pattern with distance means that the correlation will be higher when the bending puts the beams closer together. This is consistent with the change in time shift towards $t_{24} = 0$.

There is some evidence of phase addition, indicated by the positive correlation value at points around $(t_{24}, t'_{24}) = (-0.5, 0.1)$. The interpretation leading to this conclusion is:

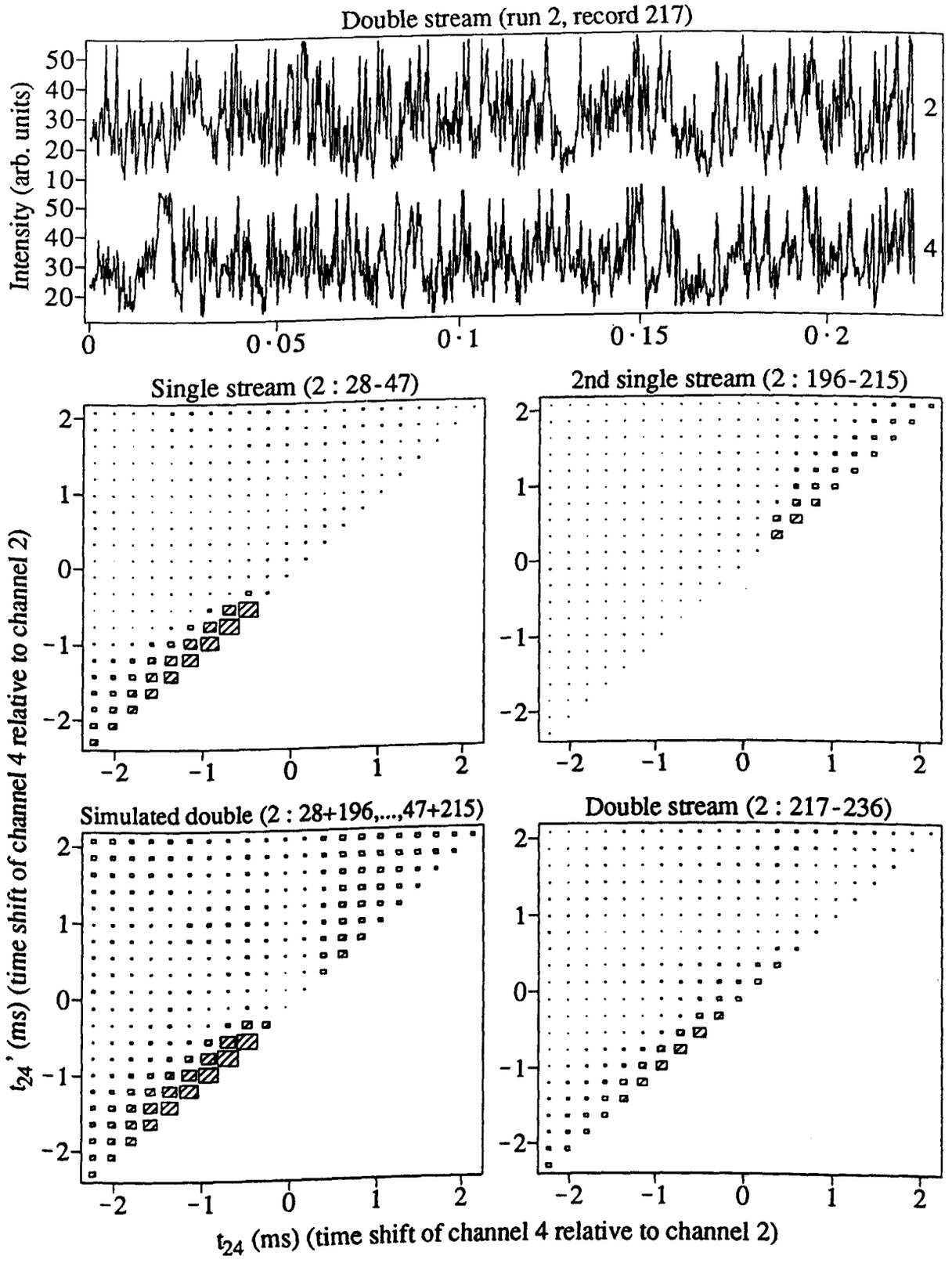

Figure 7-3 An investigation of interaction between the scintillation patterns produced by two turbulent streams. The triple correlation $T(I_2(t), I_4(t-t_{24}), I_4(t-t'_{24}))$ is plotted as a function of time shifts t_{24} and t'_{24}, for single streams in the upper graphs and for double streams in the lower graphs. The double stream is simulated by addition of the time series for the single streams, giving the result on the lower left, while the graph on the lower right is for actual scintillation produced by two streams. The correlation value is represented by rectangles, of size proportional to $|T|$, with hatching indicating positive values. The scaling of the rectangles is the same for all 4 plots.

a) the two turbulent streams produce phase fluctuations, of which the related intensity fluctuations move from detector 2 to detector 4 in 0.5–0.8 ms for one stream and from detector 4 to 2 in 0.2–0.4 ms for the other stream.

b) On occasions, two turbulent irregularities, one in each stream, lie on the same line from a light source to a detector. The scintillation pattern at the detector is related to the sum of the phase fluctuations produced by these two irregularities.

c) The opposed velocities of the two streams cause the two turbulent irregularities to go out of alignment. However, the scintillation patterns which they produce individually may both be partially correlated with the pattern which they produced when they were aligned; if so, they will be correlated with each other, giving a positive value for T at $(t_{24}, t'_{24}) \sim (-0.5, 0.2)$.

The evidence for phase interaction seen in figure 7-3 is not conclusive because:

i) the situation is complicated by another factor, thought to be refractive bending of the beams, and

ii) the interpretation is based on correlation values which are no higher than the noise level.

The fact that there are still two separate peaks in the double stream case shows that phase interaction, if it occurs at all, does not dominate in this situation; scintillation patterns corresponding to each of the two turbulent streams are present, as required for the application of the multiple-beam methods to be tested below.

7.3 Multiple-beam remote sensing

7.3.1 Three-beam test

A method was suggested in §4.1.3 to determine transverse velocity as a function of position by observation of the scintillation in three non-parallel light beams. This method is applied to each of two different crossed-laser records in figure 7-4, using signals from only 3 of the 4 detectors. These records are of scintillation produced by a single turbulent stream. For each record the triple-correlation function T_M (equation 4.12) is shown as a function of evenly spaced time shifts, which are set by the sampling interval of 200 μs plus the sampling delay time between channels (see §5.1.1). At the bottom these correlation values are plotted again, against transverse velocity and

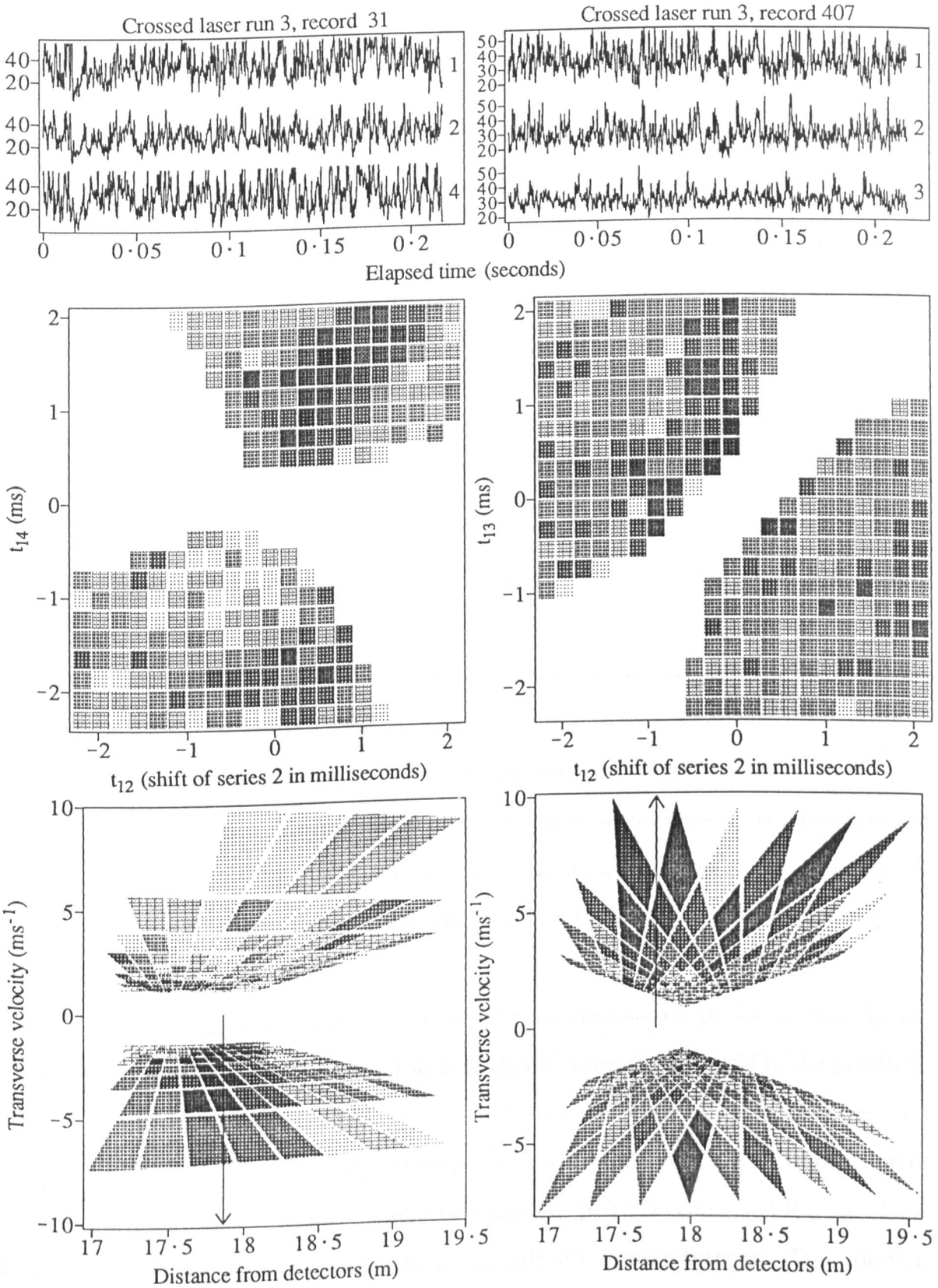

Figure 7-4 At the top, two records of scintillation from the crossed laser system (3 channels only) are plotted. The triple correlation T_M for each of these records, at time shifts which are integral multiples of the sampling interval, is plotted in the middle, with a shading density proportional (in eight steps) to T_M. At the bottom these correlograms are replotted as functions of the position and transverse velocity corresponding to each combination of time shifts. Parts of the time shift correlograms have been omitted in order to confine the lower plots to a desired range of position and velocity. The position and direction of the stream of turbulence which produced the scintillation is indicated by an arrow in each case.

position along the beams. The actual position and direction (positive or negative) of the turbulent stream is indicated by an arrow. In both cases the highest correlation (indicated by the darkest shading) occurs at the correct position and sign of the velocity. (*nb* The missing values of T_M against time shift are left out so as to restrict the position-velocity plot to convenient ranges of position and velocity.)

The records used here are not typical. Generally the results of several records need to be averaged before the result is clear. An obvious improvement is to make use of all the information available by considering all four beams. The different geometry of the position-velocity correlograms for different combinations of 3 beams (as illustrated in figure 7-4) raises the problem of how to combine them.

7.3.2 Position-velocity diagram

There are two other problems (albeit only of presentation) that are evident in figure 7-4:

a) shading is not suitable for the presentation of both positive and negative values. It is desirable to use the lightest shading for values near zero, but this makes it impossible to make a distinction between positive and negative values.

b) For small velocities, the individual points in the position-velocity correlogram are very close together. If the "rectangle" representation which was used in figure 7-2 is used here, the rectangles, which are scaled so that there is no overlap, are too small.

A solution to the three problems (*ie* these two presentation problems and the incompatible geometries seen in figure 7-4) is to choose a rectangular grid in the position-velocity plane and to use linear interpolation of the time series to obtain the required time shifts. To avoid plotting redundant points, which would give a false impression of high resolution at high velocities, one of two adjacent points is cancelled if none of the 3 required time shifts differ by more than one half of a sample interval. This solution is applied in figure 7-5, where the standard triple- and quadruple-correlation functions are calculated for three and four beams.

7.3.3 Using standard triple correlation

In figure 7-5, the standard triple correlation T (equation 7.2) is plotted against position and velocity for the four possible combinations of any three out of four series

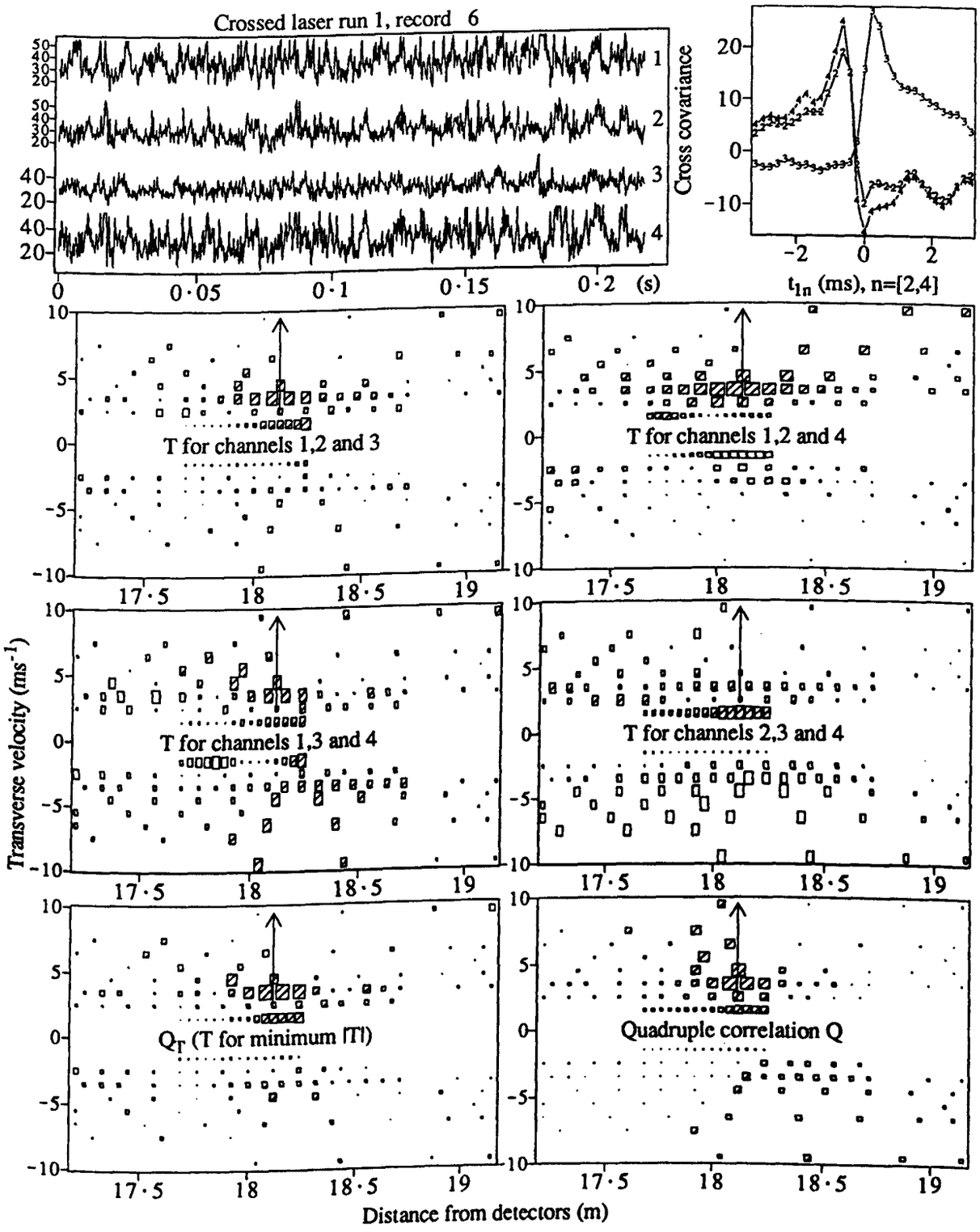

Figure 7-5 A crossed laser record of the scintillation produced by a turbulent stream is plotted at the top. The cross covariance between channels 2, 3 and 4 and channel 1 is plotted as a function of time shift on the top right. Four correlograms for different combinations of three channels of the record are plotted in the middle. These consist of values of the standard triple correlation T, calculated between the three channels after applying time shifts appropriate to the position and velocity. Linear interpolation was used to make available the time shifts required for uniform steps in position and velocity. Redundant points have been removed. At the bottom left these four correlograms are combined to produce Q_T. The standard quadruple correlation Q is applied for the four channels in the correlogram at the bottom right. In each case an arrow indicates the known position and direction of the turbulent stream.

in the record plotted at the top. For all four cases there is a peak in correlation at the correct position and direction, but the resolution of position is poor (0.5–1 m, for a turbulent stream that is 3 cm wide) and the peak occurs at different velocities for different combinations. There are also large false peaks.

This poor performance is not surprising, due to the approximately even distribution of the intensity about the unperturbed value. As T only responds to the component of the signal which is asymmetrically distributed about the average, most of the signal makes no contribution to T. This explanation is supported by reference to the cross covariance functions plotted at the top right. The cross covariance between channels 1 and 4 (labelled with a 4 on each point in the plot) goes more negative than the other functions. This indicates that the component of the signal which is correlated between channels 1 and 4 is more symmetric about the mean than the components for the other combinations. This is consistent with the fact that the combination which excludes series 4 gives the best result.

7.3.4 Four-beam test

The result is improved considerably by calculating Q_T, the value of the four triple correlations which has the minimum modulus (equation 4.10). This is shown at the lower left of figure 7-5. The large false peaks which occur at negative velocities for the combinations 1,3 and 4 and 2,3 and 4 are almost eliminated when combined with the other two combinations.

On the lower right of figure 7-5 the standard quadruple correlation

$$Q(I_1(t), I_2(t-t_{12}), I_3(t-t_{13}), I_4(t-t_{14})) =$$

$$\langle (I_1(t) - \langle I_1 \rangle)(I_2(t-t_{12}) - \langle I_2 \rangle)(I_3(t-t_{13}) - \langle I_3 \rangle)(I_4(t-t_{14}) - \langle I_4 \rangle) \rangle \qquad --(7.3)$$

is applied to all four series. The result is similar to that for Q_T on the left, but with some false correlation at negative velocities. The occurrence of such false correlation was predicted in §4.2.1, due to the positive value for Q which occurs for two pairs of correlated signals.

Thus the application of standard correlation functions to the analysis of scintillation patterns in multiple beams allows the remote measurement of the position and velocity of a single turbulent stream. This test will be extended to a double-stream case

in the next section, but in conjunction with tests of new correlation functions which are expected to give better results.

7.4 Tests of new correlation functions

Some of the new correlation functions which were introduced in §4.2.3 and §4.2.4 are tested here using the crossed-laser data. The results are compared with those for standard correlation functions. Finally both standard and new functions are applied to scintillations produced by two turbulent streams.

7.4.1 New triple-correlation functions

Various triple-correlation functions which were defined in §4.2 are compared in figure 7-6 with the standard function T. Of these, T_C (equation 4.8) and T_1 (equation 4.11) give worse results, T_{md} (equation 4.17) gives better resolution in position but a false peak for negative velocities and only T_M (equation 4.12) gives a better result overall.

These results are easily explained:

T_C This is based on cross correlations. As the cube of a waveform is more strongly peaked than the square, the triple correlation T gives a narrower peak than does a cross correlation.

T_1 This also is the sum of a product of only two signals and so the peak is wider.

T_M The narrowest peak of the three component functions T_1, T_2 and T_3 is selected by choosing the minimum value at each location in the plot. The random noise evident for T_1 is also reduced in this selection, as each of the component functions has the correct peak in the same location, but the random peaks due to noise will occur in different locations.

T_{md} This gives better resolution in position. This can be understood by considering identical signals. For these, only a slight shift of one of the signals causes the difference between the series to become much larger and so T_{md} becomes much smaller. False peaks occur because T_{md} is larger when two of the three series are correlated (see §4.2.4), compared to the situation of no correlation.

Two cases of $T_{md}(I_1, I_2, I_4; M, F)$ are calculated, with different values of the pattern matching parameters M and F. The results are not substantially different, except

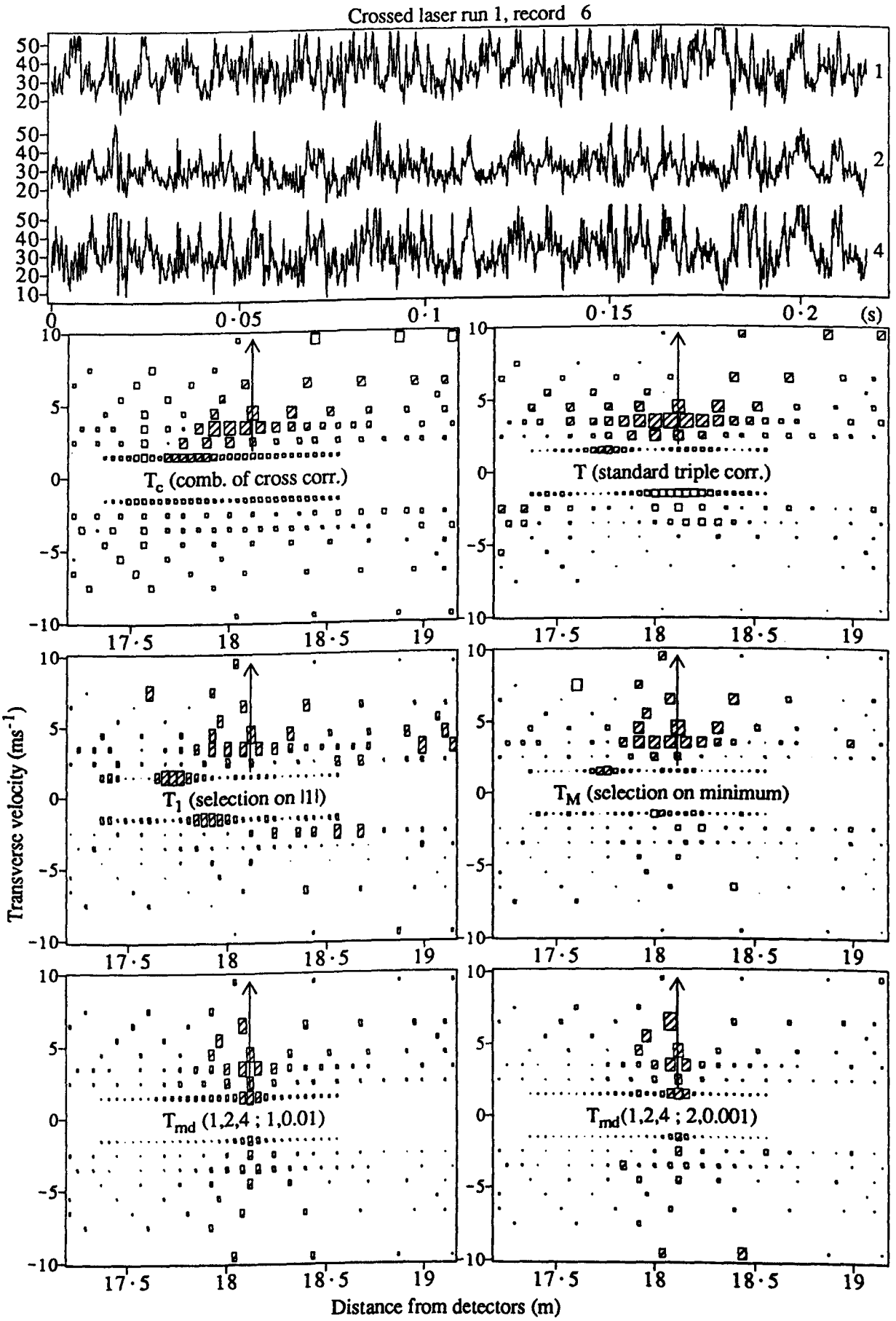

Figure 7-6 Various triple correlation functions are applied to the crossed laser record plotted at the top, with the result plotted as a function of position and velocity at the same points as in the previous diagram. Each correlogram is labelled with the correlation function applied.

that for the higher degree of pattern matching (on the lower right of figure 7-6) the correlation is more clearly peaked at the correct position and a false peak is introduced at (18.4 m,-10 ms^{-1}). This illustrates both the advantage (*ie* better resolution) and the disadvantage (*ie* chance correlation) of requiring a close similarity between the signals.

7.4.2 New quadruple-correlation functions

A similar test of new quadruple-correlation functions is presented in figure 7-7. Compared to the standard quadruple correlation Q, Q_C (equation 4.9) and Q_T (equation 4.10) give worse results and the new functions Q_M (equation 4.14), Q_{SM} (equation 4.16) and Q_{md} (equation 4.18) are roughly equivalent (considering resolution, noise and false peaks).

The same functions are applied in figure 7-8 to a record of scintillation produced by two turbulent streams. All except Q_{md} fail to detect the presence of both streams. This is logical:

- Q_C At some positions and velocities, some of the contributing cross-correlation terms can be large (either positive or negative) due to one turbulent stream, and the other terms can be large due to the other stream, so a false peak occurs.
- Q_T Although less likely, false combinations can occur as for Q_C above. Also, the cancellation of the major component of the signal which is symmetric about the mean value reduces the effectiveness of T, on which Q_T is based.
- Q False peaks (both positive and negative) can arise from two independent pairs of correlated signals (see §4.2.1 and figure 4-8b). The occurrence of such false peaks is more likely when there are two streams, rather than one. Thus the missing peak may have been cancelled by a false negative correlation associated with the stronger peak.
- Q_M It was shown theoretically (figure 4-9b) and by simulation (figure 4-16) that the selection functions would give false peaks with more than one combination of signals.
- Q_{SM} Simulation (figure 4-14) showed that the selection on sign gave larger false peaks than Q_M.
- Q_{md} This function gives a large weighting to signals which are close to identical.

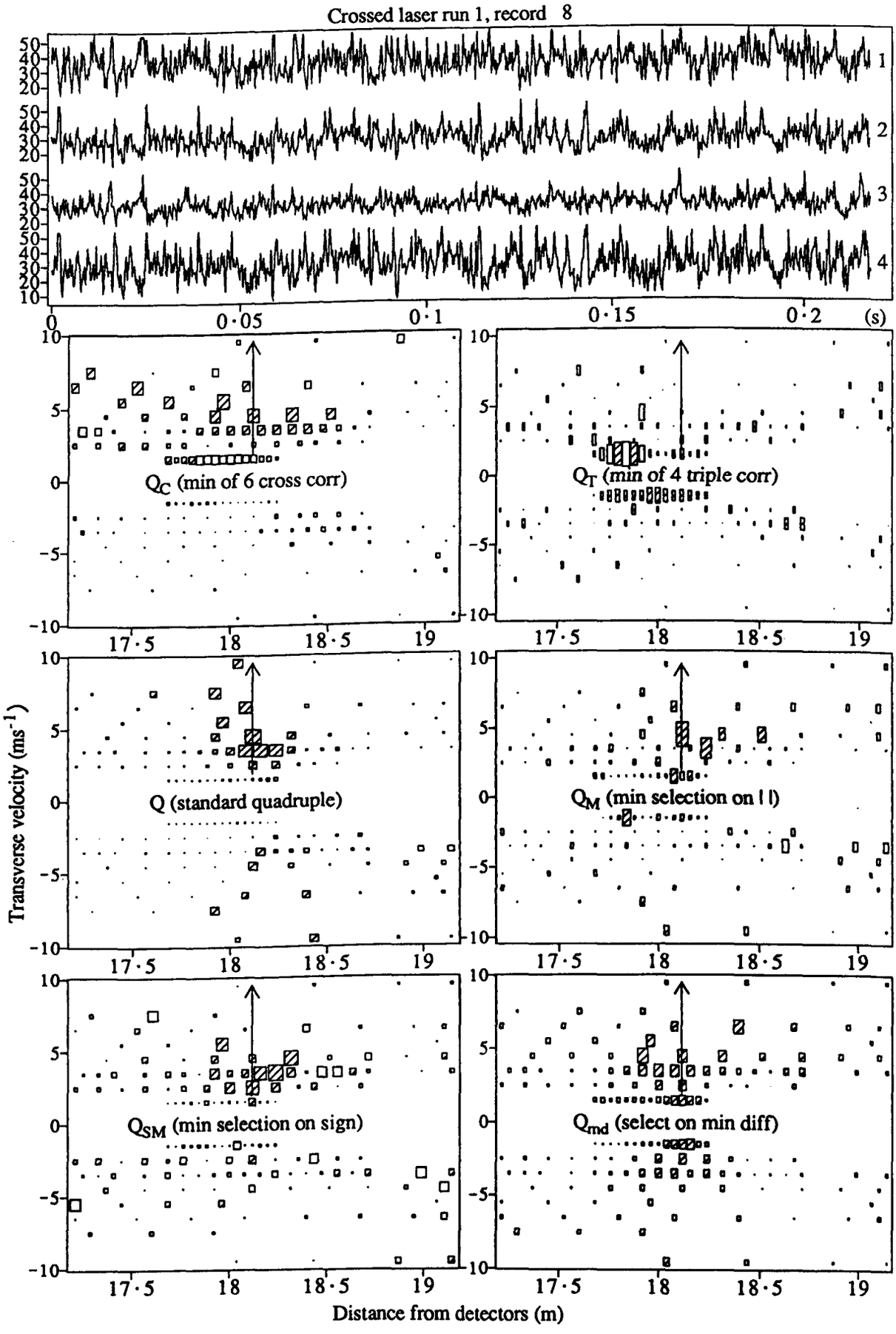

Figure 7-7 Various quadruple correlation functions are applied to the crossed laser record plotted at the top, with the result plotted as a function of position and velocity at the same points as in the previous diagram. Each correlogram is labelled in the middle with the correlation function applied.

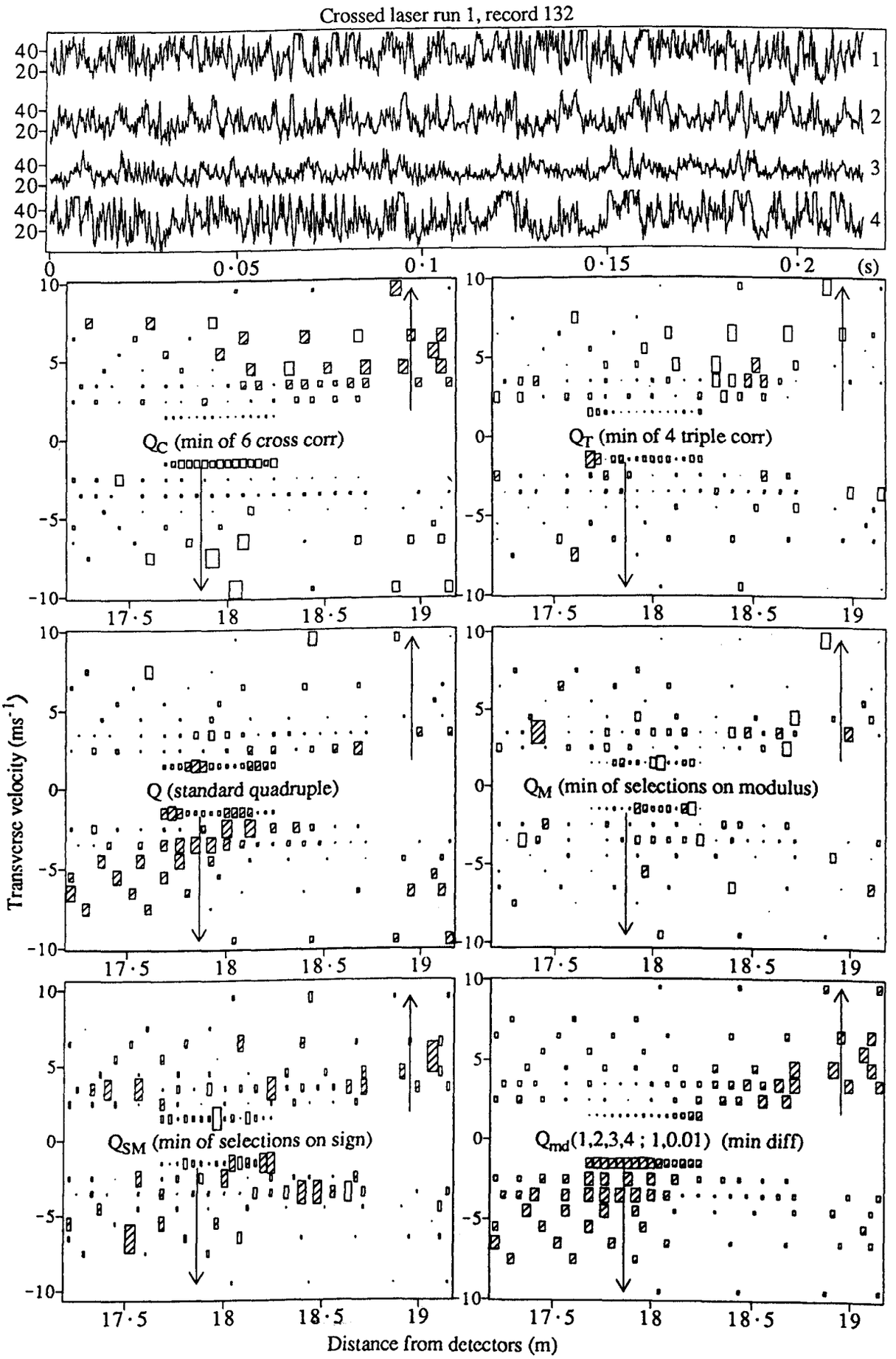

Figure 7-8 Various quadruple correlation functions are applied to the crossed laser record plotted at the top. This was produced by two turbulent streams moving in opposite directions. Each correlogram is labelled with the correlation function applied.

Thus when one stream or the other dominates the scintillation pattern, it gives a large contribution to the correlation value. Any interaction of the signals for the two streams will substantially increase the difference between the signals on different channels, thus producing relatively small contributions to Q_{md}.

Having determined that Q_{md} is the only quadruple-correlation function which can be used to detect two streams, it is necessary to determine the optimum values of the pattern matching parameters. This is done by trying different combinations of M and F in figure 7-9. To increase the resolution in position:

a) the time series are differentiated. This gives a high weighting to features which change rapidly, thus favouring smaller patterns and so increasing the resolution of the position of the turbulence.

b) The results are plotted only for velocities less than 5 ms^{-1}. This is to avoid the deterioration in resolution that results from the large uncertainty in position associated with high velocities (as seen in figure 7-4).

In figure 7-9 (where the record is of scintillation produced by two turbulent streams moving in the same direction) there is good agreement between the deduced and actual positions of the turbulence for most combinations of M and F. The resolution improves as M is increased and as F is decreased. These results confirm that the multiple-beam method can be applied using scintillation in at least some circumstances.

7.5 Overall results

Figure 7-10 presents a comparison of the deduced and actual positions of the turbulent streams and the sign of the velocity for all 25 situations set up in crossed-laser run 1. The results are plotted separately for the four combinations of single and double streams and of positive and negative velocities. The correlation function $Q_{md}(I_1, I_2, I_3, I_4; 3, 0.1)$ is plotted against actual position of a turbulent stream on the horizontal axis and postulated position on the vertical axis. Thus the vertical axis corresponds to the horizontal axis of the position-velocity diagrams in the previous few figures. All values at different velocities (of the appropriate sign) in each subrange of position are averaged. The known positions and directions of the actual turbulent streams are represented by circles. These indicate where large values of correlation

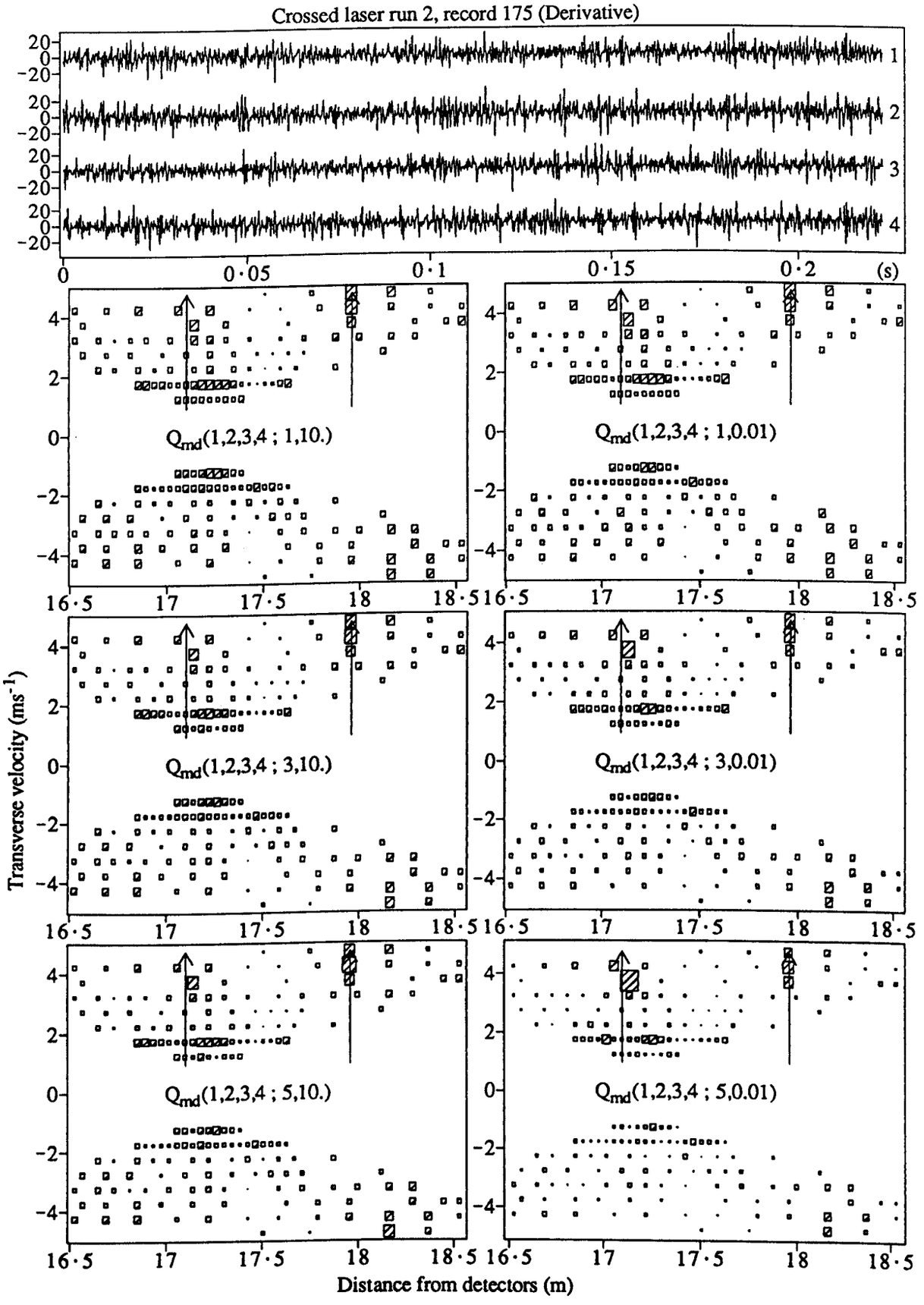

Figure 7-9 Correlation by minimum difference $Q_{md}(1,2,3,4 : M, F)$ is applied to the derivative of the intensity fluctuations produced by two turbulent streams. The analysis is applied to the record plotted at the top for six combinations of the pattern matching parameters $M = 1, 3$ and 5 and $F = 10.$ and 0.01. Large values of correlation (indicated by large shaded rectangles) occur near the two known positions (indicated by the arrows) of the turbulent streams.

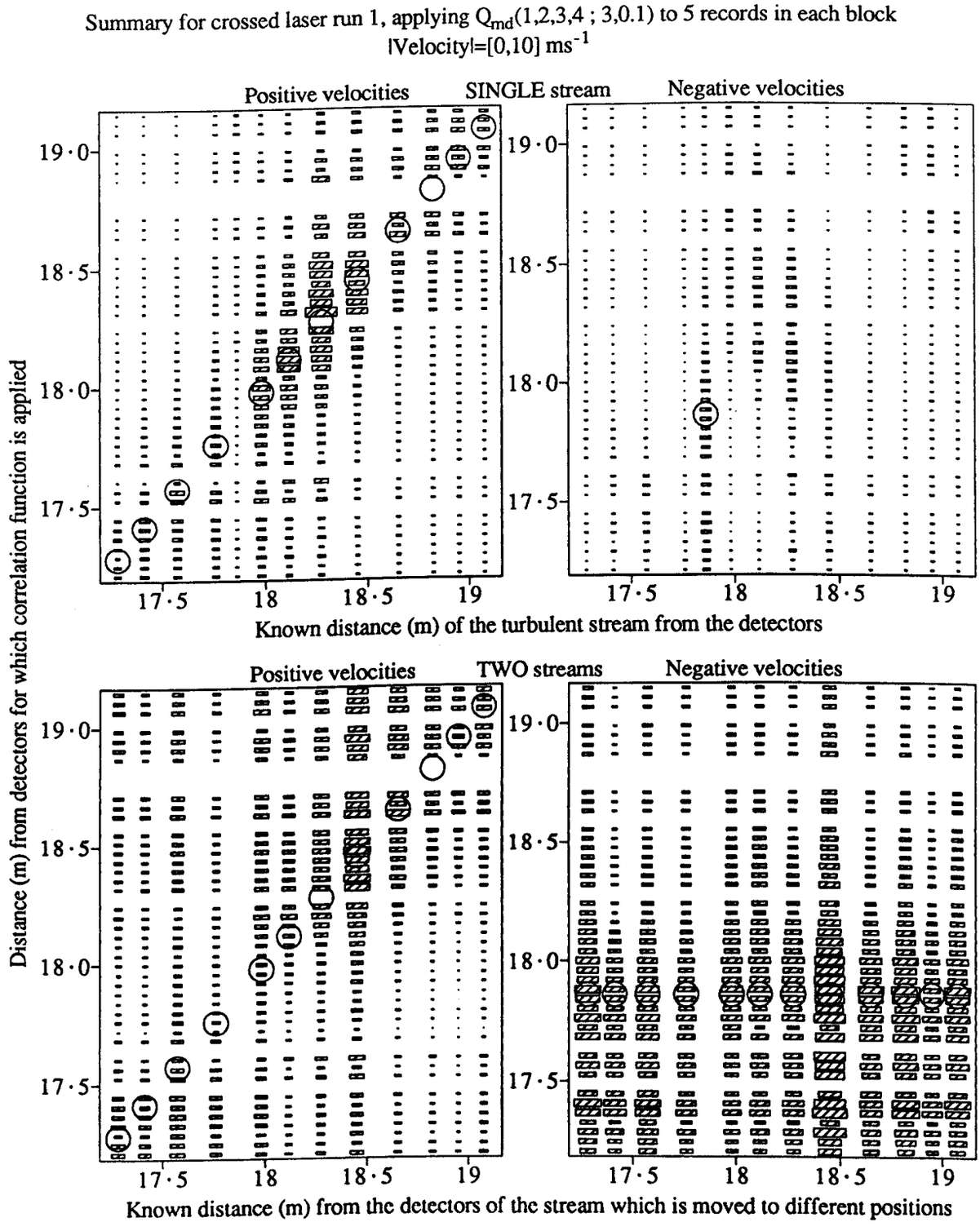

Figure 7-10 An overview of the results of crossed laser run 1. The positions of the turbulent streams deduced from the scintillation are compared with the known positions. The horizontal axis shows the known positions of the single stream (for the top graphs) and the known positions of the relocated stream in the double stream case (bottom graphs). For each of these stream positions the position-velocity correlogram is calculated using the correlation function $Q_{md}(1,2,3,4;3,.1)$. At each postulated position in these correlograms the average correlation value for all positive velocities is calculated and plotted against the vertical axis in the graphs on the left. Similarly the average correlation value for all negative velocities is plotted on the right. The circles indicate where the deduced position and actual position of a turbulent stream should coincide *ie* agreement between deduced and actual positions requires large rectangles to be coincident with the circles.

(indicated by large rectangles) should occur if the position of the turbulent streams is correctly indicated by the correlation functions.

From figure 7-10 the following conclusions can be drawn:

a) for the single streams (upper diagrams) there is a peak in the correlation value at the correct position.

b) There are some false peaks at negative velocities produced by single streams with positive velocity. These occur near crossover position P_{24} in figure 5-1, where 2 pairs of channels are well correlated with each other. Q_{md} then gives a false large value as two independent signals will be close, by chance, far more often than four independent signals.

c) For double streams (lower diagrams) there is generally a high value of correlation close to the known positions of both streams. The peaks are wider (*ie* they cover a wider range of postulated positions) and are in some cases slightly shifted from the correct position.

d) The results are wrong for streams with positive velocities which are close to the other, fixed stream (at 17.8 m). This is probably due to the change in apparent position of the crossover for the weaker stream of turbulence, caused by refraction due to the stronger stream (as discussed earlier for figure 7-3).

The overall results for run 2 are given in figure 7-11 using the same presentation, but making some changes to enhance the resolution:

i) as in figure 7-9, Q_{md} is applied to the derivative of the signals.

ii) Only velocities in the range 3–5 ms^{-1} (positive or negative) are considered.

iii) Q_{md} is applied with $F = 0.01$ rather than $F = 0.1$, to give greater weighting to signals which are very close.

iv) The results of 20 records of each situation are combined, rather than 5.

There is a significant improvement compared to figure 7-10, with the peaks in correlation being much narrower and the false peaks for the wrong direction being almost eliminated. However, some false peaks are larger relative to correct peaks.

7.6 Conclusions

The laboratory test of a multiple-beam system shows that the position of a tur-

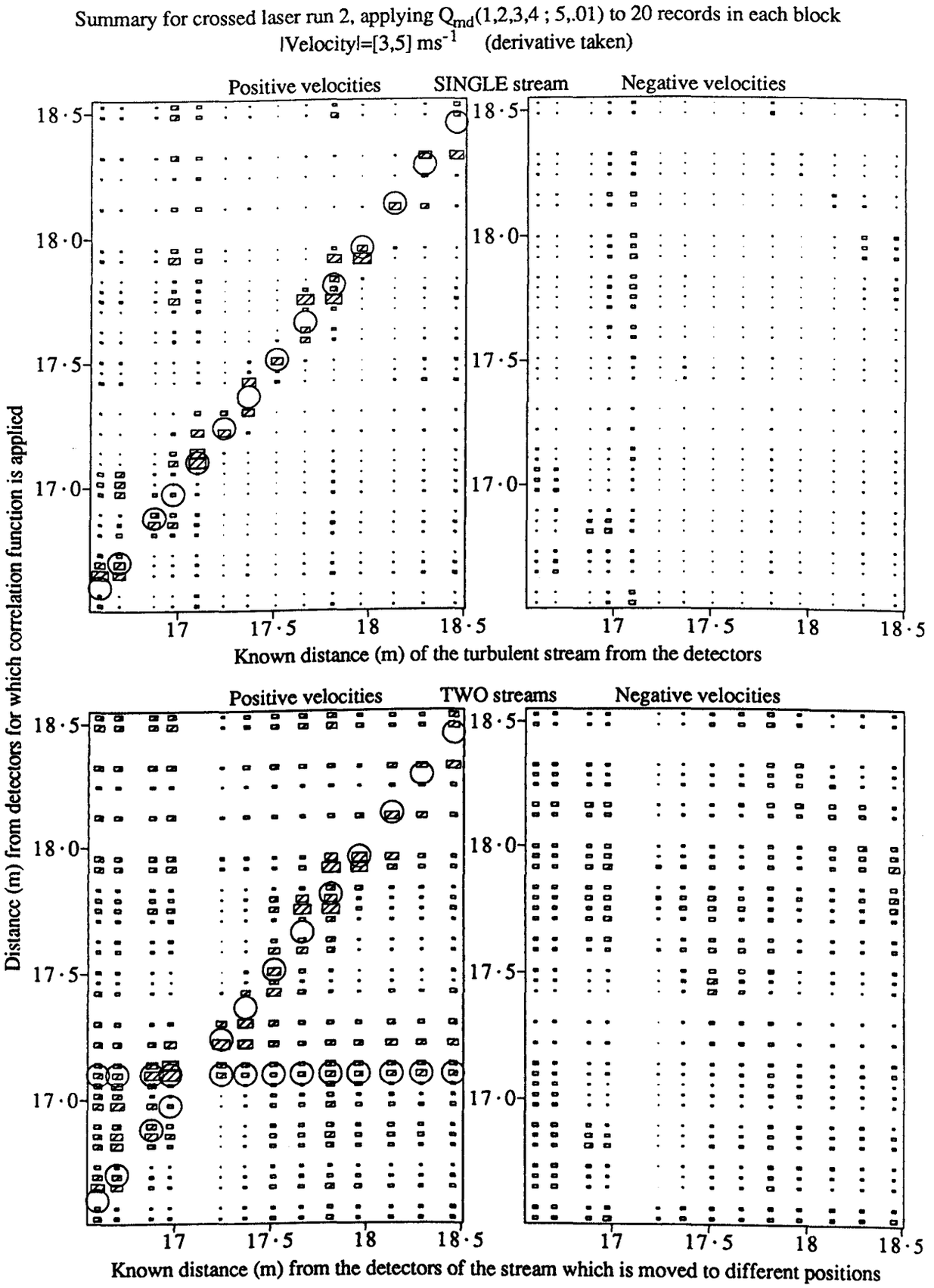

Figure 7-11 An overview of the results of crossed laser run 2. The analysis and presentation are the same as in the previous figure, except that

- Q_{md} is applied to the derivative of the time series,
- a greater degree of pattern matching is applied (using $M = 5$ and $F = 0.01$ as parameters in Q_{md}), and
- the correlation is calculated only for velocities from -5 to -3 ms^{-1} and from 3 to 5 ms^{-1}.

bulent stream can be deduced with high accuracy (to about 10 cm along a 40-m path) from the scintillations observed in either three or four beams. The transverse velocity is also obtained, but the deduced values cannot be checked as no independent measurement of the velocity was made. The sense of the velocity (*ie* positive or negative) is correctly deduced. Standard correlation functions are adequate to deduce the correct position of the stream, but new correlation functions developed in §4.2 are found to give superior results.

In the analysis of the scintillations produced by two turbulent streams acting simultaneously, it is found that there was some interaction between the patterns, other than algebraic addition of intensities. There is some evidence that the beams are refracted to and fro, leading to movement of the crossover positions of the beams. A test for the addition of phase variations which originate in the two turbulent regions gives ambiguous results, in that correlation corresponding to such addition is observed, but is not statistically significant.

Of both standard and new multiple correlation functions, only the new function Q_{md} (correlation by minimum difference) can be used to deduce the position of two turbulent streams acting simultaneously. The resolution in position is poor, but is enhanced considerably by differentiation of the signals. Even in this case, some indications of turbulence occur at wrong positions.

As the turbulence in this experiment was much stronger than that in the atmosphere, the deduction that beam bending occurred in the experiment does not imply that it will be a significant factor in the atmosphere. However, the addition of phase variations which originate in different regions will occur irrespective of the strength of the variation, so the experiment is relevant to atmospheric measurements. It is therefore unfortunate that the results of the test for phase addition are ambiguous.

The finding that Q_{md} is the only available function which gives satisfactory results in the case of two turbulent streams is of concern for applications using stellar scintillation. As it was shown in §6.9 that Q_{md} is badly affected by photon noise, it appears that no correlation function is available to analyze stellar scintillation which is produced at more than one height. However, it is still worth trying the other functions, such as Q_M, as the scintillation in the experiment is quite different to stellar

scintillation.

In conclusion, it is established in a laboratory test that multiple-beam techniques can be used to measure a profile of transverse velocity in air, by analysis of scintillation produced by refractive-index irregularities. It is confirmed that standard correlation functions are unsuitable for the analysis. New correlation functions are shown to be adequate, but further development is desirable. Some doubt is cast on whether the available correlation methods are adequate for application of the multiple-beam technique to stellar scintillation.

Chapter 8 Standard observations

This chapter presents observations and applications of stellar scintillation which are similar to work previously published by others. While each type of observation is not new, their inclusion here is justified as follows:

a) the observations presented in this chapter are all of the same set of stars over a 2-month interval at the same site. This gives a more consistent overview of the characteristics of stellar scintillation than that found in the literature, where the various types of observation described were made at different sites with different instruments.

b) The apertures used here are smaller than in previous observations, allowing the contribution of smaller scintillation patterns to be recorded.

c) The brightest star, Sirius, goes close to the zenith at Adelaide's latitude. This makes it possible to record, for a small zenith angle and small aperture, time series of the intensity of stellar scintillation which are less obscured by photon noise than previous observations carried out at mid-latitudes in the Northern Hemisphere.

8.1 Analysis of time series

Time series of the intensity of stellar scintillation were published many years ago (*eg* Butler, 1951). Although photon-counting techniques and more sensitive photomultipliers allow better measurements, these have apparently been neglected (or not published) in order to concentrate on derived functions, such as the spatial correlation of the scintillation pattern. Time series are worthy of presentation because they show characteristics which are lost in most derived functions.

Sample time series of the light intensity of Sirius on a circular 4-mm aperture are plotted in figure 8-1. One record (channel 2 only) for each of 14 nights over a 29-day interval in summer is shown. The record selected for each night is the one for which Sirius was closest to its maximum elevation of 72°. The intensity, relative to the mean for the record, is plotted against time. The average contribution of background (skylight and noise) has been subtracted, using a background record which was recorded less than 2 min after the starlight record. (Unless specified otherwise, all measurements of starlight were made using the "multiple collimator" described in §5.2.2.)

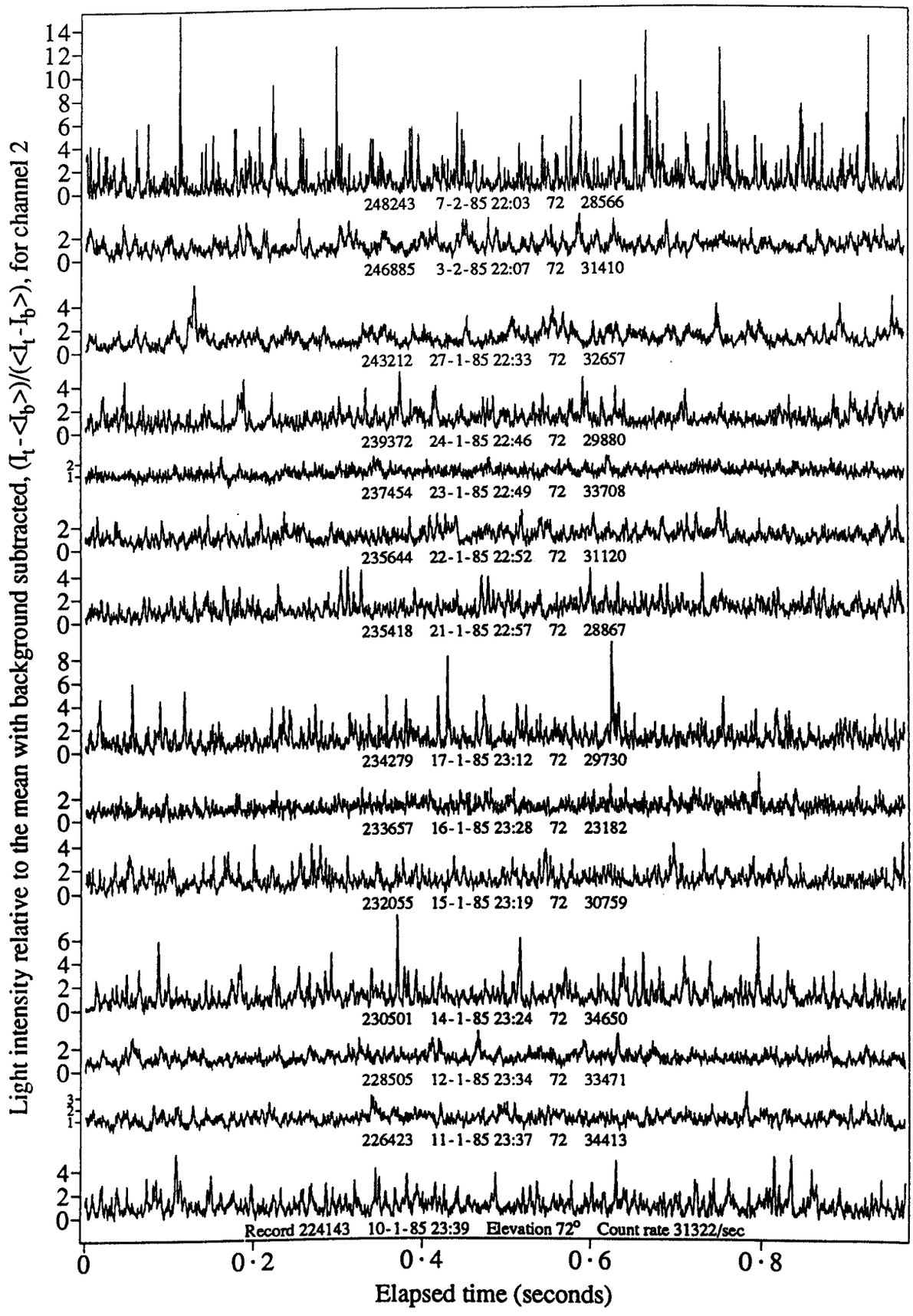

Figure 8-1 One second records of stellar scintillation for each of 14 summer nights. The instantaneous ratio of the starlight intensity to its mean is shown. All the records are for Sirius near zenith, recorded through the same 4-mm circular aperture on channel 2. (Each record is a plot of $(I_t - \langle I_b \rangle)/\langle I_t - I_b \rangle$, where I_t is the intensity in a record of starlight plus background and I_b is the intensity of the background recorded a short time (10-120 s) later.)

It can be seen in figure 8-1 that there is considerable night-to-night variation in the frequency and variance of the light intensity. The ratio of the maximum light level to the mean is 15, a value that is much higher than in previously published time series, particularly for those of stars near the zenith. The fluctuations in intensity seem to occur at random.

In the left diagram of figure 8-2 the normalized temporal autocovariance

$$Cov_n(t_{22}) = \frac{\langle I_2(t) I_2(t - t_{22}) \rangle}{\langle I_2 \rangle^2} \qquad --(8.1)$$

of the intensity I_2 on channel 2 is plotted as a function of time shift t_{22} for each of the records of figure 8-1. These have been corrected for the effect of background, using equation 4.25. The normalized autocovariance at zero time delay is the same quantity as the normalized second moment $\frac{\langle I_2^2 \rangle}{\langle I_2 \rangle^2}$ and so can be corrected for the effect of afterpulsing using the method developed in §4.5.4. In figure 8-2 the contribution due to afterpulsing is shaded. A method to calculate the contribution of afterpulsing to the autocovariance at finite time delays has not been developed, but it will be less than that at zero time delay because a chance increase in $I_2(t)$ (due to an afterpulse) will produce a greater increase in $I_2^2(t)$ than in $I_2(t)I_2(t - t_{22})$. Thus the effect of afterpulsing here is to increase the covariance at zero time delay relative to the rest of the temporal autocovariance, but not by a significant amount.

It can be seen in figure 8-2 that the covariance drops down to half the maximum value in 1–3 ms. This is consistent with the measurement of Jakeman *et al* (1976), reproduced in figure 3-5b. This similarity may be a coincidence, considering the large difference in star elevation of 21° for the observations by Jakeman *et al* compared to 72° here.

Amplitude spectra (calculated as in §6.7, but with the value for 0 Hz excluded and the rest averaged over intervals of ~10 Hz), are given for the same records on the right of figure 8-2. These show that:

c) the maximum frequency of the stellar scintillation varies from 200 to 600 Hz on different nights.

d) The maximum amplitude generally occurs at the lowest frequencies, and always below 100 Hz.

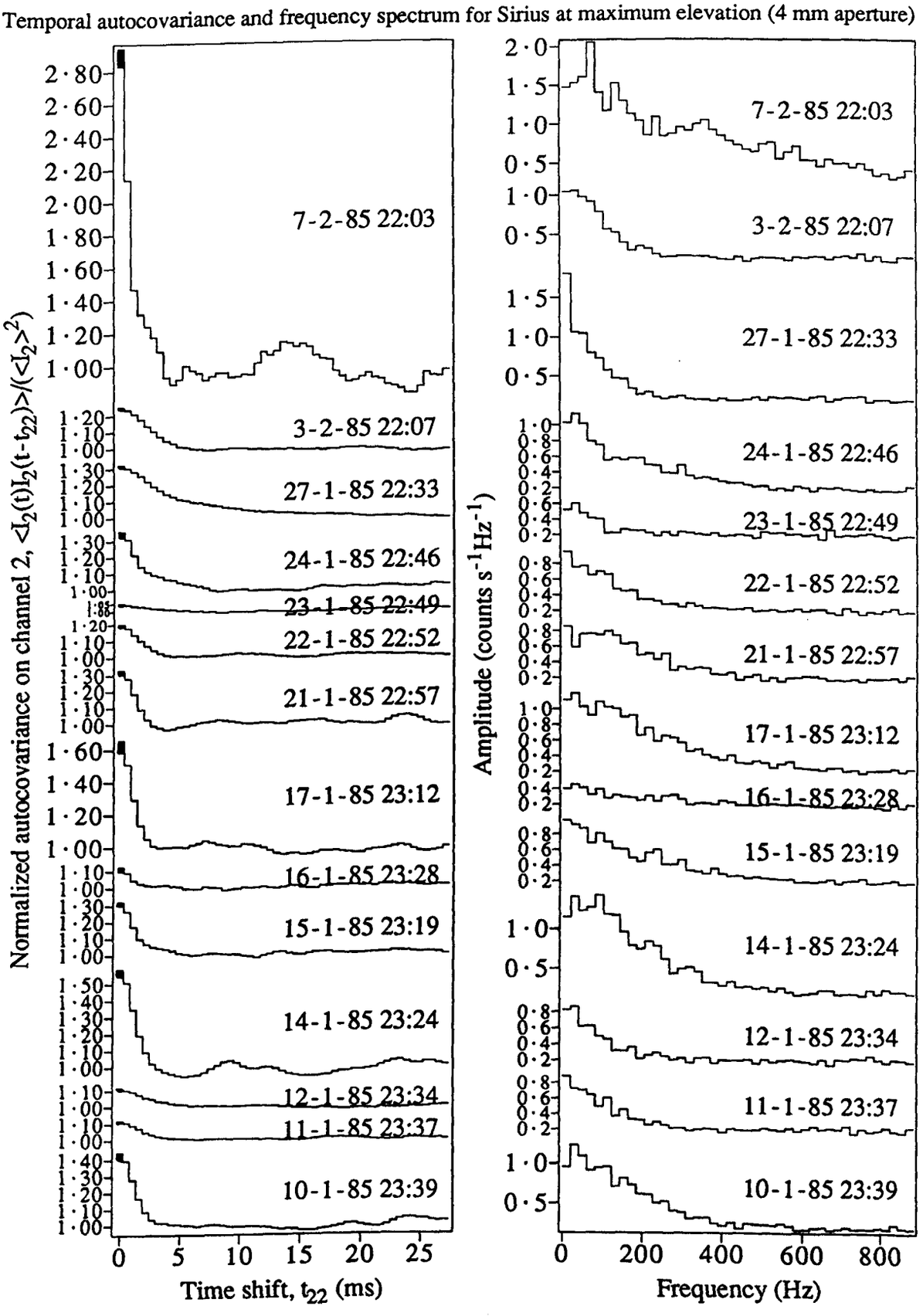

Figure 8-2 Time shifted autocovariance functions and amplitude spectra for the records plotted in the previous figure. On the left, the normalized autocovariance $\langle I_2(t)I_2(t-t_{22})\rangle/\langle I_2\rangle^2$ is plotted as a function of the time shift t_{22}. The effect of background has been removed. For zero time delay, the contribution due to afterpulsing is indicated by the shaded area. On the right, the amplitude spectrum is plotted as a function of frequency. This spectrum has been averaged over intervals of $\sim$ 10 Hz and the value at 0 Hz was not included.

These spectra are similar to those measured by Bufton and Genatt (1971) using a much larger aperture of 15.2 cm (see figure 3-5a). The maximum frequency here is about twice that reported by Bufton and Genatt. Given the much smaller aperture here, one might expect an even greater ratio. Two possible reasons why this does not occur are:

e) a larger aperture will be more sensitive to larger scintillation patterns, which are produced at greater heights (see §3.5.1) where the wind velocity tends to be high. Thus the larger patterns still produce relatively high frequencies as they travel faster than the smaller patterns.

f) Small scintillation patterns will still contribute to the signal on a large aperture as they cross its edge.

The analysis of figures 8-1 and 8-2 is repeated in 8-3 and 8-4 for observations which are similar to those above, except that they were made using a 2-mm aperture. The two data sets (for different aperture sizes) are not directly comparable, as only one night (7-2-85) contributes to both sets. On this night the maximum instantaneous intensity reaches higher levels for the smaller aperture. This indicates that there is significant structure in the scintillation pattern that is smaller than the 4-mm aperture. The maximum value of 25 times the mean level (for observations with the 2-mm aperture) is substantially larger than that previously reported in any stellar scintillation measurements. On this night the observing site was downwind of hills of height 0.7 km, suggesting that scintillation with large intensity enhancements and small pattern size is produced by strong orographic turbulence at an altitude of about 1 km.

Figure 8-5 presents a block of 7 successive time series, showing both channels. The separation between the two 2-mm apertures is written under each series, varying from 7.1 cm at the bottom of the figure to 1.1 cm at the top. It can be seen that:

g) the general appearance of the series does not change from one record to another, suggesting that it is reasonable to use only one record for each night to infer night-to-night variation, as was done in figures 8-1 to 8-4.

h) For the smallest separation of 1.1 cm, the two series are similar, with substantial decorrelation apparent at separations of 2.1 cm and greater. This indicates that the size of the scintillation patterns is generally less than 4 cm. The large peak which occurs on channel 2 but not on channel 1 indicates the presence of a very

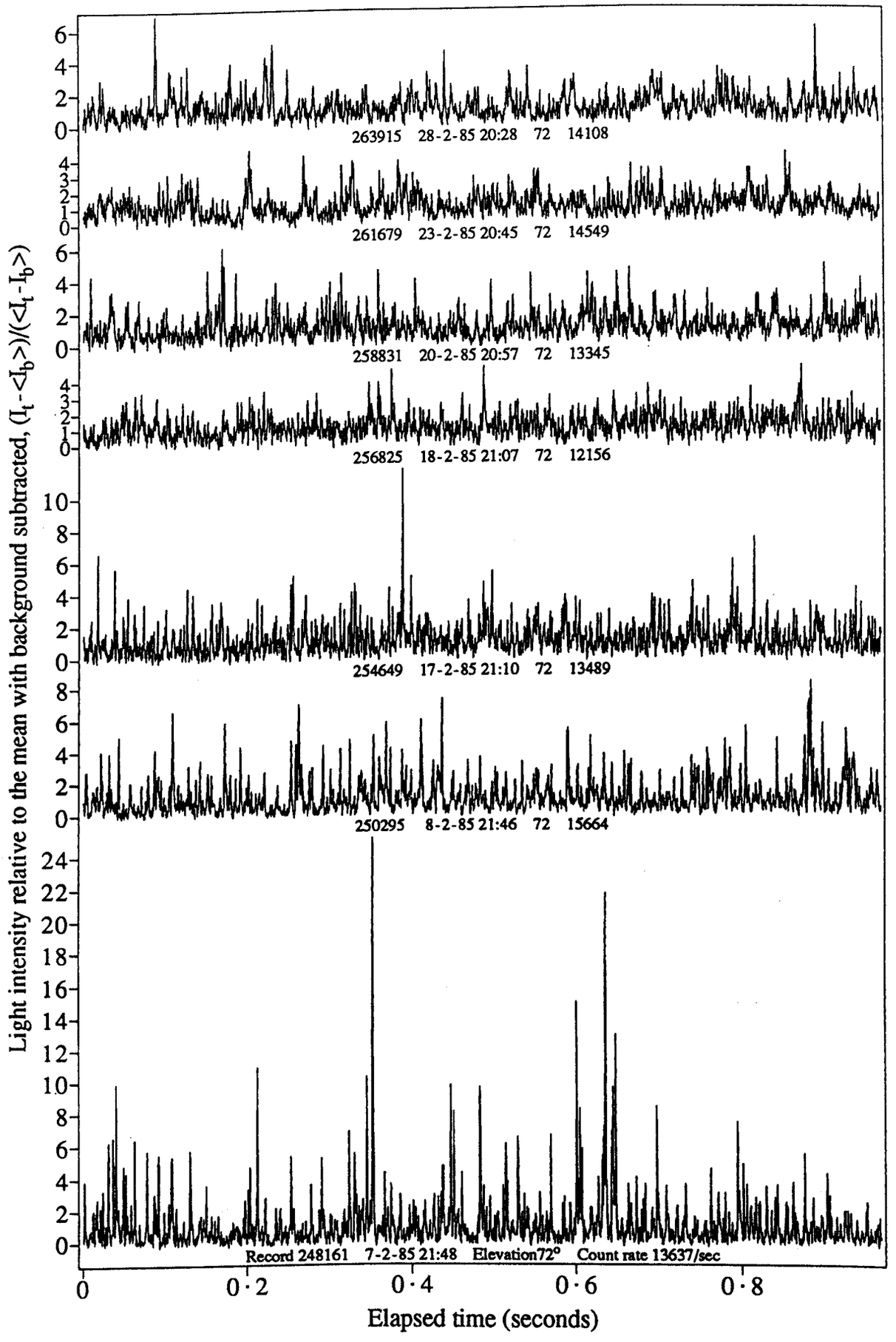

Figure 8-3 One-second records of stellar scintillation for each of 7 summer nights, recorded with a smaller aperture than the data in figure 8-1. The instantaneous ratio of the starlight intensity to its mean is shown. All the records are for Sirius near zenith, recorded through the same 2-mm circular aperture.

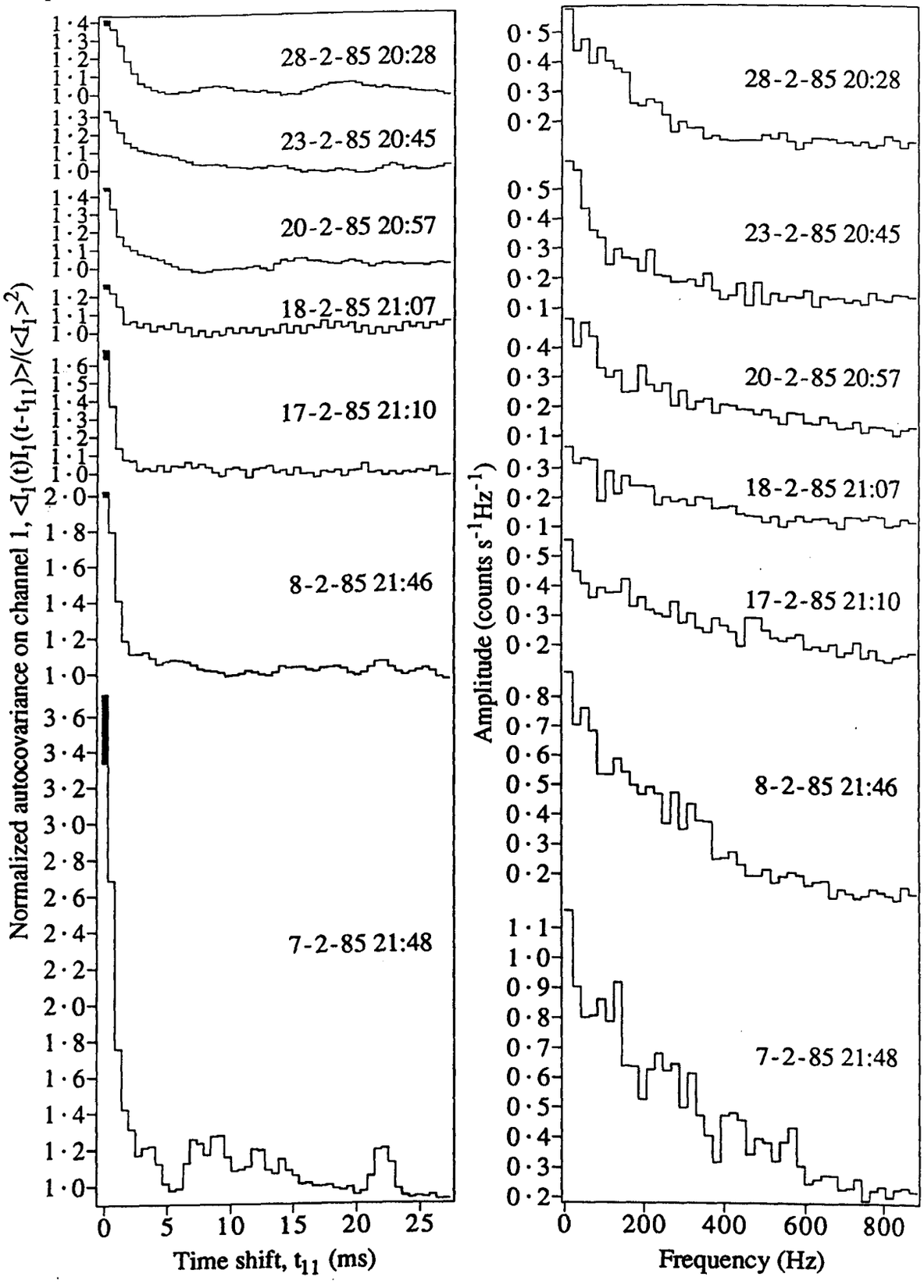

Figure 8-4 Time shifted autocovariance functions and amplitude spectra for the records plotted in the previous figure. On the left, the normalized autocovariance $\langle I_1(t)I_1(t-t_{11})\rangle/\langle I_1\rangle^2$ is plotted as a function of the time shift t_{11}. The effect of background has been removed. For zero time delay, the contribution due to afterpulsing is indicated by the shaded area. On the right, the amplitude spectrum is plotted as a function of frequency. This spectrum has been averaged over intervals of $\sim$ 10 Hz and the value at 0 Hz was not included.

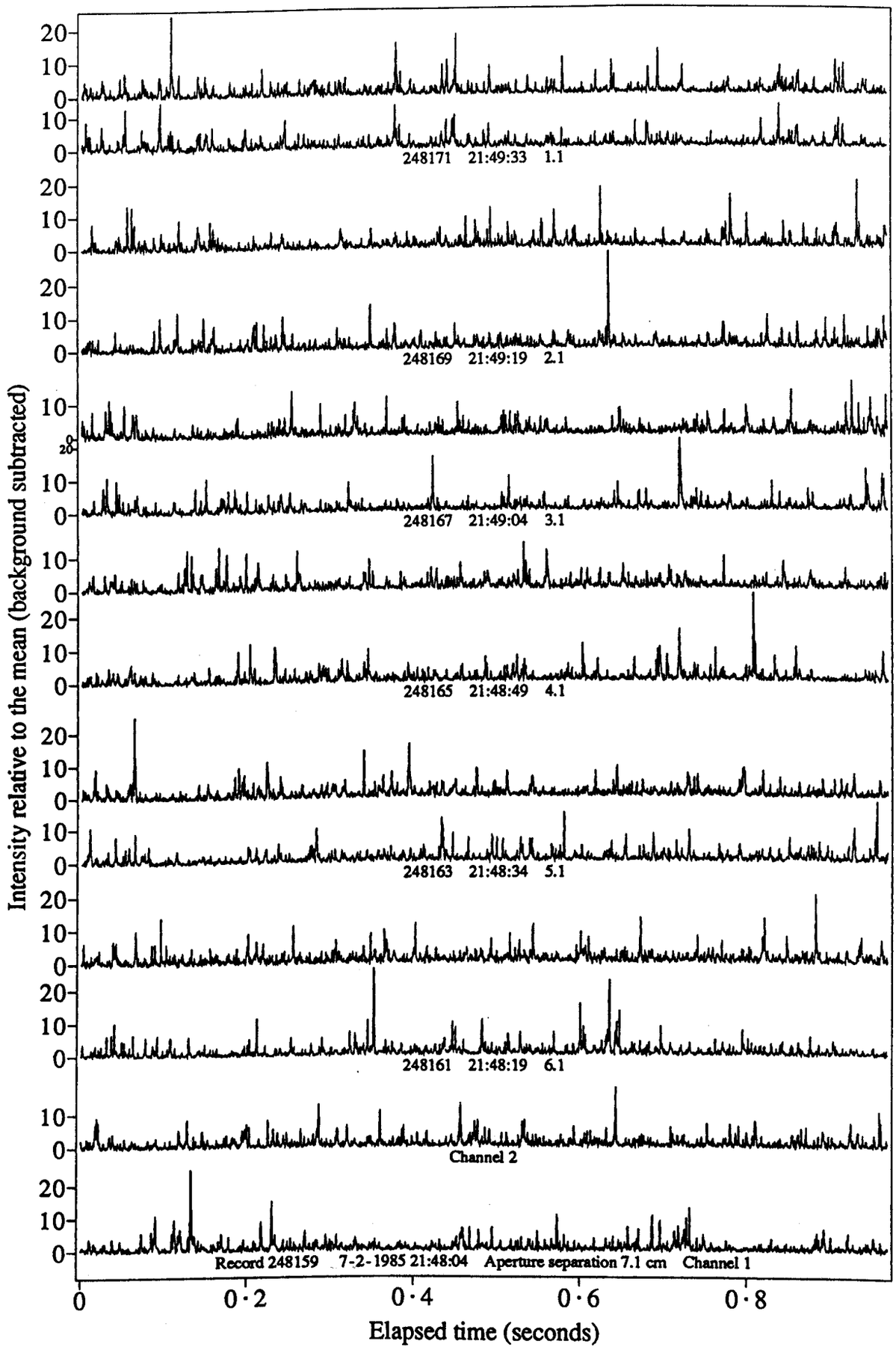

Figure 8-5 A plot of 14 records of stellar scintillation, including one (248161, channel 1) which was plotted in figure 8-3. The similarity of the statistics for all 14 records gives credibility to the practice of using one record from each night to indicate the night to night variation, as was done in figures 8-1 to 8-4.

bright patch less than 2 cm across.

i) The instantaneous intensity frequently reached more than 20 times the mean level.

8.2 Variance over time

An overview of the variation in the strength of scintillation is given in figure 8-6, showing all data taken on 29 different nights over a 47-day interval with a 4-mm aperture. The normalized second moment is plotted as a function of time for each night. Each trace joins values of the normalized second moment for several 0.97-s time series on channel 2, with the succeeding dot giving the value for the associated background record.

From figure 8-6 it can be seen that:

a) on 10 of the 15 nights where the interval of observations of Sirius is long enough to make a judgement, there is a decline in the second moment in the first two hours after last light. There is one night (17-1) where the second moment rises significantly over this interval and one (6-1) where it fluctuates substantially.

b) On one night (23-1) there was a dramatic drop in the second moment about 30 min after last light.

c) There is a tendency for the second moment to decrease in the first 3 hours after midnight on 8 nights of the 17 for which the relevant data is available. On the other 9 nights, the second moment tends to be higher overall and fluctuates substantially. There is no case of the scintillation increasing steadily over this interval.

d) The scintillation for the single star β Crucis is substantially higher than for the double star α Crucis (on 17-2), indicating that the two scintillation patterns due to the two components of α Crucis were at least partially separated in position, reducing the second moment in the manner postulated in §4.4.

A similar overview of the scintillation observed with 2-mm apertures is presented in figure 8-7. In this case a vertical line is drawn connecting the values of the normalized second moment on channels 1 and 2 for each record. The characteristics observed in the previous figure are again evident. In addition, it can be seen that:

e) for one night (7-2), where both 4-mm and 2-mm apertures were used, the scintillation is higher for the smaller apertures, as deduced above by examination of single

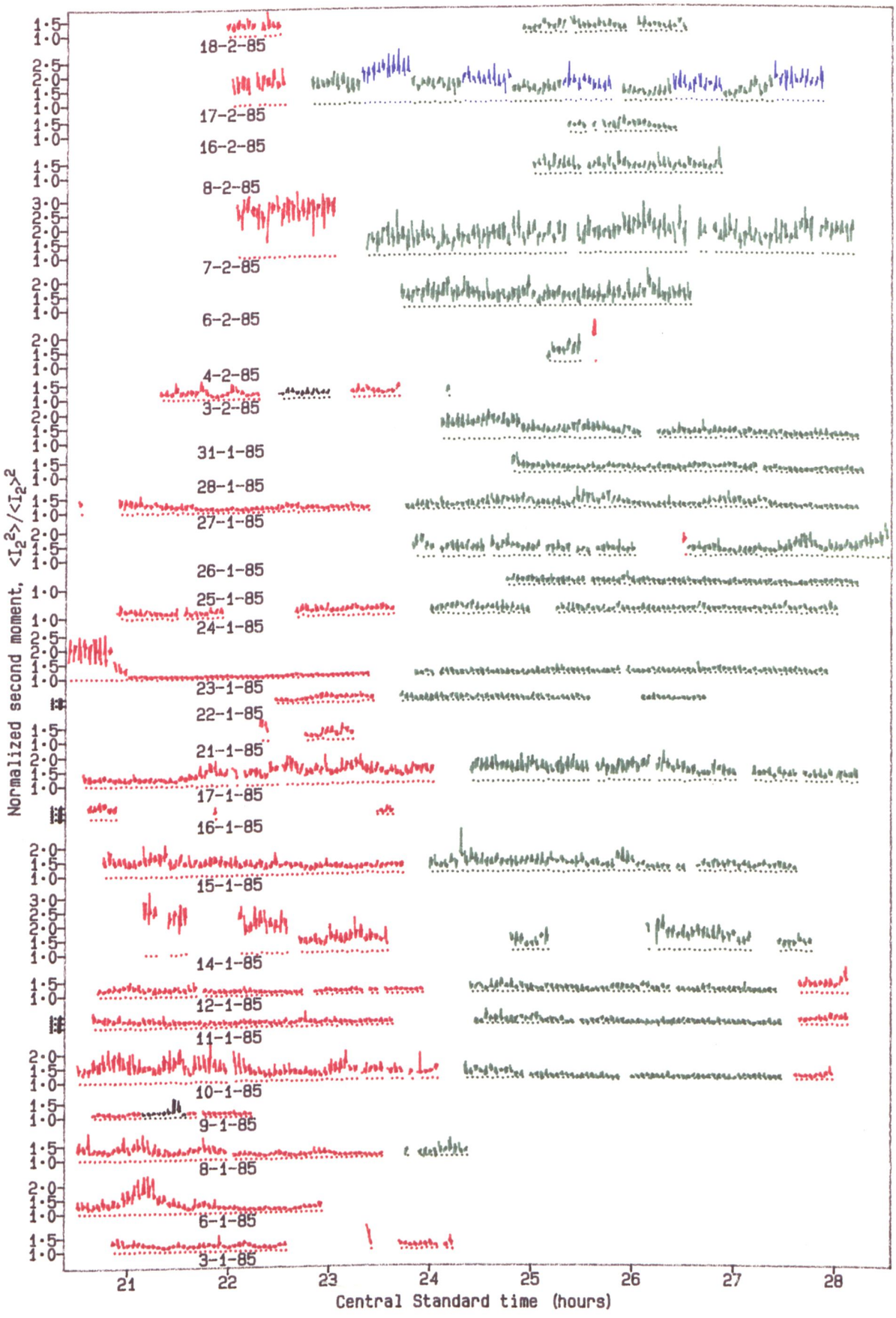

Figure 8-6 The normalized second moment of scintillation for a 4 mm circular aperture for Sirius (red), Alpha Crucis (green), Beta Crucis (blue) and Canopus (black). Values for successive records of starlight on channel 2 are joined by a trace, with a dot showing the value for the associated background record.

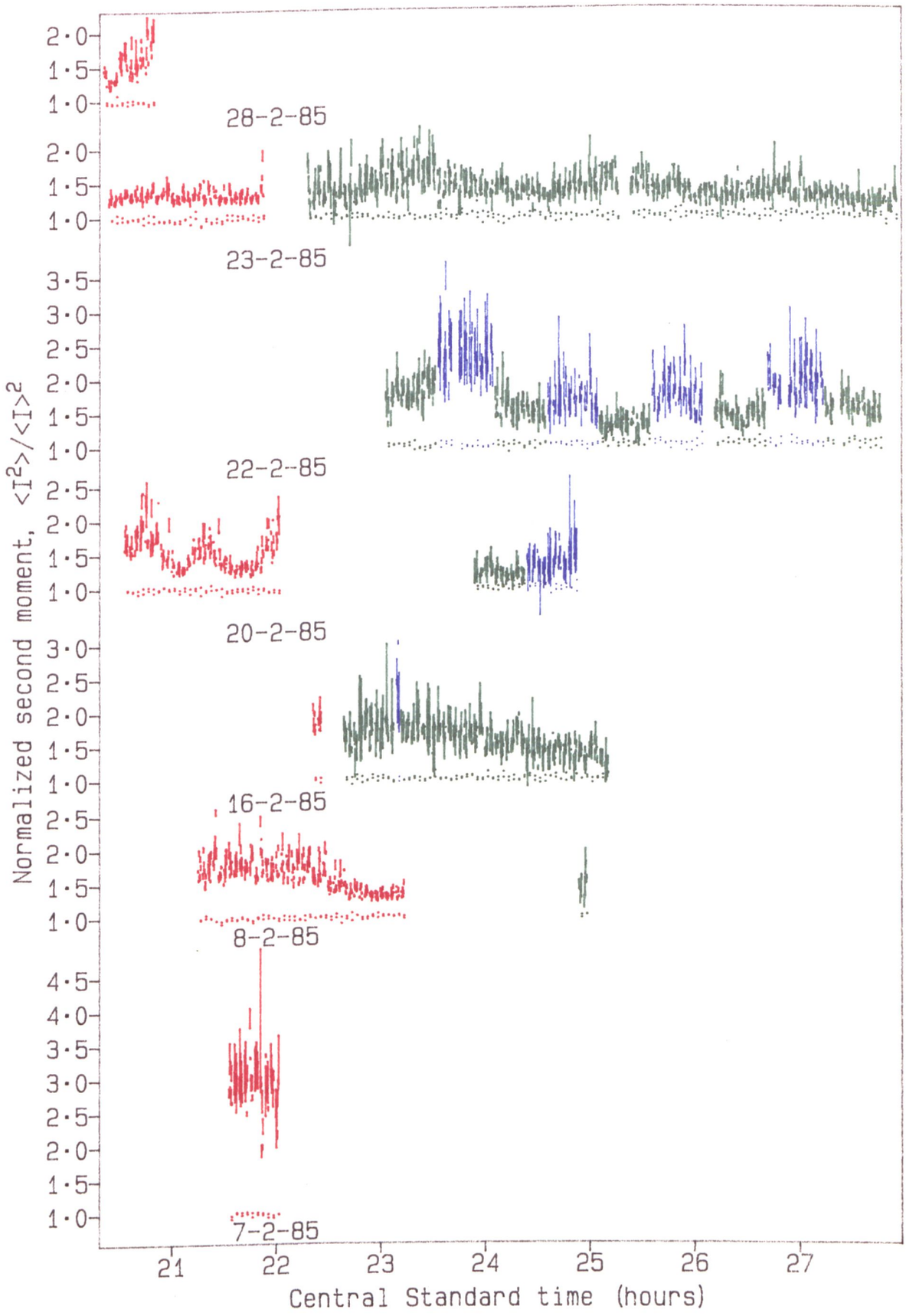

Figure 8-7 The normalized second moment of scintillation for a 2 mm aperture on several nights for Alpha Crucis (in green), Beta Crucis (blue) and Sirius (red). The values for channels 1 and 2 are connected by vertical lines. Background records are indicated by dots. (Only time series records are used.)

time series.

f) The second moment is generally higher.

g) On two nights (20-2 and 28-2) the second moment for Sirius fluctuates considerably.

Observations f) and g) may be due to the use of smaller apertures, or to the greater incidence of orographic turbulence in February 1985, compared to the previous month. In the next section, the comparison of simultaneous measurements using apertures of different sizes allows discrimination between these two alternatives.

8.3 Aperture dependence

Figure 8-8 presents an analysis of data taken to investigate "aperture dependence" at scale sizes less than 4 mm. This analysis is based on the concept that if the aperture is larger than the smallest scintillation patterns, the second moment will be reduced due to spatial convolution. Observations were made simultaneously for two different apertures: a 2-mm aperture on channel 1 and a 4-mm aperture on channel 2. Dots indicate the comparison for individual frequency distributions (left) and time series (right). The comparison is made for both the total light intensity I_t (starlight plus background) and starlight I (determined using equation 4.21).

The value of the normalized second moment $\frac{\langle I^2 \rangle}{\langle I \rangle^2}$ is greater for the 2-mm aperture in nearly all cases, indicating that there are features in the scintillation pattern which are smaller than 4 mm in size.

The results for I_t are included to allow an assessment of the possibility that the difference in the moment for the two apertures is produced by a systematic error in the method of correction for background light. This possibility arises because the difference in the moment value between the two apertures is small compared to the change involved in the correction, *ie*

$$\frac{\langle I^2_{(2\ mm)} \rangle}{\langle I_{(2\ mm)} \rangle^2} - \frac{\langle I^2_{(4\ mm)} \rangle}{\langle I_{(4\ mm)} \rangle^2} << \frac{\langle I^2 \rangle}{\langle I \rangle^2} - \frac{\langle I_t^2 \rangle}{\langle I_t \rangle^2} .$$

As the graphs are similar (apart from the change in the axis values) for I_t and I, there is no indication that the background correction introduces any bias.

The difference between the second moment for 2-mm and 4-mm apertures, measured simultaneously, is much less than the differences noted in the previous section

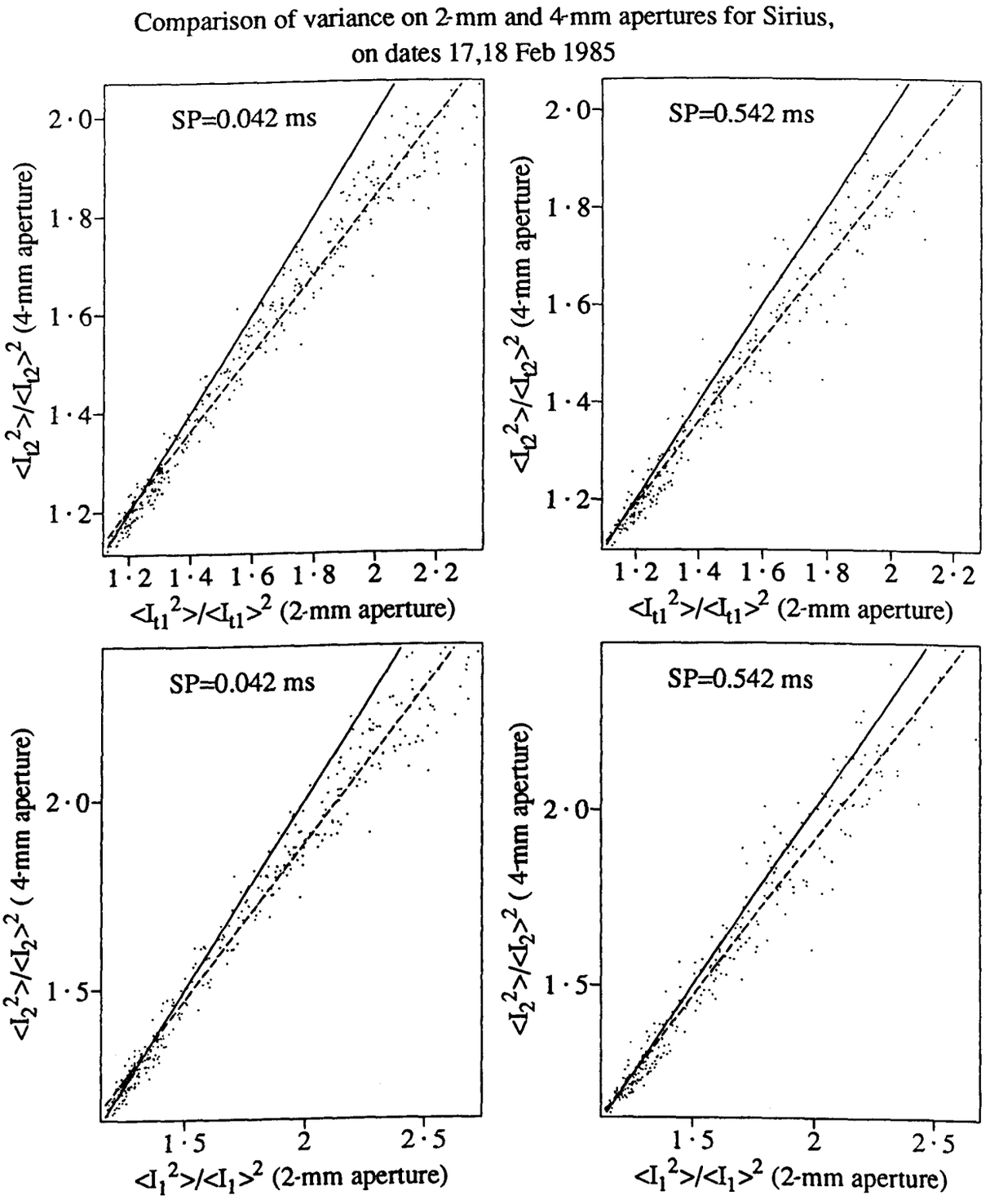

Figure 8-8 The presence of small scale structure in the scintillation pattern is revealed by a comparison of the variance for a 2-mm and a 4-mm aperture. The normalized second moments for a 2-mm aperture (on channel 1) are compared with those for a 4-mm aperture (on channel 2), for observations of Sirius. At the top the comparison is made for the total light intensity (I_{tn}, where n is the channel number), while at the bottom the correction for background has been applied to yield the values for starlight only (I_1 and I_2). In both cases the correction for afterpulsing has been applied. In each plot, dots indicate the comparison for individual records, a solid line indicates equal values and a dashed line indicates a fit by regression to the dots. Each plot is labelled with the sampling interval. In all cases, the variance of the scintillation is less for the 4-mm aperture, indicating the presence of structure in the pattern which is smaller than this aperture.

(*ie* the greater average second moment and greater variability in the second moment for 2-mm apertures in February compared to 4-mm apertures in January). Thus it is likely that the greater value of the mean and the variability of the second moment in figure 8-7 are due to a greater incidence of orographic turbulence in February 1985.

8.4 Wavelength averaging

Equation 3.7, due to Tatarski (1961), indicates that the scintillation strength is proportional to $\lambda^{-\frac{7}{6}}$, where λ represents wavelength. This dependence on wavelength has been verified using stars at zenith angles $< 40°$ by Dainty *et al* (1982). This implies that the scintillation patterns are not identical at different wavelengths and so, if a wider range of wavelengths is detected, the variance will be reduced.

In figure 8-9 the second moment of the scintillation is compared for two 4-mm apertures where one has a blue filter, reducing the range of wavelengths detected. The filter was either one or two layers of Kodak Wratten Gelatin filter number 34, which transmits blue light predominantly in the range 400–460 nm, as indicated in figure 5-10. Observations were made with the filter on one or the other of the apertures, for one or two layers of the filter.

In all four cases, the scintillation is greater on the channel with the blue filter, as predicted above. The consistency between the results for different sampling rates and channels indicates that the result is not produced by systematic errors in the corrections for afterpulsing and background.

8.5 Frequency spectra

The variation from night to night in the frequency spectrum of the scintillation of Sirius near the zenith was examined in §8.1. Here the variation over one night is examined. In figure 8-10 the frequency spectrum is plotted at different times on the same night, for two different stars and at low (30°), medium (40°–50°) and high (70°) elevations. These spectra are normalized to the same maximum value so that the relative shape of the spectrum can be compared visually. Two trends can be seen:

1) the high frequencies, (> 300 Hz) decline through the night relative to the low frequencies, irrespective of elevation. This is consistent with radiosonde readings, which at 26:30 (*ie* 2:30 am on the next calendar date) showed wind speeds at

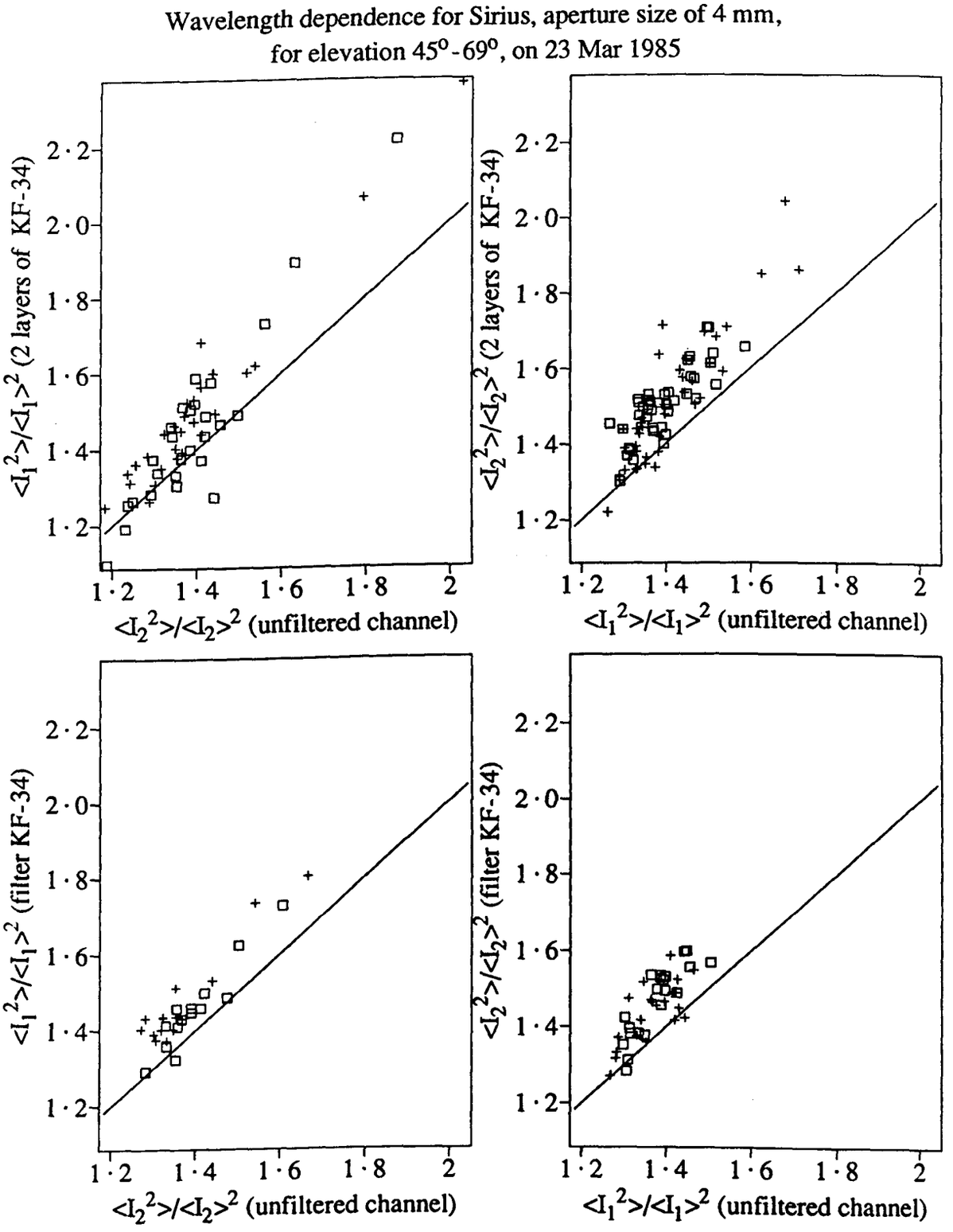

Figure 8-9 Observations of the wavelength dependence of stellar scintillation. The four graphs compare the normalized second moment of scintillation on two 4 mm apertures, of which one has a blue filter. The second moments have been corrected for afterpulsing and background. The squares indicate the comparison for individual frequency distribution records and the crosses show the comparison for time series records. Lines indicate equal values. The filters used were either one or two layers of Kodak Wratten gelatin filter number 34 (identified above as KF-34). These modify the wavelength response as shown earlier in figure 5-10. Each of the two filters was used in one or other of the two channels, giving the four combinations above. In nearly all cases the second moment is larger for the channel with the blue filter.

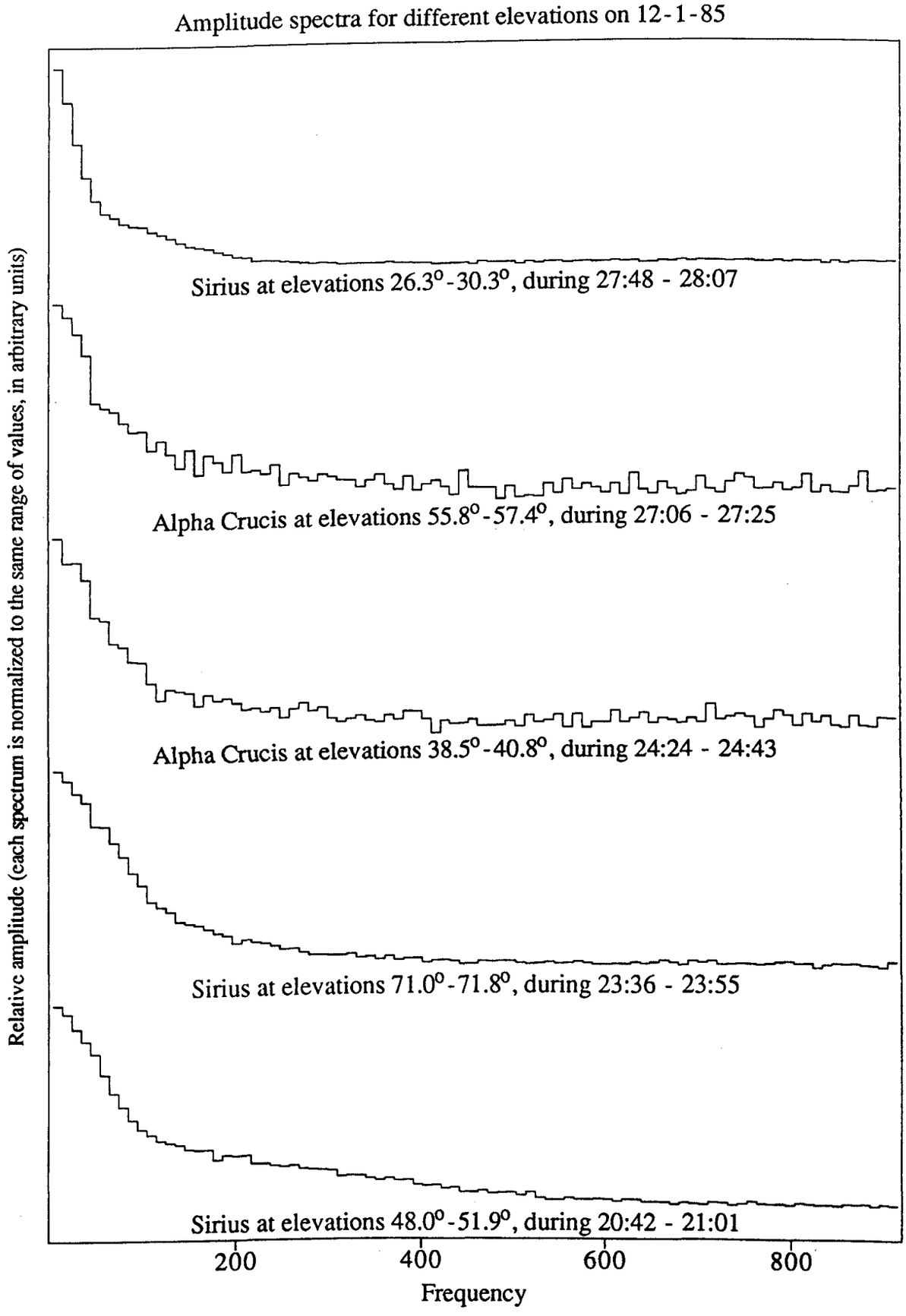

Figure 8-10 An investigation of the frequency content of stellar scintillation as a function of star elevation. The amplitude spectrum of stellar scintillation is plotted over the course of one night, with different plots for different stars and altitude ranges. The spectra are normalized so that each has the same vertical range. The mean value (at 0 Hz) has not been included. Through the night the readings progress through increasing elevation of Sirius, then increasing elevation of α Crucis and finally Sirius at low elevation.

heights below 8 km to have declined relative to those measured at 20:30.

2) Comparison of the spectra at low and high elevations (*ie* the two spectra for α Crucis and Sirius at the top) shows suppression at low elevation of the high frequencies relative to the low frequencies. This is consistent with observations by Mikesell *et al* (1951). Two factors could contribute to this:

   a) atmospheric dispersion (*ie* light of shorter wavelengths follows a tighter curved path through the atmosphere than light of longer wavelengths) will cause similar scintillation patterns at different wavelengths to be separated, thus reducing the overall variance (Young, 1969a). This effect will be more pronounced at lower elevations, where the dispersion is greater due to the larger angle of incidence relative to the horizontal planes of equal atmospheric density.

   b) For turbulence at a specific altitude, the distance from the observer increases with decreasing elevation, thus increasing the size of the scintillation patterns and hence reducing the observed frequency.

8.6 Elevation dependence of scintillation strength

As described in §3.3, Tatarski (1961) predicts that the variance of scintillation should increase as sec ϕ, for zenith angle ϕ. A recent prediction by Beran and Whitman (1988) differs from Tatarski's prediction at zenith angles $> 40°$. It has been verified in previous measurements (described in §3.5) that the variance increases with zenith angle, but the measurements are not sufficiently accurate to allow discrimination between the different predictions.

In figure 8-11 a large number of observations taken in this work are compared with the predictions. The second moment is plotted against star elevation for Sirius, combining data taken on 21 different nights using 4-mm apertures. Individual records are indicated by dots, while stepped lines indicate averages for each night: each horizontal line segment indicates the average value for all records for that night within the elevation range covered by the width of the segment. Points with bars show averages of all the data, giving the mean and standard error in the second moment within the indicated elevation range. Labelled curves indicate theoretical predictions by Tatarski (equation 3.9) and Beran and Whitman (1988) of the scintillation for the typical turbulence pro-

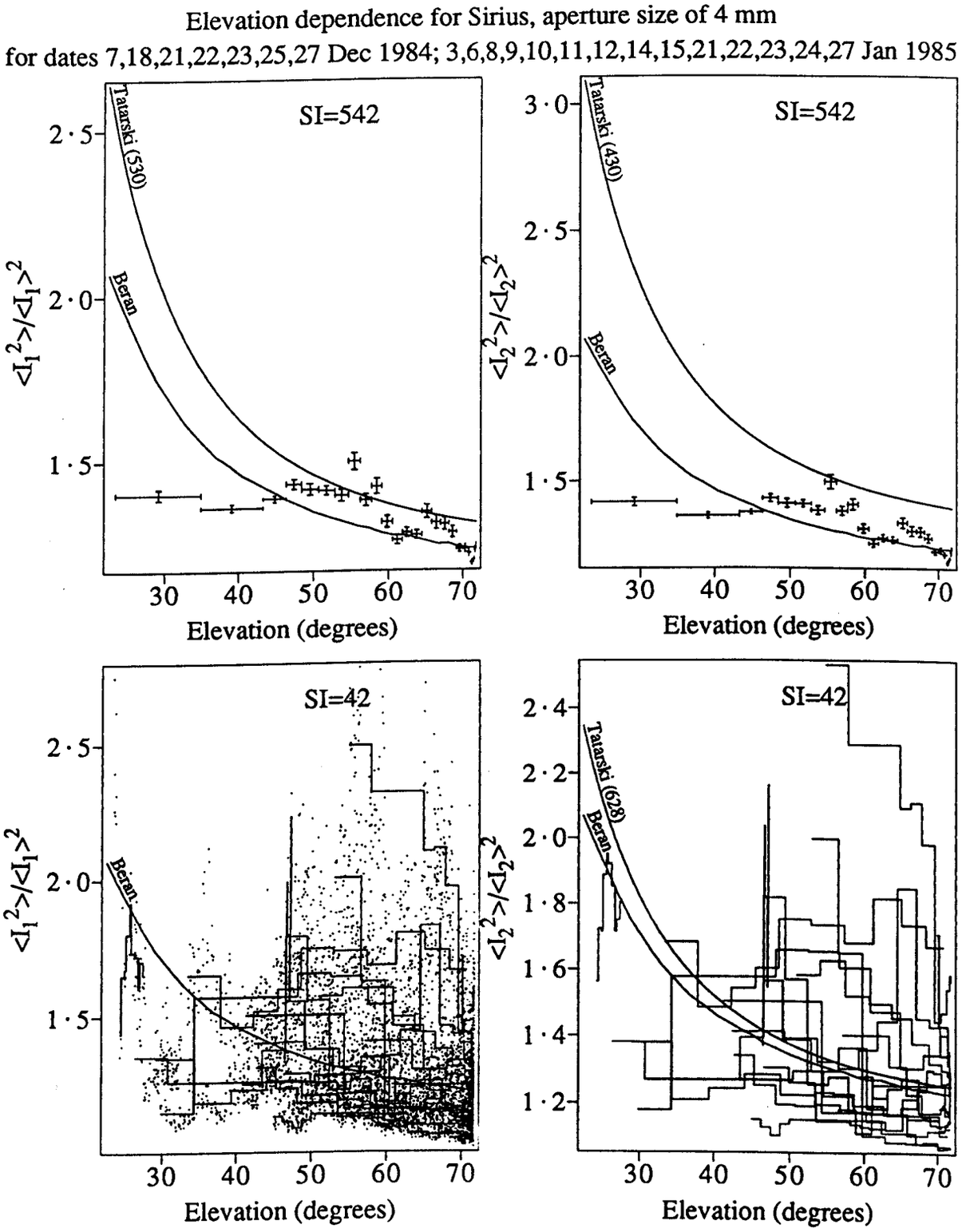

Figure 8-11 Measurements of the normalized second moment of intensity I, corrected for afterpulsing and background, are plotted against star elevation for the four data sets (channels 1 and 2, each with sampling interval SI of 42 and 542 μs). Dots represent individual records. Stepped lines show averages for each night, with each horizontal line segment indicating the average value for the subtended elevation range. Averages over all nights are indicated by points with bars, showing the mean and standard error of all values within each elevation range. The predicted second moment for a standard turbulence profile at 628 nm (Beran and Whitman, 1988) is shown by the curve labelled "Beran". The prediction of Tatarski's theory (equation 3.9) is shown by curves labelled "Tatarski (x)", with "x" indicating different wavelengths (628, 530 and 430 nm). For clarity, various features are omitted from each plot.

file specified by Beran and Whitman. The curve labelled "Beran" is reproduced from the publication of Beran and Whitman and is the result of their calculation for light of 628 nm. The curves labelled "Tatarski (λ)" are calculated by this author using equation 3.9, for wavelengths of λ = 628, 530 and 430 nm. For elevations above 50° the predictions of Beran and Whitman and of Tatarski should be the same at 628 nm. Thus the difference in the theoretical curves on the lower right of figure 8-11 indicates the presence of a small error.

From figure 8-11 it can be seen that:

a) on individual nights (solid stepped lines), both the normalized second moment and the variation with star elevation are often very different from the predictions.

b) For elevations between 50° and 70°, most averages of all the data (points with bars) lie between the predicted curves for 430 and 638 nm. The measured values tend to decrease with increasing elevation with the same slope as the theoretical curves.

c) For elevations below 50°, the average normalized second moment tends to be constant with elevation and much lower than the prediction. This is likely to be due to the atmospheric dispersion described in the previous section. However, on one night the values at 25°–30° are close to the prediction of Beran and Whitman.

In conclusion, the variance of the scintillation observed for elevations between 50° and 70° is consistent with theory, but below 50° there is great discrepancy. Night-to-night variation is considerable. Thus measurements of elevation dependence require a large number of observations, and a narrower wavelength range than used here to ensure that atmospheric dispersion is not significant.

8.7 Moment analysis

As explained in §3.4, a comparison of the higher moments with the second moment provides a test between different theories which predict the characteristics of stellar scintillation. In figure 8-12, this test is applied to data for Sirius, observed with a 2-mm aperture. The analysis is applied for frequency distributions (upper graphs) and time series (lower) for channel 1 on the left and channel 2 on the right. Results for some frequency distributions during the observation time are not included due to overflow of

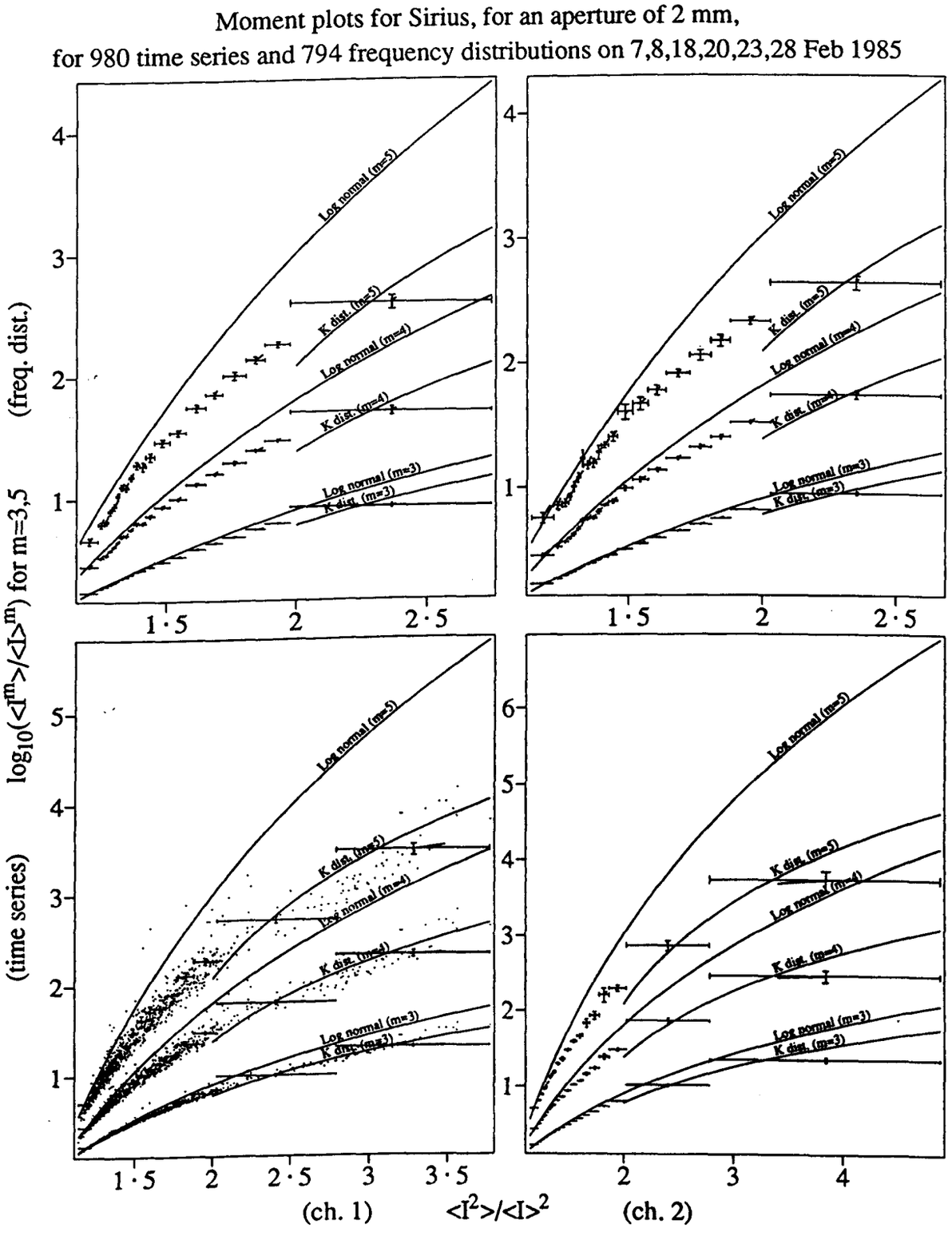

Figure 8-12 The "moment plot" for Sirius, observed with 2-mm circular apertures. The normalized higher moments $\frac{\langle I^m \rangle}{\langle I \rangle^m}$, for m=3,4 and 5, are plotted against the normalized second moment $\frac{\langle I^2 \rangle}{\langle I \rangle^2}$, where I is the instantaneous intensity. The comparison is presented for four data sets, these being frequency distributions (upper plots) and time series (lower) for both of channels 1 (left) and 2 (right). Dots indicate the comparison for single records (for channel-1 time series only). Bars indicate the mean ± the standard error of the higher moment values for subranges of the corresponding second moment values. The change produced by correction for dead time is indicated by a line drawn from each average value. Labelled curves indicate the theoretical relationships expected for the log normal and the K distributions.

the 4-bit counter used to record them. Dots indicate the comparison of higher moments with the second moment for individual records (shown only for channel-1 time series), and bars indicate the average and standard error in the higher moments for 40–50 records within subranges of the second moment. A line drawn from each average value indicates the small effect of an approximate correction (using equation 4.52) for a dead time of 30 ns.

In figure 8-12 it can be seen that:

a) the measured relationship is similar for the four sets of data. This indicates that statistical variation is not significant.

b) There is no significant difference for time series and frequency distributions, although the total sample time for frequency distributions is 2.3 times as long as that for time series. Thus there is no indication that the results are deficient due to absence of occasional large values, which would be more likely for the time series.

c) The measured relationships are close to the log normal distribution for small values of the normalized second moment and tend towards the K distribution at larger values. This is consistent with previous measurements (see figure 3-6), although values here are closer to the curve for the K distribution.

d) For values of the second moment near 2, the displacement of the higher moments from the curve for the log normal distribution is similar to that observed by Goldner and Ben-Yosef (1988) for a simulated log normal distribution with 5000 independent points.

e) The correction for dead time is small and tends to translate values parallel to the theoretical lines. Thus the dead time is not significant in producing the observed discrepancy from the log normal distribution.

The total sample time (for each subrange of the second moment) is 48 s for time series and 109 s for frequency distributions. Given the autocovariance width of ~2 ms (from figure 8-4), this means that there are $\sim 2 \times 10^4$ independent data samples for time series and $\sim 5 \times 10^4$ for frequency distributions. Thus the number of independent data samples is substantially greater than the 5000 in the simulation by Goldner and Ben-Yosef, so it is possible that the observed agreement with the K distribution is significant. However, this is subject to the the uncertainties created by statistical error

in the second moment (see §3.4), temporal averaging of the time series data and the omission of frequency distributions in which overflow occurred.

In summary, the moment plot here gives a similar result to previous observations, suggesting that the scintillation is not log-normally distributed. However, due to deficiencies in both the technique (*ie* the moment plot) and the data recording system, no firm conclusion can be drawn.

8.8 Comparison of wind and scintillation-pattern velocities

In figure 8-13 the deduced velocity of the scintillation pattern is compared with a hodograph of the wind profile measured by radiosonde. The analysis is applied to 0.97-s time series of the intensity on two 2-mm apertures, separated by 6.1 cm, at 10 different orientations. The covariance between the two apertures is calculated as a function of time shift. The velocity of the scintillation pattern is determined from the time shift and the aperture separation. The covariance is then plotted as a function of the projection of this velocity on a horizontal plane. The finite size of the detectors produces an uncertainty in the calculated velocity, portrayed by elliptical areas in the diagram. Results are shown only for particular time shifts which are selected so that the ellipses do not overlap along radial directions. A hodograph of the radiosonde profile is added: the altitude (km) of each wind measurement is printed at the wind velocity measured at that altitude, and successive measurements are connected by straight lines.

Large values of the covariance occur at velocities in agreement with the radiosonde profile for altitudes of 1 km and 10–13 km. (*nb* There is also agreement for 28 km, but this is probably coincidental, given the low turbulence strength expected at this height, as indicated in figure 3-1). It is likely that the three peaks in covariance for wind towards the northwest are actually the same peak, which is spread out due to the finite size of the scintillation patterns and given a patchy appearance by sampling, as readings at successive angles are separated by 3 min in time.)

Such agreement between wind velocity deduced from scintillation and radiosonde readings has previously been found by Rocca *et al* (1974) and Caccia *et al* (1987). The detection of scintillation produced at 12–16 km is consistent with both theory (see figure 3-2, where the maximum scintillation is predicted to come from 11–15 km) and

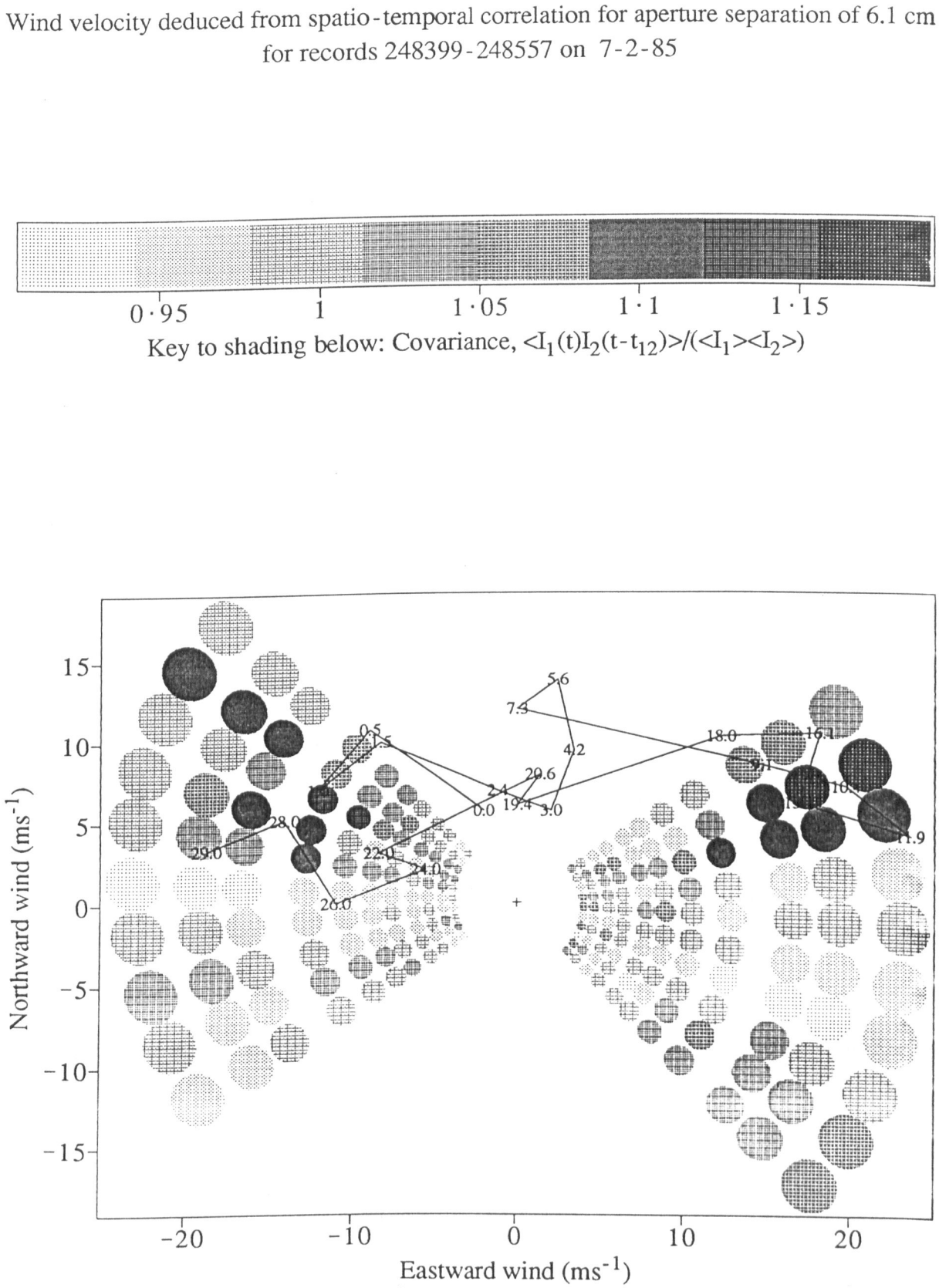

Figure 8-13 A comparison of the wind velocity measured by radiosonde and that deduced from scintillation observations. The radiosonde readings are indicated by writing the altitude (km) of each observation at the velocity measured at that height. Successive readings are joined by straight lines. The spatiotemporal correlation function of the stellar scintillation is calculated for two 4 mm apertures separated by 6.1 cm, for 10 different orientations. Shading indicates the correlation value as a function of wind velocity. The finite size of each shaded region is related to the finite size of the apertures.

previous measurements. In contrast, the detection of scintillation from an altitude of only 1 km is inconsistent with theoretical predictions; *eg* Roddier and Vernin (1977) suggest a lower limit of 2.5 km for detectable scintillation. However, the height (1 km) and wind direction (towards the northwest) suggest that the scintillation is produced by turbulence in the lee wave of the hills (of height 0.7 km) to the southeast. Such a situation may produce turbulence much stronger than normal (Barletti *et al*, 1976).

8.9 Double star scintillation pattern

The two separated components of the scintillation pattern of a double star should produce peaks in the spatial correlation function, displaced from the origin along a line parallel to the double star. To look for these peaks, an analysis similar to that used by Vernin and Roddier (1975) is presented on the left side of figure 8-14. The cross covariance between the scintillation on two apertures is plotted, for cases where the line joining the apertures is aligned parallel or perpendicular to the projection of the line joining the two components of the double star. All data available for α Crucis on about 20 nights in Jan–Feb 1985 are used. Rectangles show the results for 4-mm apertures and ellipses for 2-mm apertures. The vertical and horizontal extent of these indicate the standard error in the mean of the covariance and the uncertainty in separation due to the finite size of the apertures. The difference between covariance values in the parallel and perpendicular cases is plotted in the bottom graphs, to remove the effect of the autocorrelation peak around zero separation.

A possible source of bias in this analysis is that the parallel and perpendicular covariances were recorded at different elevations. To assess the extent of this bias, the analysis is repeated for the nearby single star β Crucis and plotted on the right of figure 8-14. If the difference in the parallel and perpendicular covariances observed for the double star is a related to the elevation angle, then it would also occur for the single star. Unfortunately there are much less data available for the single star and the statistical error is too large to make a firm conclusion.

For the double star the difference between the parallel and perpendicular covariances is positive at separations of 2 and 3 cm, for both 2- and 4-mm apertures. There is no hint of an equivalent peak for the single star, but given the large error, it is not

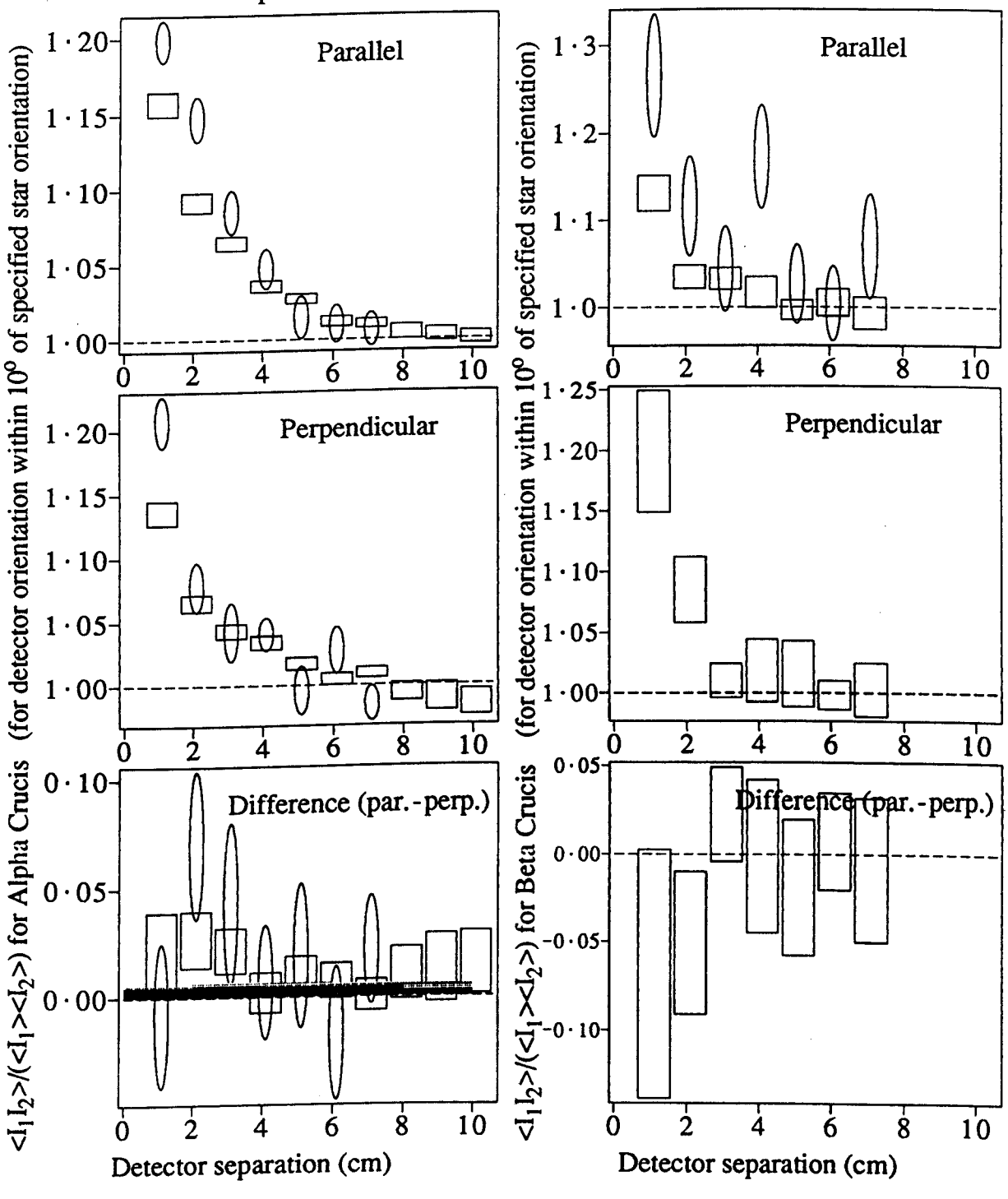

Figure 8-14 The spatial correlation function measured parallel and perpendicular to the line joining the components of a double star. This is plotted for the double star α Crucis on the left and for the single star β Crucis on the right. The spatial correlation measured parallel to the double star is plotted at the top and that measured in the perpendicular direction is plotted in the middle. The difference between the two is plotted at the bottom. Rectangles indicate values for 4 mm apertures and ellipses for 2 mm apertures. The horizontal extent of both rectangles and ellipses indicates the uncertainty in separation due to the finite size of the apertures, while the vertical extent indicates the mean $\pm$ the standard error of all the contributing values. Theoretical values of the covariance, predicted using equation 8.2 for the minimum and maximum elevation of α Crucis, are indicated by light and heavy shading respectively.

possible to conclude that the peak is only present for the double star. If the peak for the double star is caused by the presence of two similar patterns, the separation of 2–3 cm corresponds to an altitude of the turbulence of 0.7–1.4 km (using equation 4.1 with double star separation of $a = 21$ μrad and elevation angle $\alpha = 40°$–$62°$).

The shaded areas in the difference graph for α Crucis indicate the predicted values for this difference for the standard turbulence profile specified by Beran and Whitman (1988). The difference is equal to the spatial cross covariance between the scintillation patterns of the two components of the double star and and is estimated using the method employed by Azouit and Vernin (1980), using equations 3.14–3.16, *ie*

$$C_{||}(S) - C_{\perp}(S) = \left(\frac{B_1 B_2}{(B_1 + B_2)^2}\right) 2.24 k^{\frac{7}{6}} (\sec\phi)^{\frac{11}{6}} h^{\frac{5}{6}} \overline{C_n^2(h)} \Delta h \qquad -- (8.2)$$

where this is evaluated with $k = 1.26 \times 10^7$, $\phi = (90 - \alpha) = 50°$ (light shading) and 28° (heavy shading) and $\frac{B_1}{B_2} = 1.6$, as a function of detector separation S. Δh is chosen so that it transforms (by equation 4.1) to a separation interval Δs which is equal to the 2-cm width of the apparent peak at 2–3 cm.

The peak in covariance at 2–3 cm, if genuine, indicates turbulence that is about five times stronger at 1 km than in the average profile specified by Beran and Whitman (1988), *ie* the measurement here gives $C_n^2 \sim 10^{-15}$ ($m^{-\frac{2}{3}}$).

8.10 Conclusion

In this chapter many of the observations of stellar scintillation reported in the literature have been repeated, but using the same data set. The results are generally consistent with previous observations, except that smaller scintillation patterns are observed and it is deduced that substantial scintillation is produced by turbulence at lower altitudes. Both of these exceptions occur when the observing site was downwind of hills, suggesting that strong scintillation, with small pattern sizes, was produced by strong turbulence in the lee wave of the hills.

Chapter 9 New observations

The previous chapter described observations which repeated work previously published by others. In this chapter, observations and analysis are presented to show what is believed to be new information about the structure and origin of stellar scintillation.

Scintillation patterns of either small size or high intensity are investigated, using data in which such features are predominant. The scintillation pattern of a double star is examined in two dimensions and used to show clear evidence for the production of scintillation by low-altitude turbulence.

Two features of scintillation which give atmospheric information are investigated. These are the variation in scintillation strength across the sky and the association of scintillation with cloud.

Tests are applied to scintillation produced under appropriate conditions in order to investigate the refraction and phase interaction postulated in §4.1.2. Finally the probability density function of scintillation is investigated, using a modified version of the standard moment plot.

9.1 Small scale structure

Observations presented in the previous chapter indicate the presence of scintillation features less than 2 cm across (in figures 8-5 and 8-14). The characteristics of such small features are of interest for

a) comparison with theoretical predictions, and

b) evaluation of their potential as tracers of atmospheric wind.

Figure 9-1 shows the time-shifted spatial covariance of the scintillation of Sirius, measured using the "multiple collimator" described in §5.2.2. This covariance is derived from seventy 0.97-s time series of the light intensity on two apertures (one of diameter 2 mm and the other 4 mm), at 7 different separations along each of 10 different angles. The density shading is a measure of the normalized covariance of the light intensities I_1 and I_2 on the two apertures

$$Cov_n(t_{12}) = \frac{\langle I_1(t) I_2(t - t_{12}) \rangle}{\langle I_1 \rangle \langle I_2 \rangle} \qquad --(9.1)$$

where t_{12} is the time delay applied to channel 2. This time delay is varied in steps of 1.084 ms (*ie* two sample intervals).

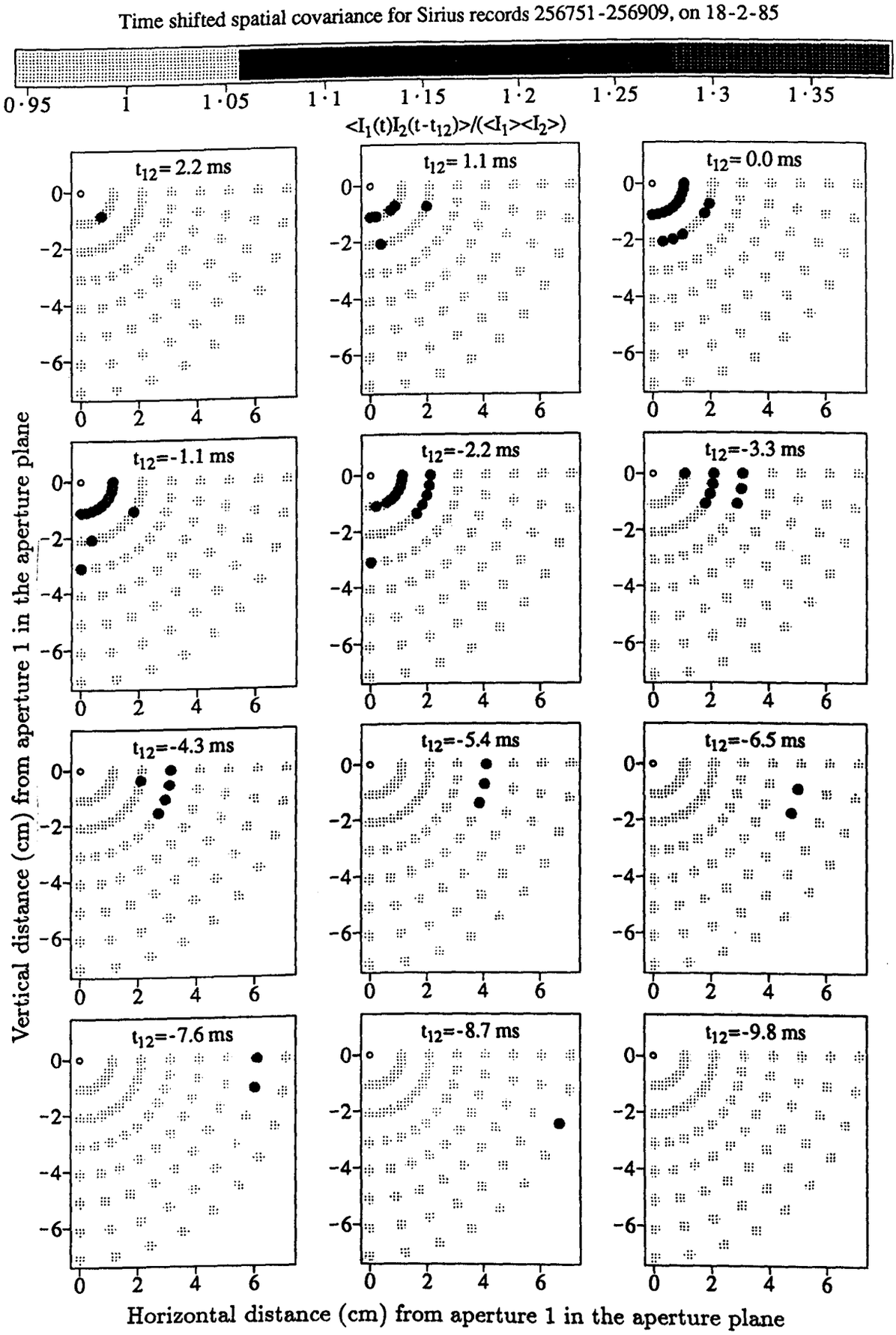

Figure 9-1 The spatial covariance of stellar scintillation, plotted as a function of the time shift applied between the fluctuations on two apertures. The open circle at (0,0) indicates the size of the aperture for channel 1. The position and size of the aperture for channel 2 is shown by shaded circles, with the density of the shading indicating the covariance between apertures 1 and 2.

Several points can be made from figure 9-1:

a) the size of the scintillation features is less than 6 cm, shown by the absence of correlation between apertures separated by 3.1 cm at zero time delay.

b) A substantial part of the scintillation consists of features less than 4 cm across, indicated by the greater correlation for 1.1-cm separation than for 2.1 cm at zero time delay.

c) At large negative values of the time delay (*eg* $t_{12} < -5$ ms) the peak in the spatial correlation is restricted to one of the available separations at each angle. This indicates that scintillation features of less than 2 cm in size are moving over several centimetres without substantial change in their structure. Thus Taylor's hypothesis of "frozen-in" turbulence (Taylor, 1938) is observed to be applicable (in this instance) to turbulence which produces small scintillation features. Taylor's hypothesis has previously been verified for 10-cm scintillation features (Caccia *et al*, 1987).

In figure 9-2 temporal auto- and cross-covariance functions are plotted as a function of time shift, for the data used to produce figure 9-1. The spatial information is given by annotation on each function. The figure is harder to interpret than the previous one, but more quantitative information is presented. The normalized autocovariance

$$Cov_n(t_{11}) = \frac{\langle I_1(t) I_1(t - t_{11}) \rangle}{\langle I_1 \rangle^2} \qquad --(9.2)$$

and the normalized cross covariance $Cov_n(t_{12})$ are plotted as functions of time shift for each record used in figure 9-1. The spatial information is given by the aperture separation Sep and aperture position angle A_{pa} written near each function, where A_{pa} is the angle of the aperture for channel 2 relative to that for channel 1 in the aperture plane. The functions are shifted vertically in the plot so that there is no overlap.

The deductions above are confirmed in this figure:

d) the relatively low covariance value at zero time delay for an aperture separation of 1.1 cm indicates the presence of features less than 2 cm across.

e) The consistent shape and size of the covariance peak with increasing time shift shows that there is little change in the scintillation patterns as they move over 7.1 cm.

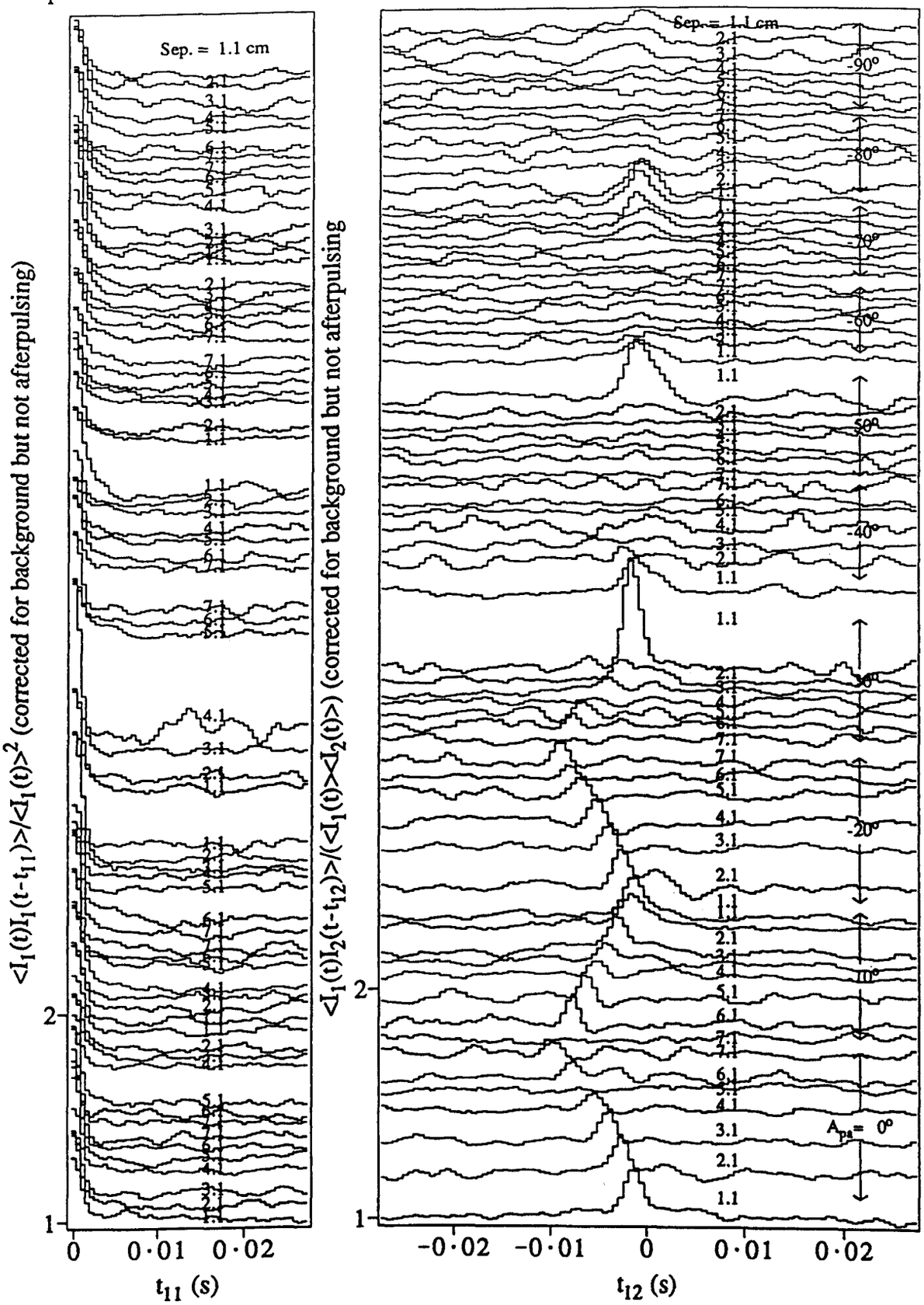

Figure 9-2 Temporal autocovariance (left) and cross covariance functions (right) are plotted for the same records as anaylzed in figure 9-1. The functions have been shifted vertically to avoid overlap. The aperture separation *Sep* and position angle A_{pa} are given for each record. This presentation is less direct than that of figure 9-1, but shows the features more clearly. The peaks in cross covariance, at larger time shifts for larger aperture separations, show that patterns less than 2 cm in size move from one detector to the other without significant change.

In addition, it can be seen that:

f) the time delay for maximum covariance at $-10°$ and $-20°$ is proportional to the aperture separation, indicating that the velocity of the scintillation pattern was constant for at least 2 min (this being the time interval required to take seven records).

g) The absence of statistical fluctuation in the size of the peaks for different records at a particular angle (*eg* $-20°$) suggests that a large number of individual features contribute to the covariance for a single record.

The number of contributing features is investigated directly in figure 9-3, where the cumulative contribution to the covariance is shown as a function of time t_{cum} through a record of N samples at intervals of Δt, *ie*

$$Cov(t_{12}, t_{cum}) = \frac{\frac{1}{N}\sum_{i=1}^{N_{cum}} I_1(t + i\Delta t) I_2(t + i\Delta t - t_{12})}{\langle I_1 \rangle \langle I_2 \rangle} - \frac{N_{cum}}{N} \qquad --(9.3)$$

where N_{cum} is the number of samples in time t_{cum}. (*nb* If I_1 and I_2 are uncorrelated, the expected value of the first term is the same as the second, giving $Cov(t_{12}, t_{cum}) = 0$.) This is plotted for the record corresponding to $Sep = 4.1$ cm and $A_{pa} = -20°$ in figure 9-2.

It can be seen in figure 9-3 that the cumulative contribution to the total covariance (for $t_{12} = -6$ and -8 sample intervals) rises in small steps, indicating that many individual features, all moving with the same velocity, contribute to the spatial covariance shown in figures 9-1 and 9-2. This indicates that stellar scintillation provides a large number of tracers of atmospheric wind velocity over short (< 1-s) time intervals, thus allowing wind measurements with high temporal resolution.

A comparison of the pattern velocity with the appropriate radiosonde profile (made in the same manner as for another night in §8.8, figure 8-13) indicates that the 2-cm scintillation features examined here had the same velocity as the wind in the height range 0.5–1 km. This is consistent with Tatarski's prediction (1961, *p*140) of the scintillation pattern size for this height range, *ie* $\sqrt{\lambda h} = 1.5$ to 2.1 cm, for $\lambda = 450$ nm. Although the domination of the scintillation pattern by turbulence at such a low height is inconsistent with accepted knowledge (see figure 3-2), the wind direction was from the southeast, giving the appropriate conditions to generate strong orographic turbulence

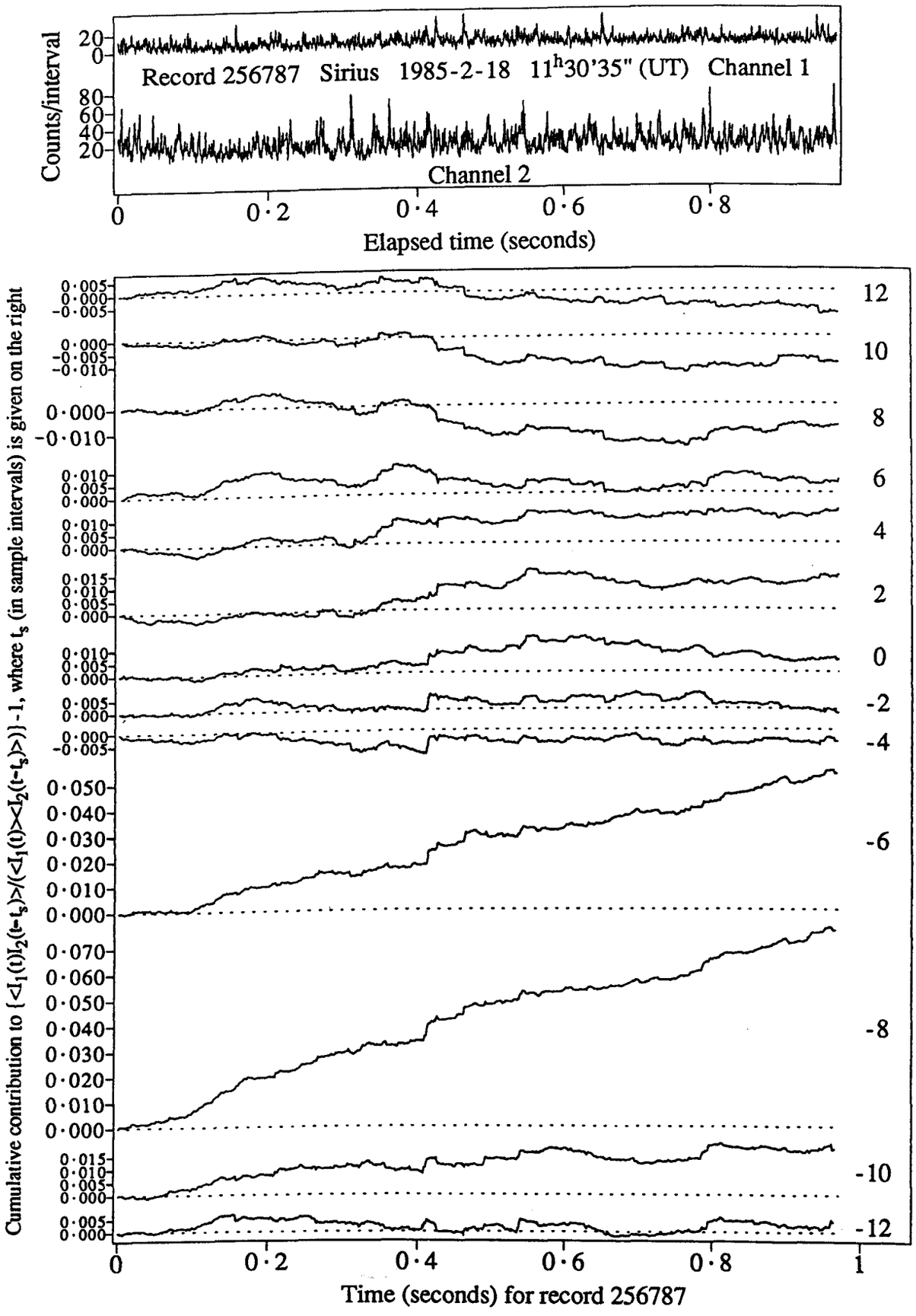

Figure 9-3 For the time series of photocounts plotted at the top, the cumulative value of the contribution to the cross-correlation is plotted below for a number of different time shifts. This cumulative correlation is plotted directly underneath the corresponding point on channel 1 of the time series. The dashed lines indicate zero correlation. The time shift (as a whole number of sample intervals, each of 542 μs) is specified on the right, where a negative shift corresponds to a shift of channel 2 to an earlier time.

below 1 km.

In summary, Taylor's hypothesis is verified on an occasion when the turbulence produces small (2-cm) scintillation features. On this occasion many individual features of the scintillation pattern made similar contributions to the spatial and temporal covariance for a 1-s record. Comparison with radiosonde readings indicates that the 2-cm features are produced by turbulence at a height of less than 1 km. This is consistent with a prediction of the pattern size for this height. These observations suggest that stellar scintillation has the potential for remote measurement of atmospheric wind velocity at an altitude of 1 km, with good time resolution.

9.2 Observations of large fluctuations in intensity

As shown earlier (in figures 8-1, 8-3 and 8-5), data on two nights (7-2-85 and 16-2-85) showed very large fluctuations in intensity, frequently exceeding 20 times the mean level. These are worthy of investigation for comparison with theoretical expectations and as possible tracers of atmospheric wind velocity; their motion and structure is examined below.

A search of the data for the two nights was made to determine if the bright features could be seen to move from one detector to another. No examples of such movement were found when the detector separation exceeded 2.1 cm, but it was observed for detector separations of 1.1 and 2.1 cm. In figure 9-4 the cumulative contribution analysis of figure 9-3 is repeated for a record showing movement of bright features. (*nb* The disparity between the count rates on the two channels is due to a smaller aperture being used for channel 2).

As in figure 9-3, there is a steady increase in the cumulative contribution to the covariance between two apertures, with a maximum rate for a time shift of -5 intervals (*ie* channel 2 is shifted to an earlier time by 2.71 ms). There are also five large steps in the cumulative covariance, coincident with large enhancements in intensity. These bright features tend to make a maximum contribution at a shift of -6 sampling intervals, and so appear to be moving at a slightly smaller speed than the major part of the scintillation pattern.

The transit time (~ -6 intervals) and the range of time shifts for which significant correlation occurs (~ -4--7 intervals) are roughly the same for bright features and

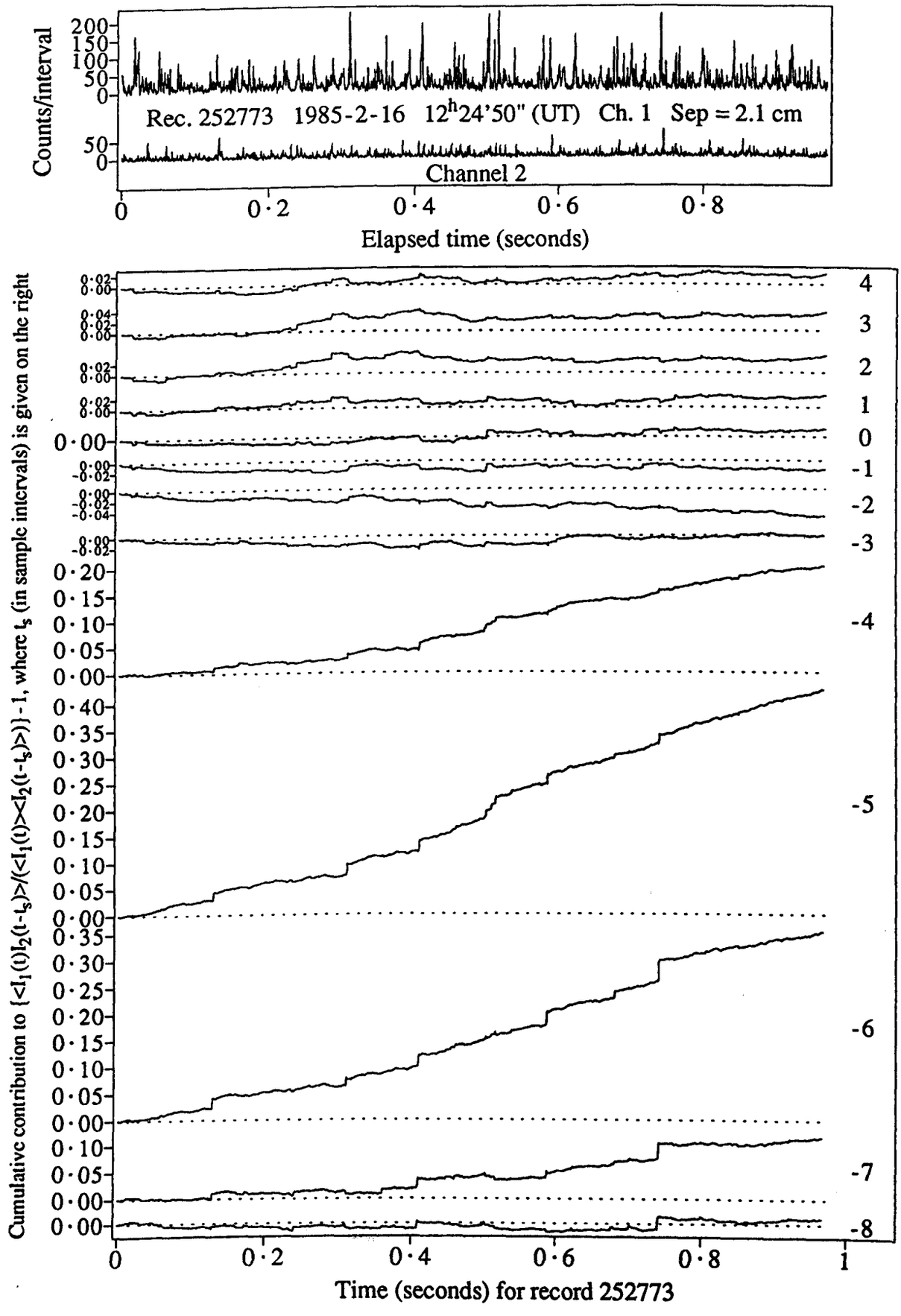

Figure 9-4 The cumulative contribution to the normalized cross-covariance is plotted as in the figure 9-3, for data which contains large enhancements in intensity. At time shifts of $t_{12} = -5$ *to* -7 there is an almost uniform contribution to the cross-covariance throughtout the record, indicated by the steady increase in the cumulative value. At these same time shifts, there are also five step-like increases in the cumulative value. These are associated with high intensity spikes in the time series.

for the rest of the scintillation pattern. Thus the bright features and the other features are approximately equal in size. As the detector separation is 2.1 cm, and the width of the peak in temporal covariance is about two-thirds of the time shift for maximum covariance, the pattern features are about 1.5 cm across. It was seen in figure 9-1 that features less than 2 cm across can be tracked out to 7.1 cm in a "scan" produced by the "multiple collimator", so the inability to track the bright features for more than 2.1 cm in this case is not due to the limitations of the technique. Thus it appears that the bright features are transient, and disappear as they move only 3 cm.

The size of features of different peak intensity is shown more directly in figure 9-5, by plotting the average of the number of photocounts seen on one detector when a particular number is seen on the other. The analysis is applied for the night (7-2-85) when the brightest features were seen, using 70 frequency distributions of Sirius for each of two aperture sizes (4 mm and 2 mm). The average of the counts on channel 2 recorded simultaneously with a specific number of counts on channel 1 is plotted as a function of the aperture separation. This function is plotted for each possible number of counts on channel 1 (0–15). For the larger apertures (right) it can be seen that:

a) the brightest features in the pattern are surrounded by a region where the intensity is above the average out to about 3 cm.

b) The darkest parts of the pattern are surrounded by a region that is darker than average out to about 4 cm.

c) There is no reduction in intensity (below the average value) associated with the bright features out to at least 7 cm. This implies that the bright features must arise from the concentration of light from over a large area (to satisfy conservation of energy, given the absence of a dark region immediately around them).

Similar results are apparent for the measurements with 2-mm apertures (left).

A postulated explanation for the absence of a large reduction in light intensity immediately surrounding the bright features is that they are produced by chance constructive interference of light from several sources in the turbulence, located at different heights and at various distances from the line of sight from detector to star. This would explain the failure (mentioned earlier) to follow their movement over more than 2.1 cm, as differential motion at different heights would lead to rapid decay of these chance su-

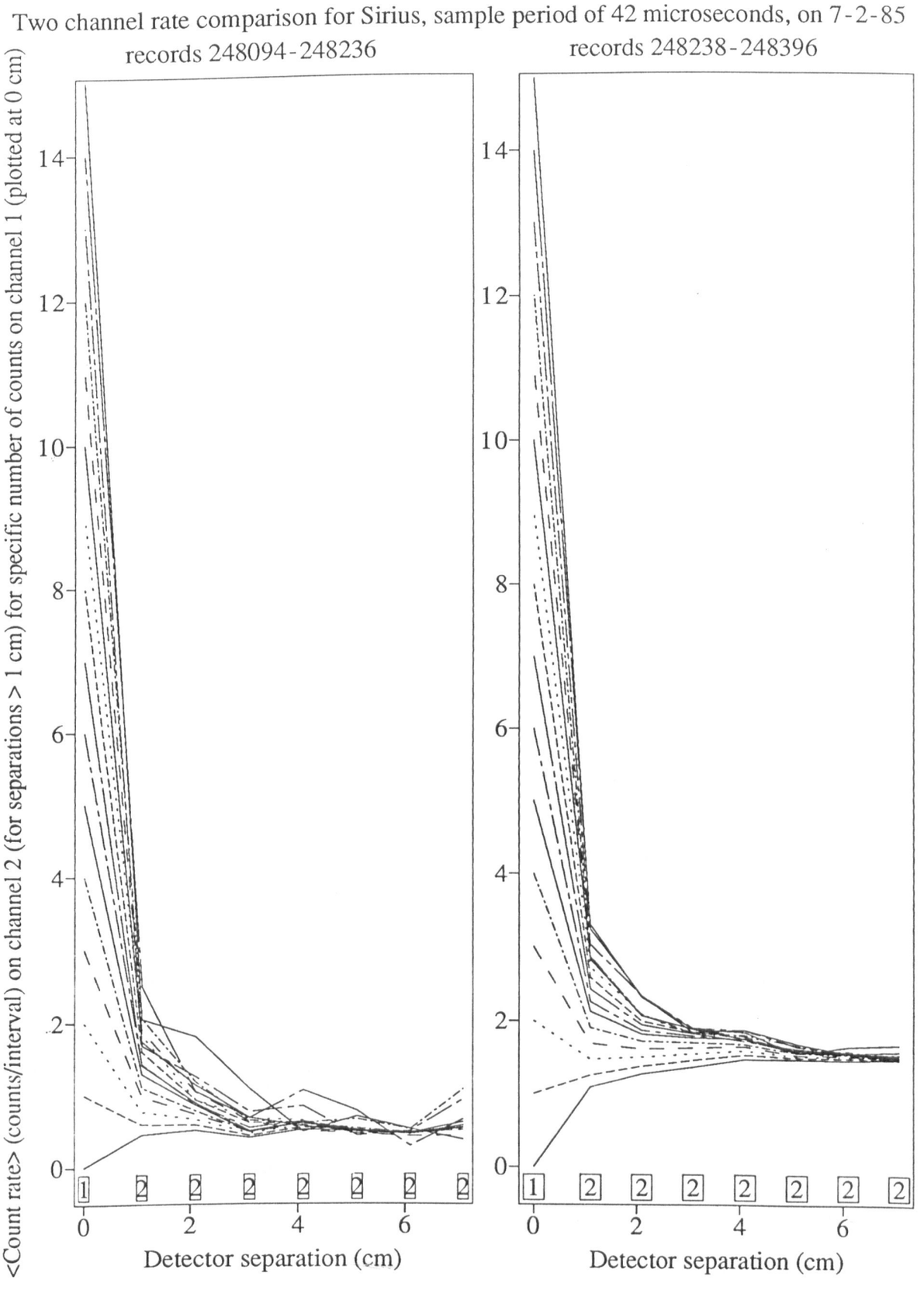

Figure 9-5 A representation of the spatial correlation as a function of instantaneous light level. For each possible number of counts/interval (*ie* 0-15 for a frequency distribution) on channel 1, the average of the concurrent count on channel 2 is calculated. This average is plotted as a function of the separation between the two apertures (1.1-7.1 cm), with the channel 1 value plotted at zero separation. Lines connect the averages of the channel 2 values and the relevant channel 1 value. The size of the apertures is indicated by the horizontal extent of the boxes (labelled with the channel number) at the bottom of the graph.

perpositions.

In summary, the bright features can be tracked from one detector to another over short (2.1-cm) distances, but they decay quickly. They can make a significant contribution to the total covariance. They are produced by the concentration of light from a wide area around them, as no associated reduction in intensity is apparent out to 7 cm.

A simulation in §4.2.4 established Q_{ur} as the best correlation function for deduction of wind profiles, provided there are large fluctuations in intensity. Thus the observation of bright features which move from one detector to another shows that circumstances exist in which Q_{ur} may be applied. However, the precision of the measurement would be poor if, as seen here, the bright features decay after moving only a short distance.

9.3 Double-star scintillation

The scintillation pattern of a double star, produced by turbulence at low (< 3 km) altitudes, is investigated below. The aims are to add to knowledge of the characteristics of scintillation and to provide information that is required in the design of systems to make wind measurements.

9.3.1 Spatial covariance

In the previous chapter the spatial covariance of scintillation patterns was measured parallel and perpendicular to the line joining the components of the double star. This was a repeat of measurements made previously by others. Obviously more information is available if the spatial covariance is measured at all angles. This is done for all available data in a 2-month interval in figure 9-6 and for a single night in figure 9-7.

Figure 9-6 shows the normalized covariance between two apertures at zero time delay for many measurements of the double star α Crucis, where the horizontal axis in the plot is aligned with the position angle of the star. These data are subject to the same complication as mentioned for figure 8-14; measurements at angles well away from 0° are restricted to particular ranges of star elevation, due to the limitation that the "multiple collimator" can rotate through only 90°. To ensure that observed features in the spatial covariance of the double star are not an artefact of this elevation dependence, the covariance is also plotted (relative to the position angle of α Crucis)

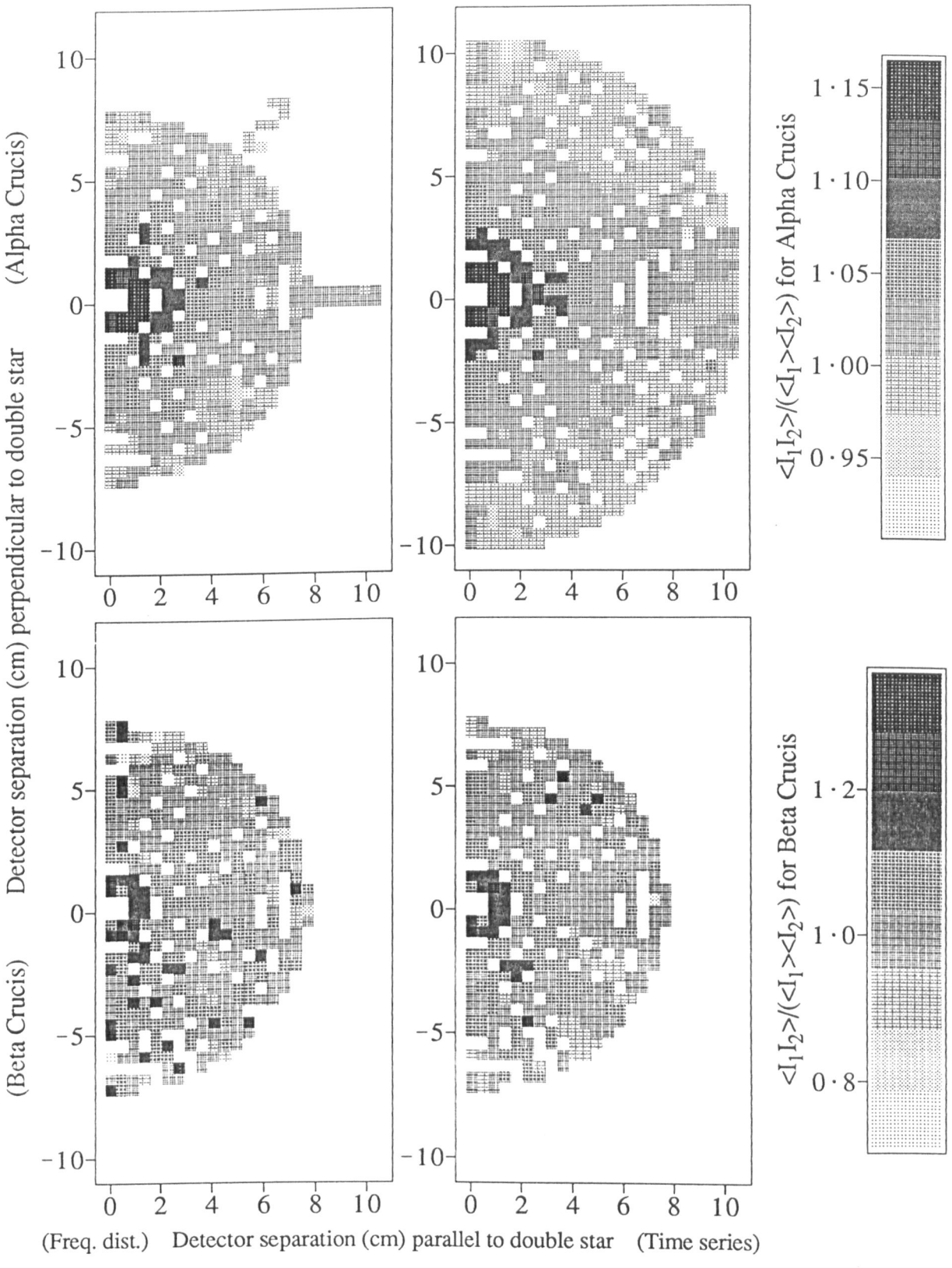

Figure 9-6 A comparison of the spatial covariance function for the scintillation pattern of a double and of a single star, applied to data for Jan-Feb 1985. The normalized covariance $\langle I_1 I_2 \rangle / (\langle I_1 \rangle \langle I_2 \rangle)$ between light intensities I_1 and I_2 incident on two apertures (either 2 or 4 mm in diameter) is plotted relative to the projection of the line joining the two components of the double star. The upper plots are for the double star α Crucis and the lower plots are for the single star β Crucis. For each star, the spatial covariance function is plotted for frequency distribution records on the left and for time series on the right.

for the nearby single star β Crucis. The results for both 2- and 4-mm apertures are combined, using all suitable data for January and February 1985. They are plotted separately for frequency distributions and time series.

For β Crucis the pattern is circularly symmetric, as expected and as observed previously for a single star (Vernin and Azouit, 1983b). For α Crucis there is a tendency towards larger covariance along the horizontal axis at separations of 2–3 cm. Thus it can be concluded that, for a significant fraction of the time, the double star produced two similar scintillation patterns separated by 2–3 cm, with the direction of separation aligned with the double star.

The same presentation is given in figure 9-7 for measurements on a single night, combining the results of four 30-min scans on each star using 2-mm apertures. The statistical fluctuation is high, as each point in the diagram is based on only 1–20 s of data, so the values are divided into only three ranges to allow trends to be discerned. For the single star the spatial covariance function is circularly symmetric. For the double star the covariance is higher along the horizontal axis, indicating the presence of two components of the double star pattern separated by $\sim$2 cm. However, the peak covariance on the horizontal axis is no larger than random peaks elsewhere in the graph. The resolution and signal-to-noise ratio does not allow the width of the autocorrelation and displaced peaks to be measured, so it is not possible to apply the second method proposed in §4.3.1 to identify the presence of atmospheric refraction.

The information in figure 9-7 is presented again in figure 9-8 in a more quantitative form, including errors and a requirement for at least two contributing records. The covariance between the detectors, for each separation, is plotted as a function of the angle between the orientation of the apertures and the expected double star pattern. The values are grouped into 10°-intervals of this angle difference and the standard error in the mean of all covariance values within each interval is plotted. For a separation of 1.1 cm (at the bottom of each graph), the covariance is significantly positive at nearly all angles, indicating the presence of features at least 2 cm across. For the double star the covariance is significantly positive at an anglular difference of $0 \pm 5°$ for both 2.1 and 3.1 cm. However, for the single star, the covariance for the same separations and angles is not significantly different from zero.

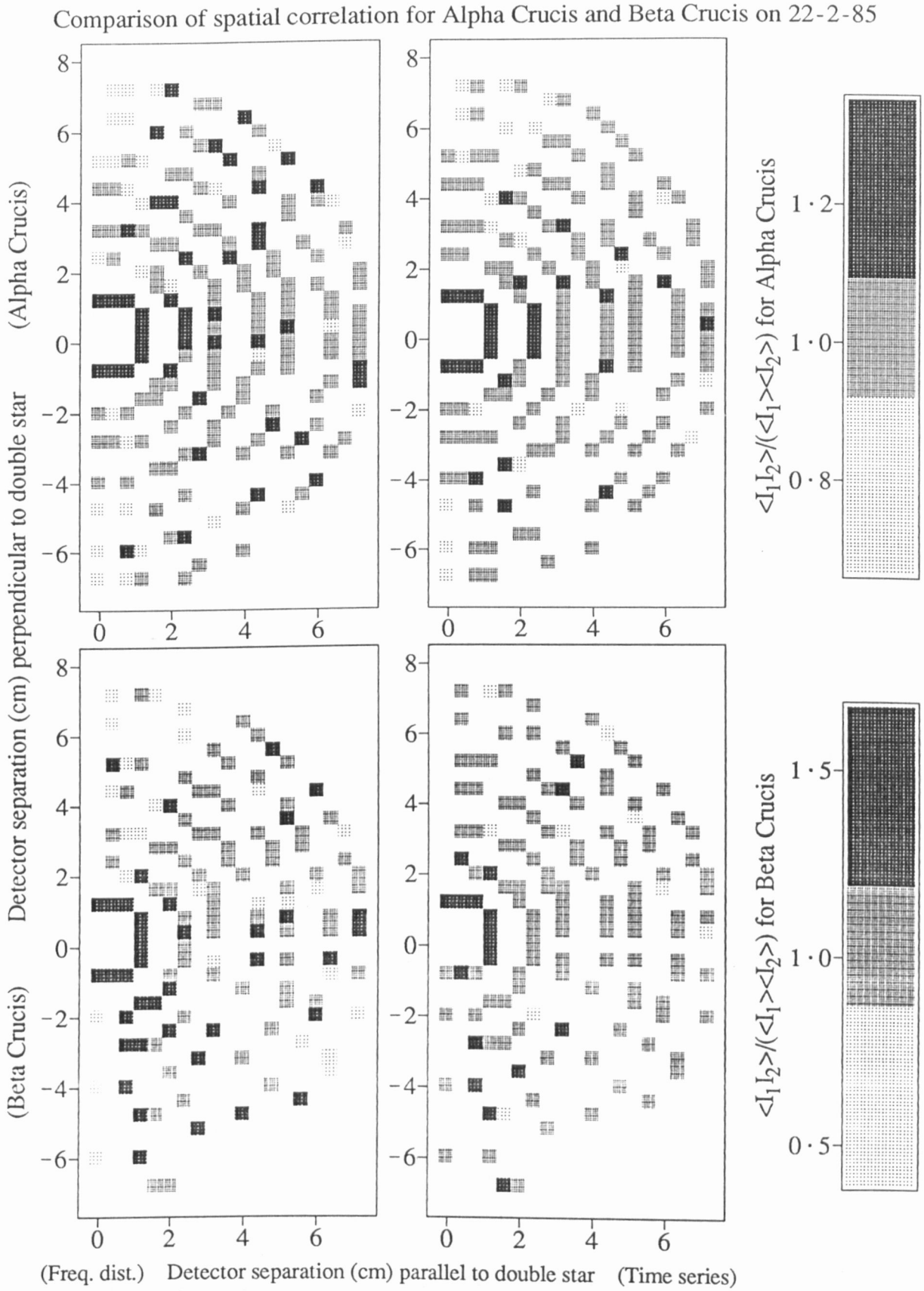

Figure 9-7 A comparison of the spatial covariance function for the scintillation pattern of a double and of a single star, applied to data for one night. The normalized covariance $\langle I_1 I_2 \rangle / (\langle I_1 \rangle \langle I_2 \rangle)$ between light intensities I_1 and I_2 incident on two 2-mm apertures is plotted relative to the projection of the line joining the two components of the double star. The upper plots are for the double star α Crucis and the lower plots are for the single star β Crucis. For each star, the spatial covariance function is plotted for frequency distribution records on the left and for time series on the right.

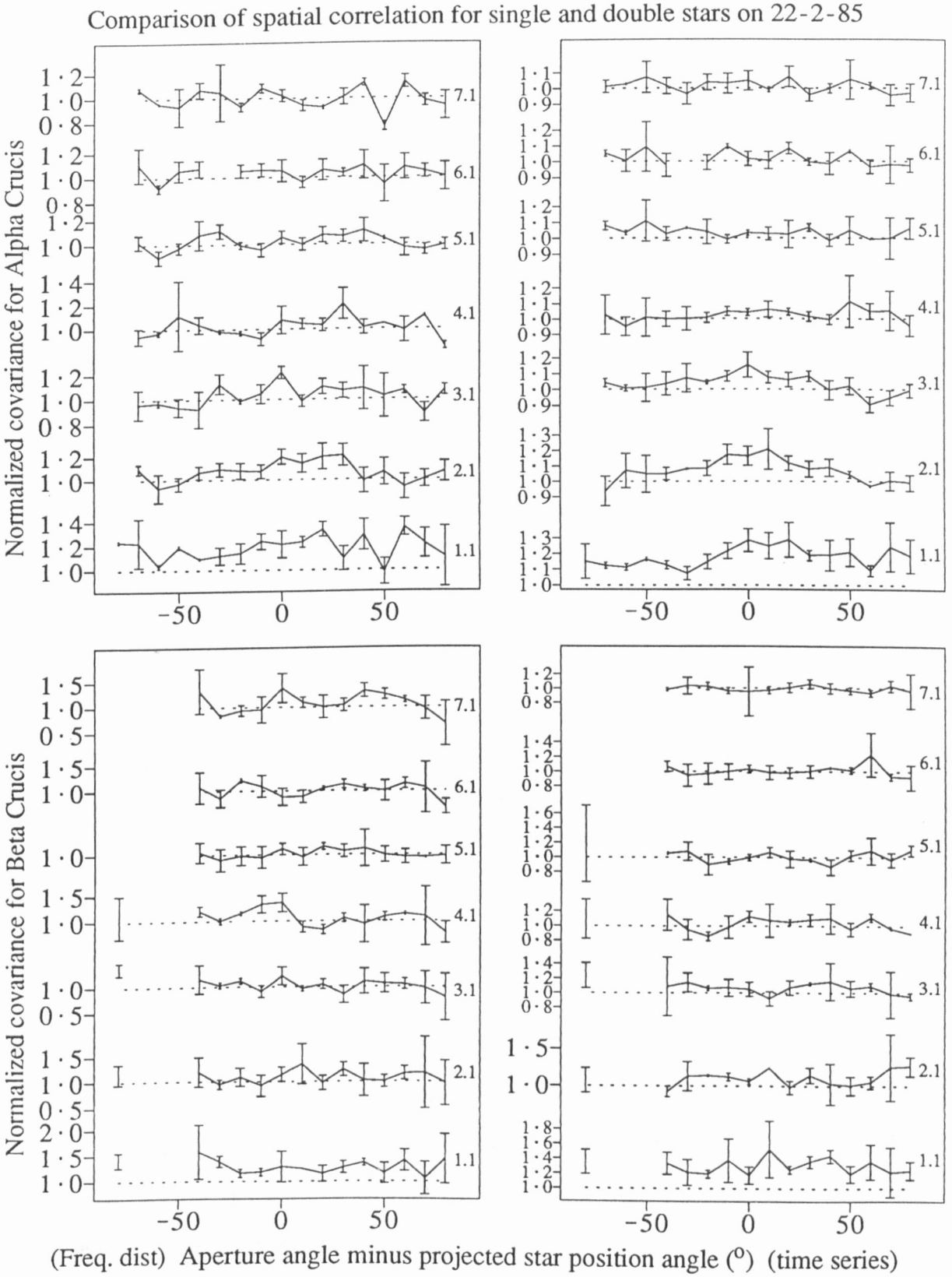

Figure 9-8 A more quantitative presentation of the spatial covariance functions plotted in figure 9-7. The difference in the angle between

a) the projection on the receiver plane of the line joining the two stars, and

b) the line joining the two apertures

is divided into 10° intervals. For all cases within each interval, the mean ± the standard error of the normalized covariance is indicated by error bars. This is done for each aperture separation, given in centimetres on the right of each function. The result is shown for α Crucis in the upper plots, for β Crucis in the lower plots, for frequency distributions on the left and for time series on the right.

Thus for a single night's data the two components of the double star scintillation pattern can be seen in a two-dimensional spatial correlation. However, the result is at the limit of detection for the present system.

9.3.2 Double-slit observations

On the basis of the tentative evidence, just described, for the presence of two components in the double star scintillation pattern, the double slit detector proposed in §4.1.4 was implemented with a slit separation of 2.4 cm. Some observations with this instrument, which are presented in figure 9-9, show clearly the presence of the double pattern of a double star. The normalized temporal auto- and cross covariance are plotted as a function of time shift for each of ten 0.97-s time series of the intensity on the two slits, for both α and β Crucis. The presence of the double scintillation pattern for α Crucis is indicated by a large value of the normalized cross covariance at zero time shift, compared to negligible covariance for the single star. As predicted in §4.4, the addition of two different patterns reduces the value of the autocovariance at zero time delay for the double star.

For both stars, there is a large peak in cross covariance at a time shift of 2.5–3 ms. Given the obvious interpretation for this (*ie* that the scintillation pattern moves from one slit to the other in this interval), it would be expected that, for the double star only:

1) there should be a second peak in the temporal autocovariance, produced by the second component of the double star pattern crossing the same detector as the first.
2) There should be another peak in cross covariance at double the time shift of 2.5–3 ms, corresponding to the upwind component of the scintillation pattern moving to the downwind aperture at an interval of 5–6 ms after the downwind component reaches the upwind aperture.

Both of these effects can be seen in figure 9-9, although they produce only a widening of the main peak rather than a clearly defined second peak.

The analysis is repeated in figure 9-10 using more data, with averages being calculated for 10 records to reduce statistical fluctuation. The conclusions for single records in figure 9-9 are confirmed.

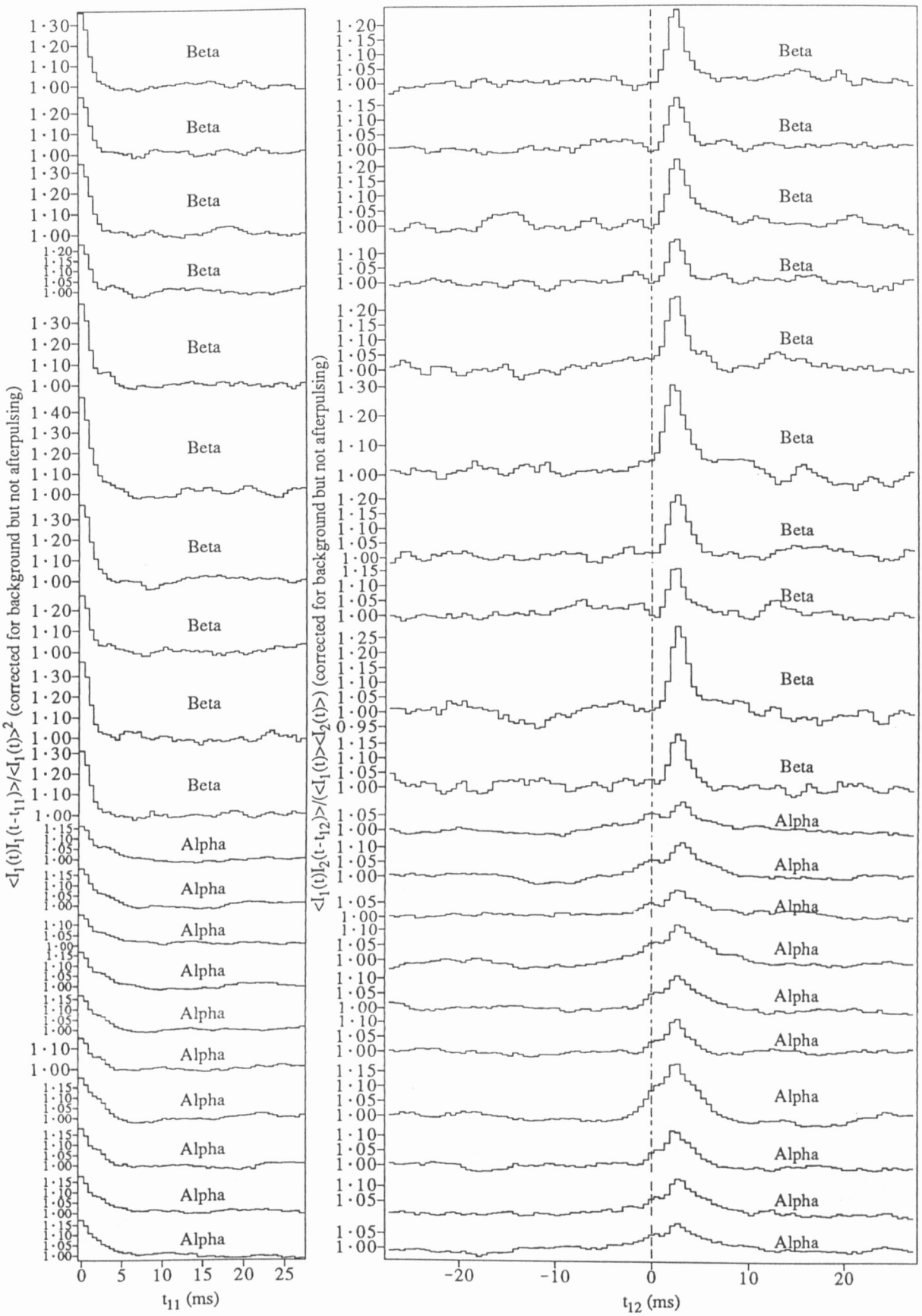

Figure 9-9 Temporal autocovariance (left) and cross covariance functions (right) of scintillation measured on two parallel 50 × 3 mm slits, separated by 24 mm. These functions are plotted for each of ten 0.97 s time series of the intensity I for each of α Crucis and β Crucis.

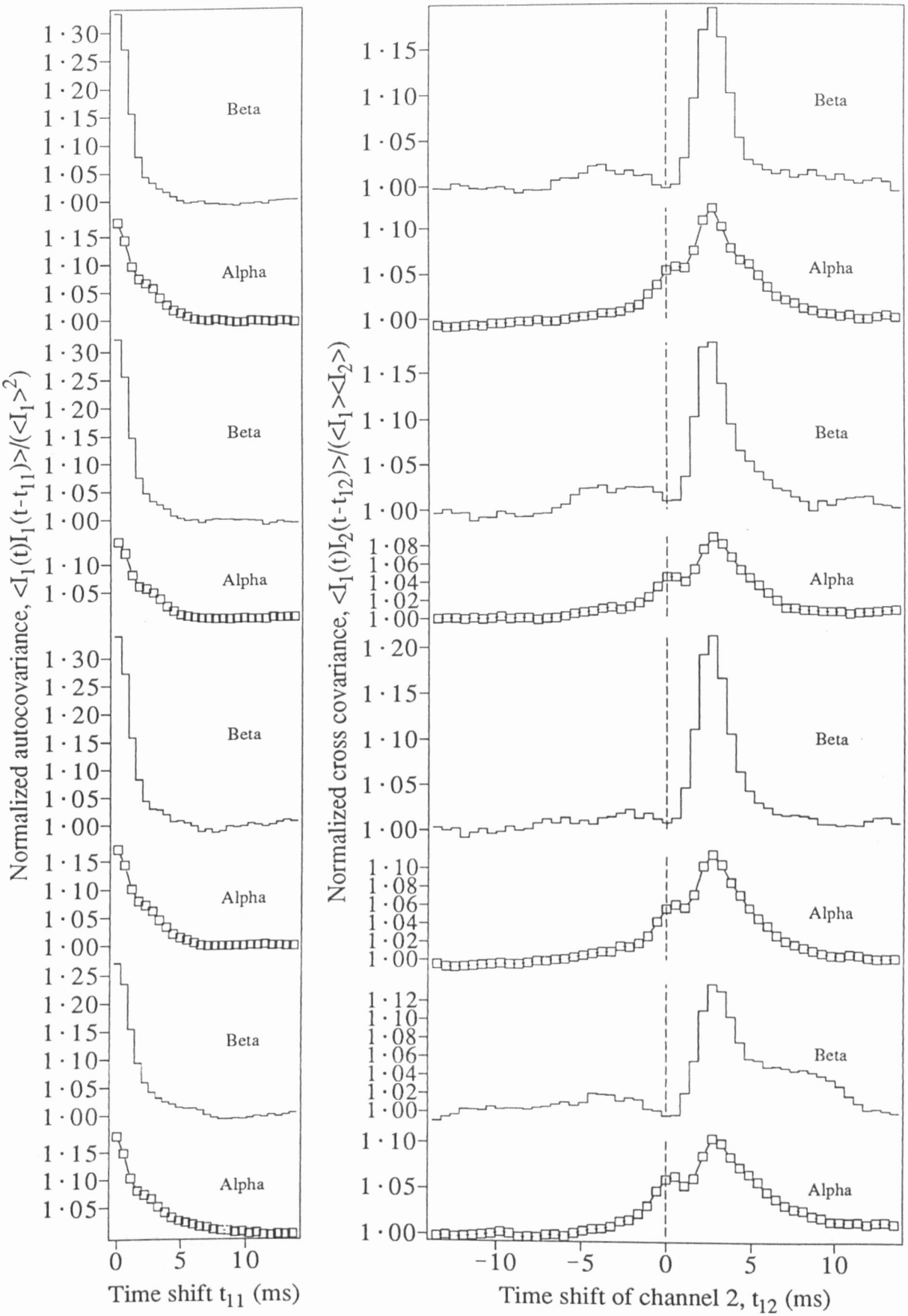

Figure 9-10 Temporal autocovariance (left) and cross covariance functions (right) are plotted for the double star Alpha Crucis (connected squares) and the single star Beta Crucis (stepped lines, which indicate resolution). Each plotted function is the average for ten 0.97 s time series of the light intensity on two parallel 50 mm × 3 mm slits, separated by 24 mm.

In summary, it is seen that, under suitable atmospheric conditions, there are two similar components in the scintillation pattern of a double star, with a separation (in this case) corresponding to a common origin at ~1 km in altitude. The scintillation patterns can be tracked from one detector to another, allowing their speed to be measured. Thus it appears that the double star scintillation pattern produced by turbulence at low altitudes is suitable for the method of measurement of wind velocity against altitude which was proposed in §4.1.4.

9.4 Atmospheric information

9.4.1 Horizontal variation of turbulence

Comparison of optical measurements of turbulence with other techniques generally requires that the same turbulence strength be present over a large horizontal distance, due to practical constraints which do not allow both instruments to access the same atmospheric volume simultaneously. It is proposed here that a test as to whether this requirement is met can be made by simultaneous measurements of the scintillation of two well-separated stars. If the same turbulence profile is present along both lines of sight, the variance of the scintillation will be identical for the two stars. If regions of different turbulence strength are displaced by the wind from one line of sight to the other, then variations in the scintillation strength of the first star should be seen for the other at a later time.

The availability in this work of two light collectors which can be pointed simultaneously at different stars allows such a measurement. A result is shown in figure 9-11, for simultaneous measurements of α and β Crucis, which are separated by ~5°. The observations consist of 255 consecutive 0.97-s time series at 10-s intervals, without the usual interruptions for background readings and telescope alignment. The mean light level for each record is plotted to show that the author managed to keep both stars in view for two manually pointed telescopes. The normalized second moment for each record is plotted as a function of time for each star. The temporal auto- and cross covariance of these series of second moment values are plotted at the bottom.

The autocovariance has a peak around zero time shift with a width of about 3 min. (The asymmetry in the autocovariance function is due to the short length of the

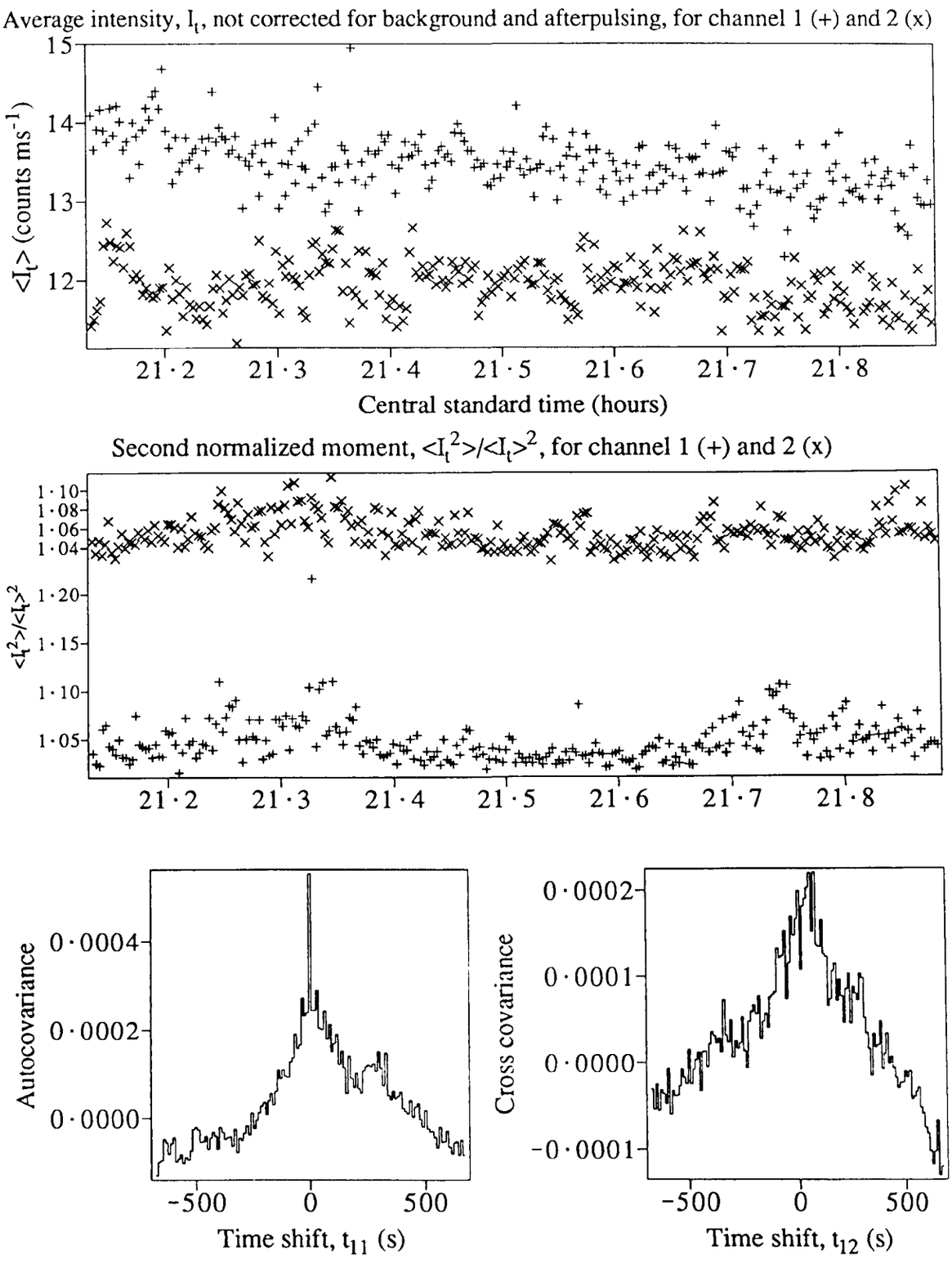

Figure 9-11 A comparison of scintillation strength observed simultaneously for two different stars. 255 time series of the intensity of β Crucis on channel 1 and α Crucis on channel 2 are analyzed. For each record the average and normalized second moment of the count rate are plotted against time in the upper two graphs. On the bottom left, the autocovariance as a function of time shift is given for the series of 255 values of the normalized second moment for channel 1. On the bottom right, the cross covariance between the series of second moments on channels 1 and 2 is plotted as a function of the time shift applied to the moments on channel 2.

series relative to the largest shift, so that the result is considerably different depending on which end of the series is truncated by the shift.) The position of the peak in cross covariance shows that the turbulent structure drifts from the line of sight to α Crucis to that to β Crucis in $\sim$1 min, corresponding to an angular velocity of $5°\text{min}^{-1}$. Thus the 5-min width of the cross-covariance peak indicates an angular size of the regions of different turbulence strength of $\sim$25°.

The angular size can be converted to horizontal size if the height of the turbulence is known. The radiosonde readings for this night show winds (southeast–east) consistent with the direction of movement of the different regions (from β to α Crucis) at heights of 0.5–1 km. For these heights, the $\sim$25°-angle corresponds to a horizontal size of $\sim$0.3–0.5 km for the regions of different turbulence strength.

In summary, it is shown by simultaneous observations of the scintillation of two well-separated stars that regions producing different scintillation strength moved from one line of sight to the other. This is interpreted as being due to horizontal variation in the strength of turbulence. It is likely that the scintillation was produced by orographic turbulence below 1 km, so the observations here may not be relevant to all sites.

9.4.2 Scintillation and cloud

Visual observations by Arago (Rayleigh, 1893) and Douglass (1897) indicated that strong scintillation is associated with cloud. This association is explored here by quantitative measurements presented in figure 9-12. This shows the scintillation of Sirius over a 3-hr interval during which a patch of low-level broken cloud moved across an otherwise clear sky. The broken cloud consisted of opaque "blobs" about 1° across, with patches of similar size of clear sky between the blobs. Thus many records of scintillation were recorded with the line of sight very close to cloud.

In the figure, the count rate, second moment, maximum count rate and sky conditions are plotted as a function of time. Some measurements of the second moment are substantially larger during the interval of broken cloud. The maximum count rate (in any of the 1792 sampling intervals of 542 μs within each record) has the highest values when the broken cloud is present, indicating that the higher second-moment values are due to enhancements of the light level due to scintillation, rather than to reductions due to obscuration by cloud. No such enhancements were seen on the numerous nights

Comparison of scintillation statistics with cloudiness for records 219551-220461 on 3-1-85.
Values plotted are for time series, channel 1 (+) and channel 2 (x).

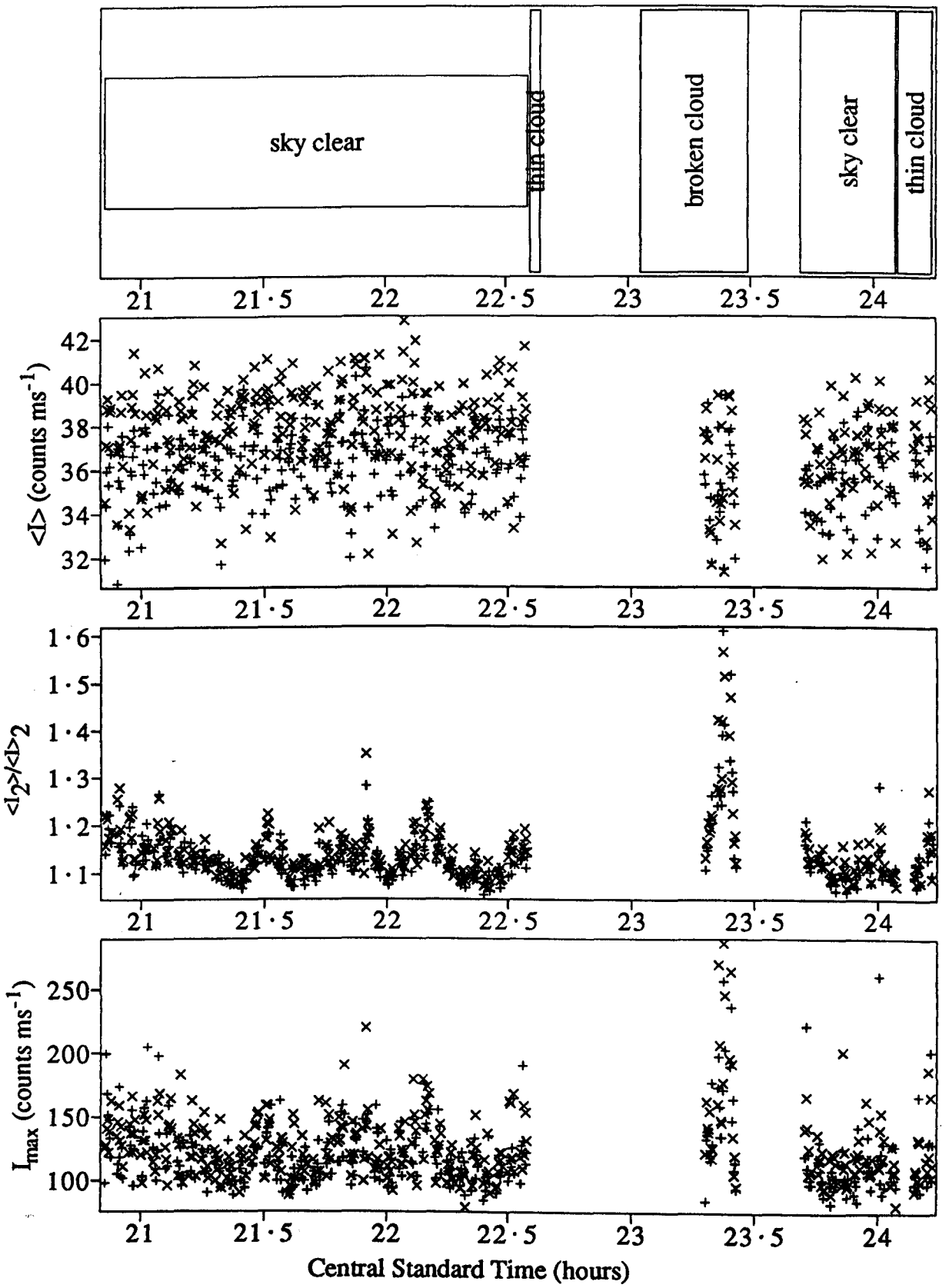

Figure 9-12 Evidence for the association of scintillation with cloud. Various characteristics of the light of Sirius on 4 mm apertures are plotted for a period which included the passage of a patch of broken cloud. This patch contained small gaps through which the star could be seen clearly for short periods. The sky conditions are shown against time at the top, with the starlight intensity $\langle I \rangle$, the normalized second moment $\langle I^2 \rangle / \langle I \rangle^2$ and the maximum intensity I_{max} (in any sample interval in each record) shown below, for channel 1 (+) and channel 2 (×).

when stars were partially obscured by high cirrus cloud.

Thus these quantitative measurements confirm earlier visual observations that scintillation is strong when associated with cloud.

9.5 Specific investigations of scintillation

It was suggested in §4.1.2 that multiple-beam methods of remote sensing using stellar scintillation may be adversely affected by

a) atmospheric refraction causing bending of the "beams", and

b) interaction of phase variations produced by turbulence at different heights.

Specific tests are applied here to investigate whether such effects occur. Finally, a modified form of the standard moment plot is calculated, to investigate the form of the probability density function of stellar scintillation.

9.5.1 Atmospheric refraction

As suggested in §4.3.1, measurement of the variation in the transit time of scintillation patterns from one aperture to another can put an upper limit on the amount of atmospheric refraction. The precision of this measurement can be increased by selecting situations where

a) the patterns and detecting apertures are both small, to reduce the uncertainty contributed by their finite size, and

b) the velocity is low, so that the time delay is large compared to the sampling interval.

A record selected to meet these conditions is analyzed in figure 9-13. The record is of scintillation on two 4-mm apertures, separated by 4.1 cm.

In this figure, the record is split into a number of equal segments and the cross covariance between the two channels is calculated as a function of time shift for each segment. The time shift giving the maximum covariance is represented by the vertical position of a horizontal line segment, which is aligned with the segment of the record for which it is calculated. The cross covariance for the whole record has a maximum value for a time shift of -4 ms, indicated by a horizontal line across the graph (at the top). Underneath this, two lines of half this length indicate that, for both the first and second halves of the record, the maximum cross covariance occurs for this same

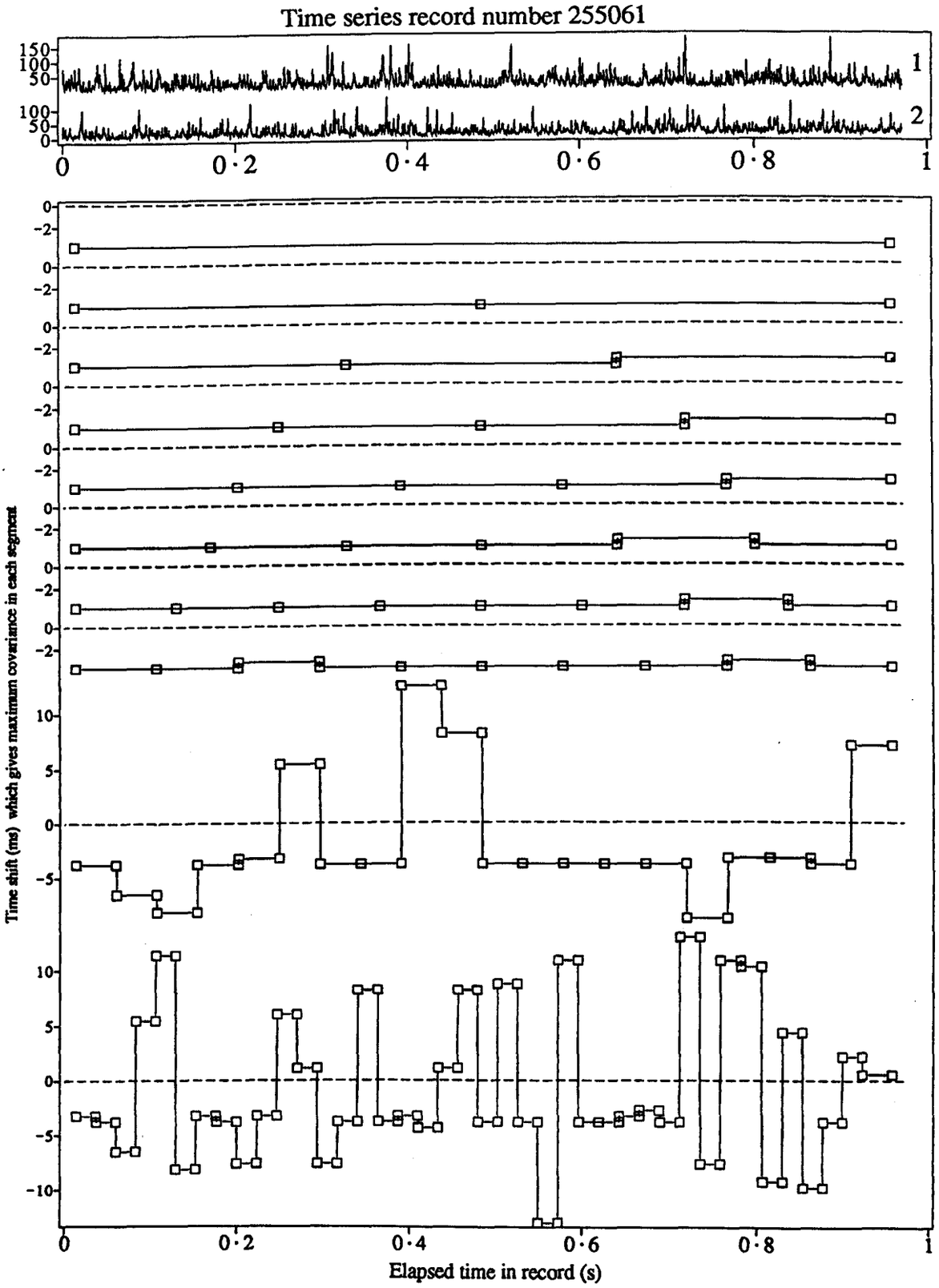

Figure 9-13 An analysis of the consistency of the apparent transit time of scintillation patterns between two 4-mm apertures, separated by 4.1 cm. The analysis is applied to the 0.97-s record plotted at the top. It involves splitting the record into a number of equal segments and calculating the cross covariance $\langle I_1(t)I_2(t-t_{12}\rangle/(\langle I_1\rangle\langle I_2\rangle)$ as a function of time shift t_{12}. The value of t_{12} which gives the largest covariance is plotted for each segment, represented by a horizontal line with squares at each end. In successive functions in the lower plot, the record is split into 1, 2, 3, 4, 5, 6, 8, 10, 20 and 40 segments. A dashed line indicates zero time shift.

time shift of −4 ms. Below this, the results are given for 3, 4, 5, 6, 8, 10, 20 and 40 segments. For division of the record into 10 or less segments, there is little variation in the time shift that produces maximum covariance. For 20 and 40 segments, there are many segments at various time shifts, but still a substantial number at the same value as for the longer segments above.

The conclusion is that the time shift (and hence pattern velocity) is constant, to within 10%, for intervals down to 0.05 s. For 20 segments, the deduced time shift (for maximum covariance) is either the same as for longer segments, or very different. This suggests that the values which are different from −4 ms are random due to insufficient signal. If the scintillation pattern was being moved to and fro by refraction, one would expect the fluctuation in the time shift to increase gradually as the segment length is reduced. There is no evidence of this, so the refraction postulated in §4.1.2 is not observed here. The fluctuation of about 10% in the deduced time shift and the aperture separation of 4.1 cm imply an upper limit of 0.4 mm in the displacement of the scintillation pattern due to refraction.

9.5.2 Phase interaction

In the crossed-beam method used by Vernin *et al* (1979) to measure turbulence strength, it is assumed that the scintillation patterns produced at different heights do not interact. However, in §4.1.2 it was suggested that phase fluctuations produced by scintillation at widely spaced heights could add together and produce transitory intensity fluctuations. This would reduce the similarity between the two scintillation patterns of a double star and hence the deduced values of turbulence strength.

Figures 9-14 and 9-15 show the results of an analysis designed to identify the possible occurrence of this interaction of phase fluctuations produced at different heights. The analysis is based on the supposition that the addition of two phase fluctuations at different heights will produce a transitory scintillation pattern which may have a small, non-linear correlation with the individual scintillation patterns that occur after the sources of the two phase fluctuations go out of alignment. It was shown in §4.3.2 that the triple correlation $T(I_1(t), I_2(t-t_{12}), I_2(t-t'_{12}))$ would have non-zero values for $t_{12} = t'_{12}$ only if the intensities produced at two different heights add algebraically, but that it could also be non-zero for $t_{12} \neq t'_{12}$ if the phase fluctuations add and produce a

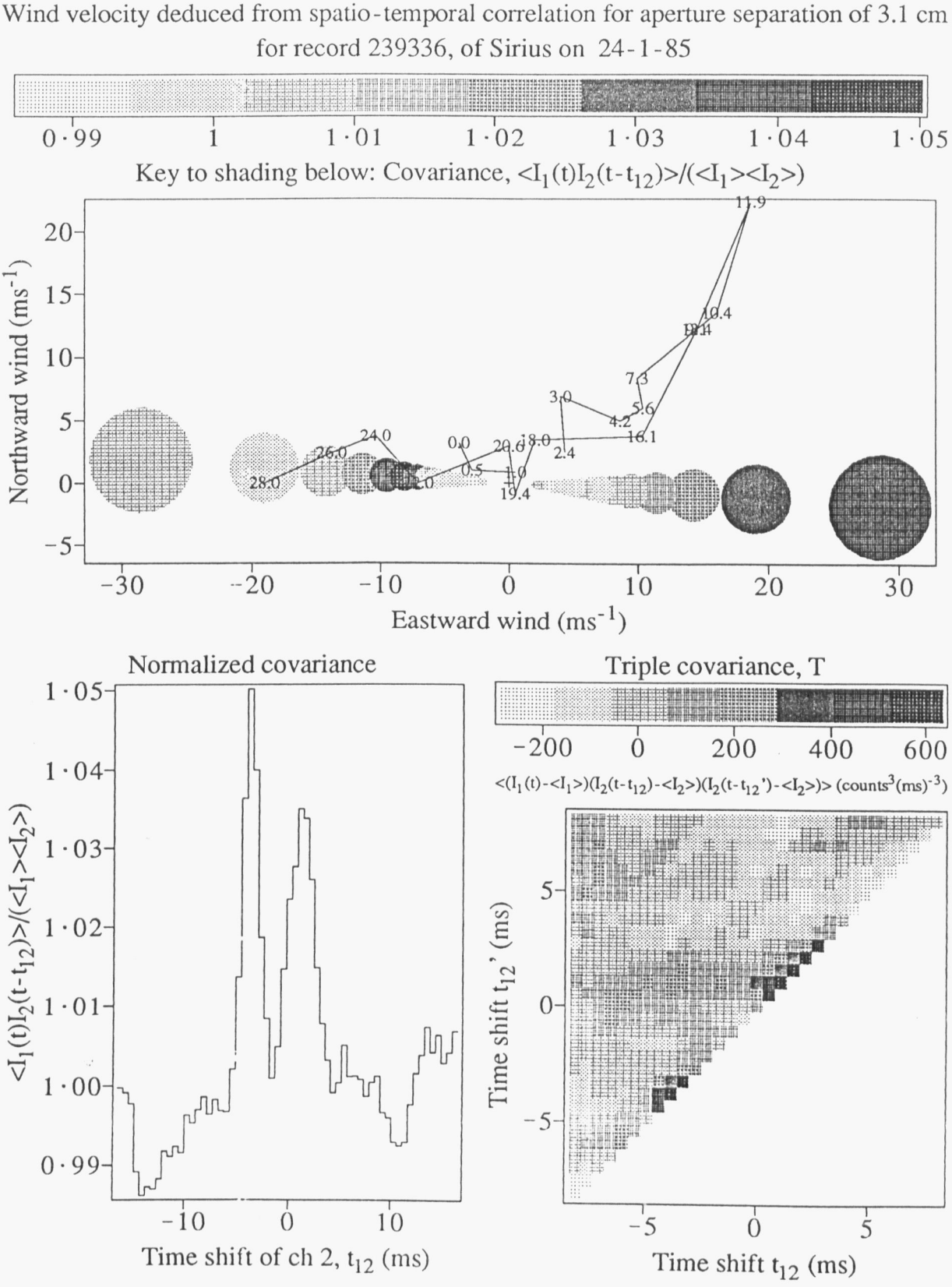

Figure 9-14 An analysis of a single time series record of scintillation patterns which were moving in opposite directions between two 4-mm apertures separated by 3.1 cm. At the top, the deduced pattern velocity (projected onto a horizontal plane) is compared with a hodograph of the wind velocity measured by radiosonde. On the lower left, the normalized covariance between the light intensity on the two apertures is plotted as a function of the time shift applied to channel 2. Two peaks at time shifts of opposite sign indicate patterns moving in opposite directions. On the right, the triple correlation T is plotted for combinations of two different time shifts applied to channel 2.

scintillation pattern which is related to their sum.

At the lower left of figure 9-14, a plot of the temporal covariance between the light intensity of the single star Sirius on two 4-mm circular apertures shows peaks at both positive and negative time shifts. A plausible explanation is that the scintillation pattern is produced by turbulence at two different heights, moving in opposite directions. The probability of getting such a situation is very low and only one such record was found among all Sirius observations in Jan.–Feb. 1985. At the top, the pattern velocity is compared with the radiosonde hodograph. This is done to check the postulate of wind in opposite directions at two different heights, but the result is confusing. The velocity of one scintillation pattern does not lie on the radiosonde profile, while the other agrees with the radiosonde measurement at 22 km, for which theory (see figure 3-2) suggests that very little signal should be observed. The explanation may be that one or both of the patterns originate in the height range 1–2.4 km, for which no radiosonde data is available on this particular night.

At the lower right of figure 9-14 the triple correlation

$$T(I_1(t), I_2(t-t_{12}), I_2(t-t'_{12})) =$$

$$\langle (I_1(t) - \langle I_1 \rangle)(I_2(t-t_{12}) - \langle I_2 \rangle)(I_2(t-t'_{12}) - \langle I_2 \rangle) \rangle \qquad --(9.6)$$

is plotted for two different time shifts t_{12} and t'_{12} of channel 2 relative to channel 1. There are, as expected, peaks in this triple correlation at t_{12}=t'_{12}= 2 and −3 ms. There is a weak positive correlation at $(t_{12}, t'_{12}) \sim (-3, 2)$, indicating that there could be some interaction between the signals for the two heights. However, this peak is no larger than other peaks at random locations caused by statistical fluctuation.

This analysis is repeated in figure 9-15, using time series of the single star β Crucis measured with the double slit aperture. For two groups of 6 or 7 records (in the two lower plots), there is no evidence of phase interaction, while for the third group (upper plot) a weak peak at $(t_{12}, t'_{12}) \sim (-2, 3)$ suggests that some interaction is occurring. Again this peak is no larger than some noise peaks.

In conclusion, for two nights on which the scintillation pattern has two contributions, apparently from different heights, there is some suggestion that some phase interaction occurred. However, the correlation peak which indicates the interaction is

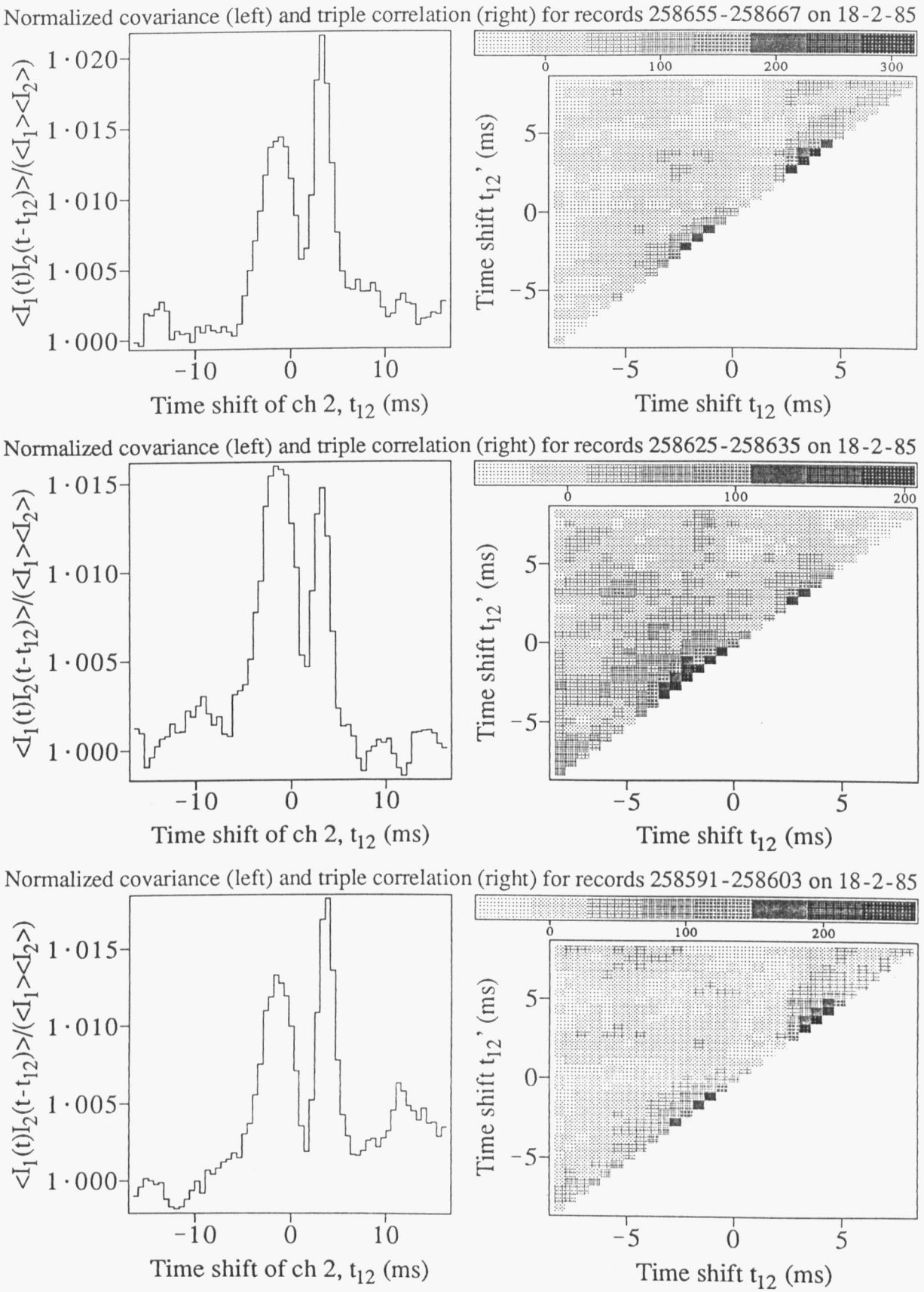

Figure 9-15 The normalized covariance and triple correlation for the scintillation of the single star β Crucis, observed with two parallel slits. Average values are presented for each of three blocks, which consist of six or seven 0.97 s time series of the light intensity on the two slits. On the left the normalized covariance between the two channels is plotted as a function of the time shift t_{12} applied to channel 2. On the right the triple correlation $T(I_1(t), I_2(t - t_{12}), I_2(t - t'_{12}))$ is plotted as a function of two time shifts t_{12} and t'_{12} applied to channel 2.

not significantly above the noise level.

9.5.3 Modified moment plot

The moment plot (described in §3.4) has been used to infer the probability density function of stellar scintillation (Parry and Walker, 1980; Dainty *et al*, 1982). However, Ben-Yosef and Goldner (1988) have suggested that this method is unsatisfactory due to practical problems. To overcome, or at least assess, some of the problems, a modified moment plot is proposed and tested below.

Ben-Yosef and Goldner suggest that the moment plot is deficient because:

a) the atmosphere may not be stationary over the interval of observations.

b) Random fluctuation in the second moment introduces a systematic error in the average of values of the higher moments, when these are grouped according to the second moment.

c) The observation interval may be too short, so that the contribution of occasional large fluctuations is missed.

A modified moment plot is now suggested; it addresses problems b) and c) by:

d) calculation of averages of the moments over the full interval of observation, to avoid the systematic error caused by grouping the values for smaller intervals.

e) Comparison of the average moments measured simultaneously on two different apertures. If the moments are significantly reduced from the actual value due to failure to detect rare fluctuations of high intensity, then statistical fluctuation in the occurrence of these high intensities on two different apertures will produce different moment values.

These modifications are incorporated in the modified moment plots in figure 9-16. Each point indicates an average of the higher moments for a block of about 70 frequency distributions, plotted against the average of the second moments. Each block is for a "scan" of Sirius with the "multiple collimator" with 2-mm apertures, in which the aperture separation was varied from 1.1 to 7.1 cm. Thus each point in the figure represents ~190 s of observations, distributed over 29 min, with different parts of the scintillation pattern being observed on the two channels. Where the points for channel 1 (□, Δ or +) and for channel 2 (×) are not close, they are joined by lines. Labelled curves indicate the expected relationship for a log normal and a K distribution.

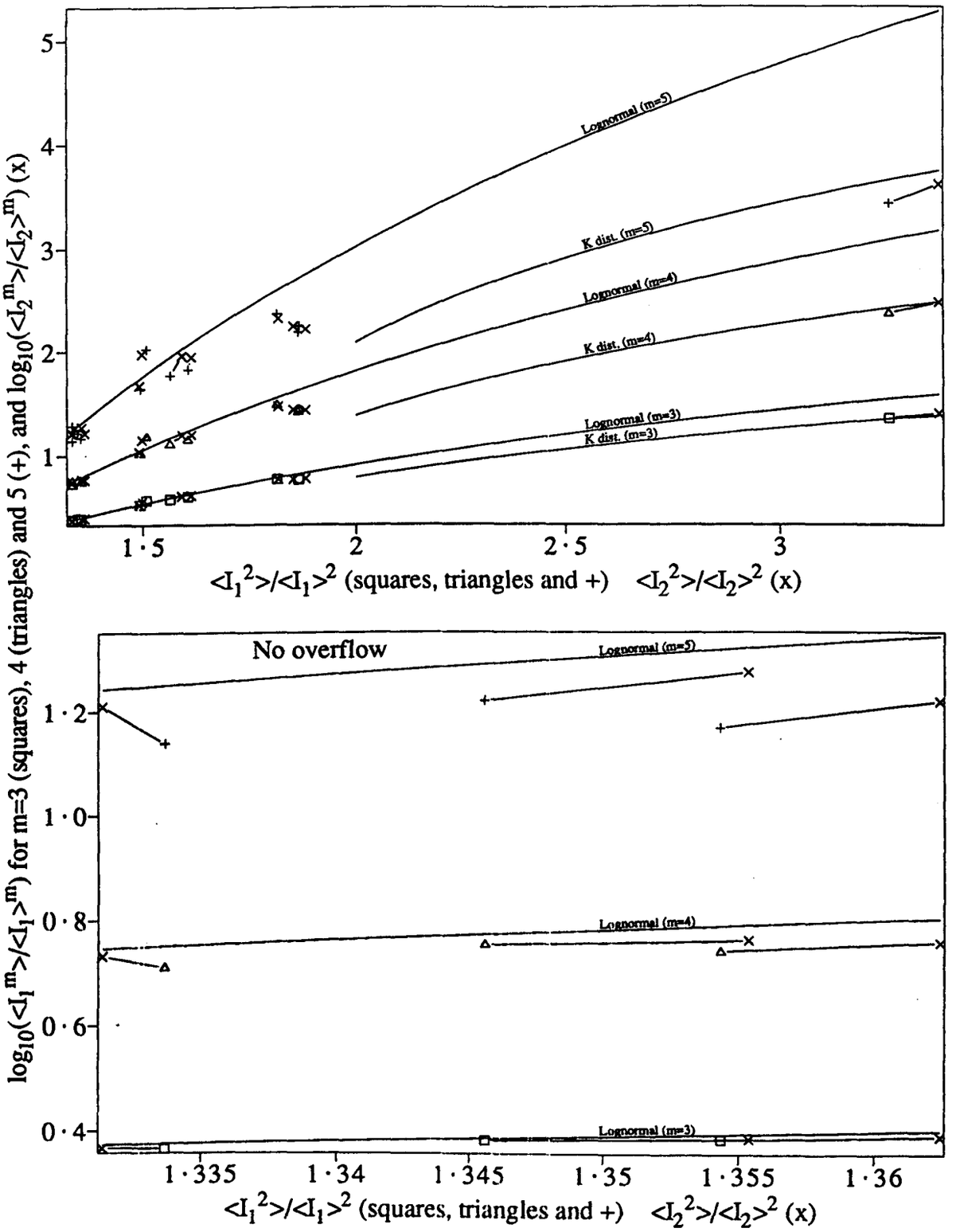

Figure 9-16 A modified moment plot, in which each plotted point compares average values for many records. Each value is the average for 68-70 frequency distributions of the light intensity on 2-mm apertures. Channel-1 values are indicated by symbols, using □, △ and + for the comparison of the normalized 3rd, 4th and 5th moments against the normalized second moment. The corresponding values for channel 2 are indicated by ×, joined to the symbol for channel 1 with a connecting line if the symbols do not overlap. Labelled lines indicate the expected relationship between the moments for the lognormal and K distributions. The results for 12 available blocks are plotted in the upper graph, with the lower graph restricted to the results for 3 blocks in which no counts were lost due to overflow of the 4-bit pulse counter.

The upper graph shows the measured relationship for the twelve available scans. In nine of these, overflow of the 4-bit counter used for frequency distributions makes the results dubious. They are included only for illustration, as they cover the same range of values as previously published moment plots (*eg* figure 3-6).

The lower graph shows the measurements for the 3 scans in which no overflow was detected. While two of these indicate that the higher moments were less than expected for the log normal distribution, the third (left) shows a value for one channel that was much closer to the theoretical curve than the other. A possible interpretation is that the distribution was actually log normal, but one or more rare features of high intensity crossed one detector but not the other, so that only one channel gives a value close to the log-normal prediction.

In conclusion, the modified moment plot gives results similar to those of the moment plot by previous authors, but allows the impact of insufficient observation time to be assessed. Even when the analysis is restricted to observations in which the light intensity did not exceed the limits of the recording system, the higher moments are less than predicted for a log normal distribution. However, a discrepancy between the moment values for simultaneous observations on separate apertures shows that the deviation from the log normal distribution could be due to failure to detect occasional large enhancements of the light intensity. Thus experimental evidence is found to support a reservation about the moment plot expressed by Ben-Yosef and Goldner (1988).

Chapter 10 Atmospheric sensing

Methods were proposed in chapter 4 to use stellar scintillation for the remote measurement of atmospheric wind velocity and for the measurement of the atmospheric isoplanatic angle. Applications of some of these methods are presented in this chapter.

Data from double-slit observations are assessed for their suitability for the application of the methods of wind measurement proposed in chapter 4. Standard correlation functions are applied to determine the wind speed in a simple case. Wind profiles are then calculated using quadruple-correlation analysis. The results are compared with standard meteorological measurements.

The isoplanatic angle in the atmosphere is investigated by comparing the scintillation of a double and of a single star, using both small circular apertures and slit apertures.

10.1 Evaluation of data available for wind analysis

It was suggested in §4.1.4 that measurements of atmospheric wind velocity as a function of height can be made if the two components of the scintillation pattern of a double star can be observed to cross two parallel slit detectors. Measurements of the spatial covariance function gave tentative evidence for the presence of two similar components in the double star scintillation pattern, separated by 1-3 cm (see §9.3.1). Appropriate to this separation, a double slit detector was implemented using the "split-lens" telescope described in §5.2.2 with a mask containing two parallel 50-mm × 3-mm slits, separated by 2.4 cm.

Double-slit measurements were taken of α Crucis on 12 nights between February and July 1985. The presence of the two components of the double star scintillation pattern is only confirmed for two of these nights, using the temporal cross-covariance function (as was done in §9.3.2). The two components were clearly separated (as seen in figure 9-10) only on 23-5-85. For this night, the clearly defined peaks in figure 9-10 suggest that the scintillation pattern was produced by turbulence at only one height. For the other night (18-2-85), two scintillation patterns were present, moving in opposite directions, as deduced from figure 9-15.

The low incidence of detection of the double star pattern does not necessarily imply

that the method is of limited use. It is likely that on most nights the scintillation pattern was produced by turbulence at heights greater than 5 km, so that the separation of the two components was greater than 10 cm. For such separations, both components of the pattern will cross both slits only if the wind direction is sufficiently close to the double star orientation.

Before applying new correlation functions, it is sensible to ensure that the double star pattern has the characteristics expected. A cumulative contribution analysis is applied in figure 10-1 to determine the relative contribution of different parts of a record of scintillation to the average covariances. (*nb* the cumulative covariance was introduced in §9.1 and specified in equation 9.3.) The cumulative contribution to the cross covariance of a double-slit record of α Crucis is plotted for various time shifts (which are integer multiples of the sampling interval of 542 μs). The contribution to the covariance builds up steadily through the record, with no sharp jumps (such as were seen in figure 9-4 for records containing large intensity fluctuations). This shows that many different features of the scintillation pattern are duplicated and that many features are transported from one slit to the other. It is not proven that the same features are both duplicated and transported, which is an essential requirement to enable measurement of the wind at a particular height. It is shown in the next section that this requirement is met.

10.2 Wind measurement using standard correlation functions

In figure 10-2 standard correlation analysis is applied to double-slit observations on 23-5-85 to deduce the height of the turbulence and its speed. The approach is to simulate double-star data from that for a nearby single star and compare the correlation functions of the simulated and actual double star. It is assumed that the scintillation is produced at one height only and that each feature of the pattern is duplicated and transported from one slit to the other. A simulated time series I_{sim} for the double star α Crucis is produced from a time series I_β of the single star β Crucis by adding a fraction of I_β to itself at a time shift t_s:

$$I_{sim}(t; r, t_s) = I_\beta(t) + rI_\beta(t - t_s) \qquad --(10.1)$$

where r is the ratio of intensities of the two components of α Crucis.

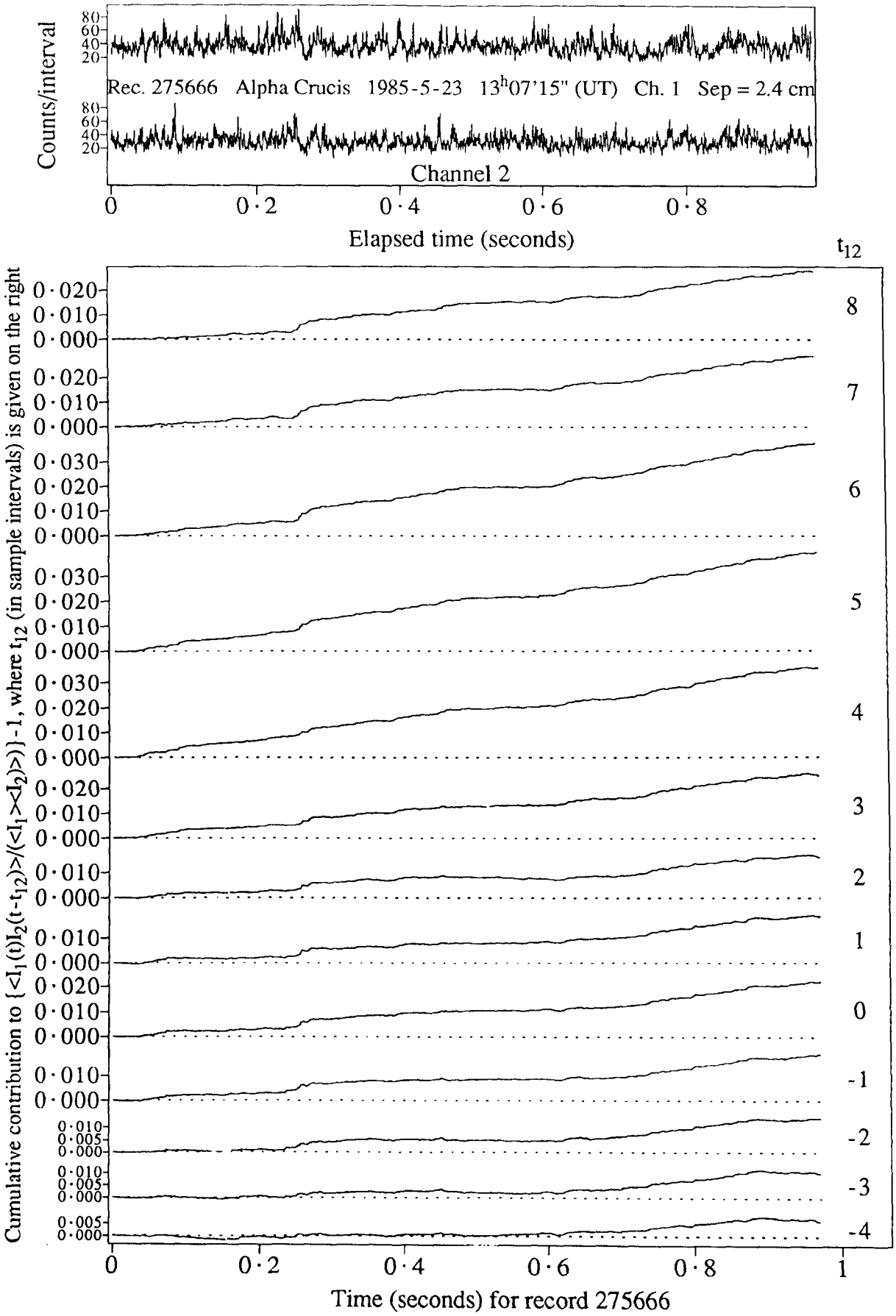

Figure 10-1 The relative contribution of different scintillation patterns to the covariance between the light on two parallel slits. At the top is a 0.97-s record of the light intensity on the two slits produced by the double star α Crucis. The cumulative contribution to the normalized cross covariance is plotted directly below each channel 1 value, for various time shifts t_{12} applied to channel 2. Dashed lines indicate zero covariance.

The upper plot of figure 10-2 shows the temporal normalized covariance between the scintillation on the two slits. The covariance is plotted against the time shift t_{12} applied to channel 2, for α Crucis (stepped line), β Crucis (circles) and $I_{sim}(r = 1.0,\ t_s = 2.2$ ms) ($\times$). For the single star β Crucis, there is a peak in covariance for a time shift of 2.57 ± 0.14 ms, indicating a pattern speed of 9.2 ± 0.5 ms^{-1} perpendicular to the slits. The width of the peak ($\sim$3 ms) corresponds to a pattern size of 3 cm. For α Crucis, there is substantial covariance near $t_{12} = 0$, indicating that there are two similar components in the scintillation pattern, separated by a distance approximately equal to the slit separation. The covariance for I_{sim} is close to that for α Crucis at $t_{12} = 0$, but is larger at $t_{12} = 5$ ms, where there is another peak produced by the upwind component of the double scintillation pattern moving to the downwind detector. The fact that this peak is smaller for the actual data than for the simulated data may be due to the scintillation pattern changing while moving through 4.8 cm. The overall similarity of the covariance functions for $|t_{12}| < 3$ ms validates the assumptions of a single height of origin for the turbulence and that all features of the scintillation pattern are duplicated.

The values of r and t_s selected to produce I_{sim} in the top graph were determined from the calculation presented in the lower graph in figure 10-2. The simulated and actual double-star scintillation are compared as a function of r and t_s by calculating the reciprocal of the average square of the difference between the temporal covariance functions:

$$R_{asd}(t_s, r) = \frac{1}{\frac{1}{31}\sum_{i=-15}^{15}\left\{\frac{\langle I_{\alpha_1}(t) I_{\alpha_2}(t-i\Delta t)\rangle}{\langle I_{\alpha_1}\rangle\langle I_{\alpha_2}\rangle} - \frac{\langle I_{sim_1}(t) I_{sim_2}(t-i\Delta t)\rangle}{\langle I_{sim_1}\rangle\langle I_{sim_2}\rangle}\right\}^2} \qquad -- (10.3)$$

where I_α is the light intensity for α Crucis, Δt is the sampling interval of 542 μs and subscripts 1 and 2 indicate the channel number. The size of the rectangles is proportional to the value of R_{asd}. It can be seen that:

a) the maximum similarity between the covariance functions occurs for a time shift of $t_s = 2.2 \pm 0.1$ ms and an intensity ratio $r = 0.8 \pm 0.2$. The latter is consistent with the expected value, calculated using information from table 5-1b, of

$$r = 10^{0.4(1.6-2.1)} = 0.63\ . \qquad -- (10.2)$$

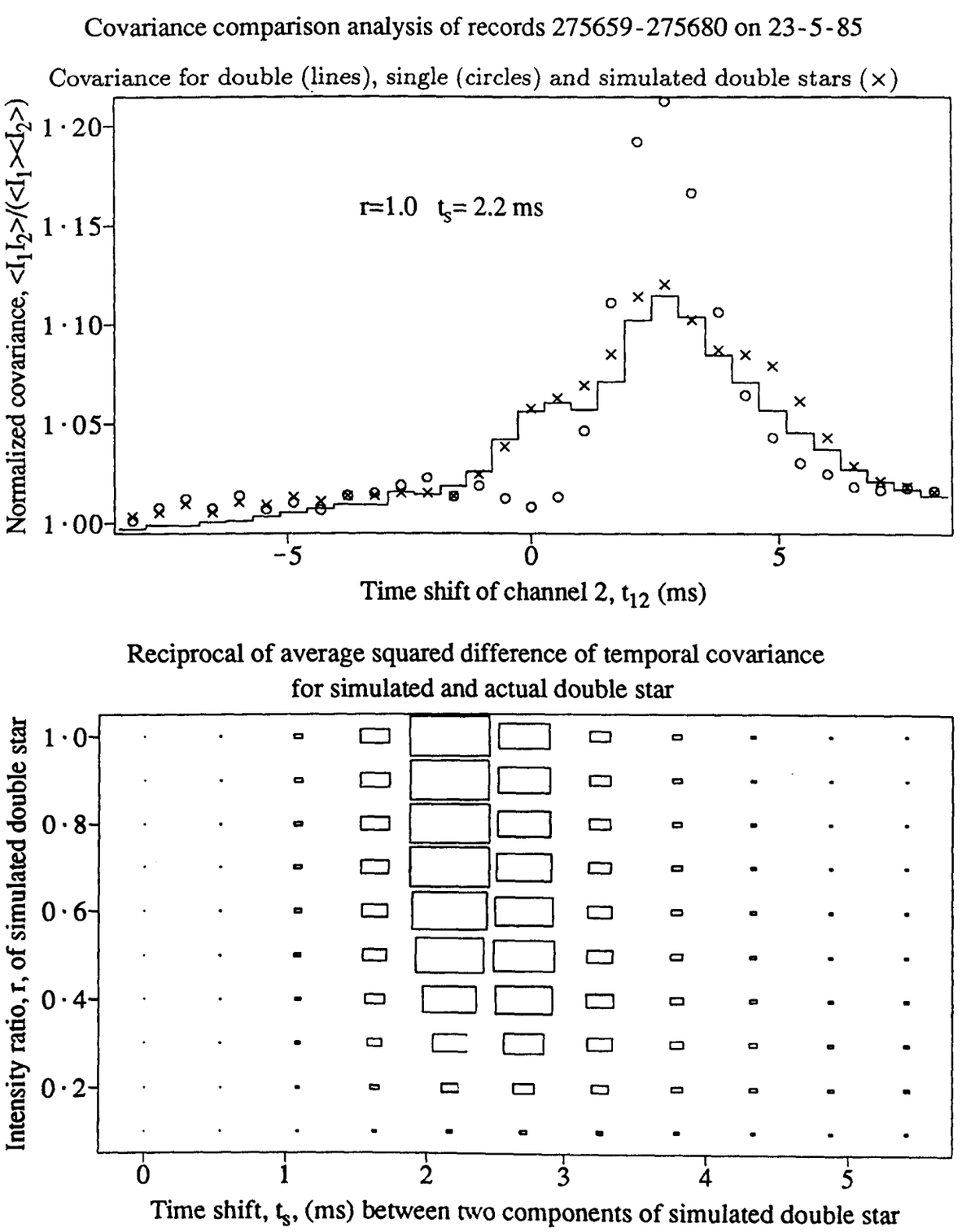

Figure 10-2 Deduction of the intensity ratio and time shift between components of the scintillation pattern of a double star. The temporal normalized cross covariance $\frac{\langle I_1(t) I_2(t-t_{12}) \rangle}{\langle I_1 \rangle \langle I_2 \rangle}$, averaged over ten 0.97-s records, is shown in the upper graph for α Crucis (lines) and β Crucis (circles), where I_1 and I_2 are the instantaneous light intensities observed on two parallel slits. The covariance is also shown for simulated double-star data (×), which is created from time series of β Crucis by assuming an intensity ratio of $r = 1.0$ and a time shift $t_s = 2.2$ ms. In the lower plot, such covariance functions for α Crucis and the simulated double star are compared for many combinations of intensity ratio and time shift, with larger rectangles indicating greater similarity. The values of r and t_s chosen for the upper plot correspond to the peak in the lower plot.

b) The method is rather insensitive to the value of r.

As the time shift t_s is the difference in arrival time of the two components of the double star pattern at one slit, the separation S_P of these components (perpendicular to the slit) is (using equation 4.3)

$$\frac{t_s}{t_{12}}|\mathbf{D}| = 2.1 \pm 0.2 \text{ cm.}$$

Using equation 4.1 and assuming the pattern velocity is perpendicular to the slits (to be justified later), the corresponding altitude of the turbulence is

$$\frac{S_P \sin\alpha}{a} = 0.9 \pm 0.1 \text{ km}$$

where $\alpha = 62°$ and $a = 21$ μrad.

Thus it is possible, using standard correlation analysis, to deduce the height and velocity of turbulence from the scintillation of a double star, when the scintillation is produced predominantly at one height. It is confirmed that the required double star signal is present in the data for 23-5-85.

10.3 Wind measurement using quadruple correlation

As explained in §4.2.1, it is not possible to use the standard correlation analysis (as used in the previous section) when the scintillation is produced at more than one height, as it is not known which peaks in the auto- and cross-covariance functions are related. A method of multiple correlation was developed in §4.2.3 to accumulate the contribution of related fluctuations in a point-by-point comparison of four series. This is applied below to the simple situation analyzed in the previous section, and then to a situation where the scintillation is produced at two different heights.

The quadruple correlation by selection Q_M (equation 4.14) is applied to search for the four correlated events produced by each duplicated feature in the scintillation pattern of α Crucis crossing each of the two slits. This "double star, double slit" (or "DSDS") correlation function is defined as

$$Q_{DSDS}(I_1, I_2, t_{11}, t_{12}) = Q_M(I_1(t), I_2(t-t_{12}), I_1(t-t_{11}), I_2(t-t_{12}-t_{11})) . \quad -- (10.4)$$

This should be positive when t_{11} is the time interval between the two components of the double scintillation pattern reaching the same slit and $-t_{12}$ is the time for the pattern to move from slit 1 to slit 2.

The DSDS correlation for a double-slit record on 23-5-85 is plotted as a function of t_{11} and t_{12} in the upper plot in figure 10-3, where higher correlation is represented by denser shading. The peak at $(t_{11}, t_{12}) \sim (4, 4)$ is the desired one which indicates the atmospheric wind. As predicted in §4.2.3, false peaks occur for $t_{11} \sim 0$, around (4,0) and (0,0), corresponding to an autocorrelation peak where parts of the same individual features are compared.

Using equations 4.3 and 4.4 (as in the previous section), the auto- and cross-correlation time shifts t_{11} and t_{12} are transformed to pattern separation and speed, both measured perpendicular to the slits. The perpendicular speed is indicated in a scale at the top of the plot and lines indicate the locus of points corresponding to separations of 1, 2, 3 and 4 cm. Thus the DSDS correlation indicates the presence of a double star pattern with a perpendicular separation of 2.5 cm moving from slit 2 to slit 1 with a speed of 6.5 ms^{-1}.

This correlogram is converted to a speed-separation plot in the lower graph of figure 10-3. The 4 lines showing the locus of the separation values (of 1, 2, 3 and 4 cm) transform to the four horizontal lines on the left. The actual peak at (speed,separation)= $(-6.5\ \text{ms}^{-1}, 2.5\ \text{cm})$ is difficult to see because the plot is dominated by the high speeds corresponding to the smallest values of $|t_{12}|$.

In figure 10-4, the same transformation is shown for another record. In this case the correlation at small values of $|t_{12}|$ is omitted in order to eliminate the larger speeds and so give good resolution around the peak in the speed-separation plot. In this case it is at (speed,separation)= $(-7\ \text{ms}^{-1}, 2\ \text{cm})$. In the bottom plot of figure 10-4, the rectangle representation (defined in figure 4-10) is used to show the same information as the middle plot. This allows better visual discrimination of the values than does the shading and so will be used for subsequent plots in this chapter.

The transformation from correlogram to speed-separation plot is shown again in figure 10-5 (using yet another record), but with the combinations of time shifts chosen to give a better distribution of plotted values in the speed-separation plot. Also, in the lower diagram, the perpendicular separation is converted to height in the atmosphere (using equations 4.1 and 4.3 to give the value on the right hand axis) and the projection (perpendicular to the slits) of the radiosonde profile is plotted. The values measured

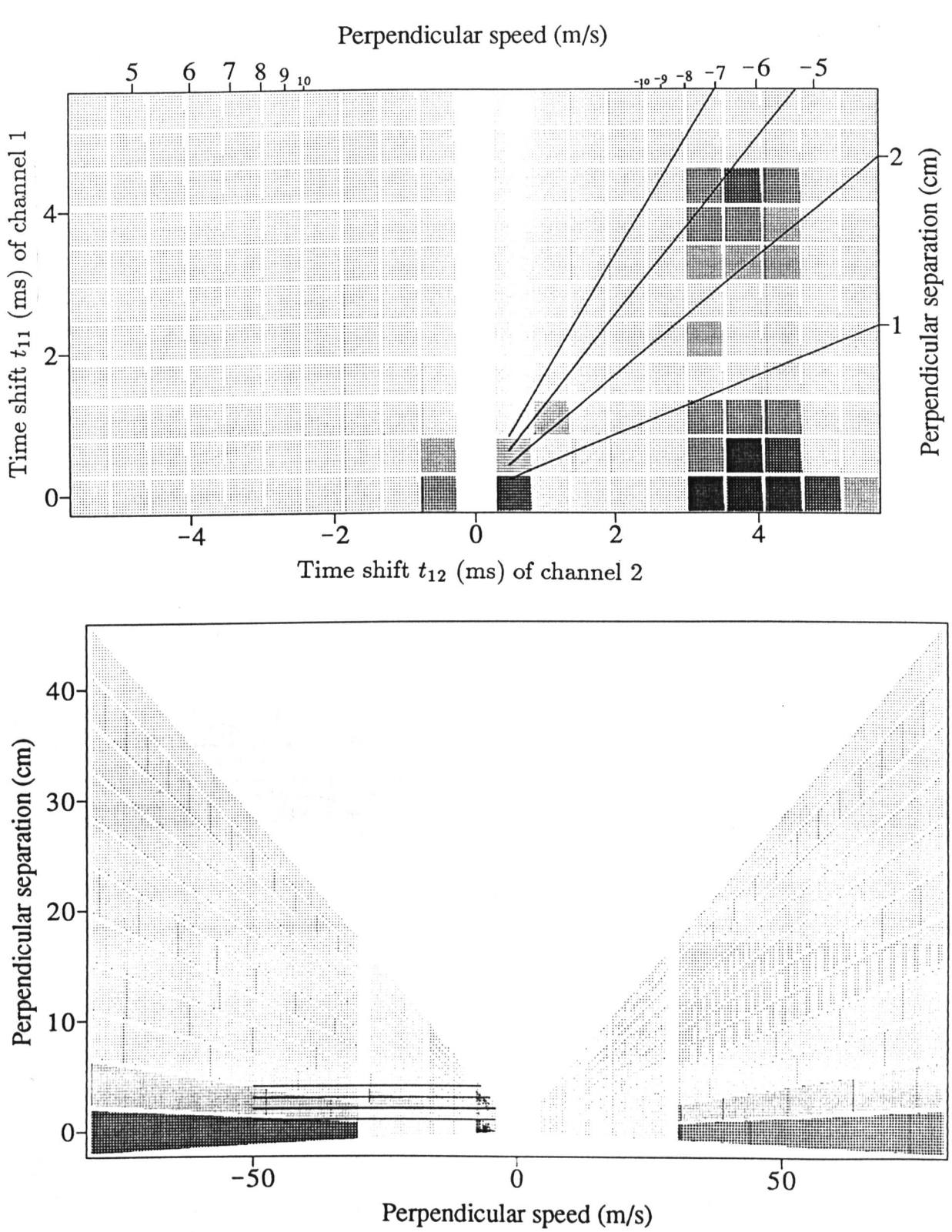

Figure 10-3 An illustration of the transformation between the "double star, double slit" (DSDS) correlation function and a separation - speed plot. At the top, the DSDS correlation function for α Crucis is plotted against the auto-correlation and cross correlation time shifts. The correlation is shown by a "density plot", where density $\propto$ |correlation|, in 8 steps. The corresponding scintillation pattern separation and speed (both perpendicular to the slit detectors) are shown on the opposite axes. Four lines are superimposed, showing the locus over negative speeds for each of the four pattern separations of 1, 2, 3 and 4 cm. (*nb* for 1 and 2 cm, the lines are identified where they meet the right hand axis.) The correlation function and the four lines are replotted below against linear axes of speed and separation.

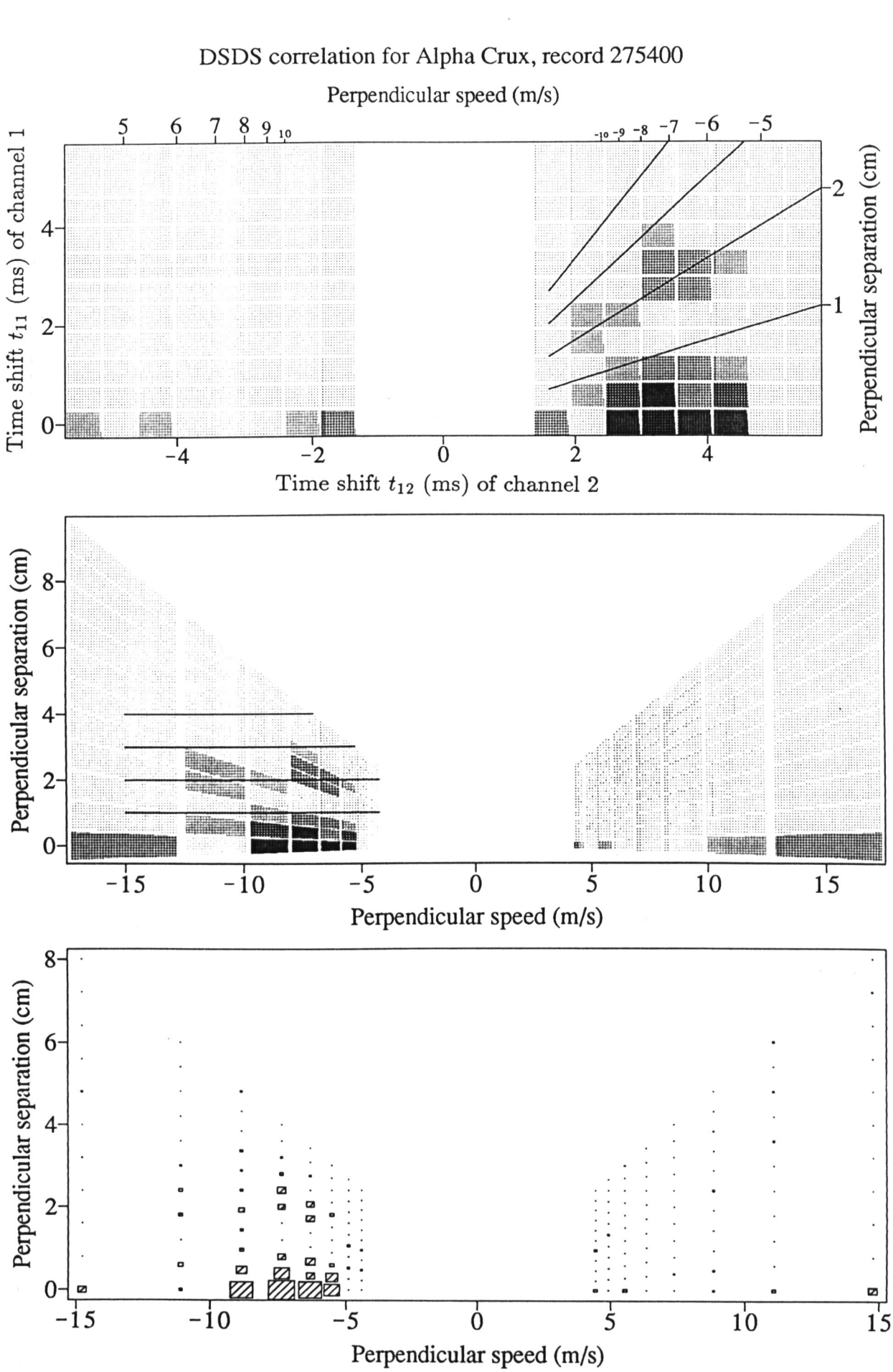

Figure 10-4 In the top and middle plots, the transformation of figure 10-3 is repeated for a different record and a smaller range of speeds. The speed-separation plot in the middle is done again at the bottom using the rectangle representation (*ie* the size of the rectangles is proportional to the correlation, with hatching for positive values).

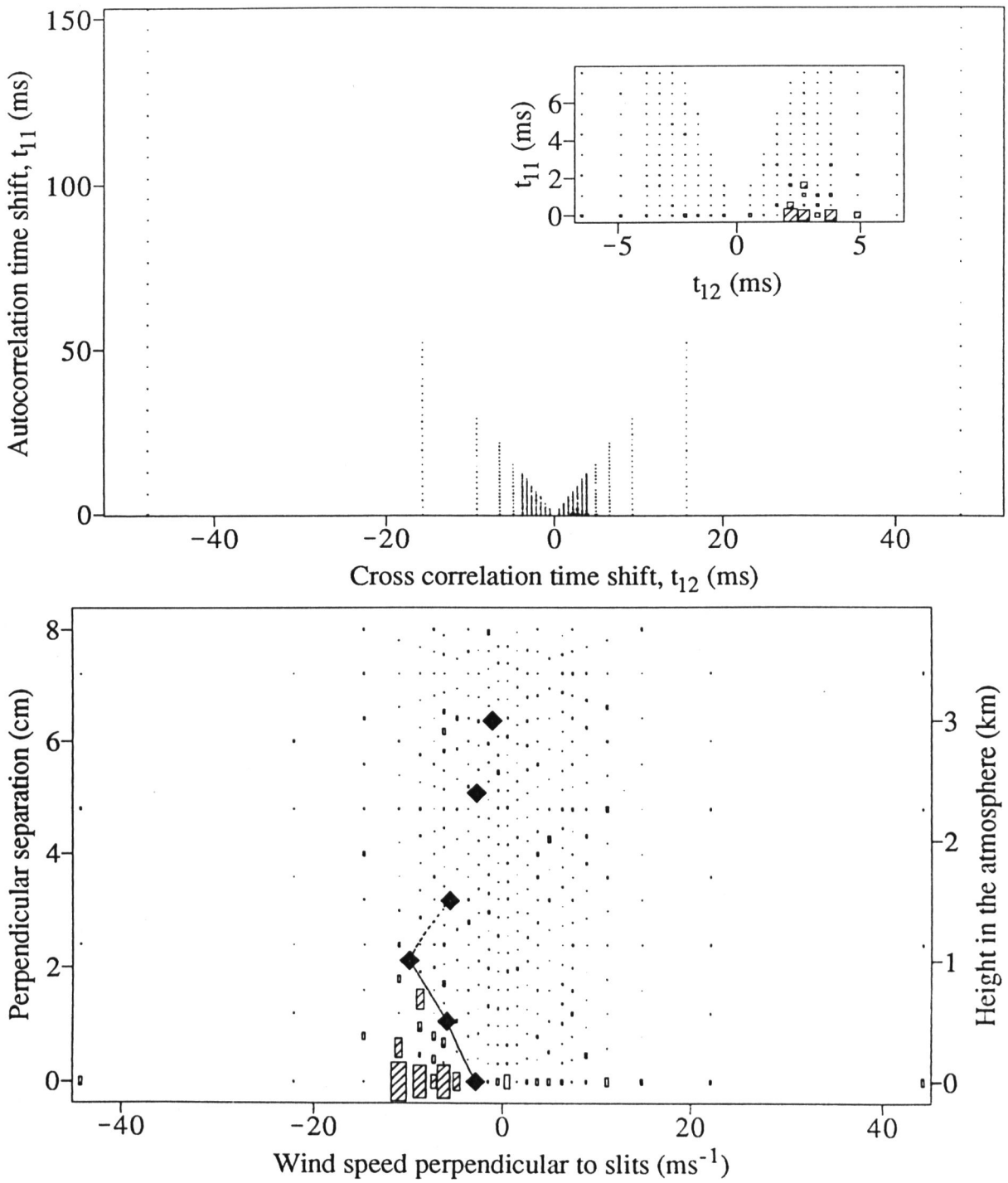

Figure 10-5 The transformation of the DSDS ("double star, double slit") correlation function (upper plot) to a speed-separation plot (below). In the upper plot, particular combinations of time shifts are chosen so as to produce an even distribution of values (at low speeds) in the speed-separation plot. The size of the rectangles is proportional to the correlation value. The values for small time shifts are replotted in an inset with greater resolution. In the lower plot, the correlation is plotted as a function of components, perpendicular to the slits, of pattern separation and speed. The altitude of the turbulence deduced from the separation is shown on the right hand axis. The perpendicular components of the wind profile measured by radiosonde are indicated by diamonds. The efficiency of the double slit in detecting both components of the double scintillation pattern is indicated by the ratio of the dash to gap length on the interpolated curves of the radiosonde profile.

by the radiosonde are indicated by filled diamonds. The lines between these indicate the projection of the wind vector calculated by interpolation between the radiosonde readings. (*nb* Some of these lines may be seen to have a small curvature. This is a consequence of the interpolation method used, in which the speed and direction are independently calculated for each height by linear interpolation between the radiosonde measurements.)

A further piece of information added in this figure is the efficiency of the double slit in detecting the four events caused by the passage of the two components of the double star pattern over the two slits. This efficiency will be 100% only if both the orientation of the double star pattern and the pattern velocity are perpendicular to the slits. For other orientations and velocities, at least one of the four required events (of a scintillation feature crossing a slit) may not occur. The efficiency is indicated in figure 10-5 by dividing the interpolated curve of the wind profile into small height ranges and plotting a fraction of the curve in each which is equal to the efficiency. Thus an equal size for a dash and the ajoining gap indicates an efficiency of 50%, where in half of the possible cases both components of the double star pattern cross both slits.

It can be seen in figure 10-5 that:

a) the detector efficiency is almost 100% up to 1 km, justifying the assumption in §10.2 that the wind velocity was perpendicular to the slits.

b) There is a large value of DSDS correlation at (-9 ms^{-1},0.7 km), close to the radiosonde profile.

c) There are even larger values for zero height, as explained earlier.

The question arises as to whether the peak at (-9 ms^{-1},0.7 km) is a genuine measurement of wind at that height, or whether it is part of the false peak at (-9 ms^{-1},0). This is resolved in figure 10-6 by comparing wind profiles deduced from the scintillation of α Crucis with profiles deduced from that of β Crucis. The profile in the latter case is calculated by treating the data for β Crucis as if it is produced by α Crucis. If the double pattern for the double star is either not present or well separated, the size of the features in the scintillation pattern will be the same for both the double and single star, giving the same false peak for low heights.

The DSDS correlation for ten 0.97-s records is averaged for each star. As the

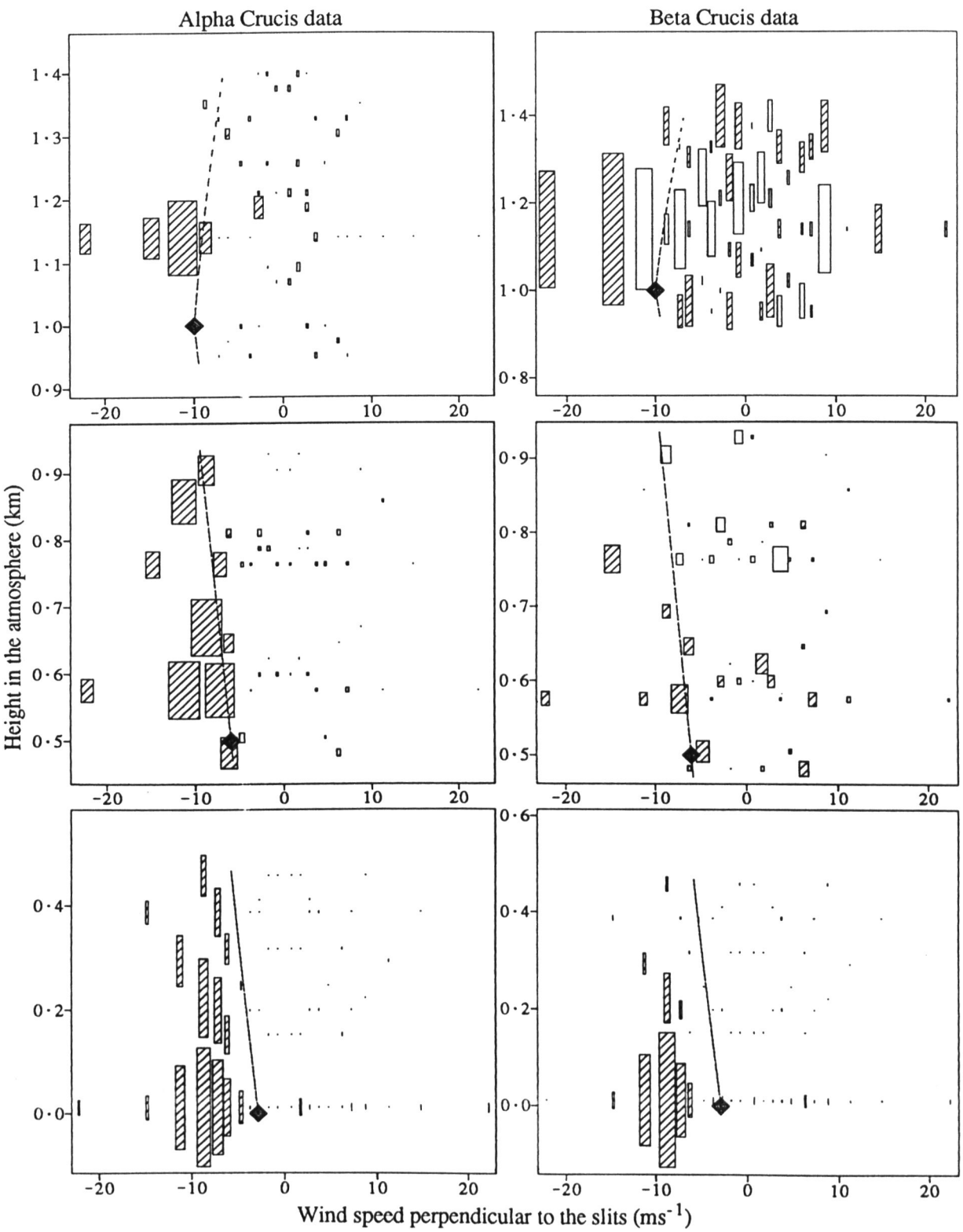

Figure 10-6 The "double star, double slit" correlation is plotted as a function of wind speed perpendicular to the slits and of height in the atmosphere. The height range is divided into three subranges. The size of the rectangles is proportional to the correlation value and is set separately for each plot. Hatching indicates positive values. The perpendicular component of the wind velocity measured by radiosonde is shown by diamonds for the individual measurements, with the connecting curves showing the projection of a linear interpolation of both speed and direction. The double slit efficiency at each height is indicated by the fraction of the curve that is filled in. The correlation for β Crucis is obtained by treating the data in the same way as for the double star α Crucis.

genuine peak is generally much weaker than the false peak at zero height, the profiles are split into three height regions so as to get adequate resolution at the greater heights. The rectangle sizes are normalized (to have maximum size without overlap) within each plot.

For the lowest height region, the deduced profiles are similar for both stars, except that the peak for the single star drops off much more rapidly with height. In the top height range (0.8–1.2 km) there is a clear peak in DSDS correlation of the double star, in agreement with the measured profile, while for the single star positive and negative values occur randomly. Thus it is confirmed that quadruple correlation can be used in the multiple-beam measurement of atmospheric wind, in the simple case where the scintillation originates predominantly at one height.

The analysis described above was repeated using the correlation function Q_{ur}, which was shown in a simulation in §4.2.4 to remove the false peak near zero height. No clear result was obtained. This is not surprising, as it was shown in analysis of street light in §6.9 that photon noise is detrimental to this function. As the relative contribution of photon noise will be reduced using larger apertures, the function may be useful if wider slits are used. This would be feasible for well-separated slits designed to match the separation of scintillation patterns produced at greater heights.

The ability of the double-slit method to measure wind with good time resolution is demonstrated in figure 10-7. The profile is deduced for individual 0.97-s records, for six single-star records on the left and six double-star records on the right. The false peak at zero height is removed by plotting the values only for the height range 0.5–2 km. For most of the double-star records there are high values of correlation (indicated by red, hatched rectangles) close to the radiosonde profile (black curve), while the distribution of values is almost random for the single star. Thus it is established that the multiple-beam method with quadruple-correlation analysis can be used to determine wind information from only 1 s of data.

On one of the twelve nights on which double-slit observations were made, the scintillation pattern was produced at two different heights. The quadruple-correlation analysis is applied to this data in figure 10-8. Comparison of the profiles for the double (left) and single star (right) shows a significant difference at negative speeds,

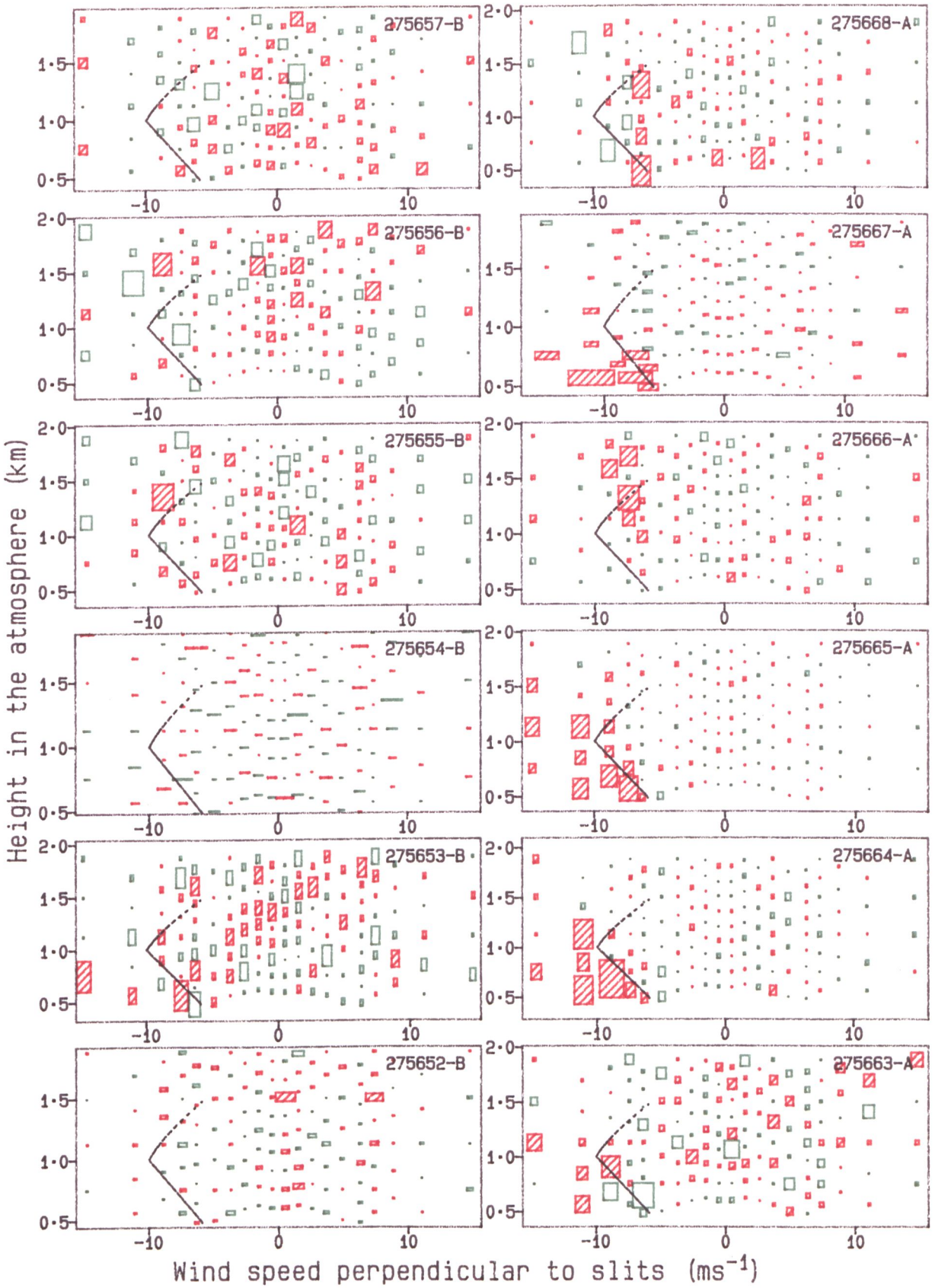

Figure 10-7 A comparison of wind profiles measured by radiosonde with those deduced from individual records of scintillation of Beta Crucis (left) and Alpha Crucis (right). The curve in black indicates the radiosonde profile, as in previous diagrams. The size of the rectangles is proprotional to the DSDS correlation and is normalized within each graph. Red rectangles (hatched) indicate positive correlation, and green (blank) negative.

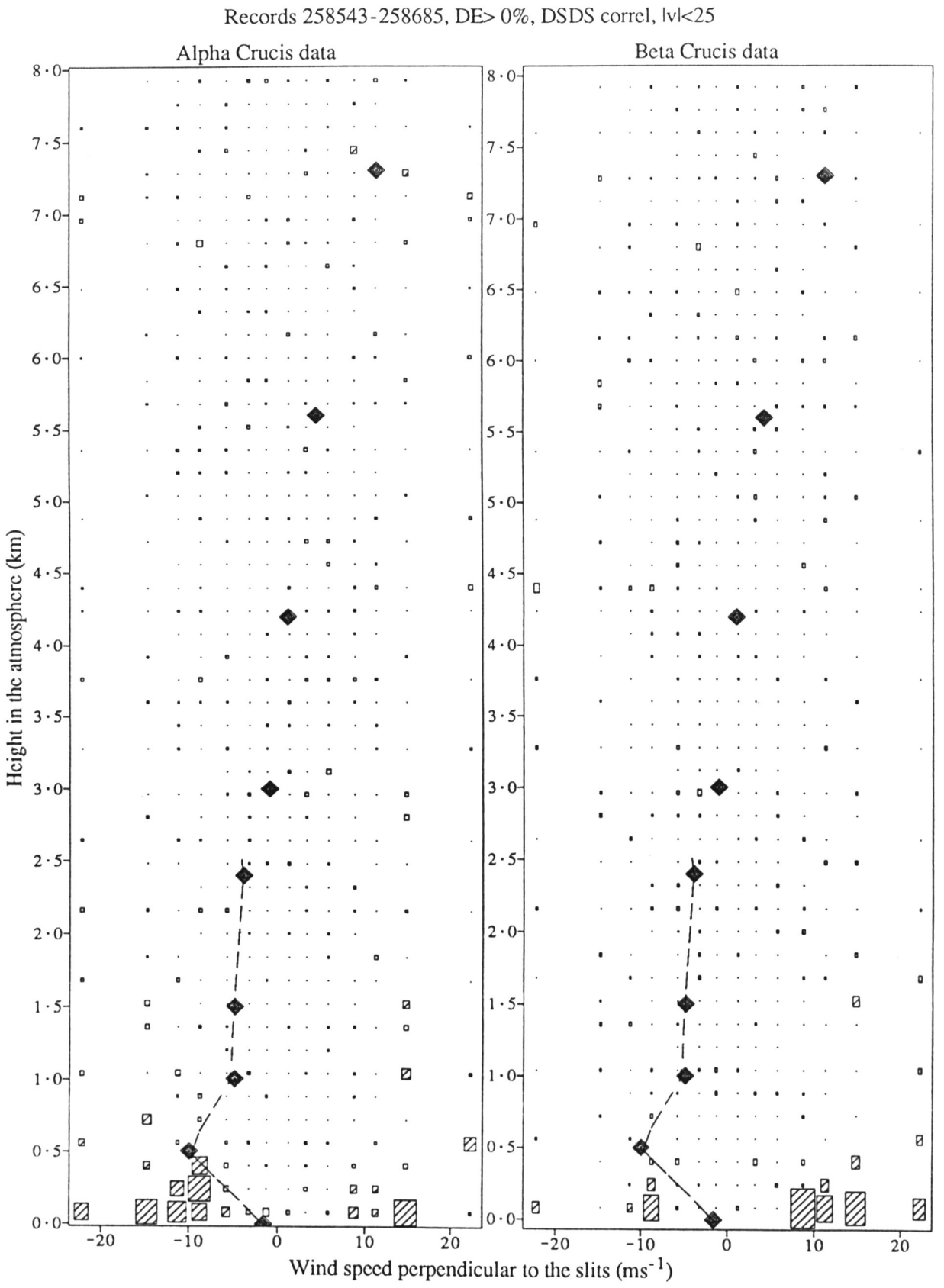

Figure 10-8 Derivation of the wind profile from scintillation produced by turbulence at two different heights. The profile on the left is deduced from the scintillation of α Crucis. That on the right is deduced by applying the same analysis to the scintillation of β Crucis. The difference between the two profiles suggests the presence of turbulence at ~0.4 km with a transverse speed ~ -10 ms^{-1}, in agreement with the radiosonde measurement. There is little difference between the profiles at positive speeds, indicating that the peaks at ~ 10ms^{-1} are due to the autocorrelation of single features. The radiosonde profile indicates wind with this speed at ~7 km.

in that the false peak at zero height extends further upwards for the double star. The interpretation is that turbulence at ~0.4 km produces two components in the double star scintillation pattern which are separated by such a small distance (1 cm) that the individual features partly overlap. The deduced speed and height is in good agreement with the radiosonde profile.

At positive speeds (8–15 ms^{-1}) large correlation values occur randomly at heights up to 2 km, for both the single and double star. The similarity suggests that these large values are due to the false peak due to autocorrelation. As the extent of this is much larger than that for the negative speeds, the pattern size for the positive speeds must be larger. A larger pattern size indicates a much greater height (as explained in §3.5.1). This is consistent with the height of 6 km deduced by looking for the appropriate speed on the radiosonde profile. As the detector efficiency is zero above 2.5 km, it is as expected that the analysis fails to detect the higher turbulent layer.

In conclusion, quadruple-correlation analysis is applied to double-star scintillation on two occasions when standard correlation analysis shows that there were two similar components in the double star pattern. On both of these occasions, the analysis correctly deduces the transverse wind speed at one particular height. On one of these occasions, the relevant scintillation pattern was mixed with another produced at a much greater height. Thus while the simultaneous measurement of wind at more than one height is not demonstrated directly, it is shown that it is possible to apply the method when the scintillation pattern originates at two different heights.

It is concluded that the multiple-beam analysis, applied to a 2-detector observation of double-star scintillation, promises to be a viable method of measurement of a wind profile.

10.4 Anisoplanatism measurements

In §4.4 a method is suggested to determine whether the atmospheric isoplanatic angle is larger or smaller than the separation angle of a double star. It is based on the principle that, if the lines of sight from a detector to the two components of a double star contain different turbulent irregularities, two independent signals will add together, thus reducing the variance of the scintillation relative to that for a nearby

single star.

The method is applied in this section to observations with small circular apertures and with slits. The results for time series on channel 1 have been published (Campbell and Elford, 1990). At the time of publication the method of correction for afterpulsing, specified in §4.5.4, had not been developed. However, the values of the normalized second moment for skylight (without afterpulse correction) are close to the theoretical value of 1 for time series on channel 1 (as seen in figure 6-10), so it was clear that afterpulsing could be neglected for this set of data. With the correction for afterpulsing now available, all four data sets (*ie* two channels at two different sampling intervals) are used in the analysis.

This method (for measurement of isoplanatism) was devised subsequent to the demise of the tape-transfer facilities, so it is applied to data which were not taken with this application in mind. Ideally it should be applied to simultaneous measurements of the scintillation of a double and single star which are close together in the sky. The best that can be achieved here with the available data is to compare measurements with a 3-min interval between those for the single and double star, which are separated by $\sim 5°$. Individual measurements of the ratio of the moments for the two stars will therefore be affected by both temporal and angular variations in the scintillation statistics. However, there is no reason for these to produce any systematic error in average values over many records.

In figure 10-9 the moment comparison for a single and double star is applied to all available data (*ie* of pairs of single records of α and β Crucis, separated by 3 min) for each of two small circular apertures of equal diameter (either 2 or 4 mm). These apertures were separated by 1.1–7.1 cm (in "scans" used to record the spatial correlation function), so that for most of the records the two channels recorded independent parts of the scintillation pattern. There are four graphs, for the four combinations of two apertures and two sampling intervals (542 μs for time series and 42 μs for frequency distributions). The normalized second moment $\frac{\langle I^2 \rangle}{\langle I \rangle^2}$ for the double star is plotted on the vertical axis against the same quantity for the single star on the horizontal axis. Small symbols, different for each of the three nights on which data is available, indicate the comparison of the normalized second moment for each pair of records. For each

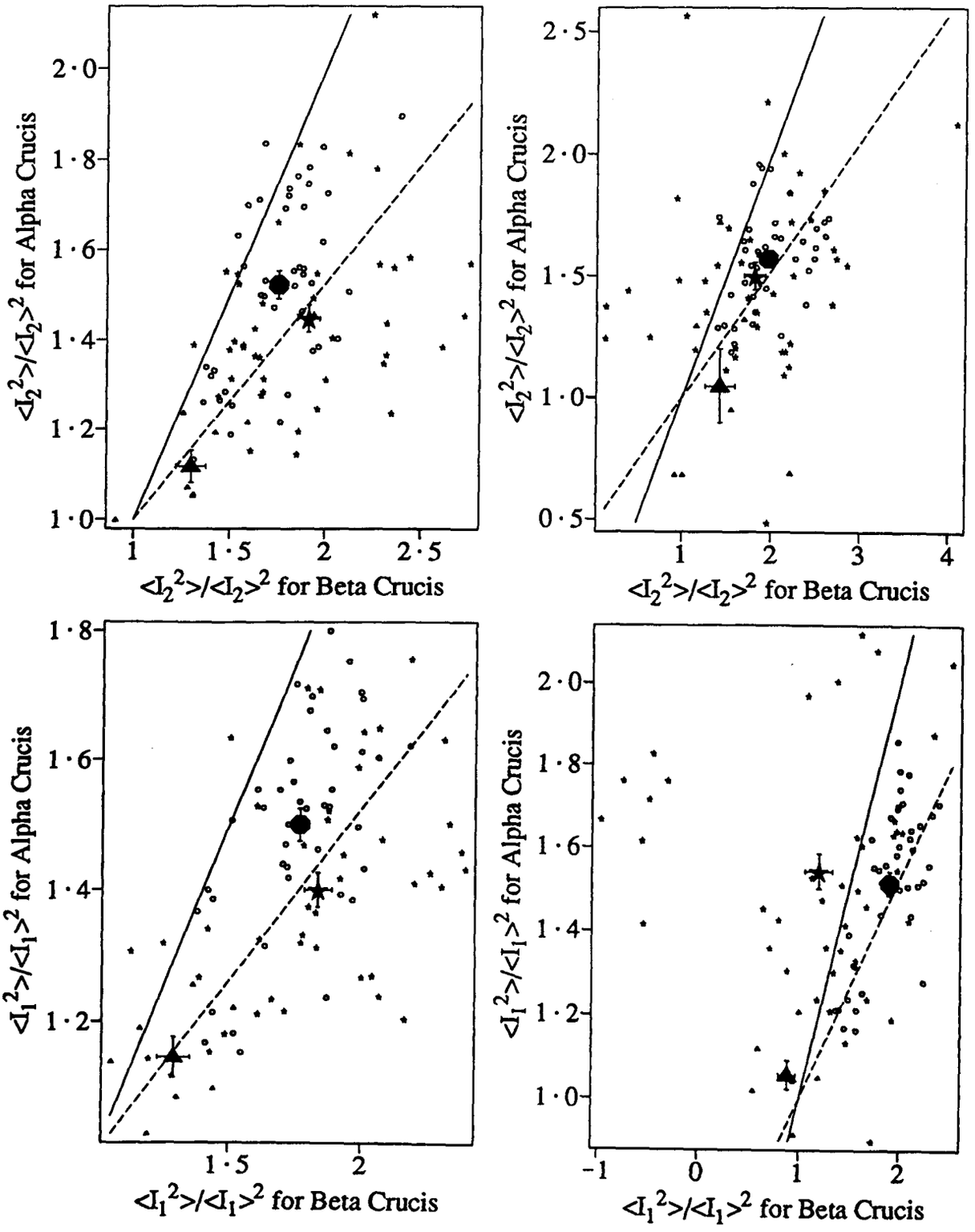

Figure 10-9 A comparison of the normalized second moments of the scintillation of a single and of a double star, observed with 2 or 4-mm apertures. This comparison is made for time series (on the left), frequency distributions (right), channel 2 (top) and channel 1 (bottom), for pairs of records of α and β Crucis. Small symbols (different for different nights) indicate the comparison for individual record pairs, while large solid symbols and error bars indicate the average and standard error (along each axis) of all values for each night. The solid line indicates equality and the dashed line indicates the expected relationship if the two components of the scintillation pattern of α Crucis are completely separated.

night, the average and standard error of all values along each axis is shown by a large solid symbol and error bars. A solid line indicates equality and a dashed line indicates the prediction of equation 4.20, which specifies the normalized second moment of the double star α Crucis, relative to that for β Crucis, if the scintillation produced by turbulence along the two paths to the double star is completely different.

If the isoplanatic angle is greater than the angular separation (21 μrad) of α Crucis, the scintillation at the detector for each of the two components of the double star will be the same. In this case the normalized second moment will be the same for the double and the single star and the points in figure 10-9 will lie around the solid line. In fact they tend to lie around the dashed line, indicating that the fluctuations for the two components are independent and so the isoplanatic angle is much less than 21 μrad.

For the time series it can be seen in figure 10-9 that:

a) for most pairs of records, the normalized second moment for the double star is substantially less than for the single star, indicating that the contributions from the two components of the double star are different to some extent.

b) The average values for two nights are close to the dashed line, indicating complete anisoplanatism over 21 μrad. On the third night the average value (represented by a circle) is above the dashed line, indicating partial isoplanatism.

c) There is little correspondence between points for individual records on different channels, but the average values are consistent. This confirms that it is valid to take averages in this situation.

For the frequency distributions there is a greater scatter of the points, and some physically impossible values (of less than 1). These problems are caused by noise spikes, which have a much greater effect on the moments for the much smaller sampling interval of the frequency distributions. particularly for the background record. The seven negative moment values on channel 1 are all related to one bad background record. However, for one night, represented by circles, the signal-to-noise ratio was better. In this case, the average value (again consistent between channels) is closer to the dashed line than for the time series. A plausible explanation is that the two similar components of the double star pattern were well separated for smaller features but overlapping for large features. The higher frequencies produced by the smaller features would be

smoothed by the relatively long sample interval of the time series but not by the shorter interval of the frequency distributions. Thus the smaller, well-separated features make a larger contribution to the values for the frequency distributions, producing values closer to the dashed line.

It is concluded that, for the three nights on which suitable data is available, a comparison of the scintillation of α and β Crucis on small circular apertures indicates that the turbulence which produces the detected scintillation is different along the two paths to the two components of the double star.

This single/double star moment comparison is repeated in figure 10-10 for all suitable data taken with the double slit detector. There are some differences in presentation relative to the previous figure:

d) except for one night, results for individual record pairs are not shown, to avoid crowding the diagram.

e) Only time series are used (as the count rate for the slit aperture often exceeds the 4-bit limit for frequency distributions).

f) Two sets of data are selected. In one set the orientation of the pattern separation vector is more than 45° away from the slit (left) while in the other it is within 20° of the slit (right).

For nearly all individual pairs of records, the normalized second moment for the double star is less than for the single star, irrespective of orientation. For the "$> 45°$" orientation, it tends to be close to the prediction using equation 4.20 (dashed line), indicating that the two components of the double star pattern were completely separated. For the parallel case ($< 20°$), the second moment is slightly less (considered along a vertical line) than the prediction. This implies that the two components of the double star pattern are detected simultaneously and are to some extent anti-correlated, so that the second moment is reduced compared to that expected for the addition of independent patterns. Such anti-correlation would arise if, when a bright feature is on the slit, the other component of the double star pattern is slightly away from the slit and so the surrounding darker region is detected.

For 23-5-85, indicated by diamonds, the comparison of the average values of the moments falls on the dashed line, indicating that the two patterns for the double star

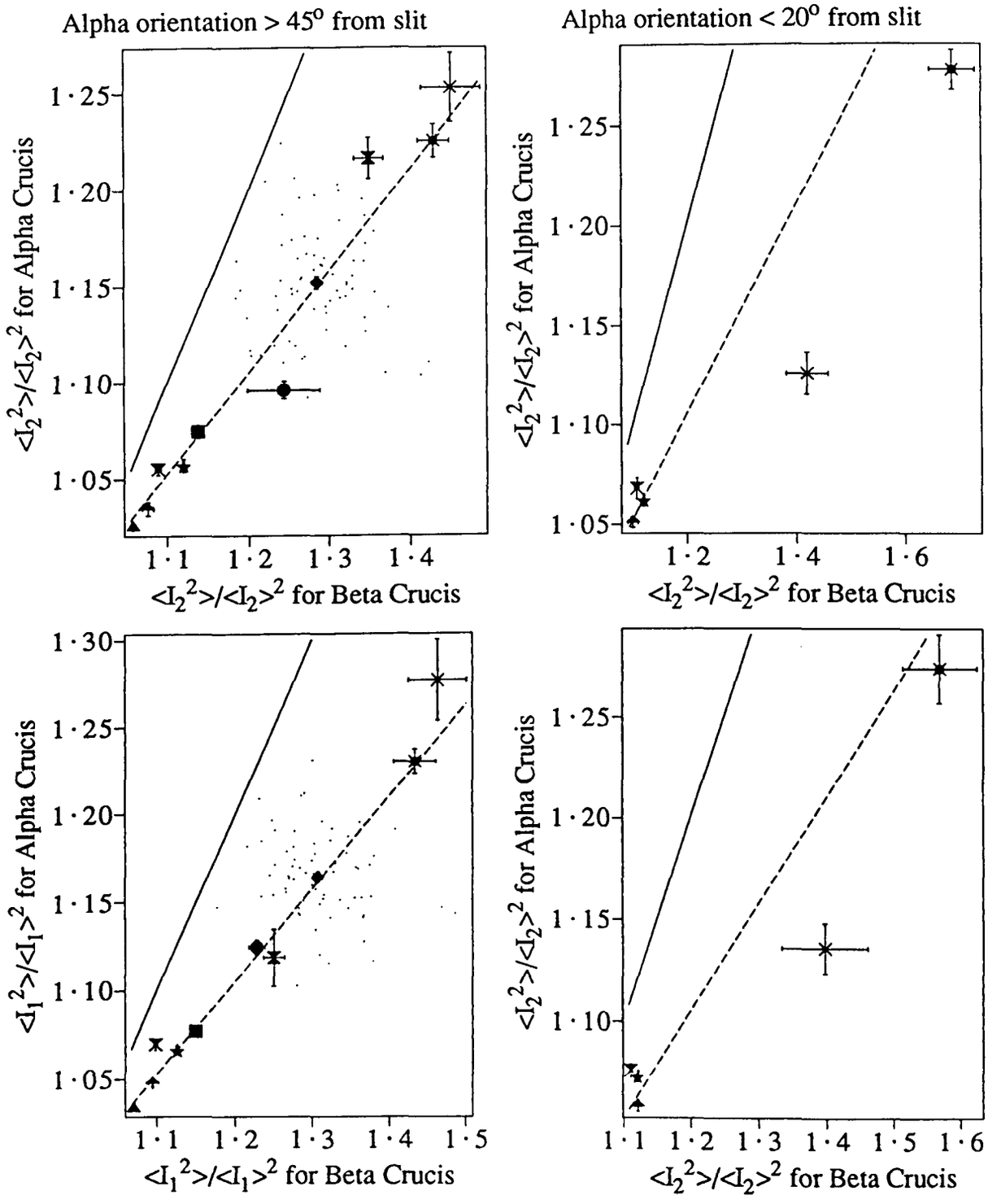

Figure 10-10 A comparison of the normalized second moments of the scintillation of a single and of a double star, observed on a 50- × 3-mm slit. This comparison is made for channel 1 (lower graphs) and channel 2 (upper graphs), with the slit at either >45° (left) or <20° (right) from the line joining the two components of the double star pattern. For 23-5-85, dots indicate the comparison for pairs of records of α and β Crucis, while a diamond and error bars indicate the mean and standard error along each axis. The mean and standard error for other nights are shown similarly, using different symbols for each night. The solid line indicates equality and the dashed line indicates the expected relationship if the two components of the scintillation pattern of α Crucis do not fall on the slit simultaneously.

were separate. This is consistent with the result of the correlation analysis applied in figure 10-2, which indicated the presence of two components in the double star pattern, separated by a distance approximately equal to the pattern size. Thus it is confirmed on this occasion that the anisoplanatism deduced by moment comparison is indeed due to the separation of the two components of the double star scintillation pattern (rather than some other effect, such as different colour for the stars or a systematic error in correction for background).

For the same data (*ie* 23-5-85) the results for individual pairs of 0.97-s records are indicated by dots. There is a large scatter about the mean, presumably due to the 3-min time difference and 5°-angle difference between measurements on α and β Crucis. However, in all cases the second moment is less for the double than for the single star. Thus observations of only 1 s in duration consistently show at least some anisoplanatism, but about 1 min of data (in 1-s intervals spread over 40 min) is required in this case to show that the anisoplanatism was complete.

In summary, comparison of the scintillation of a single and double star shows that the two components of the double star pattern were partly to completely separate for a wide range of scintillation levels on eleven different nights. This indicates that the isoplanatic angle was smaller than 21 μrad over a range of atmospheric conditions. On one night the interpretation of the result of this comparison is confirmed by standard correlation analysis, which shows that the scintillation pattern of the double star consisted of two similar, separated components. The predominant scale size on this occasion is shown to have been 3 cm, which is much smaller than the minimum aperture required in the measurement of the isoplanatic angle by previous methods.

Thus the single/double star moment comparison is shown to be a simple and inexpensive method for the measurement of isoplanatism. It's flexibility is demonstrated by its successful application to observations which were designed for wind measurement. It is shown to yield results using apertures much smaller than in any previous methods, thus allowing the angular variation of turbulence to be measured at low altitudes in the atmosphere where the horizontal separation between the two paths is small.

As explained in §2.4.2, measurement of the isoplanatic angle is important in astronomy and laser propagation. The particular ability of this new method to measure

anisoplanatism originating at low altitudes is not expected to be useful in astronomy, as astronomical observations are not made in conditions where low-level turbulence is significant. However, it may be very useful in the evaluation of schemes to precompensate upward-propagating lasers for the effects of atmospheric turbulence. Without the precompensation, any small-scale turbulence near the laser would produce scintillation within a few kilometres. The light thus concentrated would spread out again at greater distances and could be lost from the beam after propagation over the large distance to the target. It is therefore necessary to measure the isoplanatic angle for turbulence close to the laser.

Chapter 11 Conclusions and Suggestions

Summaries and conclusions of this thesis are presented. The value of further work with the existing data and equipment is considered. Suggestions are made for new methods of measurement which were devised while writing this thesis.

11.1 Conclusions concerning new techniques

New techniques developed and applied in this thesis include correction of photocount distributions for background, afterpulsing and dead time, remote sensing using multiple-beam techniques with scintillation, specific measurements of particular characteristics of stellar scintillation and measurement of atmospheric isoplanatism.

11.1.1 Photocount corrections

To measure parameters of the stellar scintillation pattern, such as moments, it is necessary to make corrections for the effect of background light, noise, photomultiplier afterpulsing and dead time.

An existing method of correction for background light allows the measurement of the normalized moments of the scintillation if the background is Poisson distributed. In this thesis the method is extended to allow this correction to be made for background with any distribution, so that the effects of noise with non-Poisson statistics (such as photomultiplier dark noise) can be removed. An attempt is reported to test the method using two records in which the stellar scintillation is similar but the background is different. The test is successful in that the moments are in agreement after the correction is applied. However, the signal-to-background ratio is not very different for the two records, so that the test is not conclusive.

A technique is introduced to deduce the probability of afterpulsing in photomultipliers from a frequency distribution of output pulses per time interval. Two variations of the technique allow the deduction of the probabilities of

a) a specific number of afterpulses following an event, and

b) initial afterpulses (following a particular event) and subsequent afterpulses (produced by an initial afterpulse).

Application of these techniques to observations of dark noise and skylight allowed the deduction of afterpulse probabilities. The deduced values are as expected for one of

the two photomultipliers, but not for the other. A plausible explanation is tendered for the second case.

A method is introduced to remove the effect of afterpulsing from frequency distributions of photomultiplier pulses. It is applied to starlight data, using the probabilities deduced by variation "a)" above. It is found that

c) correction of skylight records for the effect of afterpulsing alters the normalized second moment to be very much closer to the expected value of 1, and

d) correction of starlight records makes a substantial improvement to the consistency of the second normalized moments measured on different channels and at different sampling rates.

The success of these corrections suggests that the methods to deduce and correct for afterpulsing are valid.

A method is introduced to make an approximate correction for the effect of the dead time of the photomultiplier-amplifier combination. This is used to show that the effect is not significant in this work.

11.1.2 Multiple-beam techniques

Previously, a multiple-beam technique has been demonstrated to measure remotely a profile of transverse velocity in a fluid which is sparsely seeded with particles. Modifications are investigated in this thesis to apply the method to scintillation patterns, which are produced by irregularities in refractive index within the fluid.

To apply the multiple-beam technique to scintillation, it is shown that correlation functions are required which detect the presence of fluctuations common to all of a number of series. Standard multiple-correlation functions are shown to be inadequate for this purpose, so two new types of multiple correlation are defined. These are called "multiple correlation by selection" and "multiple correlation by minimum difference". In numerical simulation, these are shown to be superior to the standard functions, but still to have deficiencies.

A laboratory test of the multiple-beam system was conducted, using crossed laser beams. Using "multiple correlation by minimum difference", the positions of two turbulent streams (flowing simultaneously) are deduced to within 10 cm of their actual positions on a 40-m path. The transverse velocity of each stream is deduced as part

of the same analysis, but only the deduced direction (positive or negative) can be confirmed as correct as an independent measurement of the velocity was not made. Nevertheless, the correct deduction of the position and sense of the velocity of the two turbulent streams suggests that the technique works as intended.

The multiple-beam technique is further modified for application to double-star scintillation, in situations where each detector receives light from both stars. It is shown in simulation that the duplication of each signal produces an ambiguity, in that different parts of the same scintillation feature are interpreted as duplicated features produced by turbulence at low heights.

The technique is applied to observations of stellar scintillation taken with a double slit detector. Data was obtained on one particular night when the scintillation was produced predominantly at one height (of $\sim$1 km). The presence of only one turbulent layer makes it possible to produce simulated double-star data from records of a nearby single star. The height and transverse velocity are determined by adjusting their values in the simulation to get the highest similarity between cross-covariance functions for the actual and simulated data. This shows that the two components of the double star pattern were present, clearly distinguishable and moving from one slit to the other. Thus the scintillation pattern is shown, on this occasion, to be suitable for the application of the multiple-beam method.

A multiple-beam analysis, implemented with quadruple correlation by selection, is applied to the same data. It produces measurements of the transverse velocity in the range 0.5–1 km which are in reasonable agreement with meteorological measurements. As predicted, this analysis gives large false peaks at low altitudes, so that comparison with the results of the same analysis applied to a single star is necessary to identify the contribution of the false peak.

The same analysis is applied to scintillation patterns which were produced by turbulence at two different heights. The presence of turbulence at $\sim$0.4 km is deduced, with a transverse velocity in agreement with the radiosonde measurement. The parameters of the other layer cannot be determined, due to its large height and the consequent large separation of the double star pattern. However, it is thus established that the multiple-beam analysis can measure the height and velocity of one turbulent layer when

the associated scintillation is mixed with that from another layer.

The same correlation function cannot detect either of two streams in the laboratory experiment, so while this experiment is useful for development and testing of multiple-beam methods, it is not suitable for laboratory simulation of stellar scintillation.

A modification of "quadruple correlation by minimum difference", to exploit the difference in intensity between the double star components, is shown in numerical simulation to eliminate the false peak at zero height. It requires strong scintillation and is found, in a test using the 100-Hz fluctuations of street lights, to be adversely affected by photon noise. The effect of the noise is reduced if the analysis is heavily weighted towards times when correlation is present over several successive sampling intervals. No suitable stellar scintillation data is available for this technique to be tested.

11.1.3 Specific techniques for investigation of scintillation

It is suggested in this thesis that crossed-beam methods used with a double star could be subject to detrimental effects caused by atmospheric refraction and the interaction of phase variations produced at different heights. Techniques are suggested and applied to investigate these effects.

Two techniques are suggested to investigate whether the refraction is significant:

a) in the spatial correlation function of the scintillation of a double star, refraction would cause the displaced peak to be smeared out, relative to the associated autocorrelation peak around zero separation. The spatial correlation functions measured in this work were not of sufficient quality to investigate this difference, as they were acquired over many nights using just two detectors. Thus a two-dimensional array of detectors is required for this measurement.

b) Refraction is expected to cause fluctuation in the velocity of a scintillation pattern produced by a steady wind. It is confirmed for data on one night that any such fluctuation was less than 10% of the velocity, and that any displacement of the starlight by refraction was less than 4 mm.

Thus no evidence was found for refraction which would invalidate crossed-beam methods by displacing the "beams".

It is postulated that the addition of phase fluctuations produced at different heights

could produce transitory scintillation patterns which would disappear as the sources at different heights move out of alignment. It is suggested that this phenomenon may be detected by the use of triple correlation to observe three related patterns: two scintillation patterns produced at different heights and the joint pattern they produce when the sources are in alignment. The postulated interaction is investigated by finding situations where two different pattern velocities were observed, suggesting an origin at two different heights. Data is available for two nights when this situation occurred. There is some evidence of phase interaction in some cases, but not above the level of statistical noise. Thus the measurement here fails to show a definite result, but does indicate that the atmospheric conditions required to make the measurement do occur.

A method called the "moment plot" has been used previously to characterize the intensity distribution of stellar scintillation, but its accuracy has been called into question. A "modified moment plot" is suggested in this thesis, in which one of the sources of error in the moment plot is eliminated by independently averaging the moment values of different order and comparing these averages.

A modified moment plot for three 30-min scans (each containing 3 min of data) is calculated. The result is similar to previous measurements of the moment plot, with the higher moments being less than those expected for the log normal distribution. On one of the three occasions, the result for one channel was much closer to the log normal distribution than the other, providing experimental support for recent predictions that the higher moments are underestimated due to the failure to observe rare fluctuations of high intensity.

11.1.4 Measurement of atmospheric isoplanatism

A technique is proposed in which a comparison of the normalized second moments of the scintillation of a double and a nearby single star indicates the extent to which the sources of scintillation are different along the two paths to the components of the double star. This method allows atmospheric isoplanatism to be measured at scales down to the smallest features in the scintillation pattern. It can be used with apertures of any shape, allowing a measurement of isoplanatism to be made simultaneously with other parameters for which the particular aperture is designed. It can be applied at low light levels and in the presence of high background light and noise, promising

application with faint stars or in daylight. The method can be implemented on existing instruments for stellar scintillation observations, provided that they can measure a distribution of photocounts per time interval. Unlike previous methods (using scintillation), no assumptions are required concerning the spectrum of the turbulence or of the mechanism that produces the scintillation.

The technique is applied to data for one particular night for which it is known that two similar scintillation patterns due to the double star are almost separated, so that it is expected that the moment comparison should indicate almost complete anisoplanatism. It does in fact do so, confirming that the normalized second moment for the double star is less than for the single star due to the addition of two independent patterns. Thus comparison of the moments of a double and single star is shown to be a viable method to measure atmospheric isoplanatism. The predominant size of the scintillation patterns in this test is shown to be 3 cm, demonstrating that the method can be applied to measure isoplanatism over areas which are much smaller than the apertures required by imaging systems and previous methods using scintillation.

11.2 Conclusions concerning observations of scintillation

Observations were made over several years, but all reported results are for an intensive campaign in the period January–July 1985. These observations were made with either two small apertures (of 2-mm or 4-mm diameter), separated by 1.1 to 10.1 cm, or two 50-mm × 3-mm slits, separated by 2.4 cm. On some nights the observing site was downwind of hills (of height 0.7 km) and strong scintillation was observed. It is assumed that the strong scintillation is associated with strong turbulence in the lee wave of the hills.

Most observations were made either to measure wind velocity or to obtain information necessary to the design of systems to measure wind velocity. However, they provide a set of data which allows a consistent study of many characteristics of the scintillation pattern. A few extra observations with different equipment and/or methods were made to enhance this study.

11.2.1 Standard observations

Measurements which have been made by other researchers were repeated, but with

smaller apertures. In general the results are consistent with previous observations:

a) parameters of the scintillation, such as the variance and the frequency content, vary considerably from night to night.

b) There is a general tendency for the variance to decrease overnight, rapidly at first and then more slowly after midnight.

c) The frequency of the scintillation increases with increasing elevation angle.

d) The variance increases with decreasing wavelength range and aperture size.

e) The predominant component of the scintillation pattern generally has a size of a few centimetres.

f) Features of the scintillation pattern are observed to move from one detector to another, often with a speed and direction matching the wind velocity at one height in meteorological measurements.

In some of these standard observations, new information was obtained:

g) scintillation features are sometimes less than 2 cm across.

h) Bright features in the pattern sometimes reach 20–30 times the mean light level.

i) On some occasions the variance of scintillation fluctuates substantially over several minutes.

j) Application of a technique developed by Vernin *et al* (1979) to measure turbulence strength gives a value for turbulence at ~1 km which is 5 times larger than that in average atmospheric profiles.

These unusual characteristics (g–j) generally occurred when the observing site was downwind of hills. A likely explanation is that they are related to strong turbulence at ~1 km altitude in the lee wave of hills.

11.2.2 New observations

From some measurements of the time-shifted spatial correlation function it is deduced that features of the scintillation pattern which are less than 2 cm in size move over a distance of several centimetres without significant change. A "cumulative contribution" analysis indicates that many individual features, all moving with the same velocity, contributed to the observed correlation values. Thus Taylor's hypothesis of turbulence "frozen-in" to the flow is shown to be valid (on a particular occasion) for turbulence producing small scintillation patterns.

Some data were obtained at times when there were frequent large enhancements in the intensity. They were tracked from one detector to another, but only over short distances (< 3 cm). For one occasion it is shown that these bright features were of similar size to the rest of the pattern, but moving less quickly.

A form of spatial correlation is applied to investigate the structure of the intensity pattern surrounding patches with various intensities. No evidence is found of a darker region around bright features, suggesting that the bright features were produced by chance superposition of the same phase from several parts of the wavefront over a large area, rather than strong focussing produced by a single phase irregularity.

In conclusion, the "frozen-in" hypothesis is applicable for small scintillation features on some but not all occasions. The structure and rapid decay of bright features suggest that they are produced by the interference of phase variations originating at different heights. Such interaction would be detrimental to crossed-beam measurements of both wind and turbulence strength.

11.3 Conclusions concerning atmospheric measurements

11.3.1 Atmospheric information

As two telescopes were available, simultaneous observations could be made on two different stars. It is shown for one occasion that regions with different scintillation statistics moved from one line of sight to the other, indicating that the turbulence was not in uniform layers covering large areas of the sky, but in patches of differing strength which moved with time. It is deduced that the patches had a horizontal size of $\sim$0.3–0.5 km at heights of $\sim$0.5–1 km.

The long standing visual observation that scintillation is stronger in association with cloud is confirmed quantitatively on one occasion by a recording of the variance of scintillation over a time interval which included the passage of an area of cloud consisting of small blobs.

11.3.2 Conclusions on wind measurement

Observations were made with the double slit detector on 12 different nights. As detailed earlier (§11.2.1), the occurrence of the two separated patterns of the double star is seen on two occasions. In both cases the multiple-beam analysis indicates a

transverse wind speed at one particular height which is in agreement with radiosonde measurements, with the height in each case being 1 km or less. The failure to detect the double pattern on the other nights could be due to the two patterns being either too close together, too far apart, or too dissimilar for the double-slit technique to work. It is concluded in the next section that the first option is not the cause.

On most occasions when the method was applied, the wind was not from the southeast and the scintillation level was low. Under these conditions it is expected that the scintillation would be produced at heights of several kilometres, producing a double star pattern with similar components separated by more than 10 cm. In this case there would be only a small probability of the wind direction being such that both components would cross both of the slits. Thus the failure to measure the wind speed on 10 of the 12 nights does not necessarily indicate that there is a problem with the method, but rather that a variety of slit separations should be used. However, the third possibility (that the patterns were too dissimilar, as might occur if there is interaction of phase variations produced at different heights) is not eliminated.

11.3.3 Conclusions on isoplanatism

The single/double star moment comparison, summarized in §11.1.4, is applied to measurements with small (2-mm or 4-mm) circular apertures on 3 nights and with the double slit on 12 nights. Over a wide range of scintillation levels, it is found that the scintillation of the double star was close to that predicted (from that of the single star) by assuming that the sources of scintillation along the two paths to the components of the double star were completely unrelated. Thus the isoplanatic angle associated with the observed scintillation was substantially less than 21 μrad on all occasions.

These deductions preclude the explanation that the failure to observe the components of the double star scintillation pattern on most nights was due to overlap of the components. However, they do not discriminate between the other two possibilities; both a large separation between the components and a lack of similarity (due to the addition of different phase variations along the two paths) would produce independent contributions on a single detector.

On one occasion complete anisoplanatism is shown for 3-cm scintillation features originating at $\sim$1 km. On another, the detection of turbulence at $\sim$0.4 km by multiple-

beam analysis indicates at least partial anisoplanatism at this height. This evidence of anisoplanatism arising in the lowest kilometre may have serious implications for proposed methods to precompensate upward-propagating laser beams for the effects of atmospheric turbulence. These schemes are only possible if the isoplanatic angle is sufficiently large. As previous measurements of the isoplanatic angle are insensitive to low-altitude turbulence, the significance of such turbulence on the proposed compensation techniques may not have been adequately investigated.

The site in this work is at low altitude and near to hills, while ground–space laser beams with precompensation for turbulence could be at high altitude sites. Thus the atmospheric distortion should be much smaller at the laser sites and so these measurements of anisoplanatism may not be relevant. However, as the double/single star moment comparison is a simple and inexpensive technique, it would be sensible to apply it before committing the huge resources required for the development of the compensated laser systems.

11.4 Further work with the existing data and equipment

11.4.1 Further work with the data

A substantial part of the analysis applied in this thesis required an ideal multiple-correlation function, capable of deducing the presence of signals common to all of three or four series. Such a correlation function could not be devised. If this problem can be solved in the future, the existing data would be useful to make an immediate test. Therefore the data and analysis programs are worthy of preservation.

11.4.2 Site considerations

The site used for this work was generally satisfactory, particularly as the local topography provides a source of strong scintillation in summer, when clear skies are the norm. The recent installation of bright security lights is not expected to be detrimental for observations with the "multiple collimator", but would make it necessary to install shielding for the "split-lens" telescope.

A disadvantage of an urban site is that the 100-Hz fluctuation of street lighting complicates the determination of the photomultiplier afterpulse probability, by adding a fluctuating component to the skylight, which was used in this work as a "constant" light

source. A simple solution would be to install a well-regulated light in the equipment.

To measure the actual value of the isoplanatic angle using the moment comparison would require measurements on several stars with different separations. Observations would be required on much fainter stars than used in this work and a dark site may be necessary. Such a site is available at a field station operated by the Dept. of Physics and Mathematical Physics at the University of Adelaide.

11.4.3 Hardware modifications

The recording system described in §5.2.5 writes to 7-track computer tape, which cannot now be read by any computer at the University of Adelaide. If the existing equipment is to be used, it must be interfaced with a new system for recording data. This could be done in three different ways:

a) replace the interface to the Kennedy incremental recorder with one to some other recording device and put a new subroutine (in 6502 machine code) to transfer data from the memory of the SYM-1 microcomputer to this new device.

b) Implement the RS-232 interface on the SYM-1 and use it to transfer data from the SYM-1 to a modern personal computer.

c) Remove the digitizer and SYM-1 microcomputer and connect the pulse counters directly to a personal computer.

While option c) requires the most work, it is the best option because it would allow substantial increases in the recording capability (*eg* longer data sets and higher frequencies), in the ease of changing the parameters of recording and in the ease of writing better preprocessing programs. It would allow the use of the extensive range of software that is available for data analysis on personal computers, including "on-line" analysis.

A major disadvantage of the present system is the requirement for manual star tracking and (in the case of the "multiple collimator") aperture selection. These require considerable patience, agility and manual dexterity over several hours. The tracking could be accomplished using a commercial system for amateur astronomy, preferably an alt-azimuth mounting with computer control. This would be a significant improvement, as it would allow fast switching from one star to another and unattended operation for some measurements. Automation of aperture selection in the "multiple collimator"

(currently done by moving an optical cable from one hole to another by hand) would require a custom-built mechanical device and so is not recommended. It would probably be cheaper to use a two-dimensional image intensifier, as used by Azouit and Vernin (1980).

11.4.4 Useful measurements with the refurbished system

There are some measurements which are performed better with the equipment used for this thesis, rather than with an image intensifier system:

a) measurement of moments (*ie* of $\frac{\langle I^n \rangle}{\langle I \rangle^n}$ for $n = 3, 4, 5...$ and instantaneous intensity I) should be made with photomultipliers as they have better signal-to-noise performance at low light levels than other devices (Candy, 1985b).

b) The single/double star moment comparison to measure isoplanatism should also be made using photomultipliers, as it requires accurate determination of moments at low light levels.

Some techniques proposed in this thesis gave unsatisfactory results due to the lack of sufficient or suitable data, such as:

c) the observation of interaction between turbulence produced at different heights.

d) The use of the function Q_{ur} to produce a wind profile without the false peak at low altitudes.

e) Double-slit observations in a situation where the height and speed of two turbulent layers can be deduced simultaneously.

These observations could be made if the present system were to be returned to operation.

11.5 Suggestions for new techniques

During the writing of this thesis two new techniques were devised and are described below.

11.5.1 Extended-source wind sensing

Just as a double star produces two scintillation patterns, an extended source will produce a scintillation pattern in which each feature of the source is reproduced *ie* the scintillation pattern will be the convolution of the pattern for a single star with the intensity distribution of the source, with a "magnification" determined by the height of

the turbulence. Suitable sources are a group of stars of approximately equal magnitude within a small region, or a part of the Moon.

A suggested instrument to exploit such an extended source for atmospheric measurements would be a telescope with an aperture plane mask which is a negative image of the source. This would enhance the signals due to turbulence at the particular height which produces an "image" in the scintillation pattern which has the same size as the image in the mask. For example, there would be occasions when turbulence at the point of inversion between the source and the image in the mask would produce a bright point on all transmitting parts of the mask at the same time. To make a wind measurement at the height of the inversion point would require the mask to have a second, similar negative image displaced from the first one in the direction of the wind, so that the wind speed could be determined by the time delay between similar signals.

To determine a wind profile would require measurements with a large number of masks of different magnification and direction of duplication. Thus the method would not be practical unless the different aperture masks could be implemented electronically.

A further extension of this technique would be to use it for measurement of wind in the atmosphere along horizontal paths, using a random scene as the source.

11.5.2 Wind measurement based on the Earth's rotation

A factor that has been neglected in this thesis (because its effect was not significant in the measurements made) is that a small fraction of the velocity of the scintillation pattern is produced by the Earth's rotation. For example, for a star passing through the zenith, the scintillation pattern produced by stationary turbulence at an altitude of 10 km moves at 0.7 ms^{-1} towards the east, due to the Earth's rotation. The speed and direction will be different for another star at any other altitude or azimuth. Thus the height may be deduced from the difference in the velocities of the scintillation patterns of two stars.

To apply this method requires that:

a) the wind velocity must be uniform over an area which is intersected by the lines of sight to both stars.

b) The velocities of the scintillation patterns must be determined with sufficiently high accuracy to allow the small difference to be measured.

Bibliography

Air Force Cambridge Research Laboratories *Handbook of Geophysics and Space Environments* ed. by S. L. Valley (1965).

Allen, C. W. *"Astrophysical Quantities"* 207 3rd edn. Univ. of London, Athlone press (1973).

Anderson, J. A. *J. opt. Soc. Am.* **25,** 152–155 (1935).

APS study: Science and Technology of Directed Energy Weapons, edit. by Pake, E. *Rev. mod. Phys.* **50**, S98–S104 (1987).

Aristotle *"De Caelo"* Book 2, ch. 8, par. 290a, 18 (*circa* 330 B.C.) Clarendon Press (1922).

Azouit, M. & Vernin, J. *J. Atmos. Sci.* **37,** 1550–1557 (1980).

Azouit, M., Vernin, J., Barletti, R., Ceppatelli, G., Righini, A. & Speroni, N. *J. appl. Meteorol.* **19,** 834–838 (1980).

Barakat, R. *J. opt. Soc. Am.* **66,** 211–216 (1976).

Barletti, R., Ceppatelli, G., Paternò, L., Righini, A. & Speroni, N. *J. opt. Soc. Am.* **66,** 1380–1383 (1976).

Batchelor, G. K. *"The Theory of Homogeneous Turbulence"* Cambridge (1953).

Ben-Yosef, N. & Goldner, E. *Appl. Opt.* **27,** 2167–2171 (1988).

Beran, M. J. & Whitman, A. M. *Appl. Opt.* **27,** 2178–2182 (1988).

Booker, H. G., Ratcliffe, J. A. & Shinn, D. H. *Phil. Trans. R. Soc. A* **242,** 579–607 (1950).

Boutet, R. *Annls. Géophys.* **5,** 310–312 (1949).

Breitenberger, E. *Prog. nucl. Phys.* **4,** 56 (1955).

Brown, J. H. & Good, R. E. *"Thermosonde and UHF Radar Measurements of C_n^2 at Westford, Massachusetts - July 1981"* AFGL-TR-84-0109 (1984a).

Brown, J. H. & Good, R. E. *"Thermosonde C_n^2 measurements in Hawaii - August 1982"* AFGL-TR-84-0110 (1984b).

Bufton, J. & Genatt, S. H. *Astr. J.* **76,** 378–386 (1971).

Bufton, J. L. *"An investigation of Atmospheric Turbulence by Stellar Observations"* NASA Technical Report R-369 (1971).

Bufton, J. L., Minott, P. O., Fitzmaurice, M. W. & Titterton, P. J. *J. opt. Soc. Am.* **62,** 1068–1070 (1972).

Bufton, J. L. *Appl. Opt.* **12,** 1785–1793 (1973).

Burke, J. J. *J. opt. Soc. Am.* **60,** 1262–1264 (1970).

Butler, H. E. *Nature* **167,** 287–288 (1951).

Butler, H. E. *Proc. R. Irish Acad.* **54,** 321 (1952).

Caccia, J. L., Azouit, M. & Vernin, J. *Appl. Opt.* **26,** 1288–1294 (1987).

Caccia, J.-L. & Vernin, J. *J. Geophys. Res. D* **95,** 13683-13690 (1990).

Campbell, L. & Elford, W. G. *J. atmos. terr. Phys.* **52,** 313–320 (1990).

Candy, B. H. *Rev. scient. Instrum.* **56,** 183–193 (1985a).

Candy, B. H. *Rev. scient. Instrum.* **56,** 194–200 (1985b).

Chandrasekhar, S. *Mon. Not. R. astr. Soc.* **112,** 475 (1952).

Chonacky, N. & Deuel, R. W. *Appl. Opt.* **27,** 2214–2221 (1988).

Churnside, J. H., Hill, R. J., Conforti, G. & Consortini, A. *Appl. Opt.* **28,** 4126–4132 (1989).

Coates, P. B. *J. Phys. E: Sci. Inst.* **4,** 201–207 (1971).

Coates, P. B. *J. Phys. D: Appl. Phys.* **5,** 915–930 (1972).

Coates, P. B. *J. Phys. D: Appl. Phys.* **6,** 1159–1166 (1973).

Coulman, C. E. *Boundary Layer Meteorology* **4,** 169–177 (1973).

Coulman, C. E. *Ann. Rev. Astron. Astrophys.* **23,** 19–57 (1985).

Coulman, C. E., Vernin, J., Coqueugniot, Y. & Caccia, J. L. *Appl. Opt.* **27,** 155–160 (1988).

Dainty, J. C., Levine, B. M., Brames, B. J. & O'Donnell, K. A. *Appl. Opt.* **21,** 1196–1200 (1982).

Dainty, J. C. *"Laser Speckle and Related Phenomena"* Springer-Verlag, Berlin (1984).

Douglass, A. E. *Popular Astronomy* , (June 1897), reprinted in *"Amateur Telescope Making"*, Book 2, 585–605 Scientific American Inc. (1972).

Eaton, F. D., Peterson, W. A., Hines, J. R. & Fernandez, G. *Appl. Opt.* **24,** 3264–3273 (1985).

Elford, W. G. *private communication* (1975).

Ellison, M. A. & Seddon, H. *Mon. Not. R. astr. Soc.* **112,** 73–87 (1952).

Fante, R. L. *Proc. IEEE* **63,** 1669–1692 (1975).

Fante, R. L. *Proc. IEEE* **68,** 1424–1443 (1980).

Fried, D. L. & Seidman J. B. *J. opt. Soc. Am.* **57,** 181–185 (1967).

Fried, D. L. *J. opt. Soc. Am.* **72,** 52–61 (1982).

Gifford, F. Jr. & Mikesell, A. H. *Weather, Lond.* **8,** 195 (1953).

Gifford, F. Jr. *Bull. Am. met. Soc.* **36,** 35–36 (1955).

Goldner, E. & Ben-Yosef, N. *Appl. Opt.* **27,** 2172–2177 (1988).

Good, R. E., Watkins, B. J., Quesada, A. F., Brown, J. H. & Loriot, G. B. *Appl. Opt.* **21, 3373–3376** (1982).

Hill, R. J. & Clifford, S. F. *J. opt. Soc. Am.* **68,** 892–899 (1978).

H. M. Nautical Almanac Office *Explanatory Supplement to the Astronomical Ephemeris* Her Majesty's Stationery Office, London (1961).

H. M. Naut. Almanac Off. *The Star Almanac for Land Surveyors for the year 1985* Her Majesty's Stationery Office, London (1984).

Hocking, W. K. *J. atmos. terr. Phys.* **45,** 89–102 (1983).

Huffer, C. M., Trinklein, F. E. & Bunge, M. *"An Introduction to Astronomy"* Holt, Rinehart and Winston, Inc., N.Y. (1967).

Illingworth, V (ed.) *"A Dictionary of Astronomy"* Pan in association with The Macmillan Press, London (1979).

Isacker, J. Van *Institut Royal Météorologique de Belgique Publications Serie B* **8,** 1–110 (1953).

Iyer, R. S. & Bufton, J. L. *Opt. Commun.* **22,** 377–381 (1977).

Jakeman, E., Pike, E. R. & Pusey, P. N. *Nature* **263,** 215–217 (1976).

Jakeman, E., Parry, G., Pike, E. R. & Pusey, P. N. *Contemp. Phys.* **19,** 127–145 (1978).

Jakeman, E. & Pusey, P. N. *"Inverse scattering problems in optics"* in *Topics in current Physics* **20** ed. by Baltes, H. P. Springer-Verlag, Berlin (1980).

Keller, G. *J. opt. Soc. Am.* **45,** 845 (1955).

Kodak *"Kodak Wratten filters for scientific and technical use"* 22nd edn. Eastman Kodak Co., Rochester, N.Y. (1965).

Kolmogorov, A. N. *Comptes rendus (Doklady) de l'academie des science de l'URSS* **32** 16–18 (1941) reprinted in *"Turbulence, Classic papers on Statistical theory"* ed. by Friedlander S. K. & Topper, L. 159–161 Interscience Publishers, Inc., N. Y. (1961).

Krall, H.R. *IEEE Trans. Nucl. Sci* **NS-14,** 455–459 (1967).

Labeyrie, A. *Astron. Astrophys.* **6,** 85–87 (1970).

Lawrence, R. S. ESSA Tech. Rep. ERL168-WPL12 *Pt* 3.3 (1970)

Little, C. G. *Mon. Not. R. astr. Soc.* **111,** 289–302 (1951).

Lo, C. C. & Leskovar, B. *IEEE Trans. Nucl. Sci* **NS-30,** 445–450 (1983).

Lohmann, A. W. & Wirnitzer, B. *Proc. IEEE* **72,** 889–901 (1984).

Loos, G. C. & Hogge, C. B. *Appl. Opt.* **18,** 2654–2661 (1979).

Mascart *"Traité d'Optique"* **t. iii** 347–349 (1893).

Mandel, L. *J. opt. Soc. Am.* **70,** 873-874 (1980).

Megaw, E. C. S. *Nature* **166,** 1100–1101 (1950).

Mikesell, A. H., Hoag, A. A. & Hall, J. S. *J. opt. Soc. Am.* **41,** 689–695 (1951).

Mikesell, A. H. *Publs. U. S. nav. Obs., 2nd series* **17,** 141 (1955).

Minnaert, M. *"Light and colour in the open air"* (*circa* 1940) Bell (1959).

Minnaert, M. & Houtgast, J. *Z. Astrophys.* **10,** 86–99 (1935).

Morton, G. A. *Appl. Opt.* **7,** 1–10 (1968).

Newton, Sir I. *"Opticks"* (1730) Book 1, pt. 1, 110–111 in 4th. edn. by Dover (1952).

Nisenson, P & Stachnik, R. V. *J. opt. Soc. Am.* **68,** 169–175 (1978).

Ochs, G. R. & Lawrence, R. S. *"Measurements of Laser Beam Spread and Curvature"* ERL 106.WPL 6 (*circa* 1970).

Ochs, G. R. & Lawrence, R. S. *"Temperature and C_n^2 Profiles Measured Over Land and Ocean to 3 km Above the Surface"* NOAA TR ERL 251-WPL 22 U. S. Dept. of Commerce (1972).

Ochs, G. R., Wang, T.-i, Lawrence, R. S. & Clifford, S. F. *Appl. Opt.* **15,** 2504–2510 (1976).

Ochs, G. R. & Hill, R. J. *Appl. Opt.* **24,** 2430–2432 (1985).

Parry, G. & Walker, J. G. *J. opt. Soc. Am.* **70,** 1157–1159 (1980).

Paske, W. C. *Rev. scient. Instrum.* **45,** 1001–1003 (1974).

Peskoff, A. *J. opt. Soc. Am.* **58,** 1032–1040 (1968).

Protheroe, W. M. *Science, N.Y.* **134,** 1593–1599 (1961).

Protheroe, W. M. *Q. Jl. Roy. met. Soc.* **90,** 27–38 (1964).

Pusey, P. N. in *"Photon Correlation Spectroscopy and Velocimetry"* ed. by Cummins, H. Z. & Pike, E. R. Plenum, N. Y. (1977).

Ratcliffe, J. A. *Rep. Prog. Phys.* **19,** 188–267 (1956).

Rayleigh, Lord *Phil. Mag., series 5* **36,** 129–142 (1893).

Reiger, S. H. *Astr. J.* **68,** 395 (1963).

Rocca, A., Roddier, F. & Vernin, J. *J. opt. Soc. Am.* **64,** 1000–1004 (1974).

Roddier, C. & Vernin, J. *Appl. Opt.* **16,** 2252–2256 (1977).

Roddier, F *Prog. in Opt.* **xix,** 281–376 (1981).

Sasaki, O. & Sato, T. *Appl. Opt.* **18,** 3522–3525 (1979).

Schneiderman, A. M. & Karo, D. P. *J. opt. Soc. Am.* **68,** 338–347 (1978).

Shapiro, J. H. *IEEE Trans.* **COM-19,** 410–414 (1971).

Shapiro, J. H. *J. opt. Soc. Am.* **65,** 65–68 (1975).

Singleton, R. C. *IEEE Trans* **AU-17,** 93–103 (1969).

Spiegel, M. R. *"Theory and Problems of Statistics"* Schaum's Outline Series – McGraw-Hill, N.Y. (1972).

Stebbins, J. *Sky. Telesc.* **3,** 5 (1944).

Tatarski, V.I. *"Wave Propagation in a Turbulent Medium"* McGraw-Hill, New York (1961).

Taylor, G. I. *Proc. of the Royal Society, A* **clxiv,** 476–490 (1938), reprinted as *"The spectrum of turbulence"* in *"The Scientific Papers of Sir G. I. Taylor"* **ii** Cambridge U. P. (1960).

Townsend, A. A. *Q. Jl. Roy. met. Soc.* **91,** 1 (1965).

Van Albada-Van Dien, E. *Astron. Astrophys. Suppl. Ser.* **52,** 193–202 (1983).

Vernin, J. & Roddier, F. *J. opt. Soc. Am.* **63,** 270–273 (1973).

Vernin, J. & Roddier, F. *C. r. hebd. Séanc. Acad. Sci., Paris Série B* **280,** 463–465 (1975).

Vernin, J., Barletti, R., Ceppatelli, G., Paternò, L., Righini, A. & Speroni, N. *Appl. Opt.* **18,** 243–247 (1979).

Vernin, J. & Azouit, M. *J. Opt.* **14,** 5–9 (1983a).

Vernin, J. & Azouit, M. *J. Opt.* **14,** 131–142 (1983b).

Vernin, J. & Pelon, J. *Appl. Opt.* **25,** 2874–2877 (1986).

Weigelt, G. P. *Optica Acta* **26,** 1351–1357 (1979).

Whitman, A. M. & Beran, M. J. *J. opt. Soc. Am. A* **2,** 2133–2143 (1985).

Williams, A. & Smith, D. *Nucl. Instrum. Meth.* **112,** 131–135 (1973).

Winick, K. A. & Marquis, D. vL. *J. opt. Soc. Am. A* **5,** 1929–1936 (1988).

Witherell, P. G. & Faulhaber, M. E. *Appl. Opt.* **9,** 73–78 (1970).

Yamashita, M., Yura, O. & Kawada, Y. *Nucl. Instrum. Meth.* **196,** 199–202 (1982).

Young, A. T. *Appl. Opt.* **8,** 869–885 (1969a).

Young, A. T. *Appl. Opt.* **8,** 2431–2446 (1969b).